

**STUDIES ON THE GAS SENSING PERFORMANCE  
OF SINGLE AND MULTICOMPONENT OXIDES FOR  
ACETONE DETECTION**

**THESIS  
SUBMITTED FOR THE DEGREE OF  
DOCTOR OF PHILOSOPHY (SCIENCE)  
OF  
JADAVPUR UNIVERSITY  
2022**



**By**

**Puja Ghosh**

**Index No.: 173/18/Phys./26**

**Registration No.: SOPHY1117318**

**Functional Materials and Devices Division  
CSIR-Central Glass & Ceramic Research Institute  
196 Raja S. C. Mullick Road, Jadavpur  
Kolkata-700032, India**



## CERTIFICATE FROM THE SUPERVISORS

This is to certify that the thesis entitled “*STUDIES ON THE GAS SENSING PERFORMANCE OF SINGLE AND MULTICOMPONENT OXIDES FOR ACETONE DETECTION*” submitted by **Smt. Puja Ghosh** who got her name registered on **18th September, 2018 (Registration No.: SOPHY1117318 and Index No.: 173/18/Phys./26)** for the award of Ph. D. (Science) degree of Jadavpur University, is absolutely based upon her own work under the supervision of Dr. Parukuttyamma Sujatha Devi, Chief Scientist, Chemical Sciences and Technology Division, CSIR-NIIST, Thiruvananthapuram, Kerala-695019, India and Dr. Shrabanee Sen, Principal Scientist, Functional Materials and Devices Division, CSIR-CGCRI, Kolkata, West Bengal-700032 and that neither this thesis nor any part of it has been submitted for either any degree/diploma or any other academic award anywhere before.

*Sujatha.P 08/08/22*

Dr. P. Sujatha Devi  
Chief Scientist  
Chemical Sciences and Technology Division  
CSIR-NIIST  
Thiruvananthapuram, Kerala 695019

*Shrabanee Sen 08/08/22*

Dr. Shrabanee Sen  
Principal Scientist  
Functional Materials and Devices Division  
CSIR-CGCRI  
Jadavpur, Kolkata 700032



डॉ. पी. सुजाता देवी / Dr. P. SUJATHA DEVI  
मुख्य वैज्ञानिक एवं प्रमुख / Chief Scientist & Head  
रसायन विज्ञान तथा प्रौद्योगिकी प्रभाग  
Chemical Sciences and Technology Division  
सी एस आई आर- राष्ट्रीय अंतरविषयी विज्ञान तथा प्रौद्योगिकी संस्थान  
CSIR-National Institute for Interdisciplinary  
Science and Technology, Govt. of India  
तिरुवनन्तपुरम/Thiruvananthapuram-695 019



Dr. Shrabanee Sen  
Principal Scientist  
Functional Materials and Devices Division  
CSIR-Central Glass & Ceramic Research Institute  
Kolkata - 700 032

*Dedicated to*  
*Baba-Maa*

## **ACKNOWLEDGEMENTS**

*It gives me immense pleasure to express my deepest gratitude to those people whose guidance, assistance and un-towering belief in me helped me accomplish this journey. Therefore, I would like to thank the following persons for their help, dedication, prayers and support and wish that my thanks extend beyond the limit of this format.*

*At the outset, I would like to convey my heartfelt gratefulness to my supervisors who introduced me to this world of research and development in the area of sensors with great enthusiasm. I would like to express my sincere gratitude to my supervisor Dr. P. Sujatha Devi (Chief Scientist, Chemical Sciences and Technology Division, CSIR-National Institute for Interdisciplinary Science and Technology, Kerala and formerly Chief Scientist and Head Functional Materials and Devices Division, CSIR-Central Glass and Ceramic Research Institute, Kolkata) under whom I joined as an INSPIRE PhD student. I also thank Dr. Shrabanee Sen, Principal Scientist, Functional Materials and Devices Division, CSIR-Central Glass and Ceramic Research Institute for accepting to guide me as a supervisor along with Dr. P. Sujatha Devi. I thank both of them for their valuable inputs, guidance and needful support as well as the necessary suggestions during the course of my PhD program. Without their constant support and resourceful guidance, it would have never been possible for me to carry out this research work. I am grateful to acknowledge the excellent mentorship and guidance and moral support of both my supervisors over the years.*

*I heartily thank all the scientists, technical staff, research scholars and fellows of Functional Materials and Devices Division. Among them, as a special mention, this acknowledgement would remain incomplete without giving regards to Mrs. Mousumi Baral Narjinary (Senior Technical Officer, CSIR-CGCRI) for her enormous support throughout in sensor fabrication and characterization.*

*I also want to express my deepest gratitude to Dr. Koushik Biswas (Principal Scientist, Speciality Glass Division, CSIR-CGCRI), subject expert of my RAC of Jadavpur University for providing me valuable suggestions and moral support in many aspects.*

*I acknowledge Innovation in Science Pursuit for Inspired Research (INSPIRE) program of Department of Science and Technology, Government of India for the fellowship and contingency grant for carrying out my PhD work.*

*I really feel honoured for having come across brilliant teachers/mentors throughout my whole career. I would like to convey my genuine appreciation and profound gratitude to all of them. I am highly obliged to Dr Suman Kumari Mishra (Director, CSIR-CGCRI), Dr K. Muraleedharan (Ex-Director) and Dr. A. Ajayaghosh (Ex-Director, CSIR-NIIST) for their benevolent permission and various requisite approvals to carry out my research work.*

*I extend my thanks to all the members of Electron Microscopy Section, X-ray Characterization Section, X-ray Photoelectron Spectroscopy section and Central Material Characterization*

*Section of CSIR-CGCRI for their full assistance, cooperation, and kind support that I received from them for carrying out various characterizations needed during the pursuit of my research work and make it a successful one. I shall fail in my appreciation, if I do not recognize the cooperation and support received generously from scientists of several divisions and laboratories along with staff from the civil, electrical, canteen, store, library, reception, security section and the administrative offices of CSIR-CGCRI.*

*I would like to give huge and warm thanks to my seniors, juniors and fellow research scholars Pratanuda, Arindamda, Parthada, Debuda, Soumitadi, Krishnada, Anuragda, Sumitadi, Hassanda, Saranidi, Subasda, Ipsitadi, Abhishekda, Shewli, Gaurav, Sourav Maity and Sourav Mondal, Arindam, Pounomi, Soumya, Animesh, Deepak for their constant help, constructive criticism and astonishing support during the PhD period. I am also thankful to other seniors, juniors and friends of CSIR-CGCRI namely Subhankarda, Taniadi, Aditidi, Ganga, Susmitadi, Partha, Preeti, Payeldi, Sukanyadi and others. The sweet memories of their association in CSIR-CGCRI will remain with me forever. I would like to extend my thanks to all of my juniors and fellow research scholars from CSIR-NIIST namely Manikandan, Rishad, Aneesha, Swathy and Akshay for their enormous help and support.*

*Words keep falling short to express my deepfelt gratitude to my beloved Dadu, Dimma, my parents (Maa-Baba), parents-in law (Maa-Bapi), masimoni and meson and entire family members who have continuously encouraged and mentally supported me to overcome all the challenges during my PhD journey, keeping me aside from any difficulties in the family. Without their heartfelt blessing and un-ending support, I believe I would not reach my goal.*

*I find no exact word to thank my husband (Sayantan) for his all-round support during this journey. I am thankful to him for his countless support, understanding and for bearing me with my fluctuating mind in every situation.*

*Also thankful to my one and only sister (Mistu) for her unconditional, unwavering and relentless support and motivation during the entire course of my thesis work.*

*Last but not the least; I'm greatly privileged to thank "Almighty God" for giving me the strength, faith and bestowing me with unconditional blessings towards successful completion of my thesis.*

.....  
**Puja Ghosh**

## **ABSTRACT**

In the recent past, there has been a great impetus to design and develop functional nanomaterials for sensor applications. Among the various materials available, metal oxide semiconductors (MOS) stand out as a promising class of materials for gas sensor development due to their simplicity and low cost. The conductivity of metal oxide nanostructures changes with the surface adsorption and desorption of gas molecules which in turn strongly depend on the shape and the size of the nanostructures. The main lacunae of the semiconductor based thick film sensors however, lies in their high operating temperature and lack of selectivity to any particular gas. Taking into consideration of the importance of detecting acetone as a biomarker in breath for non-invasive detection of diabetes, this thesis work has been focused on developing nanomaterials and sensors thereby for acetone detection. As nanotechnology-enabled sensors offer significant advantages over conventional sensors, our focus was to employ nanomaterials of n-type, p-type and multicomponent oxides to achieve better sensitivity and selectivity, and low operating temperature for developing acetone sensors.

The thesis work has focused on the development of nano-structured semiconducting oxide materials based on  $\text{TiO}_2$ ,  $\text{Fe}_2\text{O}_3$ ,  $\text{WO}_3$ ,  $\text{BiFeO}_3$ ,  $\text{Zn}_2\text{SnO}_4$  and other mixed oxides for fabricating sensors to detect acetone. The major emphasis was given on preparation of above-mentioned materials having variable size, shape, morphology and surface properties. In-depth characterization of the synthesized materials was carried out in order to understand the size effect on various properties and their response towards acetone. Thick film sensor elements using such materials was fabricated and sensing parameters *viz.* sensitivity, selectivity, stability, reproducibility, response time, recovery time etc. were measured.

Initial work was focused on preparing various phases of  $\text{TiO}_2$ , their characterization and property evaluation followed by sensing characteristics evaluation. As the response of single phase  $\text{TiO}_2$  based materials was not good, we synthesized a composite  $\text{Na}_{0.23}\text{TiO}_2$ -anatase  $\text{TiO}_2$

nanorod as a sensing material showing higher and significant sensing properties at room temperature towards various concentrations of acetone. As a continuation of this work, next focus was to understand the acetone sensing characteristics of various iron oxides and the effect of different structure on sensing performance. In this work response of the materials have been studied through DC and AC measurements. Here we could establish iron oxide fibers as a better structure exhibiting improved sensing characteristics than other shapes. Improved surface modified  $\text{WO}_3$  fiber samples exhibited 90% acetone sensing at  $150^\circ\text{C}$  operating temperature which will be an improved material for developing acetone sensor for practical application due its lower operating temperature.

In this work, we have also focused on ternary metal oxide-based sensing materials for acetone sensor development for futuristic applications. Here, our attention has been to discover vacancy-induced sensing properties of sonochemically synthesized p-type  $\text{BiFeO}_3$  nanoparticle exhibiting rapid response, recovery time, good selectivity, stability and reproducibility. In this thesis work we have also proposed  $\text{Zn}_2\text{SnO}_4$  exhibiting exceedingly high response time of around 2 seconds towards acetone with 96% response at comparatively lower operating temperature.

Thus, in this thesis work response of various n-type and p-type single component nanostructured oxides and multicomponent oxides towards different concentrations of acetone have been demonstrated along with comparison and understanding of sensing mechanism through AC and DC electrical measurement techniques. Some of the studied materials exhibited exceedingly high response of 96% and above towards acetone which has been projected as potential candidates for developing sensor modules for non-invasive detection of diabetes through acetone sensing from exhaled breath.

## *Table of Contents*

<b>Particulars</b>	<b>Page No.</b>
<b>ACKNOWLEDGEMENTS</b>	i-ii
<b>ABSTRACT</b>	iii-iv
<b>CHAPTERS</b>	1-204
<b>Chapter 1: Background and Literature Review</b>	1-40
1.1. Introduction	1
1.2. Sensor in General	2
1.3. Essential Characteristics of an Ideal Sensor	2
1.4. Gas Sensor: An Overview	4
1.5. Areas of Application for Chemical Gas Sensor:	5
1.6. Review of the Gas Sensing Technologies	6
1.7. Types of Gas Sensor	6
1.7.1. Sensors Based on Reactivity of Gas	6
1.7.2. Sensors Based on Physical Properties of the Gas	8
1.7.3. Sensor Based on Gas Sorption	9
1.7.3.1. Field Effect Transistor (FET) Based Gas Sensors	9
1.7.3.2. Schottky barrier/Heterocontact Sensors	10
1.7.3.3. Conductive Polymer Sensors	10
1.7.3.4. Fibre-Optic Sensors	10
1.7.3.5. Microbalances	10
1.8. Metal Oxide Based Gas Sensor	11
1.9. Performance of Gas Sensors- Influencing Factors	13
1.10. Gas Sensing Characteristics of Metal Oxides based Gas Sensor	17
1.11. Metal Oxides for Gas Sensor Applications	20
1.12. Sensor as Biomarker Detection	22
1.13. Gas Sensing Mechanism and Working Principle of SMO Gas Sensors	24
1.14. Acetone Gas Detection	27
1.15. Motivation and Scope of the Present Work	28
1.16. Objectives of the Present Work	30
1.17. References	32





<b>Chapter 2: Synthesis and Characterization Techniques</b>	<b>41-80</b>
2.1. Introduction	41
2.2. General Methods for the Synthesis of Nanomaterials	42
2.2.1. Sonochemical Synthesis	42
2.2.2. Solid State Synthesis	43
2.2.3. Hydrothermal Synthesis	44
2.2.4. Electrospun Technique	44
2.3. Synthesis of Different Binary and Ternary Metal Oxide	46
2.3.1. Anatase Cube, Rutile Rod and Composite Rod	46
2.3.1.1. Synthesis of Anatase TiO <sub>2</sub> Nanocube	46
2.3.1.2. Synthesis of Rutile TiO <sub>2</sub> Nanorod	46
2.3.1.3. Synthesis of Composite Nanorod	47
2.3.2. Synthesis of different phases of Iron Oxides	47
2.3.2.1. Synthesis of $\gamma$ -Fe <sub>2</sub> O <sub>3</sub> Nanoparticle	47
2.3.2.2. Synthesis of Fe <sub>3</sub> O <sub>4</sub> Nanoparticle	48
2.3.2.3. Synthesis of $\alpha$ -Fe <sub>2</sub> O <sub>3</sub> Nanoparticle	48
2.3.2.4. Synthesis of $\alpha$ -Fe <sub>2</sub> O <sub>3</sub> Fiber	48
2.3.3. Synthesis of different morphology of Tungsten Oxide	49
2.3.3.1. Synthesis of WO <sub>3</sub> Nanoparticle	49
2.3.3.2. Synthesis of WO <sub>3</sub> Nanofiber	49
2.3.4. Synthesis of Bismuth Ferrite	50
2.3.5. Synthesis of Zn <sub>2</sub> SnO <sub>4</sub>	50
2.3.5.1. Sonochemical Synthesis of Zn <sub>2</sub> SnO <sub>4</sub> Nanoparticles	50
2.3.5.2. Solid State Synthesis of Zn <sub>2</sub> SnO <sub>4</sub> Nanostructures	51
2.3.5.3. Hydrothermal Synthesis of Zn <sub>2</sub> SnO <sub>4</sub> Nanoparticles	52
2.4. Characterization of the Synthesized Powder Samples	52
2.4.1. Structural Analysis	52
2.4.1.1. Thermogravimetric Analysis	53
2.4.1.2. Differential Thermal and Scanning Calorimetry Analysis	53
2.4.1.3. X-ray Diffraction Analysis	55
2.4.2. Microstructural Characterization	57
2.4.2.1. Field Emission Scanning Electron Microscopy	57



2.4.2.2. Transmission Electron Microscopy	59
2.4.3. Spectroscopic Techniques	60
2.4.3.1. Fourier Transform Infrared Spectroscopy	60
2.4.3.2. UV-Visible Spectroscopy	62
2.4.3.3. Raman Spectroscopy	63
2.4.3.4. X-ray Photoelectron Spectroscopy	65
2.4.4. Specific Surface Area Analysis	65
2.4.5. Zeta Potential Measurement and Particle Size Analysis	67
2.4.6. DC Current-Voltage ( <i>I-V</i> ) Characteristics Measurement	68
2.5. Sensor Fabrication Details	69
2.5.1. Fabrication of Sensors	69
2.5.2. Substrate Preparation, Coating on Substrate and Heat Treatment	70
2.5.3. Stabilization of the Coated Sensing Material	72
2.6. Gas Sensing Measurement Details	73
2.6.1. Gas Selectivity Measurement	75
2.6.2. Measurement of Sensor Stability	75
2.6.3. Sensor Terminology	76
2.7. Conclusion	77
2.8. References	77
<b>Chapter 3: Performance of Single Component Metal Oxide-based Acetone Sensor</b>	<b>81-159</b>
3.1. Introduction	81
3.2. TiO <sub>2</sub> Based Oxides: Phase Dependence on Acetone Sensing (Anatase, Rutile, Anatase-Na <sub>0.23</sub> TiO <sub>2</sub> Composite)	82
3.2.1. Introduction	82
3.2.2. Structural and Optical Properties Analysis	83
3.2.3. Microstructural Study	85
3.2.4. Surface Area Analysis	86
3.2.5. Acetone Sensing	87
3.2.6. Anatase-Na <sub>0.23</sub> TiO <sub>2</sub> composite nanorod based Acetone Sensing	90
3.2.7. Thermal Analysis	91
3.2.8. Effect of pH on Phase and Morphology Formation	91



3.2.9. Optimization of Hydrothermal Conditions	93
3.2.10. Phase Evaluation	96
3.2.11. Mechanism of Phase and Morphology Transformation	98
3.2.12. Transmission Electron Microscopic (TEM) Analysis	99
3.2.13. X-ray Photoelectron Spectroscopic (XPS) and Surface Area Analysis	101
3.2.14. Acetone Sensor Application	104
3.2.15. Conclusion	109
3.3. Fe <sub>2</sub> O <sub>3</sub> Based Oxides: Phase and Shape Dependence on Acetone Sensing	110
3.3.1. Introduction	110
3.3.2. Results and Discussion	110
3.3.2.1. Nanoparticles of $\gamma$ -Fe <sub>2</sub> O <sub>3</sub> and Fe <sub>3</sub> O <sub>4</sub> and their sensing Behaviour	110
3.3.2.2. Surface Area	116
3.3.2.3. Magnetic Study	117
3.3.2.4. Sensing Properties	118
3.3.2.5. Gas sensing mechanism	124
3.3.2.6. Electrical Impedance Spectroscopy (EIS) Measurements	125
3.3.3. Nanoparticles and Nanofibers of $\alpha$ -Fe <sub>2</sub> O <sub>3</sub>	128
3.3.3.1. Structural and Morphological Analysis	128
3.3.3.2. Sensing Measurements	130
3.3.4. Conclusion	135
3.4. Fiber and Particle Based WO <sub>3</sub> for Acetone Sensing	136
3.4.1. Introduction	136
3.4.2. Results and discussions	137
3.4.3. Sensing Measurements Data	142
3.4.4. Gas Sensing Mechanism	150
3.4.5. Conclusion	153
3.5. References	154
<b>Chapter 4: Ternary Metal Oxide-based Acetone Sensor</b>	<b>160-198</b>
4.1. Background	160
4.2. BiFeO <sub>3</sub> (BFO) Nanoparticles for Acetone Sensing: Synthesis, Characterization and Performance evaluation	160

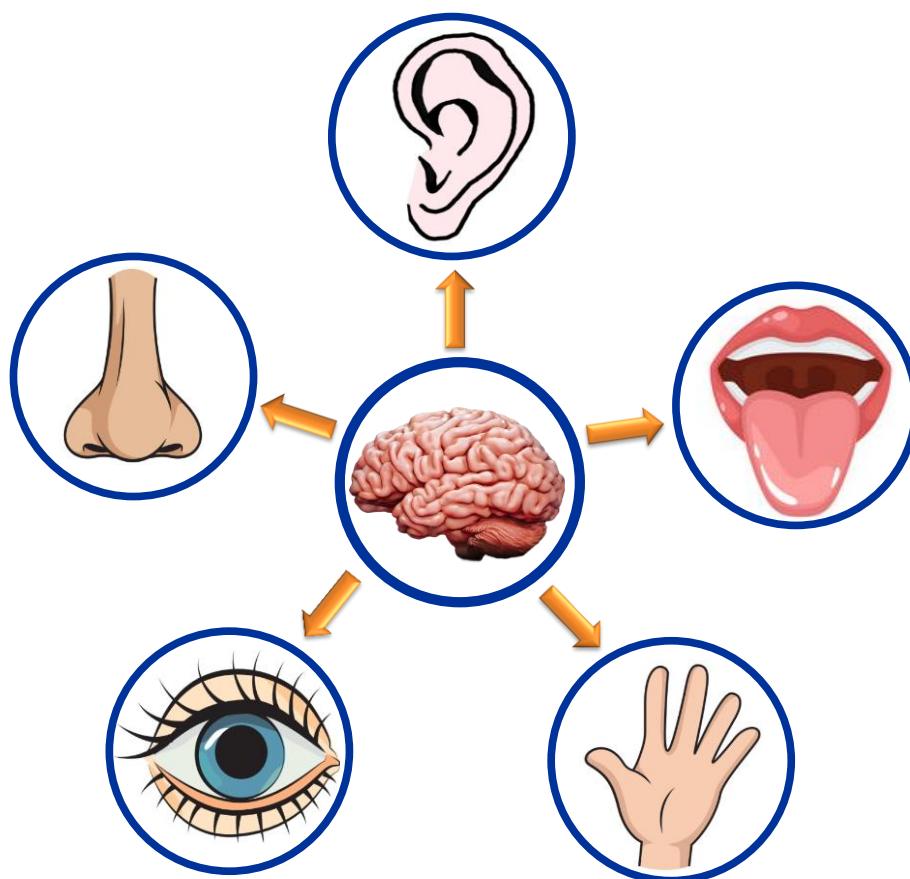


4.2.1. Introduction	160
4.2.2. Thermogravimetric analysis	161
4.2.3. Structure and Optical Analysis	162
4.2.4. Transmission Electron Microscopy Study	164
4.2.5. X-ray Photoelectron Spectroscopy Study	165
4.2.6. Magnetic Study	168
4.2.7. Microstructural Analysis of fabricated BiFeO <sub>3</sub> Nanoparticles based Film	169
4.2.8. Acetone Sensor Application	170
4.2.9. Impedance behavior under dry air and acetone	175
4.2.10. Gas Sensing Mechanism	177
4.2.11. Conclusions	178
4.3. Zn <sub>2</sub> SnO <sub>4</sub> based material for Acetone Sensing	180
4.3.1. Background	180
4.3.2. Results and Discussion	181
4.3.3. Sensor Measurements	183
4.3.4. Conclusion	195
4.4. References	195
<b>Chapter 5: Summary and Conclusions</b>	<b>199-204</b>
<b>Symbols and Abbreviations</b>	<b>205-207</b>
<b>Publications and Conferences</b>	<b>208-212</b>



# CHAPTER-I

## Background and Literature Review



*Sensors have been developed mimicking nature's creations which are the five sensory organs. This chapter initially discusses the history of development of sensors and then goes on to explain the basics of a sensor, the different types of gas sensors, their characteristics, the areas of applications of such sensors, their advantages and drawbacks of each type of sensors. Then enumeration has been done on the current status of the latest development of different types of Gas Sensors and their applications in the real world. One such latest area of research is how Sensors can be used as Biomarker to detect various physiological disorders, so that such detection becomes non-invasive and painless. With the turn of the millennium, Diabetes has been one of the most widely found disorders. Thus, we have focused in developing different single and multicomponent metal oxide-based gas sensor as our research topic which will pave a new era of non-invasive methodology of diabetes detection. The sensor aims towards reliable measurement of Acetone concentration in human breath so that the Blood Glucose level can be detected in a painless manner.*

### **1.1. Introduction:**

Nature has endowed humans and animals with five primary sense organs namely eyes, ears, tongue, skin and nose. To mimic nature's creations has long been an interesting human endeavour and consequently with time and effort many developments had happened in the world. Today there are cameras that mimic the eyes, microphones with tape-recorder that mimic the ears and tactile sensors that mimic the skin. Similarly, for mimicking the function of nose and tongue, chemical sensors have been developed. These sensors perform the important task of sensing chemical analytes and also giving quantitative information of the concentration of analyte in the environment. Thus, sensors have the function of converting a certain stimulus into a measured signal. The stimulus can be mechanical, thermal, electromagnetic, acoustic or chemical in origin, while the measured signal is typically electrical in nature, although pneumatic, hydraulic and optical signal may also be employed. Gas detection instruments are increasingly needed for safe environmental monitoring and process control [1-3]. Such detection units are important in monitoring of toxic gases like CO, SO<sub>2</sub>, Cl<sub>2</sub>, combustible gases like methane, LPG, CNG, hydrogen and automobile exhaust pollutants like SO<sub>x</sub>, NO<sub>x</sub>, hydrocarbons etc. Similarly, gas sensors are of paramount importance for detection of fire/smoke, explosive, nerve gas, ozone layer damaging halocarbons (CFC), freshness of fruits and fishes, and in medical diagnostic like breath alcohol analyzer, diabetes detection etc [4-13]. In recent years, with increasing demand and development of sensors, sensor technology has flourished as a need for physical, chemical and biological recognition systems and as a result of that transducing platforms also have grown. In today's life, sensors are used in applications ranging from environmental pollution monitoring, medical and health care diagnostics, disease detection, industrial manufacturing like fermentation and process control, air quality and food quality monitoring and food quality monitoring, defence, safety and security areas.

### **1.2. Sensor in General:**

‘The word ‘Sensor’ traces its origin to a word of Latin origin ‘sentire’, meaning of this Latin word is ‘to perceive’ or ‘to sense’ [14]. Thus, taking clue from the Latin word it can be easily perceived that sensor is a type of device which can receive an input in the form of physical, chemical or any other signals and then transform that signal into any output which can be easily measured by any suitable methodology. As enumerated in a study, a sensor is best defined as an entity which gives suitable response when exposed to any external stimulus, which can be in the form of an energy variation, and the response is obtained in the form of an output and such output can be functionally related to the input energy/stimulus and measured in a suitable way [15]. Sensor, depending on its type, detects any physical signal or chemical signal in the form of various organic and inorganic compounds and converts these physio-chemical inputs/signals into an electrical output, a few common sensing devices which contains sensors are phototransistor, microphone, thermocouple, photoresistor, hydrophone, seismometer, or even the daily-used thermometer. Sensor can also be designated as any device that converts any signal from one form to another much like what a transducer does. Sensors are thus an interface between the physical world, where inputs are plenty, and the world of measurable outputs which may be in the form of electrical outputs or any other suitable output. Depending on the sensing ability, sensors can be classified into two types, namely Type I and type II sensors. Type I sensors are those which detect only the presence of a stimulus and produces a suitable measurable output. Type II sensors are those which along with detecting the presence of any stimulus can also measure the quantity or value/volume of any input stimulus.

### **1.3. Essential Characteristics of an Ideal Sensor:**

Essential but simple characteristics of a sensor unit have been discussed in various ways like:

- The sensor should have higher sensitivity and the sensitivity is measured by the change of signal per analyte concentration unit.
- It is essential that a sensor should have the ability to overcome the environmental effects like temperature, humidity, shock, vibration etc. which can influence negatively on the performance of the sensors.
- As a general characteristic, sensor should be inexpensive yet reliable and durable.
- Selectivity is one of the most important characteristics that determine whether a sensor can give the response selectively towards specific single analyte gas.
- Sensor should have the ability to provide reproducible results and good stability of sensing response for a certain period of time.
- Resolution can be calculated with the lowest concentration difference which should be distinguished by sensor.
- Response time is calculated by the time for sensor responding to a step concentration change from ground to certain peak value after injecting target gas.
- Recovery time is the time taken by the sensor to return to its initial stage after removing the target gas.
- Another vital point for ideal sensor is working temperature at which temperature the sensor shows maximum sensitivity.
- Life cycle can be measured by the time period at which the sensor will operate continuously.

All the above parameters have been addressed to characterize the sensing properties of a semiconductor material-based gas sensor. An ideal metal oxide-based gas sensor should have the ability of high sensing response, dynamic range, low range detection limit, good selectivity and long-term stability, small response and recovery time and long period of life cycle.



### **1.4. Gas Sensor: An Overview**

Among various categories of sensors, gas sensors are a group of chemical sensors and due to its wide nature of applications across various fields; these are one of the most common type of sensors seen in and around us. Gas sensor generally interacts with a gas to which the sensor is sensitive and as an output it measures the concentration of gas. Actually, gas sensor is a type of transducer (transducer is a device that converts one form of input energy into another form of output energy which can be measured) when exposed to an input stimulus in the form of presence of gas to which the sensor is sensitive, it produces an electrical signal where the magnitude of the signal is generally proportional to the concentration of the target gas. Thus, these types of Sensors are Type 2 gas sensors which can not only detect the presence of a particular gas but also can detect the concentration of the gas. Gas sensors are commonly used in a plethora of industrial and domestic uses ranging from various safety measures, process control and improvement activity, defence department, monitoring of environment and many other commercial as well as domestic applications. Examples of the requirement of sensors in various applications are plenty in our environment. To explain through an example, it can be seen that timely detection of leakage of hydrogen gas may not be possible without a suitable sensor because of the colourless, tasteless, odourless nature of hydrogen gas making it near impossible for its detection by a normal human being. Acetone is also a colourless, volatile gas, which is very difficult to detect without any sensor device, and its detection is very important because acetone may cause toxic effects on the central nervous system of our body. Other odourless gases like Liquefied Petroleum Gas (LPG) thus have to be mixed with a pungent smelling methyl-mercaptan to enable quick detection by human beings, so that appropriate measures can be taken on time. Gas sensors have also been found its use in non-invasive detection of various diseases by breath analysis.

### **1.5. Areas of Application for Chemical Gas Sensor:**

#### **❖ Safety in Domestic, Industrial Sector:**

- Fire or Smoke detection (CO, LPG, CNG, methane, hydrogen), natural gas heating.
- Detection of toxic gases like CO, NH<sub>3</sub>, H<sub>2</sub>S.
- Explosive Detection.
- Detection of Fire/Smoke
- Nerve Gas/ Poison Gas Detection like Sulfur mustard
- Boiler control

#### **❖ Monitoring Environmental Pollution and Control:**

- SO<sub>x</sub>, NO<sub>x</sub>, CO, HC, CO<sub>2</sub> etc. detection.
- Halocarbons like CFC detection.

#### **❖ Food and Biomedical Applications:**

- Food Quality Detection (Freshness of fruits, fishes, Grading of Argo products like tea, coffee, spices etc.).
- Odour Detection (Sulphides, Amines).
- Process control
- Packaging quality control (off odours)

#### **❖ Medical Field**

- Biomarker for Breath VOC analysis.
- Disease detection through breath analysis (nitric oxide present in asthma patients, acetone present in diabetic patients' breath).

#### **❖ Automobile:**

- Drivers' cabin air quality.
- Filter control
- Gasoline vapour detection

### ❖ **Military:**

- Chemical and biological warfare.

### ❖ **Mine:**

- Detection of harmful gases in mines (methane detection).

## **1.6. Review of the Gas Sensing Technologies**

For the development of smaller and inexpensive gas sensors, the global research community has been focusing on designing sensor devices which exhibit high sensitivity or response, selectivity and stability with respect to a specific application. A large variety of sensors have been established based on different sensing principles such as semiconductor gas sensors, optical sensors, thermal conductivity sensors, mass sensitive devices like quartz microbalance sensors, catalytic sensors, dielectric sensors, electrochemical sensors and electrolyte sensors etc. Actually, the gas molecules interact or adsorb onto the surface of a gas sensitive material, then the electrical characteristics of the material changes in presence of target gases, by which we can measure the presence and concentration of gas. The electrical parameters extracted can be in a wide range such as DC resistance, AC resistance, AC impedance, Field Effect Transistor (FET) threshold voltage, phase change of a wave which propagated across the sensor surface, resonant frequency etc.

## **1.7. Types of Gas Sensor:**

Depending on the operating principle, different kinds of sensor systems can be designated for gas monitoring for different applications. According to detection principles, commonly used gas sensors can be classified into the following three groups:

### **1.7.1. Sensors Based on Reactivity of Gas**

These sensors generate a signal by measuring some aspects of chemical reactions of the analyte.

### *(a) Electrochemical Sensor*

Electrochemical sensors are one type of detectors that measure the concentration of target gas by oxidizing or reducing the target gas at an electrode and measuring the resulting current. Actually, oxidization process takes place at the anode and reduction at the cathode side. Electrochemically reducible gases like oxygen, nitrogen oxides and chlorine are sensed at the cathode while oxidizable gases such as carbon monoxide, nitrogen dioxide, hydrogen and hydrogen sulfide are sensed at the anode side [16]. The output of electrochemical cell is directly proportional to the concentration or partial pressure of gaseous species. Depending on whether the output is an electromotive force (for open circuit voltage) or an electrical current (for closed circuit), the electrochemical gas sensors are classified as potentiometric or amperometric. Incidentally, biosensor comprise a biological recognition element (e.g., biocatalysts like enzymes, microorganism, tissue materials and bioligands like antibodies, nucleic acids, lectins) which interact with the target analyte and a transducer which is mostly of electrochemical type. Selectivity of electrochemical sensors is quite good, but their life expectancy is short [17,18].

### *(b) Combustible gas sensor/microcalorimetric gas sensor/pellistor*

Combustible gases are allowed to burn with air on surface of a small ball or film of a catalytically active metal. The catalyst (e.g., Pt, Pd or Rh) is kept around 500-600°C. The heat of combustion is balanced by a reduction in electrical heating power. The power consumption serves as the symbol indicating the concentration of flammable gases. These sensors have long stability but are susceptible to catalyst poisoning with consequent erroneous results [19].

### *(c) Colorimetric paper tape*

Gases like isocyanates, arsine, phosphine, chlorine can be detected by noting the colour change of paper tapes in presence of gas, colour change can be measured by using light reflectance technology [20].

### *(d) Chemiluminescence*

Certain chemical reactions generate light, which can be measured with great sensitivity. The most common application of chemiluminescence in gas detection is the measurement of nitric oxide by reaction with ozone [21].

### *(e) Semiconductor Sensor*

They are primarily based on n-type semiconducting oxides and their resistance values drop drastically in presence of reducing gases owing to the reaction of the latter with metastable adsorbed oxygen species on surface of the semiconductor. Semiconductor sensors show poor selectivity in addition to baseline drift. However, they are quite cheap, rugged and can last up to ten years [22,23]. For an n-type material, resistance increases in presence of an oxidizing gas and it decreases in presence of reducing gases. Similarly for p-type oxides, resistance decreases in presence of oxidizing gases and it increases in presence of reducing gases.

### **1.7.2. Sensors Based on Physical Properties of the Gas**

Such sensors generally leave the analytic gas undisturbed. Through the sensors of this group are complex and expensive, they are quite selective.

#### *(a) Non-dispersive infrared*

All gases, excluding monoatomic molecules such as helium and argon, and symmetric diatomic molecules such as nitrogen and oxygen, have the characteristic absorption in the infrared region. It is possible to determine the concentration of the detected gas by irradiating infrared to sample gas and measuring strength of the infrared ray in absorption wavelength range [24].

#### *(b) Photoacoustic Sensors*

If a short pulse of IR ray is passed through an absorbing gas, the absorbed light energy becomes heat. The sudden expansion of the gas generates a pressure, or acoustic wave, which can be

measured with a microphone. Since photometric error is eliminated in the process, very sensitive detection is possible using these sensors [25,26].

### *(c) Thermal Conductivity Sensors*

To compensate for the inability of many detectors to measure high concentrations of gas, some instruments incorporate a thermal conductivity filament which is used to compare the thermal conductivity of the sample gas with that of air or purge gas. Although this method is by no means as sensitive or selective in the determination of flammable gases, it does find some application where high gas concentrations are encountered and also during gas purging operations [27,28].

### **1.7.3. Sensor Based on Gas Sorption**

#### *1.7.3.1. Field Effect Transistor (FET) Based Gas Sensors*

FET based sensor works on the Metal Oxide Semiconductor junction principle. Since the invention of the first ISFET (Iron Selective Field Effect Transistor) by Bergvelt in 1970 and Pd gate Si-FET gas sensor in 1975 by Lundstrom et. al., the FET gas sensor area became wider by the use of catalytic metals, like porous metal layers of platinum (pt), iridium (Ir) and semiconductors [29-32]. On the other side MOSFET based gas sensors are complex in nature and are more difficult to fabricate. Due to the compatibility of the FET structure with microfabrication processes, Chemical FET (CHEMFET) remained as a reasonable solution to chemical sensing. Palladium has been used as a gate for the standard oxide layer and a chemically sensitive metal [33]. Unlike CHEMFET, an Ion Selective FET (ISFET) is simply a MOSFET without a conductive gate. Charges from sensitive chemical accumulate on the top of this membrane and get amplified. It has some limitation in usage due to the susceptibility of this membrane to environmental poisoning. Therefore, CHEMFET, although less selective and sensitive than ISFET, has become more potential for practical gas sensing applications.

### ***1.7.3.2. Schottky barrier/Heterocontact Sensors***

When a semiconductor such as ZnO is brought into contact with a metal such as Au, a barrier layer forms and the barrier height may be appreciably affected because of the presence of surface states due to adsorbed moisture or gas present in the ambient. Further work is needed for real-life applications of such sensors [34,35].

### ***1.7.3.3. Conductive Polymer Sensors***

Certain polymers such as polyanilines and polythiopenes are electrically conductive and the conductivity changes (due to charge transfer and swelling of the polymer) when certain gases are absorbed by the polymers. Although there are many technical problems like temperature and humidity sensitivity, baseline drift, the potential low cost and the tuning feature of the polymer sensors are attracting a great deal of attention from the developers [36,37].

### ***1.7.3.4. Fiber-Optic Sensors***

When light is passed through a glass/plastic fiber via total internal application, some of the light energy (evanescent wave) extends beyond the surface of the fiber (up to a few nanometers). Adsorption of a gas on the surface coating may change the refractive index (or colour) and effectively, the amount of light reflected inside the fiber is changed. The change is detected by a receiver at the other end of the fiber [38,39].

### ***1.7.3.5. Microbalances***

Mass sensitive sensors detect a weight change of an adsorptive layer by use of a quartz microbalance. As the mass of the coating increases due to gas adsorption, the natural rate of vibration of the crystal slows down. The resulting frequency shift can be measured electronically with great sensitivity. Surface Acoustic Wave (SAW) sensors are also mass

sensors where the variations in the surface characteristics of a piezoelectric substrate due to gas adsorption are reflected in the frequency shift of the Rayleigh waves [40,41].

In conclusion, gas sensors based on semiconducting metal oxides are the most well explored sensors for R&D purpose. However, major issues with selectivity and stability of semiconductor sensors are still unresolved in this area.

### **1.8. Metal Oxide Based Gas Sensor**

In 1953, W. H. Brattain and J. Bardeen and in 1954 by Heiland [42-44] had demonstrated the gas sensor in such a way that the adsorption of gas molecules on the surface of a semiconductor germanium could reflect a vital change in the base resistance and there has been a sustained effort to make use of the change for gas detection in 1962 by Seiyama et al. [45]. In 1953, S. R. Morrison also made an explanation on the change in conductivity and contact potential in germanium as a function of the ambient atmosphere [46]. N. Taguchi fabricated a gas sensing alarm system by using resistive type gas sensing devices and finally Semiconductor Gas Sensor (SGS) based on the metal oxide-based materials [47]. At first this type of sensors were used for the detection of gas leak in home and industrial application under the name Taguchi Gas Sensor (TGS) with sales both in Japan and overseas. Subsequently a company has been formed named “Figaro Engineering Inc.” in 1969 and they produced sensors and commercialized from the company as Figaro Sensors. Even today, this company remains as one of the major gas sensor manufacturing companies globally.

The detection technique of the metal oxide based thin or thick film sensor based on the change of base resistance of the sensing surface layer derived from the adsorption reaction of the target gas molecules. Therefore, metal oxide sensors are also known as ‘Chemiresistors’. In the field of gas sensing application, the metal oxide-based gas sensor has achieved immense attention as a simplest type gas sensor among various technologies. Metal oxide-based gas sensor’s characteristics such as compact device size, durability, low cost, simple fabrication



method, easy measurement method and because of its good sensing ability makes them superior to other sensors. Simplicity of fabrication in the chemiresistor is however counter balanced by inherent limitations in selectivity. Some of the major advantages and disadvantages of the gas sensors are given below [48,49].

### Advantages of Metal Oxide based Sensors

- High Sensitivity
- Lower response and recovery time
- Higher surface area
- High area/volume ratio
- Lower operating temperature
- Small and Compact size
- Simple Operation
- Cost Compatibility

### Disadvantages of Metal Oxide based Sensors

- Difficulties in achieving the desired sensitivity
- Selectivity
- Stability

### Ways to improve the properties of semiconductor gas sensor

- Addition of Catalyst
- Controlling the size of particles (Grain size effect)
- Porous nature in sensing material
- Controlling the thickness of coating
- Temperature modulation

- Filters for selectivity
- Functionally gradient bi-layer sensor
- Pattern recognition
- Adopting technique of surface modification
- Finding new materials having good sensing characteristics
- Develop newer method for sensor fabrication
- Advanced techniques for film deposition
- n/p heterocontacts
- Dual sensor configuration based on interior pore structure

### **1.9. Performance of Gas Sensors-Influencing Factors**

A variety of methods have been utilized to increase the quality of the gas sensors. The interaction between the surface of the sensor materials and the target gas can be influenced by many internal and external factors such as natural properties of the base sensing materials, surface area, microstructural modification of sensing layers, operating temperature and humidity etc. There are many widely used metal oxide semiconductor based commercially available gas sensor with thick and thin film fabrication form of sensing material in the market. Though they are showing better sensitivity at a certain operating temperature but selectivity of this type of gas sensor remains as a vital challenge to recover.

So, there has been a reviewed interest in developing metal oxide semiconductor-based gas sensing materials with improved sensitivity and selectivity. It is focused on the different electrical and structural properties of the sensing material to optimize the improved characteristics of the semiconducting metal oxide types gas sensor.

Various sensing properties of a material broadly depends on both structural characteristics of sensing material and nature of the detecting gas as shown in Figure 1.1.

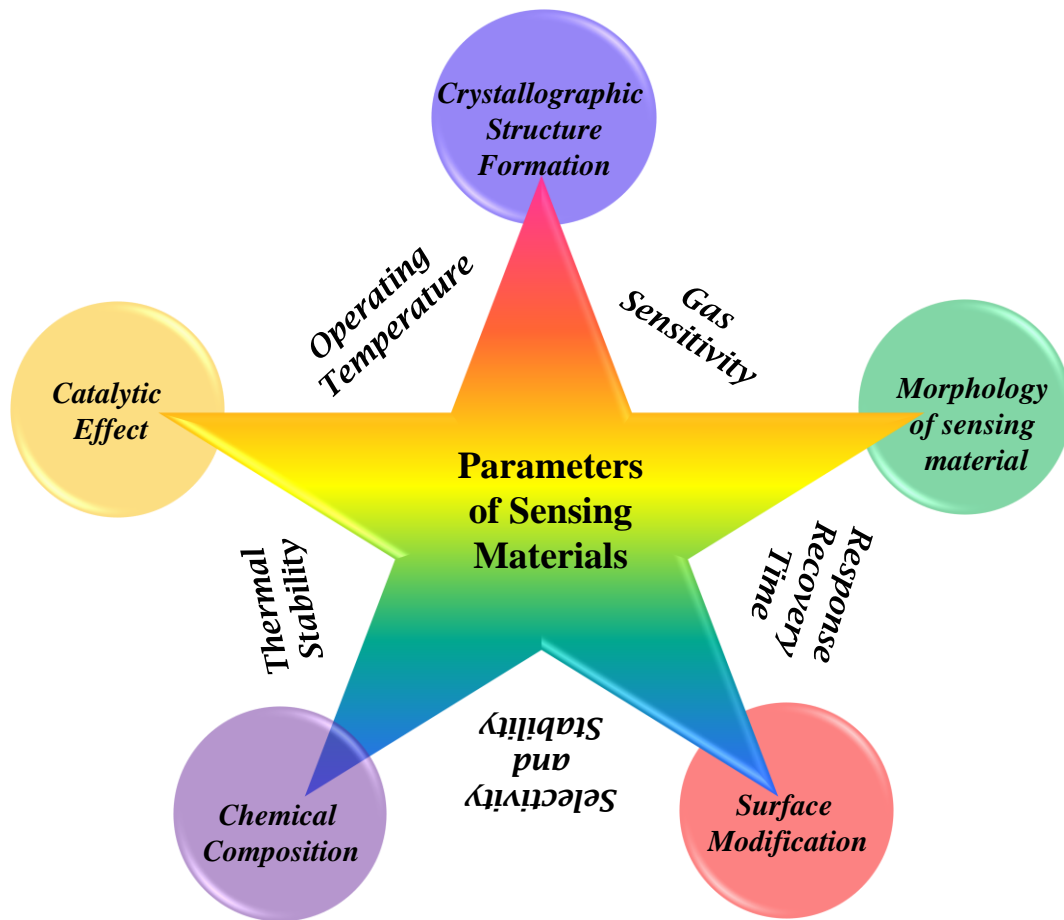


**Figure 1.1:** Influencing factors of gas sensor materials on sensing performance.

The increment of catalytic activity with size can be rationalized on the basis of the increase in the surface to volume ratio with decrease in grain size. And it is well known that the sensitivity and stability are interconnected sensing parameters and smaller grain size results higher sensing response. But at the same time, the stability of the gas sensor may decrease with smaller sized dispersed grains on account of agglomeration of particles. Dependence of grain size on various properties of a sensing material is presented in Figure 1.2.

Thus, during the process of improving the performance of sensors by way of changing the sensing parameters of sensors, interdependence between parameters needs to be taken into consideration.

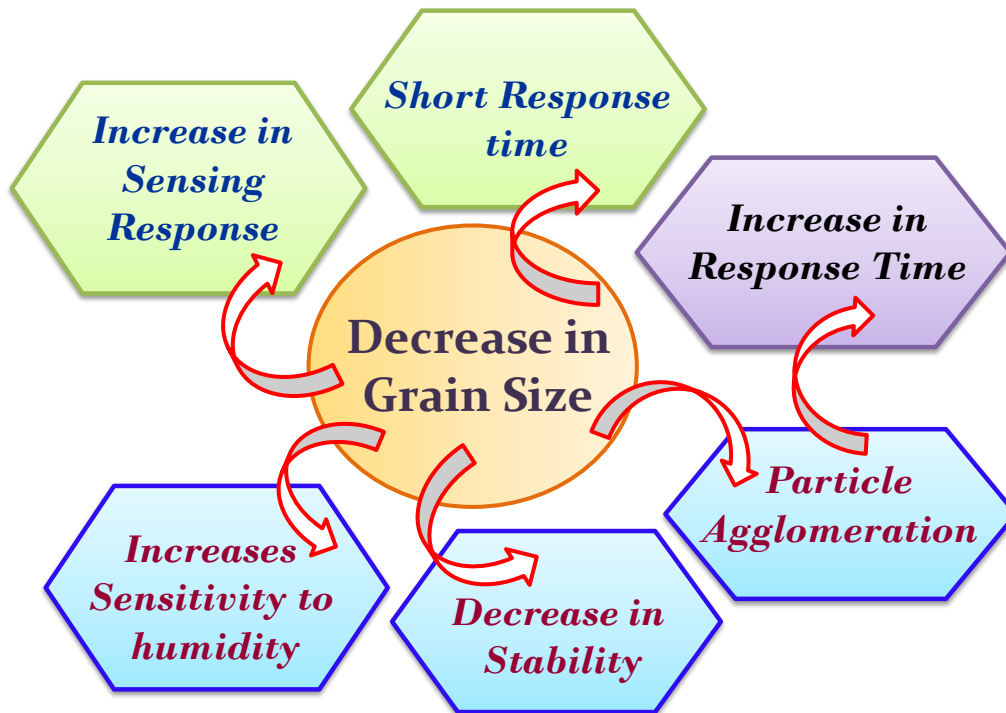


**Figure 1.2:** Influence of grain size decrease in gas sensing properties.

- ❖ Gas sensing procedure is highly depended on the surface reaction with gas molecules.
- ❖ Various metal oxide-based sensing materials have different activation energy to the target gases.
- ❖ In case of composite metal oxides-based sensing material, gas sensing performance is much higher than single composite-based sensing materials.
- ❖ To improve the sensitivity nature of pure metal oxides, noble metal can be used as oxidation catalytic effect.
- ❖ Higher surface area of the sensing material is required always to enhance the sensing nature by providing large reaction contact region at the time of reaction with target gases and gas sensing materials.
- ❖ The sensing nature can be influenced by the crystallographic structure factor of the sensing materials.

- ❖ Higher surface area with porous structure of the metal oxide is well-accepted for improving sensing properties as it provides lots of small grains with pores on the surface of the sensing materials.
- ❖ High operating temperature is always disadvantage for sensing property because small grains are being agglomerate into large particle size which can decrease the catalytic properties and surface area of the gas sensing materials that can affect the sensitivity.
- ❖ One of the most important parameters is grain size to increase the sensitivity and stability of the gas sensor.
- ❖ Now research has been focused on developing one-dimension sensing materials with improved surface area and higher sensitivity for the fabrication of next generation gas sensing materials.
- ❖ Various external causes like temperature and humidity can be negative factor for different sensing parameters at the time of testing sensitivity.
- ❖ Another important influencing parameters is operating temperature with can play a vital role in sensing nature.
  - ✚ The response and recovery time can be greatly depended on the operating temperature as it shows exponential nature with operating temperature
  - ✚ The main mechanism of the sensor is established by adsorption and desorption process which is a temperature activated procedure.
  - ✚ Different physical properties of the semiconductor-based materials such as Debye length, charge-carrier concentration and work function etc. have been influenced by the operating temperature.
  - ✚ As it is well known that the charge-carrier concentration increases at higher operating temperature which causes decrease in Debye length that is responsible for decreasing in sensitivity at higher operating temperature.

### 1.10. Gas Sensing Characteristics of Metal Oxides based Gas Sensor

#### ➤ Sensitivity

Sensitivity of a sensor can be defined as the relationship between input physical signal and output electrical signal. The sensitivity mechanism of the metal oxide-based sensor is based on the chemiresistive principle of the material that can be described in terms of resistance or conductance. The sensitivity can be defined in presence of reducing gas or oxidizing gas for both n-type material and p-type material. The sensitivity of the metal oxide based sensor is defined as,  $S = (R_a - R_g)/R_g$ , here,  $R_a$  and  $R_g$  are the resistance value of the sensing material in presence of air and analyte gas. A typical sensitivity graph is shown in Figure 1.3.

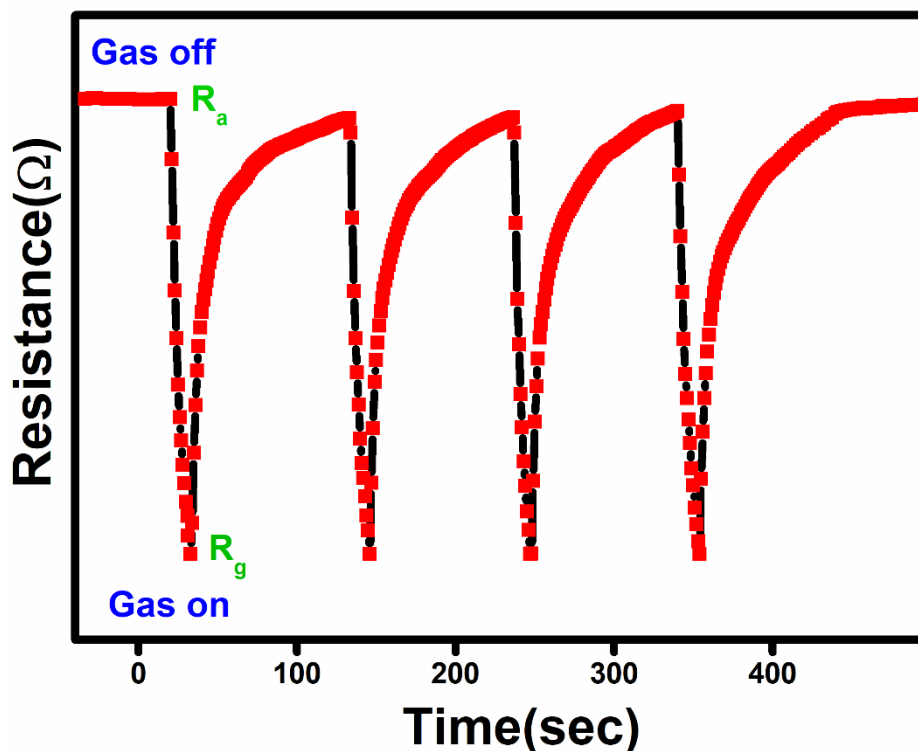
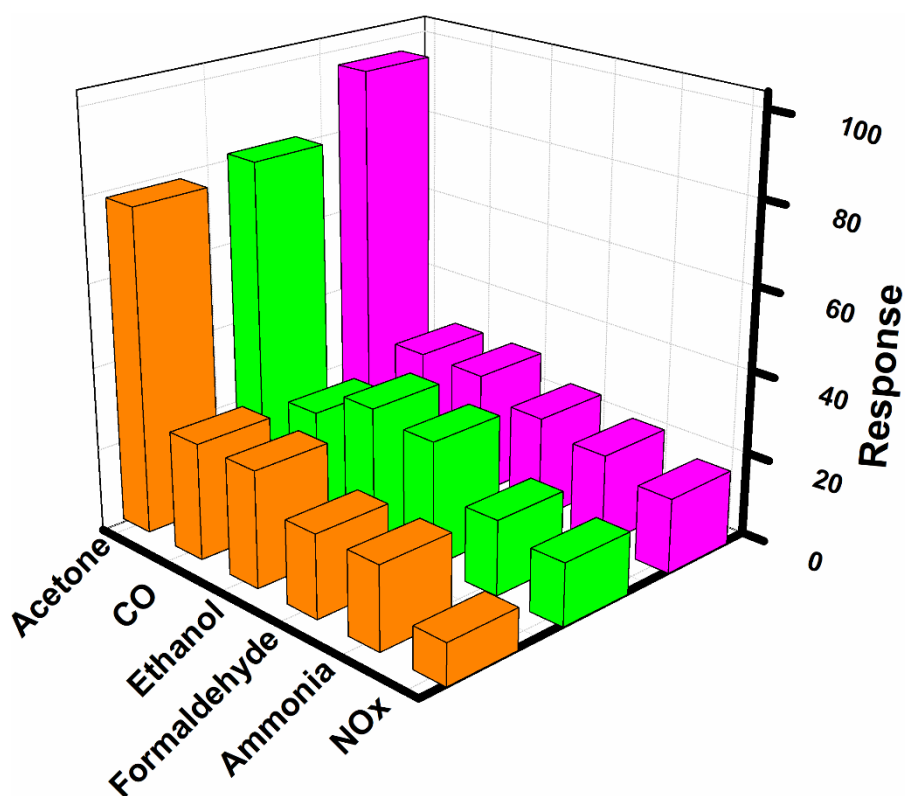


Figure 1.3: Sensitivity nature of gas sensor.

#### ➤ Selectivity

**Selectivity** of a sensor is the ability to detect a target gas without being affected by the presence of other interfering gases. Selectivity has always been a major hurdle for solid state gas sensors.

Selectivity can be improved by (i) choosing a suitable catalyst and/or dopant which shifts the sensitivity maximum towards the target gas (ii) selecting an optimum temperature where the chosen gas is most active (iii) using a filtration membrane or multilayer sensors for selective adsorption and reaction and (iv) using arrays of partially sensitive sensors in conjunction with pattern recognition and multicomponent analysis. Selectivity nature of a sensor for various gases is depicted in Figure 1.4.



*Figure 1.4: Selectivity nature of gas sensor.*

### ➤ Response and Recovery Time

Response time can be calculated as the time required for a gas sensor to reach 90% of its total response in dynamic nature after injecting the target gas. On the other side recovery time is defined as the time required for a sensor to return to 90% of its initial state after removing the target gas. A typical gas sensor showing response and recovery time on exposure to an analyte gas is shown in Figure 1.5.

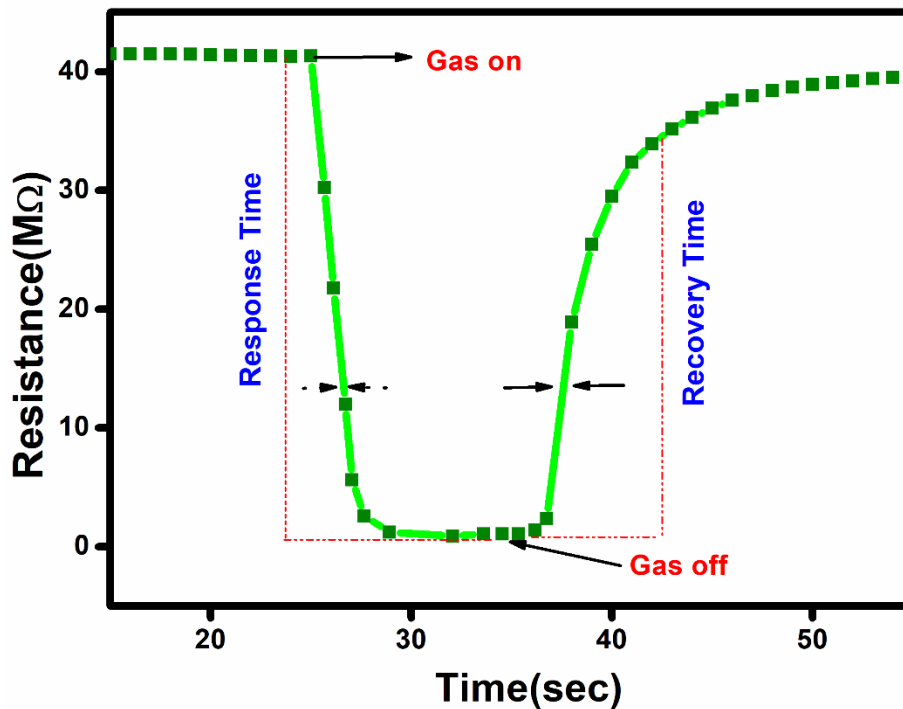


*Figure 1.5: A typical gas sensor showing response and recovery time on exposure to an analyte gas.*

➤ **Detection Limit**

At the operating temperature of the sensor under given conditions, the detection limit can be identified by observing the lowest concentration of the gas that can be detected by the gas sensor.

➤ **Accuracy**

Accuracy can be described as the extent of closeness of the measurement as compared to the actual value.

➤ **Dynamic Range**

It can be calculated by the concentration range between the lower detection limit and the upper detection limit of the gas concentration.

➤ **Repeatability**

It is an important parameter for gas sensing properties that can be observed by showing the same dynamic curve after injecting and removing target gas at a certain time period at same environmental condition.



➤ **Stability**

The stability of the gas sensor is most important point for developing device application. It is an ability of a gas sensor to maintain the sensitivity unaltered for a certain time period as shown in Figure 1.6

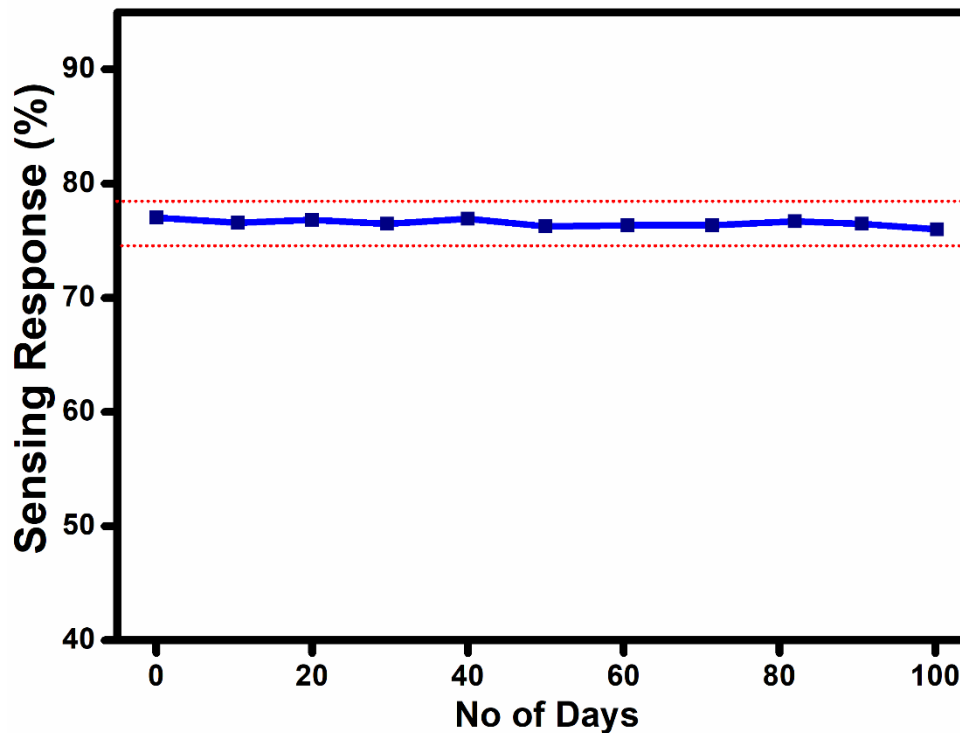


*Figure 1.6: Stability nature of gas sensor.*

➤ **Life Cycle**

Life cycle can be identified by the length of time period at which the gas sensor can operate continuously by repetitive nature.

### **1.11. Metal Oxides for Gas Sensor Applications**

Metal oxides which are selected for gas sensors are basically chosen based on their electronic structure which exhibit a wide range of different electronic, electrical and physical properties. Their electrical nature ranges from insulators (e.g.,  $\text{Al}_2\text{O}_3$ ,  $\text{MgO}$  etc.) through wide-band gap and narrow-band gap semiconductors ( $\text{TiO}_2$ ,  $\text{SnO}_2$ ) to match Pt, Pd etc [50]. Due to unique surface properties, high catalytic activity and wide band gap, oxides of complicated

nanocomposite materials are also suitable for sensor applications e.g.,  $\text{WO}_3$  ( $\text{H}_2$  and alcohol detection),  $\text{Mn}_2\text{O}_3$ ,  $\text{Co}_3\text{O}_4$  and  $\text{NiO}$  (CO detection) [51,52]. Binary transition-metal oxides (pure  $\text{TiO}_2$ ,  $\text{V}_2\text{O}_5$ ,  $\text{WO}_3$  etc.) and perovskites ( $\text{SrTiO}_3$ ,  $\text{LiNbO}_3$  etc.) having  $d^0$  configuration which represents the highest oxidation state that can possibly be attained. Thus, these oxides can't gain any more oxygen but can lose and these show many features of non-transition metal oxides and higher gap of 3-4 eV. Stoichiometric, post-transition-metal oxides ( $\text{ZnO}$ ,  $\text{SnO}_2$  etc.) and  $d^0$  transition-metal oxides may be reduced, but can never be oxidized. Only pre-transition-metal oxides with  $d^0$  and post-transition metal oxides with  $d^{10}$  electronic configurations find applications as sensors. The post-transition oxides  $\text{ZnO}$ ,  $\text{In}_2\text{O}_3$ ,  $\text{SnO}_2$ , as well as majority of transition-metal oxides are active in 'redox' reactions [53]. The different semiconducting oxides which were used as gas sensors traditionally have been listed in Table 1.1.

**Table 1.1: Different Semiconducting Oxides Used as Gas Sensor:**

Material	Crystal Structure	Approx. Bandgap (eV)	Different Gases Detected	References
<b>SnO<sub>2</sub></b>	Rutile	3.6	SO <sub>x</sub> , NO <sub>x</sub> , CO <sub>x</sub> , Alcohol, H <sub>2</sub> , CH <sub>x</sub> , H <sub>2</sub> S, NH <sub>3</sub>	50, 53, 54-56
<b>ZnO</b>	Wurzite	3.4	O <sub>2</sub> , CO, CH <sub>4</sub> , H <sub>2</sub> , H <sub>2</sub> O, C <sub>2</sub> H <sub>5</sub> OH, C <sub>2</sub> H <sub>6</sub> , NO <sub>x</sub> , Acetone	57-65
<b>TiO<sub>2</sub></b>	Anatase, Rutile	3.2	CO, SO <sub>2</sub> , NH <sub>3</sub> , Alcohol, O <sub>2</sub> , O <sub>3</sub> , NO <sub>x</sub> , H <sub>2</sub> , Acetone	66-72
<b>In<sub>2</sub>O<sub>3</sub></b>	Bixbyite	2.7	O <sub>3</sub> , H <sub>2</sub> , CO, C <sub>3</sub> H <sub>8</sub> , NO <sub>x</sub> , Cl, C <sub>2</sub> H <sub>5</sub> OH	73, 74
<b>Fe<sub>2</sub>O<sub>3</sub></b>	Rhombohedral, Cubic bixbyite, Orthorhombic	2.3	H <sub>2</sub> , CO <sub>2</sub> , O <sub>2</sub> , CO, CH <sub>4</sub> , NO <sub>2</sub> , H <sub>2</sub> O, O <sub>3</sub> , i-C <sub>4</sub> H <sub>10</sub> , LPG, C <sub>3</sub> H <sub>8</sub> , Alcohol, Acetone	75-77
<b>WO<sub>3</sub></b>	Monoclinic	3.0	H <sub>2</sub> S, NO <sub>x</sub> , O <sub>3</sub> , NH <sub>3</sub> , H <sub>2</sub> , Ethanol, Petrol, Acetone	78-81
<b>Bi<sub>2</sub>O<sub>3</sub></b>	Monoclinic	2.9	H <sub>2</sub> , CO <sub>2</sub> , O <sub>2</sub> , Smoke, CO	82, 83
<b>NiO</b>	Cubic (rock-salt)	3.7	H <sub>2</sub> , CO <sub>2</sub> , O <sub>2</sub> , CH <sub>4</sub> , NH <sub>3</sub> , SO <sub>2</sub> , CO, NO <sub>2</sub>	84, 85

<b>V<sub>2</sub>O<sub>5</sub></b>	Orthorhombic	2.3	Amine, Ethanol, Ammonia, H <sub>2</sub>	86-89
<b>Cr<sub>2</sub>O<sub>3</sub></b>	Hexagonal	3.4	H <sub>2</sub> , CO <sub>2</sub> , O <sub>2</sub> , CH <sub>4</sub> , NH <sub>3</sub> , NO <sub>2</sub>	90
<b>Co<sub>3</sub>O<sub>4</sub></b>	Cubic	2.0	H <sub>2</sub> S, NH <sub>3</sub> , CO, CH <sub>4</sub> , C <sub>3</sub> H <sub>8</sub> , Ethanol, Acetone	91, 92
<b>CdO</b>	Cubic rocksalt	2.18	H <sub>2</sub> , CO <sub>2</sub> , O <sub>2</sub> , Acetone	93-95
<b>CeO<sub>2</sub></b>	Fluorite	3.19	O <sub>2</sub> , H <sub>2</sub> , CO <sub>2</sub> , H <sub>2</sub> S, C <sub>2</sub> H <sub>5</sub> OH	96-99
<b>Nb<sub>2</sub>O<sub>5</sub></b>	Pseudohexagonal, Monoclinic	3.4	CO, NH <sub>3</sub> , Ethanol, Acetone	100-102
<b>Mn<sub>2</sub>O<sub>3</sub></b>	Bixbyite	1.29	Ethanol, Ammonia, Humidity	103-104
<b>BiFeO<sub>3</sub></b>	Rhombohedral	2.2-2.8	Acetone, Ethanol, SO <sub>2</sub> , Formaldehyde, Ammonia	105-107
<b>LaFeO<sub>3</sub></b>	Orthorhombic	2.46 - 2.31	Formaldehyde, Acetone, SO <sub>2</sub> , Ethanol, NO <sub>2</sub> , Methanol	108-111
<b>BaTiO<sub>3</sub></b>	Tetragonal	3.2	H <sub>2</sub> S, NO <sub>2</sub> , CO, CO <sub>2</sub> , LPG, O <sub>2</sub> , Humidity, Ammonia, H <sub>2</sub> O <sub>2</sub>	112-115
<b>SrTiO<sub>3</sub></b>	Cubic	3.2	Ethanol, H <sub>2</sub> S, Ammonia, CO, Hydrogen, CO <sub>2</sub> , Propane, NO, O <sub>2</sub>	116-119
<b>Zn<sub>2</sub>SnO<sub>4</sub></b>	Cubic	3.2 - 3.9	Ethanol, CO, Acetone, Hydrogen, Ammonia, Methanol, Ethanol	120-122

### 1.12. Sensor as Biomarker Detection:

With changing ways of lifestyle such as continuous usage of electronic gadgets and food habits there is a noticeable reduction in physical activity of human beings resulting in various physiological disorders. Diabetes is one of such physiological disorders, which have taken a front seat as diabetes is a disease, which affects many other parts of the body. Thus, diabetes has been increasingly becoming a more and more serious health problem attracting attention of people from all fraternities such as Medical Professionals, Scientists, Pharamceutical companies so that affordable solutions can be provided for early detection, monitoring and cure.

Currently, it is estimated that approximately 475 million people have been suffering from this problem all over the world reported by recent findings [123]. In another Diabetes survey, conducted by World Health Organisation (WHO) carried out recent year, it was reported that more than 77 million Indians have been affected by Diabetes and it is expected that this data will rise up to 134 million by 2045. The number of people affected by Diabetes was more than 7.2% of the adult population at that time [124,125]. Currently from global statistics of World Health Organisation (WHO), 1.6 million deaths are recorded due to diabetes and finally becoming the ninth leading cause for human death all over the world and by the end of year 2035, the number of deaths is estimated to increase to 592 million due to diabetes [126,127].

Diabetes mellitus is a group of heterogeneous metabolic disease. The major result, which is insufficient insulin secretion or resistance to insulin resulting in uncontrolled movement of blood glucose (BG), levels in body; most common is high blood glucose level. Several diagnostic mechanism or pathological tests are available in market for the detection or monitoring of diabetes. Among the various methodologies prevalent in the market, blood glucose meter is the most common and widely used methodology to determine the glucose concentration in blood. But the major drawback of this methodology is the invasive nature of testing making the testing procedure not only painful but also inconvenient for blood sampling in daily basis as it requires extra step of sterilisation of the finger tips, proper disposal of the needles, test vials etc. Further, due to the fact that the test vials (strips) can be used only once, regular purchase of the strips makes this entire process costly, though lower than the traditional tests done in pathological labs. Thus, there was always a search for non-invasive but reliable methodology for testing blood glucose levels. Research in this field have paved a new pathway towards advanced measurement technology like breath analysis which provides a non-invasive and painless disease diagnosis method by monitoring the metabolic status of a biomarker in the

exhaled breath components [128-130] with an aim to relate the concentration of a biomarker (generally a VOC i.e., volatile organic compound) as an indicator of any disease.

According to the various studies in this field, it has been found that there are about 3500 chemical species present in the exhaled breath and among them maximum are volatile organic compounds (VOCs). The concentration of these VOCs generally remains very low lying in the range of ppm (parts per million) to ppb (parts per billion) [131,132]. An abnormality in concentration of a specific VOC/gas in the breath is considered as a marker or indicator of a particular disease or metabolic disorder, such VOC/gas present in the breath is known as a breath biomarker in the research field of breath analysis.

Biomarker is one of the most interesting tools to detect various diseases and to monitor the health status and other abnormalities in health condition and other disease stating, prognosis and prediction [133]. The earliest recorded medical histories of diabetes from ancient Greece at the time of Hippocrates note that sufferers had the smell of rotten apples on their breath. This odour is acetone. Everything changed in early 70s, when Linus Pauling (1971) published a seminal article demonstrating analytical methodology used to identify approximately 250 compounds in breath. For this reason, modern breath analysis has concentrated on acetone as a biomarker of diabetes. It is a non-invasive and rapid method for detection of diabetes. Acetone is a compound present in breath that is not significantly affected by mouth flora.

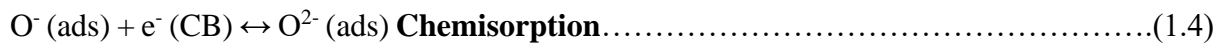
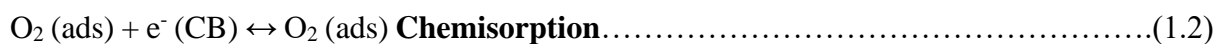
### **1.13. Gas Sensing Mechanism and Working Principle of SMO Gas Sensors**

The gas sensing mechanism of typical resistive SMO based device involves two key functions viz. (i) recognition of a target gas through gas–solid interaction which induces electronic change of oxide surface i.e., receptor function and (ii) transduction of surface phenomenon into resulting change in ionosorbed (physisorbed and chemisorbed both are possible) oxygen is reflected as a change in electrical resistance of the sensor material i.e., transducer function

[134]. The basic mechanism that causes the conductivity of the material to change upon adsorption or reaction of molecules at the surface is a consequence of the chemical state of the adsorbed species. Semiconducting metal oxide is a nonstoichiometric (defect) oxide having oxygen vacancies and electron donor states.

When such semiconducting metal oxide is heated at a certain high temperature in air, oxygen is chemisorbed on the oxide surface in the form of  $O^{2-}$ ,  $O^-$  or  $O_2^-$  depending upon operating temperature with a negative charge. Then donor electrons in the crystal surface are transferred to the adsorbed oxygen, resulting in leaving positive charges in a space charge layer leading to reduction of conductivity.

The following reactions depict the probable surface reactions:



Depending on the temperature, oxygen is ionosorbed on the surface predominantly as  $O^{2-}$  (below  $\sim 150^\circ\text{C}$ ) or as  $O^-$  (between  $\sim 150\text{-}400^\circ\text{C}$ ). Above  $400^\circ\text{C}$ , the parallel formation of  $O^{2-}$  generally occurs [135]. So, this negative surface charge trapped in oxygen species causes an upward band bending of the conduction and valence band and an electron depleted region which is called as space-charge layer ( $T_s$ ) [136-139]. At grain boundaries, adsorbed oxygen forms a potential barrier, which prevents carriers from moving freely. The electrical resistance of the sensor is attributed to this potential barrier. In the presence of reducing or combustible gas produces a counter reaction, where the reducing gas reacts with the highly reactive chemisorbed oxygen and hence, the surface density of the negatively charged oxygen decreases and frees the bound electrons, so the barrier height in grain boundary is reduced. The reduced

barrier height decreases sensor resistance. Energy band diagram of semi-conducting metal oxide is depicted in Figure 1.7.

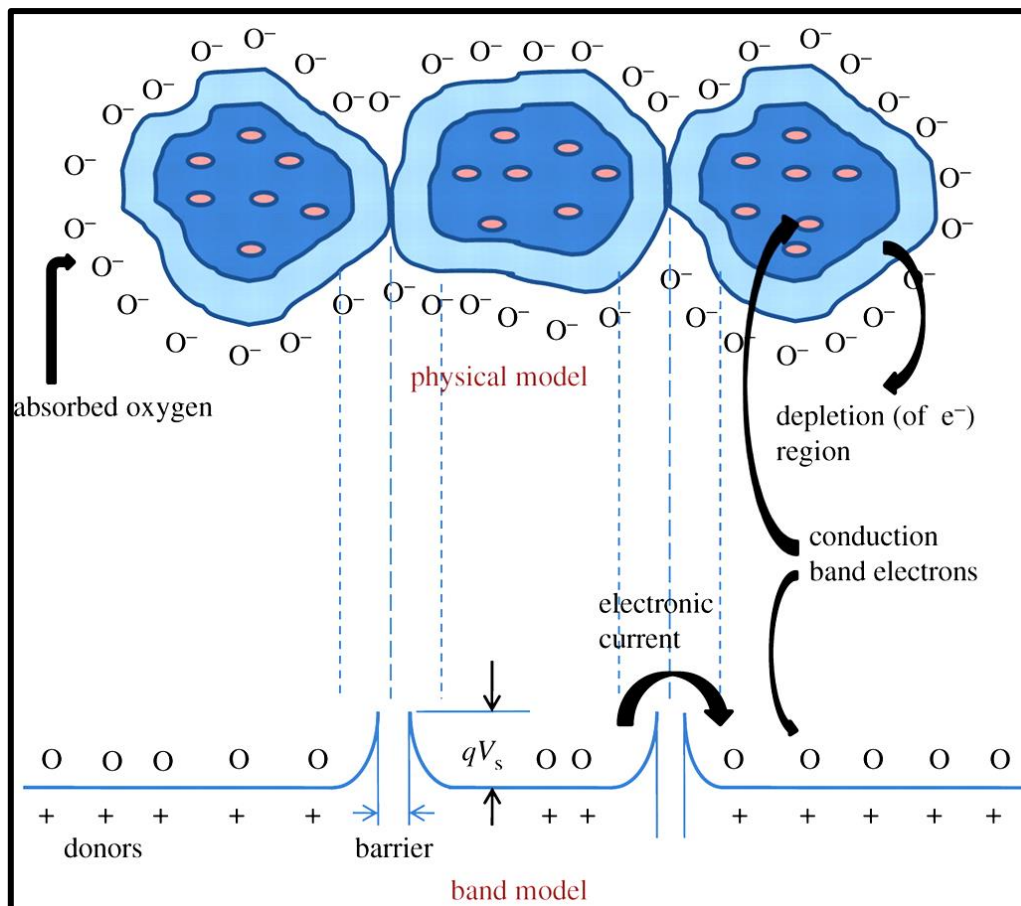


Figure 1.7: Energy band diagram of semiconducting metal oxide [140]

The amount of resistance change is proportional to the concentration of the reducing gas in the ambient, which is believed to be the dominant sensing mechanism of surface conductive gas sensors. However, the concentration of charged oxygen species is limited to <1% of the total number of surface states. It is unlikely that a change in <1% of surface coverage causes a factor of 100 change in the total resistance. Therefore, the surface barrier at the intergranular contact must play an important role in achieving high sensitivity of the sensors. The intergranular contact consisting of the space charge layer depleted of electrons is usually more resistive than the bulk. The total conductance is then determined by the percolation path through the low resistance of bulk grains in series with the high resistance of intergranular

contacts. Electrons must overcome the intergranular contact barrier in order to cross from one grain to another for conduction. In this case, the sensor resistance (R) can be written as:

$$R = R_0 \exp (E_b / KT) \dots\dots\dots(1.5)$$

where  $R_0$  is a constant and  $E_b$  is the barrier height. It can be shown that  $E_b$  is proportional to the square of the coverage and consequently the conductivity has an exponential dependence on the square of the coverage.

The relationship between film conductivity ( $\sigma$ ) and the gas concentration (c) follows a power law that can be described by:

$$\sigma = K.c^n \dots\dots\dots(1.6)$$

n = Positive for oxidizing gas and negative for reducing gas.

The sensitivity of a sensor is calculated from either of the following relations:

$$S = (R_a - R_g) / R_a \times 100 \dots\dots\dots(1.7)$$

$$S = R_a / R_g \dots\dots\dots(1.8)$$

Where  $R_a$  is the sensor resistance in air at a particular temperature and  $R_g$  is the sensor resistance in gas at the same temperature.

#### **1.14. Acetone Gas Detection:**

Acetone is a volatile, flammable liquid which is colourless which is having a pungent odour, sometimes seems like a mint aroma. The upper and lower explosive limits of Acetone are 12.8% and 2.6% respectively. Vapour pressure of Acetone is 180 mmHg. In the field of Chemistry, chemical compound having at least one atom of Carbon (C) and Hydrogen (H) are classified as organic compounds and such compounds turning volatile at room temperature are often referred as Volatile Organic Compounds (VOCs). Acetone is one of the elementary compounds of VOCs, with chemical formulae of  $(CH_3)_2CO$  and IUPAC nomenclature of 2-Propanone and CASA number of 67-64-1. Acetone has a molecular weight of 58.08g/mole and density of 0.79g/cm<sup>3</sup> at 20°C.



Acetone is soluble in water and is widely used as a cleaning agent in laboratories and various organic solvents. It can also be dangerous to human health if inhaled in substantial amount or the skin is exposed substantially. Inhalation/Contact can result in various health issues such as dizziness, headaches, drowsiness, eye irritation, drying of skin leading to dermatitis. Acetone in mild concentration can be a narcotic and has toxic impact on the CNS (central nervous system) of human body. Apart from the industrial uses, acetone is also a key biomarker, present in human breath among no less than 3500 various VOCs, concentration of which may vary from parts per million (ppm) to parts per trillion (ppt). Presence of acetone in human breath helps to detect/diagnose various diseases. It has been clinically found that acetone concentration in breath of human beings can be correlated with many diseases such as diabetes, asthma, lung cancer, halitosis. Acetone is generally generated upon being infected with any microorganism/antigen and also as a product/by-product of various biological processes and oxidative stress. After the same is produced in the body, acetone gets excreted in the blood which subsequently diffuses into the lung from where it finds its place in the exhalation. Thus, the analysis of concentration of acetone in human breath, if can be done with the required accuracy, can be used for determining/diagnose/monitoring of various diseases non-invasively and painlessly. Till date, many efforts have been given towards the development of inexpensive yet accurate sensors which are capable of detecting the level of Acetone gas at ppb level, simultaneously such sensors also need to be simple in design so that it can be scaled up largely for use among mass.

### **1.15. Motivation and Scope of the Present Work**

As discussed in section 1.10, acetone level detection in breath is considered as a biomarker for type-I and type-II diabetes. For a diabetic patient the acetone concentration level is 1.7 to 3.7ppm in human breath, for pre diabetic the range is between 0.9-1.7ppm and the normal range lies within 0.3-0.9ppm as shown in Figure 1.8 [129]. Naturally insulin helps to break down the

glucose in human body for the smooth entry into the blood cells. This glucose provides enough energy for cell to work. But when there is a lack of energy from glucose then it tries to burn the fat for the cell energy. When the fat is burning the energy is released as 2-propanone, chemically speaking a type of ketone such as acetone. Presence of acetone in human breath has been considered as symptom of diabetes.

<b>Fasting Plasma Glucose</b>			
<b>Normal</b>	<b>Pre Diabetes</b>	<b>Diabetes</b>	<b>Post Diabetes (Ketoacidosis)</b>
<b>&lt; 100 mg/dl</b>	<b>100-125 mg/dl</b>	<b>≥ 126 mg/dl</b>	<b>≥ 250 mg/dl</b>
<b>Breath Acetone</b>			
<b>Normal</b>	<b>Pre Diabetes</b>	<b>Diabetes</b>	<b>Post Diabetes (Ketoacidosis)</b>
<b>0.3-0.9 ppm</b>	<b>0.9-1.7 ppm</b>	<b>1.7-3.7 ppm</b>	<b>≥ 3.7 ppm</b>

*Figure 1.8: Acetone Concentration level in Human body and breath.*

Development of chemiresistive metal oxide-based acetone sensors is the future of non-invasive point of care diabetes management. However, use of metal oxides presents some challenges in chemiresistive sensing applications, i.e., sensitivity, selectivity and stability. Nanotechnology enabled sensors offer significant advantages over conventional sensors. This may be in terms of better sensitivity and selectivity, lower production cost, reduced power consumption as well as improved stability. Our research motivation has been to develop nano-structured sensor materials to address some of the challenging issues in the area of sensor development.

Our interest was to focus on both n-type and p-type semiconducting materials in addition to choosing both single component and multicomponent materials. For this purpose, metal oxides such as Tungsten Oxide, Iron Oxide, Titanium Di-oxide, Bismuth Ferrite and  $Zn_2SnO_4$  have

been selected due to their n-type and p-type conducting behaviour with high catalytic behaviour both in oxidation and reduction reaction.

### **1.16. Objectives of the Present Work**

The main objective of the thesis work was preparation followed by characterization of selected binary and ternary metal oxides and their response towards wide range of concentrations of acetone gas to establish them as potential material for fabricating breath analyzer in the field of biomedical application as demonstrated in Figure 1.10. The thesis work focuses on the synthesis and characterization of selected materials to understand the crystallographic modification, size effect, morphology and phase dependency on the electron transport properties and overall, the gas sensing mechanism. In addition to size effect, it is also necessary to understand the effect of crystallographic phase changes and morphology dependency on the physicochemical properties and gas sensing mechanism of the selected materials. The specific objectives of the work embodied in this thesis are summarized as follows:

- ❖ In order to understand the effect of crystallographic modifications of single component oxides on acetone sensing mechanism, the work was focussed on different phases of  $\text{TiO}_2$  exhibiting different morphology and physico-chemical properties, which can be suitable for room temperature-based acetone sensing application.
- ❖ To explore the effect of different phases and surface morphology of iron oxide-based metal oxides such as  $\text{Fe}_2\text{O}_3$  and  $\text{Fe}_3\text{O}_4$  on the acetone sensing behaviour. Studies on the influence of the shapes and the surface area of  $\text{WO}_3$  oxide material on the sensing performance. For this purpose,  $\text{WO}_3$  nanofiber and nanoparticle were synthesized by different chemical process to establish a correlation between the synthesis-morphology-properties in controlling the sensing performance.

- ❖ To Establish the gas sensing ability and different chemical and electrical properties correlation with the sensing mechanism of the synthesized ternary metal oxide like  $\text{BiFeO}_3$ .
- ❖ To demonstrate the size effect of  $\text{Zn}_2\text{SnO}_4$  oxides synthesized by three different synthesis techniques and establish their potential as acetone sensing material for a wide range of concentration of acetone.
- ❖ To explore the current-voltage ( $I$ - $V$ ) characteristics of the prepared sensor devices in air and in presence of acetone gas.
- ❖ To identify ways to improve the lower concentration sensing ability of the sensor devices with higher sensitivity at comparatively lower operating temperature.
- ❖ Trying to correlate the electrical properties with the sensing mechanism by explaining the impedance measurements of the sensor devices in presence of air and acetone.

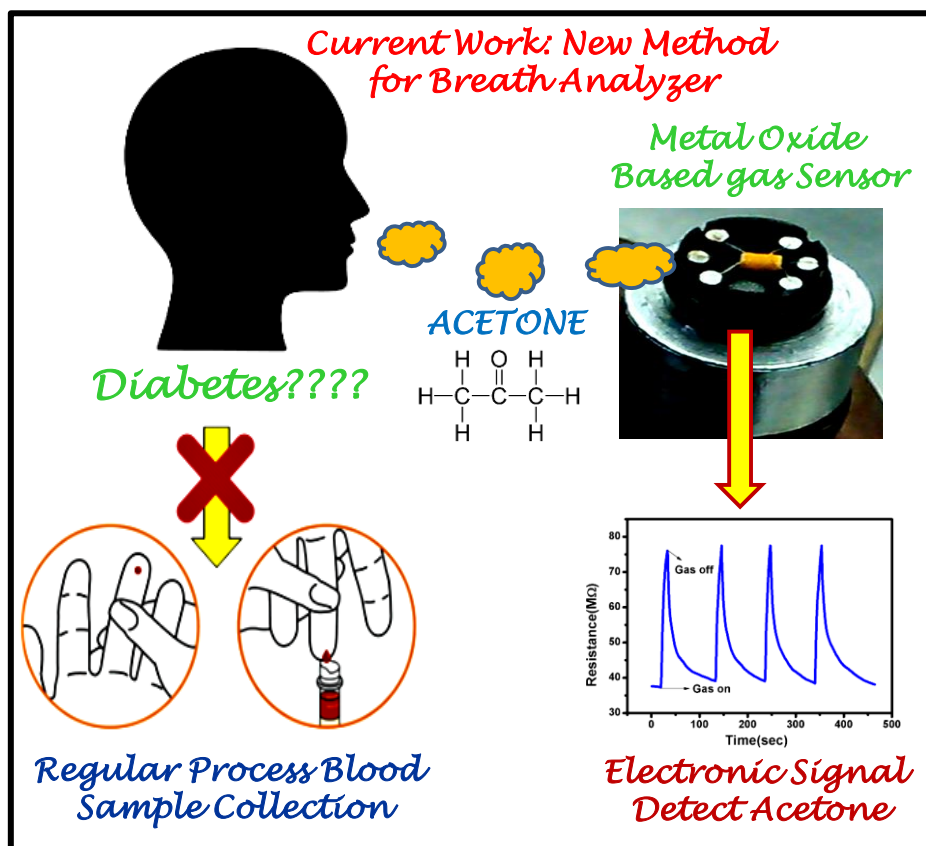


**Figure 1.9:** Schematic diagram of our research work of diabetes detection through acetone sensing method.

Based on the envisaged aim and objectives, work has been carried out as organized into five chapters based on the structure-property-performance correlation of the metal oxide-based sensor materials to understand the sensing mechanism and electrical properties of the fabricated sensor devices. The thesis is divided into Five Chapters, the first chapter based on Background and Literature Review (**Chapter 1**), Synthesis and Characterization Techniques (**Chapter 2**), Binary Metal Oxide based Gas Sensor (**Chapter 3**), Ternary Metal Oxide based Gas Sensor (**Chapter 4**), and Summary and Conclusions (**Chapter 5**).

### **1.17. References**

1. Regiart, M.; Pereira, S. V.; Spotorno, V. G.; Bertolino, F. A.; Raba, J. *Sens. Actuators B* **2013**, *188*, 1241.
2. Gardner, J. W.; Yinon, J. *Phys. Chem.* **2004**, *159*.
3. Sinclair, I. R. *Sensors and Transducers* **2001**.
4. Moos, R.; Müller, R.; Plog, C.; Knezevic, A.; Leye, H.; Irion, E.; Braun, T.; Marquardt, K-J.; Binder, K. *Sens. Actuators B* **2002**, *83*, 181.
5. McGeehin, P. *Sens. Rev.* **2000**, *20*, 106.
6. Hunter, G. W.; Chen, L.Y.; Neudeck, P. G.; Knight, D.; Liu, C. C.; Wu, Q.H.; Zhou, H.J.; Makel, D.; Liu, M.; Rauch, W. A. *Sensors Magazine*, San Jose, California, United States.
7. Westbrook, M. H.; Turner, J. D. Bristol and Philadelphia, **1994**.
8. Kallergis, K. M. *Air & Space Eur.* **2001**, *3*, 197.
9. Kohl, D.; Kelleter, J.; Petig, H. *Sens. Update*, **2001**, *9*, 161.
10. Merhav, S. Springer-Verlag, **1996**.
11. Fleming, W. J. *IEEE Sens. J.* **2001**, *1*, 296.
12. Zhuiykov, S.; Miura, N. *Sens. Actuators B* **2007**, *121*, 639.

13. Abad, E.; Zampolli, S.; Marco, S.; Scorzoni, A.; Mazzolai, B.; Juarros, A.; Gómez, D.; Elmi, I.; Cardinali, G. C.; Gómez, J. M.; Palacio, F.; Cicioni, M.; Mondini, A.; Becker, T.; Sayhan, I. *Sens. Actuators B* **2007**, *127*, 2.
14. Usher, M. J.; Keating, D. A.; Palgrave Macmillan, *2nd revised edition*, **1996**, 13.
15. Göpel, W.; Hesse, J.; Zemel, J. N. ISBN 3-527-26767-0, VCH Verlagsgesellschaft, Weinheim, Germany **1991**.
16. Mari, C. M.; Barbi, G. B. *Kluwer Academic Publishers*, **1992**, 329.
17. Pejcic, B.; Marco, R. D. *Electrochimica Acta* **2006**, *51*, 6217.
18. Preidel, W.; Rao, J. R.; Mund, K.; Schunck, O.; David, E. *Sens. Actuators B Chem.* **1995**, *28*, 71.
19. Sommer, V.; Tobias, P.; Kohl, D. *Sens. Actuators B Chem.* **1993**, *12*, 147.
20. Shao, J.; Lin, H.; Yu, M.; Cai, Z.; Lin, H. *Talanta* **2008**, *75*, 551.
21. Tahirovic, A.; Copra, A.; Miklicanin, E. O. *Kurt Kalcher*. **2007**, *72*, 138.
22. Korotcenkov, G.; Brinzari, V.; Stetter, J. R.; Blinov, I.; Blaja, V. *Sens. Actuators B Chem.* **2007**, *128*, 51.
23. Kohl, D. *Sens. And Actuators* **1989**, *18*, 71.
24. Lopez, F.; Frutos, J.; *Sens. Actuators A* **1993**, *37*, 502.
25. Li, J.; Gao, X.; Fang, L.; Zhang, W.; Cha, H. *Optica & Laser Technology*, **2007**, *39*, 1144.
26. Besson, J. P.; Schilt, S.; Thevenaz, L.; *Spectrochimica Acta Part A: Molecular and Biomolecular Spectroscopy*, **2006**, *63*, 899.
27. Tardy, P.; Coulon, J. R. *Sens. Actuators B* **2004**, *98*, 63.
28. Kimura, M.; Manaka, J.; Satoh, S.; Takano, S.; Igarashi, N.; Nagai, K. *Sens. Actuators B* **1995**, *25*, 857.
29. Lundström, I.; Shivaraman, S.; Svensson, C.; Lundkvist, L. *Appl. Phys. Lett.* **1975**, *26*, 55.
30. Bergveld, P. *Sens. Actuators B* **2003**, *88*, 1.

31. Lundström, I.; Sundgren, H.; Winqvist, F.; Eriksson, M.; Krantz-Rülcker, C.; Lloyd-Spetz, A. *Sens. Actuators B* **2007**, *121*, 247.
32. Andersson, M.; Wingbrant, H.; Petersson, H.; Unéus, L.; Svenningstorp, H.; Löfdahl, M.; Holmberg, M.; Lloyd Spetz, A. *American Scientific Publishers*, **2006**, *4*, 139.
33. Wingbrant, H.; Svenningstorp, H.; Kubinski, D. J.; Visser, J. H.; Andersson, M.; Unéus, L.; Löfdahl, M.; Lloyd Spetz, A. *American Scientific Publishers* **2006**, *6*, 205.
34. Glot, A.; Bartolomeo, E. D.; Traversa, E. *Journal of the European Ceramic Society*, **1999**, *19*, 715.
35. Salehi, A.; Nikfarjam, A.; Kalantari, D. J. *Sens. Actuators B Chem.* **2007**, *124*, 118.
36. Zeng, W.; Zhang, M. Q.; Rong, M. Z.; Zheng, Q. *Sens. Actuators B Chem.* **2007**, *124*, 118.
37. Persaud, K. C. *Materials Today* **2005**, *8*, 38.
38. Wade, S. A.; Wallbrink, C. D.; McAdam, G.; Galea, S.; Hinton, B. R. W.; Jones, R. *Sens. Actuators B Chem.* **2008**, *131*, 602.
39. Weiwei, Yue.; Aiya, Z.; Baoshan, H.; Xinxia, C. *Sens. Actuators B Chem.* **2008**, *130*, 21.
40. Lieberzeit, P. A.; Afzal, A.; Rehman, A.; Dickert, F. L. *Sens. Actuators B Chem.* **2007**, *127*, 132.
41. Shen, C. Y.; Liou, S. Y. *Sens. Actuators B Chem.* **2008**, *131*, 673.
42. Heiland, G. *Phys. Chem.* **1954**, *138*, 459.
43. Heiland, G. *Phys. Chem.* **1955**, 415.
44. Heiland, G.; Mollwo, E.; Stockman, F. *Solid State Physics*, Academic Press Inc. New York, **1959**.
45. Seiyama, T.; Kato, A.; Fujiishi, K.; Nagatani, M. *Anal. Chem.* **1962**, *34*, 1502.
46. Morrison, S. R. *Physical Rev.* **1956**, *104*, 619.
47. Taguchi, N. *Jpn. Patent No. 47-38840*, **1962**.
48. Barsan, N.; Koziej, D.; Weimar, U. *Sens. Actuators B* **2007**, *121*, 18.

49. Szabo, N.; Lee, C.; Trimboli, J.; Figueroa, O.; Ramamoorthy, R.; Mohler, S.M.; Soliman, A.; Verweij, H.; Dutta, P.; Akbar, S. *J. Mater. Sci.* **2003**, *38*, 4239.
50. Korotcenkov, G. *Mater. Sci. Eng. B* **2007**, *139*, 1.
51. Kanazawa, E.; Sakai, G.; Shimano, K.; Kanmura, Y.; Teraoka, Y.; Miura, N.; Yamazoe, N. *Sens. Actuators B* **2001**, *77*, 72.
52. Dakin, J.; Culshaw, B. *Artech House Telecommunication Library*, Boston **1988**, 1.
53. Calatayud, M.; Markovits, A.; Menetrey, M.; Mguig, B.; Minot, C. *Catal. Today* **2003**, *85*, 125.
54. Vuong, D. D.; Sakai, G.; Shimano, K.; Yamazoe, N. *Sens. Actuators B* **2005**, *105*, 437.
55. Mishra, R. K.; Kushwaha, A.; Sahay, P. P. *RSC Adv.* **2014**, *4*, 3904.
56. Brousse, T.; Schleich, D. M. *Sens. Actuators B* **1996**, *31*, 77.
57. Zenga, Y.; Zhanga, T.; Yuanb, M.; Kanga, M.; Lua, G.; Wanga, R.; Fana, H.; Hea, Y.; Yang, H. *Sens. Actuators B* **2009**, *143*, 93.
58. Benamara, M.; Massoudi, J.; Dahman, H.; Dhahri, E.; El Mir, L.; Ly, A.; Debliquy, M.; Lahem, D. *J Mater Sci-Mater El* **2020**, *31*, 14249.
59. Hjiri, M.; Bahanan, F.; Aida, M. S.; Mir, L. E.; Neri, G. J. *Inorg. Organomet. Polym. Mater.* **2020**, *30*, 4063.
60. Narayana, A.; Bhat, S. A.; Fathima, A.; Lokesh, S. V.; Surya, S. G.; Yelamaggad, C. V. *RSC Adv.* **2020**, *10*, 13532.
61. Aljaafari, A.; Ahmed, F.; Awada, C.; Shaalan, N. M. *Front. Chem.* **2020**, *8*, 456.
62. Selvaraj, B.; BalaguruRayappan, J. B.; Jayanth Babu, K. *Mater. Sci. Semicond. Process* **2020**, 112.
63. Du, H.; Yang, W.; Yi, W.; Sun, Y.; Yu, N.; Wang, J. *ACS Appl. Mater. Interfaces* **2020**, *12*, 23084.



64. Singh, P.; Simanjuntak, F. M.; Wu, Y.-C.; Kumar, A.; Zan, H.-W.; Tseng, T.-Y. *J. Mater. Sci.* **2020**, *55*, 8850.
65. Sholehah, A.; Faroz, D. F.; Huda, N.; Utari, L.; Septiani, N. L. W.; Yulianto, B. *Chemosensors* **2019**, *8*.
66. Lee, J. S.; Ha, T. J.; Hong, M. H.; Park, C. S.; Park, H. H. *Appl. Surf. Sci.* **2013**, *269*, 125.
67. Teleki, A.; Pratsinis, S. E.; Kalyanasundaram, K.; Gouma, P. I. *Sens. Actuators B* **2006**, *119*, 683.
68. Li, S.; Li, F.; Rao, Z. *Sens. Actuators B* **2010**, *145*, 78.
69. Wang, Q.; Dong, X.; Pang, Z.; Du, Y.; Xia, X.; Wei, Q.; Huang, F. *Sensors (Switzerland)* **2012**, *12*, 17046.
70. Zeng, W.; Liu, T.; Wang, Z.; Tsukimoto, S.; Saito, M.; Ikuhara, Y. *Sensors* **2009**, *9*, 9029.
71. Seo, M. H.; Yuasa, M.; Kida, T.; Huh, J. S.; Shimano, K.; Yamazoe, N. *Sens. Actuators B* **2009**, *137*, 513.
72. Zeng, W.; Liu, T.; Wang, Z. *Physica E* **2010**, *43*, 633.
73. Wagner, T.; Sauerwald, T.; Kohl, C.-D.; Waitz, T.; Weidmann, C.; Tiemann, M. *Thin Solid Films* **2009**, *517*, 6170.
74. Wang, Y.; Liu, B.; Cai, D.; Li, H.; Liu, Y.; Wang, D.; Wang, L.; Li, Q.; Wang, T. *Sens. Actuators B* **2014**, *201*, 351.
75. Jing, Z.; Wang, Y.; Wu, S. *Sens. Actuat. B* **2006**, *113*, 177.
76. Liu, X.; Zhang, J.; Guo, X.; Wu, S.; Wang, S. *Nanotechnology* **2010**, *21*, 095501.
77. Liang, S.; Zhu, J.; Wang, C.; Yu, S.; Bi, H.; Liu, X.; Wang, X. *Appl. Surf. Sci.* **2014**, *292*, 278.
78. Yao, Y.; Ji, F. X.; Yin, M. L.; Ren, X. P.; Ma, Q.; Yan, J. Q.; Liu, S. Z. *ACS Appl. Mater. Interfaces* **2016**, *8*, 18165.
79. Yin, M. L.; Yu, L. M.; Liu, S. Z. *Mater. Lett.* **2017**, *186*, 66.

80. Wang, Z. H.; Fan, X. X.; Han, D. M.; Gu, F. B. *Nanoscale* **2016**, *8*, 10622.
81. Shen, J. Y.; Zhang, L.; Ren, J.; Wang, J. C.; Yao, H. C.; Li, Z. J. *Sens. Actuators B* **2017**, *239*, 597.
82. Xu, Z.; Tabata, I.; Hirogaki, K.; Hisada, K.; Wang, T.; Wang, S. *RSC Adv.* **2012**, *2*, 103.
83. Li, Y.; Zhang, Z.; Zhang, Y.; Sun, X.; Zhang, J.; Wang, C. *Ceram. Int.* **2014**, *40*, 13275.
84. Wang, C.; Cheng, X.; Zhou, X.; Sun, P.; Hu, X.; Shimanoe, K. *ACS Appl Mater Interfaces* **2014**, *6*, 12031.
85. Gao, H.; Zhao, L.; Wang, L.; Sun, P.; Lu, H.; Liu, F. *Sens. Actuators B Chem.* **2018**, *255*, 3505.
86. Zhuiykov, S.; Wlodarski, W.; Li, Y. *Sens. Actuators B* **2001**, *77*, 484.
87. Yan, W.; Hu, M.; Wang, D.; Li, C. *Appl. Surf. Sci.* **2015**, *346*, 216.
88. Li, Y.; Huang, Z.; Rong, S. *Sens. Mater.* **2006**, *18*, 241.
89. Raible, I.; Burghard, M.; Schlecht, U.; Yasuda, A.; Vossmeier, T. *Sens. Actuators B* **2005**, *106*, 730.
90. Nguyen, H.; El-Safty, S. A. *J. Phys. Chem. C* **2011**, *115*, 8466.
91. D. Barreca, D. Bekermann, E. Comini, A. Devi, R.A. Fischer, A. Gasparotto, *Sens. Actuators B* **2011**, *160*, 79.
92. Liu, Y.; Zhu, G.; Ge, B.; Zhou, H.; Yuan, A.; Shen, X. *Cryst Eng Comm* **2012**, *14*, 6264.
93. Xu, D.; Guan, M.; Xu, Q.; Guo, Y.; Wang, Y. *Funct. Mater. Lett.* **2013**, *06*, 1350035.
94. Rajput, J. K. et al. *Appl. Surf. Sci.* **2017**, *409*, 8.
95. Nwanya, A. C. et al. *Sens. Actuators B* **2015**, *206*, 671.
96. Liu, J. Y.; Dai, M. J.; Wang, T. S.; Sun, P.; Liang, X. S.; Lu, G. Y.; Shimanoe, K.; Yamazoe, N. *ACS Appl. Mater. Interfaces* **2016**, *8*, 6669.
97. Yoon, J. W.; Kim, J. S.; Kim, T. H.; Hong, Y. J.; Kang, Y. C.; Lee, J. H. *Small* **2016**, *12*, 4229.

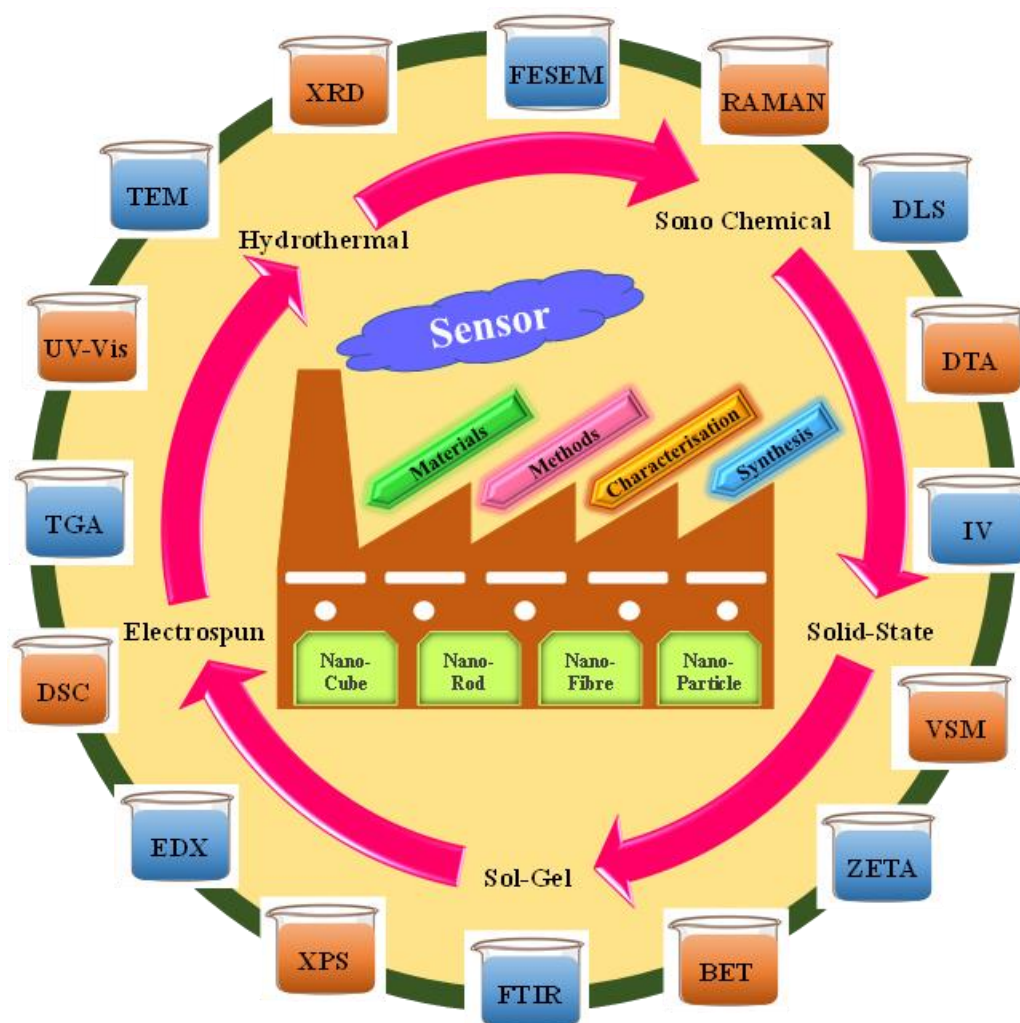
98. Qin, W. F.; Xu, L.; Song, J.; Xing, R. Q.; Song, H. W. *Sens. Actuators B* **2013**, *185*, 231.
99. Chen, Y. J.; Xiao, G.; Wang, T. S.; Zhang, F.; Ma, Y.; Gao, P.; Zhu, C. L.; Zhang, E.; Xu, Z.; Li, Q. H. *Sens. Actuators B* **2011**, *156*, 867.
100. Kondo, H. T. H.; Takeuchi, T.; Igarashi, I. Proceedings of the 3rd Sensor Symposium, Japan, **1983**, 185.
101. Rosenfeld, D.; Schmid, P. E.; Széles, S.; Lévy, F.; Demarne, V.; Grisel, A. *Sensors and Actuators B* **1996**, *37*, 83.
102. Chambon, L.; Maleysson, C.; Pauly, A.; Germain, J. P.; Demarne, V.; Grisel, A. *Sensors and Actuators B* **1997**, *45*, 107.
103. Li, Y.; Gong, J.; He, G.; Deng, Y. *Synth Met* **2011**, *161*, 56.
104. Gouraria, H.; Lumbreras, M.; Landschoot, R. V.; Schoonman, J. *Sens. Actuators B* **1998**, *47*, 189.
105. Waghmare, S. D.; Jadhav, V. V.; Gore, S. K.; Yoon, S. J.; Ambade, S. B.; Lokhande, B. J.; Mane, R. S.; Han, S. H. *Mater. Res. Bull.* **2012**, *47*, 4169.
106. Poghossian, A. S.; Abovian, H. V.; Avakian, P. B.; Mkrtchian, V.; Haroutunian, M. *Sens. Actuators B* **1991**, *9*, 545.
107. Zhou, J. P.; Xiao, R. J.; Zhang, Y. X.; Shi, Z.; Zhu, G. Q. *J. Mater. Chem. C* **2015**, *3*, 6924.
108. Chen, T.; Zhou, Z.; Wang, Y. *Sens. Actuators B Chem.* **2009**, *143*, 124.
109. Hao, P.; Qiu, G.; Song, P.; Yang, Z.; Wang, Q. *Appl. Surf. Sci.* **2020**, *515*, 146025.20.
110. Qin, J.; Cui, Z.; Yang, X.; Zhu, S.; Li, Z.; Liang, Y. *Sens. Actuators B Chem.* **2015**, *209*, 706.
111. Yang, K.; Ma, J.; Qiao, X.; Cui, Y.; Jia, L.; Wang, H. *Sens. Actuators B Chem.* **2020**, *313*, 128022.
112. Patil, L. A.; Suryawanshi, D. N.; Pathan, I. G.; Patil, D. G. *Sens. Actuators B* **2014**, *195*, 643.

113. He, X.; Hu, C.; Xi, Y.; Wan, B.; Xia, C. *Sens. Actuators B Chem.* **2009**, *137*, 62.
114. Mallick, S.; Ahmad, Z.; Qadir, K. W.; Rehman, A.; Shakoor, R. A.; Touati, F.; Al-Muhtaseb, S. A. *Ceram. Int.* **2020**, *46*, 2949.
115. Patil, R. P.; More, P. V.; Jain, G. H.; Khanna, P. K.; Gaikwad, V. B. *Vacuum* **2017**, *146*, 455.
116. Hu, Y.; Tan, O.K.; Cao, W.; Zhu, W. *Ceram. Int.* **2004**, *30*, 1819.
117. Mastelaro, V. R.; Zílio, S. C.; da Silva, L. F.; Pelissari, P. I.; Bernardi, M. I.; Guerin, J.; Aguir, K. *Sens. Actuators B Chem.* **2013**, *181*, 919.
118. Kajale, D. D.; Gaikwad, V. B.; Jain, G. H.; Khanna, P. K. *IEEE: Piscataway* **2008**, 422.
119. Zaza, F.; Orio, G.; Serra, E.; Caprioli, F.; Pasquali, M. *AIP Conf. Proc.* **2015**, 1667, 020004.
120. Han, X.-G.; Cao, X.-W.; Li, L.; Wang, C. *Sens. Actuators B Chem.* **2013**, *185*, 383.
121. Jiang, Y.-Q.; He, C.-X.; Sun, R.; Xie, Z.-X.; Zheng, L.-S. *Mater. Chem. Phys.* **2012**, *136*, 698.
122. Yang, H. M.; Ma, S. Y.; Jiao, H. Y.; Chen, Q.; Lu, Y.; Jin, W. X.; Li, W. Q.; Wang, T. T.; Jiang, X. H.; Qiang, Z.; Chen, H. *Sens. Actuators B Chem.* **2017**, *245*, 493.
123. GBD 2017 Disease and Injury Incidence and Prevalence Collaborators. *Lancet Lond Engl.* **2018**, *392*, 1789–858.
124. Pradeepa, R.; Mohan, V. *Indian J. Ophthalmol* **2021**, *69*, 2932-2938.
125. International Diabetes Federation. *IDF Diabetes Atlas*. 9th ed. Brussels, Belgium: International Diabetes Federation; **2019**.
126. World Health Organization. The top 10 causes of death. Available from: <http://www.who.int/en/news-room/fact-sheets/detail/the-top-10-causes-of-death>; **2021**.
127. Tao Z, ShiA, Zhao J. *Cell Biochem Biophys.* **2015**, *73*, 181-5.
128. Manolis, A. *Clin. Chem.* **1983**, *29*, 5.

129. Zhang, Q.; Wang, P.; Li, J.; Gao, X. *Biosens. Bioelectron.* **2000**, *15*, 249.
130. Tjoa, S.; Fennessey, P. *Anal. Biochem.* **1991**, *197*, 77.
131. Moorhead, K.; Lee, D.; Chase, J.; Moot, A.; Ledingham, K.; Scotter, J.; Allardyce, R.; Senthilmohan, S.; Endre, Z. *Methods Progr. Biomed.* **2008**, *89*, 226.
132. Mayes, P.; Murray, R.; Granner, D.; Rodwell, V. *Harper's Biochemistry* **2000**, 130.
133. Deng, C.; Zhang, J.; Yu, X.; Zhang, W.; Zhang, X. *J. Chromatogr. B* **2004**, *810*, 269.
134. Franke, M.E.; Koplín, T.J.; Simon, U. *Small* **2006**, *2*, 36.
135. Matsunaga, N.; Sakai, G.; Shimano, K.; Yamazoe, N. *Sens. Actuators B* **2003**, *96*, 226.
136. Samson, S.; Fonstad, C. G. *J. Appl. Phys.* **1973**, *44*, 4618.
137. Jarzebski, Z. M.; Marton, J. P. *J. Electrochem. Soc.* **1976**, *123*, 299.
138. Maier, J.; Göpel, W. *J. Solid State Chem.* **1988**, *72*, 293.
139. Göpel, W.; Schierbaum, K. D. *Sens. Actuators B* **1995**, *26*, 1.
140. Sharma, S.; Madou, M. *Phil. Trans. R. Soc. A* **2012**, *370*, 2448-2473.

# CHAPTER-II

## Synthesis and Characterization Techniques



*This chapter describes a brief overview of different techniques and procedures that have been used to synthesize single and multi-component-based metal oxides such as Anatase, Rutile,  $\text{Na}_{0.23}\text{TiO}_2\text{-TiO}_2$  composite, Iron Oxide,  $\text{WO}_3$ ,  $\text{BiFeO}_3$ ,  $\text{Zn}_2\text{SnO}_4$ . Synthesis of these compounds exhibiting nano-structures like rod, nanoparticle, composite, fibre employed by techniques such as sonochemical, sol-gel, hydrothermal, solid state and electrospun are discussed in this chapter. Details of various characterization techniques such as XRD, TGA, DSC, BET, VSM; morphological analysis such as FESEM, TEM in addition of different spectroscopic analyses such as UV-Vis, FITR, Raman, XPS etc. have been highlighted. The fabrication protocols of the sensor device using the synthesized materials have been systematically illustrated with relevant schematics. Different DC and AC measurements were used for testing sensor device and to understand various sensing parameters and attempts were made to co relate the sensing mechanism with structural properties of the metal oxides.*

### 2.1. Introduction

In recent times, nanoscience and nanotechnology has become one of the hottest R & D area across the globe. Nanoscience comprises of manipulating and developing materials at nanoscale level (1 to 100nm) with fascinating size and shape dependent properties for diverse set of applications. Selecting an appropriate synthetic route ultimately determines the successful synthesis of nanostructured materials as their physical properties and applications are heavily dependent upon the synthetic techniques [1-4]. The importance of choosing a proper synthetic route in designing nanostructured materials has been the driving force for the development of new methodologies. Therefore, a variety of techniques has been evolved for the synthesis of nanomaterials as described in Figure 2.1.

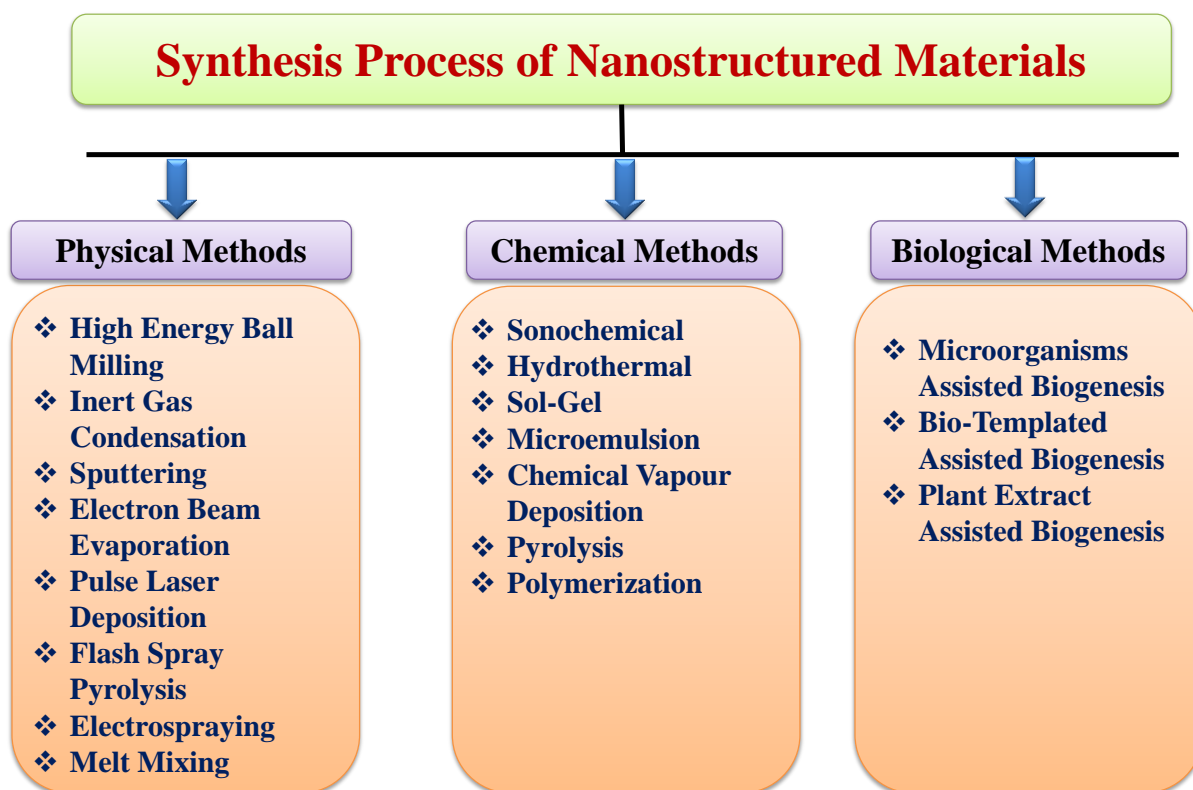


*Figure 2.1: Depicting different synthesis process for nanostructured materials.*

In Figure 2.1 different processes of synthesizing various forms of nanostructured materials are presented. This chapter also deals with different characterization techniques, details of sensor

fabrication process, stabilization of sensing material, gas sensing measurement setup and measurement technique, selectivity and stability property study along with current-voltage characteristics study. The different terminologies used in the study of gas sensors have also been defined and described in this chapter.

### **2.2. General Methods for the Synthesis of Nanomaterials**

#### **2.2.1. Sonochemical Synthesis**

Among all the synthesis techniques, sonochemical synthesis is a well-accepted technique for synthesis of nanostructured materials where ultrasonic irradiation induces high energy chemical reaction in solution phase. Sonochemistry originates from the extreme transient conditions induced by ultrasound, which produces unique hot spots that can achieve temperatures above 5000K, pressures exceeding 1000atm, and heating and cooling rates in excess of  $10^{10}\text{K}\cdot\text{s}^{-1}$  [5]. These conditions are distinct from other conventional synthetic techniques such as photochemistry, wet chemistry, hydrothermal synthesis, or flame pyrolysis. The ultrasound generates the acoustic cavitation in the solution which enhances the reaction speed by increasing the reactivity of the reagents, directs the growth process of the materials and facilitates the phase transfer catalysis etc. Cavitation in principle is the formation, growth and impulsive collapse of bubbles in liquid through an adiabatic process which consequently creates intense local heating, high pressure, acute cooling and heating and liquid jet streams for sonochemical synthesis. This indeed increases the chemical activity in solution through primary or secondary radical reactions instead of directly affecting the vibration energy of the chemical bond of the reagents. The primary process in sonochemistry is the generation of metal atoms from sonolysis of weak metal-carbon bonds from volatile organometallic compounds inside the collapsing bubble that then diffuse into the bulk liquid to form functional nanomaterials. Whereas, secondary sonochemical products may arise from chemically active species (e.g., organic radicals from sonolysis of vapour) that are formed inside the bubble, but



then diffuse into the liquid phase and subsequently react with solution precursors to form a variety of nanostructured materials [6,7]. Typical laboratory scale ultrasonic horns deliver roughly 10 to 1500W of acoustic energy into the liquid during sonication. In this thesis work, sonication induced precipitation technique has been adopted for the synthesis of  $Zn_2SnO_4$  in a basic medium. Probe diameter of titania horn of the ultrasonic unit was 25mm and at the time of synthesis, the ultrasonic power was fixed at 250W and the ultrasonic frequency at 25kHz.

### **2.2.2. Solid State Synthesis**

Solid State Synthesis process is a temperature directed reaction system, which is driven by the diffusion of solids following the restriction of the phase boundary leading to the formation of product having superior thermodynamic stability. There are some basic steps of this conventional synthesis process, which are summarily described here.

- The selection of starting material should be in a way that such materials have well defined compositions and necessary surface area for maximum contact between reactants. Reactive materials are more preferable compared to inert one.
- The mixing of the reactants in actual stoichiometric proportion is quite necessary. The mixing of the material is performed by grinding with mortar and pestle or by the process of ball milling and pelletized in order to ascertain the close contact of the crystallites and to decrease the diffusion distances.
- The mixture has to be heated eventually at certain temperature with proper cycle of heating in proper environment.

Requirement of high temperature, possibility of incomplete reaction, formation of compositionally inhomogeneous products, the predominance of kinetically controlled product over thermodynamically controlled one and the unavailability of the desired morphology are the main concerns of this particular synthesis procedure [8]. In this thesis work, nanostructure

of  $\text{Zn}_2\text{SnO}_4$  has been synthesized using the reactive precursors of ZnO rods and  $\text{SnO}_2$  nanoparticles in a one-step process.

### **2.2.3. Hydrothermal Synthesis**

Hydrothermal synthesis process is one of the most widely used techniques for synthesizing nanomaterials having different morphology. The word ‘Hydrothermal’ consists of two significant terminologies such as ‘Hydro’, which means water and ‘Thermal’, which means heat. This is a special case of a “solvothermal” process when heterogeneous chemical reaction occurs in a closed system of Teflon lined sealed autoclave in the presence of aqueous or non-aqueous solvents to dissolve and recrystallize materials at a temperature above the solvent boiling point and at a pressure above 1 atm. This process exploits the required solvent properties by tuning the synthesis parameters to produce desired products. The autoclave material has been coated with Teflon having higher thermal expansion coefficient. Different parameters of the resultant products such as phase, crystallite size, shape or morphology can be varied by varying the reaction parameters, during synthesis process, like solvent nature, pH of the solution, concentration of the precursor, time and temperature [9,10]. Recently this technique has been successfully hybridized with other process such as microwave, electrochemistry, ultrasound, mechano-chemistry, hot pressing etc. In this thesis work, hydrothermal synthesis has been used for the synthesis of Anatase  $\text{TiO}_2$  nanocubes, Rutile  $\text{TiO}_2$  rod,  $\text{TiO}_2$  composite rod,  $\text{Zn}_2\text{SnO}_4$  nanoparticle, and  $\text{WO}_3$  nanoparticle.

### **2.2.4. Electrospun Technique**

Fabrication of 1D nanofibers by electrospinning has received much attention recently due to the diverse potential applications of 1D structures. In electrospinning technique, the polymer-based fiber has been produced by accelerating a jet of charged polymer solution in an electric field. The electrospinning unit consists of three major components; a high-voltage power

supply, a spinneret or metallic needle and a collector. The high voltage power supply generates an electric field between a syringe with a needle tip and a grounded collector drum covered with aluminium foil. Electrostatic charging of the fluid at the needle tip of the syringe results in formation of the familiar Taylor cone and single fluid jet is ejected from the apex [11]. A resultant charged liquid jet starts ejecting at a certain threshold when the electrostatic forces overcome the surface tension of the polymer solution. Different characteristic features of the fiber such as length, diameter, porosity, alignment and other ones can be controlled by variation of different parameters like molecular weight, distribution and architecture of the polymer. This can be further controlled by changing the viscosity, conductivity and surface tension of the solution. In electric potential, flow rate of the droplet from syringe, distance between the capillary and collection screen, temperature, humidity and air velocity inside the chamber, motion and size of the target screen and the gauze of the needle, these different parameters are really very important for synthesis of different kind of fiber [12]. In this thesis work, we have synthesized  $\text{WO}_3$  fiber and iron oxide fiber by using different types of polymers. The working mechanism of the electrospinning system has been exhibited in Figure 2.2.

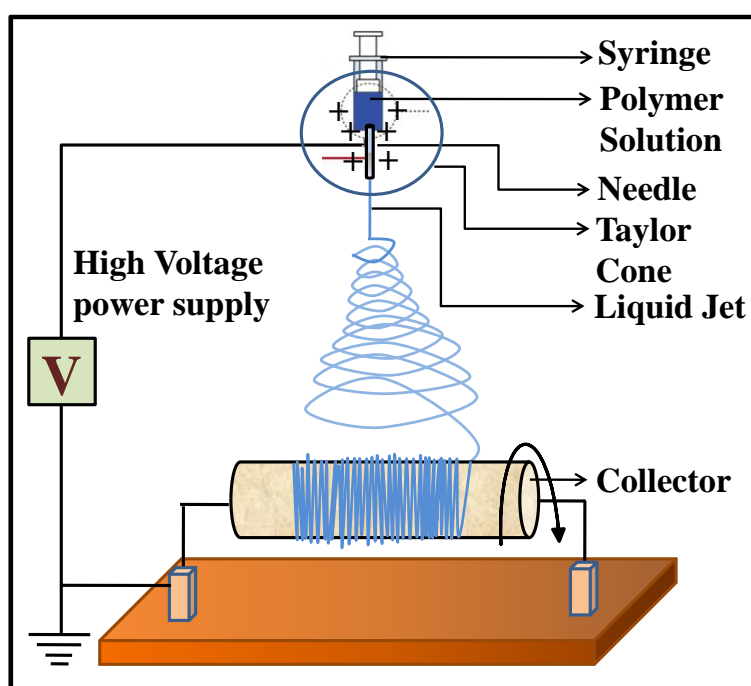


**Figure 2.2:** Components of a basic Electrospun unit.

## **2.3. Synthesis of Different Binary and Ternary Metal Oxide**

### **2.3.1. Anatase Cube, Rutile Rod and Composite Rod**

#### **2.3.1.1. Synthesis of Anatase TiO<sub>2</sub> Nanocubes**

The synthesis of anatase TiO<sub>2</sub> nanocubes has been described in details in the work reported by Mukhopadhyay et al. (2016) [13]. At first a stock solution of Ti<sup>4+</sup> was prepared by mixing titanium (IV) isopropoxide (TTIP) and triethanolamine (TEOA) at a molar ratio of TTIP/TEOA=1:2 to avoid the exceedingly fast hydrolysis of Ti<sup>4+</sup> during the addition of deionized water. Then Na-oleate of 0.2mol.dm<sup>-3</sup> has been prepared by mixing oleic acid (C<sub>18</sub>H<sub>34</sub>O<sub>2</sub>, Merck, India) and NaOH with the stock solution under constant stirring. The pH of the mixed solution was adjusted to 10 ± 0.5 and the total volume of the stock solution was made up to 30ml. The resulting mixture was placed into a closed flask and aged for 24h at 100°C for gel formation. The viscous gel was transferred to a Teflon-lined autoclave and aged at 140°C for 72h to nucleate and grow the TiO<sub>2</sub> particles. The product obtained was centrifuged at 14,000rpm by washing with water for many times and dried under vacuum at 120°C temperature for further characterization.

#### **2.3.1.2. Synthesis of Rutile TiO<sub>2</sub> Nanorod**

Rutile TiO<sub>2</sub> nanorod was synthesized by hydrothermal process using a volume of 25ml aqueous solution containing 1.7mmol of TTIP under vigorous stirring for 2h followed by 1h aging at room temperature. Concentrated 36% HCl was added properly to the solution and pH ≤ 1.5 is maintained. Then the whole mixture was transferred into a 45mL Teflon-lined stainless-steel autoclave, sealed and was heated at temperature 160°C for 5h and then the mixture was cooled to room temperature. Then the formed product was centrifuged at 11,000rpm and then washed with water and ethanol for several times. The resultant white product was dried at 120°C under vacuum and collected for further application [14].

### **2.3.1.3. Synthesis of Composite Nanorod**

Anatase TiO<sub>2</sub> and Na<sub>0.23</sub>TiO<sub>2</sub> composite nanorod has been synthesized by hydrothermal synthesis technique. At first 2g of commercial anatase TiO<sub>2</sub> nanoparticles (J.T Baker Chemical Co., Baker Analyzed Reagent 1-4162, USA) was converted to 1.87g of mixed phase of anatase TiO<sub>2</sub> and Na<sub>0.23</sub>TiO<sub>2</sub> nanorods. The nanorods are formed under extreme basic condition by hydrothermal treatment. In detail, 2g commercial anatase TiO<sub>2</sub> powder was mixed with 10 g of NaOH (Merck, Germany) at a pH of 12 in 25ml of de-ionized water under constant stirring for 2h and transferred into a 50mL Teflon lined autoclave kept at 180°C for 48h. The pH of the synthesis was also varied keeping other condition as identical. The prepared white product was centrifuged at 10,000rpm and successively washed with 0.1M HCl (Merck, Germany) to reduce the solution to pH ~7. The collected product was dried under IR lamp at ~80°C and annealed at 500°C for 2h to convert to the final product [15].

### **2.3.2. Synthesis of different phases of Iron Oxides**

#### **2.3.2.1. Synthesis of $\gamma$ -Fe<sub>2</sub>O<sub>3</sub> Nanoparticle**

At first 100mL of 0.1M [Fe(NO<sub>3</sub>)<sub>3</sub>·9H<sub>2</sub>O] solution was prepared. Hydrazine hydrate was added dropwise to the ferric nitrate solution and a red gelatinous precipitate was formed, and the pH became 3.30. Further, more hydrazine hydrate was added followed by sonication (ultrasonic power 250W, ultrasonic frequency 30kHz and probe diameter 25mm) for 15min till the pH reached 5.12. Addition of hydrazine was continued until a brownish solution was formed and sonicated for 2h until the pH reached 7.12. At the time of synthesis, the flow rate used for the addition of hydrazine was 0.5ml/s. The precipitate was washed with water followed by ethanol and centrifuged at 10,500rpm. The centrifuged precipitate was dried at 70°C for 24h in a hot air oven and then ground using mortar and pestle, and the product was collected carefully. After adding 1,10-phenanthroline to the filtrate part, no red coloration was observed which confirmed

the complete precipitation of Fe(III) present in the solution as well as no formation of Fe(II) during hydrolysis [16].

### **2.3.2.2. Synthesis of Fe<sub>3</sub>O<sub>4</sub> Nanoparticle**

Initially, 50mL of 0.1M [FeCl<sub>2</sub>·4H<sub>2</sub>O] and 50mL 0.2M [FeCl<sub>3</sub>·6H<sub>2</sub>O] solution was prepared. Then the solution was kept for 10min in the probe sonicator (ultrasonic power 250W, ultrasonic frequency 30kHz and probe diameter 25mm) and NH<sub>4</sub>OH was added to the mixture to reach the pH to 9. After continuous sonication for 30min the solution became black in colour and centrifuged the solution at 10,000rpm for washing with deionized water. After washing the sample was collected and kept for drying at 45°C.

### **2.3.2.3. Synthesis of α-Fe<sub>2</sub>O<sub>3</sub> Nanoparticle**

For synthesis of α-Fe<sub>2</sub>O<sub>3</sub>, firstly 100mL of 0.1M [Fe(NO<sub>3</sub>)<sub>3</sub>·9H<sub>2</sub>O] solution was prepared and directly added hydrazine in the ferric nitrate solution to maintain pH 7. Then the mixture solution was kept for sonication for 2h and light-yellow precipitate was collected and further centrifuged at 11000rpm and washed with water properly followed by ethanol. After centrifuging the precipitate sample was collected and was dried at 100°C for 24h. For confirmation of presence only Fe(III) in the solution, 1,10-phenanthroline was added to check no red coloration in the final product. After that the sample was calcined at 600°C for 6h at a heating rate of 5°C/min.

### **2.3.2.4. Synthesis of α-Fe<sub>2</sub>O<sub>3</sub> Fiber**

To synthesis Fe<sub>2</sub>O<sub>3</sub> fibres, 25wt% of PVP solution in 9mL ethanol was added to 1.5mL of 1.5g Iron(III) nitrate monohydrate aqueous solution under stirring. The resulting solution was stirred for 4 hours at room temperature to form a uniform viscous solution. Fibers were synthesized using an Espin Nanotech electrospinning unit. For electrospinning, the viscous solution was

transferred to a plastic syringe equipped with metallic needle. The fibers are collected on a rotating drum collector placed 14 cm distance apart from the spinneret. The solution flow rate of 1mL/h was controlled by a syringe pump, a potential of 14KV was applied between the spinneret and collector. To get Fe<sub>2</sub>O<sub>3</sub> fibers, the composite of PVP and Iron(III) nitrate monohydrate are calcined at 500°C for 5h at a heating rate of 2°C/min.

### **2.3.3. Synthesis of different morphology of Tungsten Oxide**

#### **2.3.3.1. Synthesis of WO<sub>3</sub> Nanoparticle**

Tungsten Oxide (WO<sub>3</sub>) particles were prepared by hydrothermal synthesis process. At first 5gm of Sodium tungstate dehydrate (Na<sub>2</sub>WO<sub>4</sub>.2H<sub>2</sub>O) was dissolved in 150ml deionized water to form a transparent solution. Concentrated hydrochloric acid (37%) was added drop-wise in the solution and yellowish tungstic solution was thoroughly formed. The prepared solution was transferred into a Teflon lined autoclave which was kept at 95°C for 24h in an oven. Then the collected product was centrifuged with deionized water for several time and kept it at 110°C for drying. The powder thus collected and calcined at 500°C for 5h.

#### **2.3.3.2. Synthesis of WO<sub>3</sub> Nanofiber**

For the synthesis of WO<sub>3</sub> fibers, chemical reagents are used as purchased without further purifications. Ammonium metatungstate hydrate and Polyvinylpyrrolidone (PVP) (MW = 55000) was purchased from Sigma Aldrich chemicals, ethanol was purchased from Spectrochem India. 27 wt% of Polyvinylpyrrolidone (PVP) (MW = 55000) solution in 11.5ml ethanol was added to 1.2ml aqueous solution of 1.6g Ammonium metatungstate hydrate under stirring. The resulting solution was stirred for 4h under ambient temperature to form a uniform viscous solution. Fibres were synthesized using an Espin Nanotech electrospinning unit. For electrospinning, the viscous solution was transferred to a plastic syringe equipped with metallic needle. The fibres were collected on a rotating drum collector placed 14cm

distance apart from the spinneret. The solution flow rate of 1 ml/hr was controlled by a syringe pump, a potential of 14KV was applied between the spinneret and collector. To get WO<sub>3</sub> fibers, the composite of PVP and Ammonium metatungstate fibers were calcined at 500°C for five hours at a heating rate of 2°C/min.

### **2.3.4. Synthesis of Bismuth Ferrite**

0.5mM each of bismuth nitrate [Bi(NO<sub>3</sub>)<sub>2</sub>·5H<sub>2</sub>O] and ferric nitrate [Fe(NO<sub>3</sub>)<sub>3</sub>·9H<sub>2</sub>O] was prepared by dissolving the required amount of the same in acidified distilled water. Hydrazine hydrate [N<sub>2</sub>H<sub>4</sub>, 50-60%] was added drop wise as a precipitating agent to the above solution, which resulted in the formation of red gelatinous precipitate at a pH~4. The sonication was continued using the ultrasonic processor Takashi U1800 30kHz and allowed to run for 30min. Further addition of hydrazine hydrate changed the colour of gelatinous precipitate to brownish black at a pH of 7.2. The addition of hydrazine hydrate solution was continued for 2h until the pH reached ~10. The obtained final precipitate was allowed to settle down and centrifuge at 10,000rpm with several washings with water and ethanol, respectively. In order to confirm the complete precipitation of Fe(III) present in the solution, a pinch of 1,10-phenanthroline was added to the filtrate part which indicated no red colour and thus confirming the complete precipitation of Fe(III) present in the solution, during hydrolysis. The centrifuged precipitate was further dried at 80°C for 24h in a hot air oven and then calcined at 500°C for 2h to get BFO sample which was used for further studies.

### **2.3.5. Synthesis of Zn<sub>2</sub>SnO<sub>4</sub>**

#### **2.3.5.1. Sonochemical Synthesis of Zn<sub>2</sub>SnO<sub>4</sub> Nanoparticles**

Controlled synthesis of pure Zn<sub>2</sub>SnO<sub>4</sub> was achieved by ultrasonication (ultrasonic power 250W, ultrasonic frequency 25kHz, probe diameter 25mm) followed by calcination. In a typical synthesis 0.01(M)  $\equiv$  0.27256g of Zinc chloride and 0.005(M)  $\equiv$  0.35058g of Tin(IV)



chloride pentahydrate were dissolved in 200ml deionised water under constant stirring for 15minutes maintaining the final mole ratio of Zn and Sn of 2:1. 2ml Ammonia solution was added drop-wise to the mixture which immediately reacted with  $ZnCl_2$  and  $SnCl_4$  resulting a slurry like white precipitation. The pH of the final solution was maintained  $\sim 9$ . The colloidal solution containing the precipitate was sonicated (Ultrasonic power 250W, ultrasonic frequency 25kHz, probe diameter, 25mm) for 7.5min, was repeated for 4 times. Between two successive ultrasonication steps, the mixture was stirred on a magnetic stirrer for 5min to make the solution homogeneous. The precipitate was collected by filtration and washed with distilled water to remove undesirable anions such as  $Cl^-$  followed by drying under IR lamp around  $70^\circ C$  for 4h and finally ground well to form a fine powder. Considering the mass loss in percentage from the TG analysis the as-synthesized powder was calcined for 8h at  $600^\circ C$ ,  $800^\circ C$ ,  $900^\circ C$  and  $1000^\circ C$  at a heating rate of  $100^\circ C/h$  [17].

### **2.3.5.2. Solid State Synthesis of $Zn_2SnO_4$ Nanostructures**

The starting materials, ZnO rods and  $SnO_2$  particles were synthesized through solution processed sonochemical synthesis followed by thermal annealing at  $300^\circ C$  and  $600^\circ C$ , respectively [P. P. Das et. al., 2014; S. Banerjee et. al., 2011]. The ZnO rods have been prepared by sonochemical method by using  $NH_4OH$  and zinc acetate. For this reaction, ammonia solution [30% GR, Merck Ltd. Mumbai, India] was added dropwise with 250mL of 0.1M zinc acetate [ $(CH_3COO)_2Zn \cdot 2H_2O$ , Merck, Germany], under sonication (ultrasonic power 250 W, ultrasonic frequency 25 kHz, probe diameter 25 mm) until the pH reached 9. Ammonia was added dropwise for getting homogeneous precipitation and this precipitation was centrifuged and again dispersed in 400mL of water and then stirred in a magnetic stirrer for 6h at temperature  $80^\circ C$ . The obtained precipitate was centrifuged at 10,000rpm for 10 min and washed with distilled water and dried under IR lamp at  $70^\circ C$  and calcined at  $300^\circ C$  for 4h. For  $SnO_2$  particle synthesis, required amounts of  $SnCl_2 \cdot 2H_2O$  was mixed thoroughly in HCl under

sonication (ultrasonic processor, model-PR 1000, Oscar Ultrasonics, India, 1000 W) for 30min and dropwise  $\text{NH}_4\text{OH}$  was added to the mixture. The sonication was continued for 2h until the pH of the mixture reached 9 and the mixture was centrifuged and washed with distilled water followed by acetone. The obtained sample was dried in a vacuum and calcined at  $600^\circ\text{C}$  for 6h. For a typical batch synthesis of  $\text{Zn}_2\text{SnO}_4$ , ZnO rods and  $\text{SnO}_2$  particles were mixed in a molar ratio of 2:1 and ground thoroughly in an agate mortar with successive dropwise addition of ethanol at short intervals to make the mixture homogeneous. The mixture was calcined at  $800^\circ\text{C}$  and  $1000^\circ\text{C}$  for 8h for further studies [18].

### **2.3.5.3. Hydrothermal Synthesis of $\text{Zn}_2\text{SnO}_4$ Nanoparticles**

In a typical synthesis, 0.525g of Zinc chloride and 0.675g of Tin(IV) chloride pentahydrate were dissolved in 50ml of water/ethylene glycol (volume ratio 1:1) under constant stirring on a magnetic stirrer followed by the drop-wise addition of 25ml of 1.3M triethylamine (TEA) to the solution resulting in the formation of white slurry. The mixture was further stirred continuously for 2h. It was then transferred into three Teflon-lined autoclaves and kept at  $175^\circ\text{C}$  in an oven for 24h, followed by a natural cooling. The precipitate was then washed thoroughly with distilled water for several times to remove the excess amine and dried under IR lamp at  $\sim 80^\circ\text{C}$  and finally annealed at  $500^\circ\text{C}$  for 2h. The annealed sample has been considered for further characterizations [19].

## **2.4. Characterization of the Synthesized Powder Samples**

### **2.4.1. Structural Analysis**

The synthesized powder samples have been characterized by various analytical techniques to confirm phase purity and homogeneity. The techniques that have been used are thermal analysis to understand the stability of materials, powder X-ray diffraction to understand the purity and microstructure analysis to understand the size and shape of the materials.

### **2.4.1.1. Thermogravimetric Analysis:**

The technique of thermal analysis comprises of a series of methods, which detect the changes in the physical and mechanical properties of the given substance by the application of heat or thermal energy. The physical properties include mass, temperature, enthalpy, dimension, dynamic characteristics, etc. Thermogravimetric Analysis (TGA) measures the weight change of the material with respect to temperature. The measurement is normally carried out in controlled atmosphere including air, ambient or inert atmosphere. The specimen powder is placed on a refractory pan (often made of porcelain or platinum or alumina). The pan, in the hot zone of the furnace, is suspended from a high precision balance. A thermocouple is in close proximity to the specimen but not in contact, so as not to interfere with the free float of the balance. The balances are electronically compensated so that the specimen pan does not move when the specimen gains or losses weight. Thus, thermogravimetric analysis involves monitoring the weight of the sample while varying temperature at a controlled rate. In order to understand the thermal decomposition nature of the samples, TGA of the as prepared samples were carried out from room temperature to 1000°C at a heating rate of 10°C/min on a NETZSCH 449C simultaneous thermal analyzer. About 20mg of powder was used for thermal analysis study. From the TGA data, the percent weight change of the sample at different temperatures was observed and on the basis of its calcination temperature of the material of interest was determined.

### **2.4.1.2. Differential Thermal and Scanning Calorimetry Analysis:**

In Differential Thermal Analysis (DTA), the temperature difference between a reactive sample and a non-reactive reference, usually  $\alpha$ -alumina, is measured as a function of time, providing useful information about the thermodynamics and kinetics of reactions while the reference material and the substance under study are subjected to a controlled program. The reference

material is usually an inert substance, with about the same mass as the sample and does not undergo any transformation. Under constant pressure the change in enthalpy of the reaction is equivalent to the area under DTA peak where the sample and the reference heat capacities and thermal conductivities are same. Various thermal information of the material such as melting temperature, glass transition temperature, and phase formation/transition and reaction kinetics can be obtained from DTA study. Thermal events under both reactive (e.g. in air) and inert conditions (e.g. in nitrogen, helium or argon) can also be investigated. In DTA; temperature difference ( $\Delta T$ ) is plotted on the ordinate, and temperature (T) is on the abscissa. Here for endothermic reaction, the temperature difference is considered to be negative and for exothermic changes it is positive in nature.

Differential Scanning Calorimetry (DSC) measures the temperatures and heat flows associated with transitions in materials as a function of time and temperature in a controlled atmosphere. Throughout the experiment both the sample and reference are maintained nearly at the same temperature. The temperature program for DSC analysis is designed such that the sample holder temperature increases linearly with time. The reference should have well defined heat capacity over the temperature range to be studied. These measurements provide quantitative and qualitative information about physical and chemical changes that involve endothermic or exothermic processes, or changes in heat capacity ( $C_p$ ). The advantage of DSC is the ease and speed with which it can be used to see transitions in materials. Actually, similar kind of thermal information can be obtained from both the DSC and DTA study. DSC measures the energy directly whereas DTA measures the difference in temperature between the sample and the reference when they are both put under the same heat treatment conditions. From the DTA curve we can calculate the change of heat of reaction with respect to temperature and on the other side the change in enthalpy with respect to temperature was measured from DSC graphs collected on a Netzsch STA 449C instrument. DSC and DTA both measurements were carried

out from room temperature to 1000°C temperature in air at a heating rate of 10°C/min, using 20mg of powder samples.

#### **2.4.1.3. X-ray Diffraction Analysis:**

X-rays are basically electromagnetic radiations which have the photon energy in between range of 100eV-100keV and can penetrate into the materials and give the whole crystallographic structural properties of the molecules. This technique has been performed to understand the different structural and crystallographic information such as phases of materials, crystal structure, lattice parameter, size, defect state, strains and other structural patterns. X-rays are generated when electron beam accelerated towards a high voltage field and bombards a target either stationary or rotating. Most common targets used in the tubes of X-ray include Cu-K $\alpha$  and Mo-K $\alpha$  radiation, emitting 8KeV and 14KeV X-rays corresponding to the wavelengths of 1.54Å and 0.8Å, respectively. At first X-ray interact directly with the electrons of the atoms and at the time of interaction from the incident beam some photons will be deflected away from the direction where they originally travel or diffraction occurs. The scattered X-rays give the information about the electron distribution of the materials. If we assume that an X-ray beam is reflected by an atomic plane according to Snell's law (incident beam, reflected beam and normal in one plane and angle of incidence equal angle of reflection) both rays can reinforce each other in the reflected direction only if their path difference is an integer time  $\lambda$ . So, the condition for a diffraction (peak) to occur can be represented by the Bragg's law [20]:

$$2d \sin \theta = n\lambda \text{ with } n = 0, 1, 2, 3, 4 \dots \dots \dots (2.1)$$

Where, ' $\lambda$ ' is the wavelength of the X-ray, ' $\theta$ ' is the scattering angle and n indicates an integer represents the order of the diffraction peak. The relation between the inter layer spacing (d-value) and lattice parameters (a, b and c) is as described:

$$1/d^2 = h^2/a^2 + k^2/b^2 + l^2/c^2 \dots \dots \dots (2.2)$$

In this thesis work, the lattice parameters of different crystallographic materials synthesized such as many binary and ternary metal oxides have been calculated by using equation (2.2).

Crystal size of material was measured by using Scherrer equation (2.3) from line broadening  $T=K\lambda/\beta\cos\theta$  .....(2.3)

Here  $\theta$  is considered for a specific XRD diffraction peak,  $K$  is dimensionless shape factor close to 1,  $\beta$  is full width at half maximum of the peak and  $T$  is the mean crystallite size for the specific crystal plane of the peak. The phase identification of the powder samples was carried out on a X'pert pro MPD XRD of PAN analytical with Cu  $K\alpha$  radiation ( $\lambda= 1.5406 \text{ \AA}$ ) and the total scan was performed starting from  $5^\circ$  to  $90^\circ$  with a scan rate of  $2^\circ/\text{min}$ . The crystal structure of the synthesized materials and the phase identification were determined by comparing the recorded data with peaks and relative intensities of "standard" data provide by international centre for diffraction data. This was done with the help of JCPDS (Joint Committee on Powder Diffraction Standards, 1969) index file (PCPDFWIN, version 1.10). PCPDFWIN includes automated search MATCH FUNCTION that compares the sample pattern with the ICDD database. Hence, X-rays help in the elucidation of crystallographic characteristics of the material (Figure 2.3).

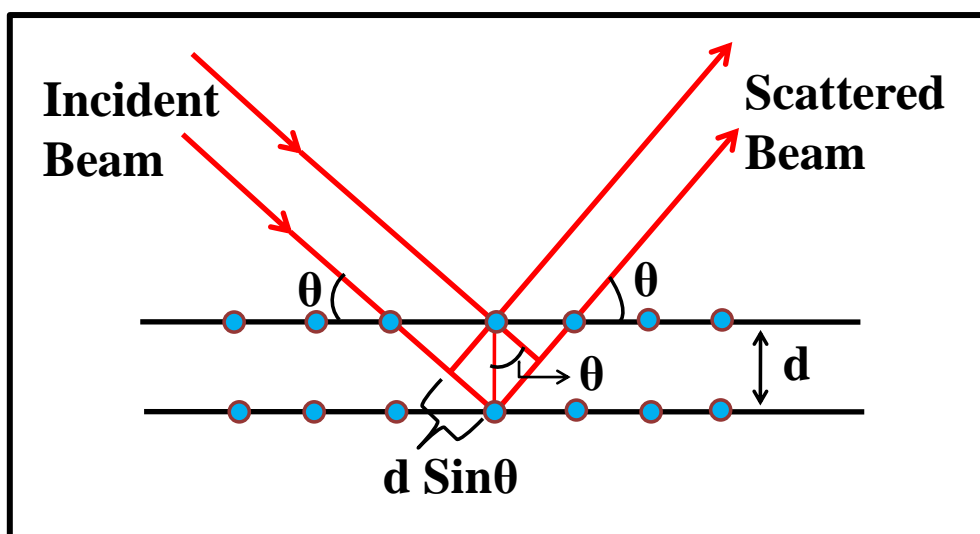


*Figure 2.3: Schematic diagram of principle X-ray diffraction process.*

### **2.4.2. Microstructural Characterization:**

The microstructural characteristics can be studied by using an electron microscope (EM) which is a beam of electrons use to illuminate a specimen and produce a magnified image. In comparison with a light-powered optical microscope, an electron microscope has greater resolving power as electrons have wavelengths about 100,000 times shorter than visible light (photons). For elemental and chemical composition study of the sample, Energy-dispersive X-ray spectroscopy (EDS or EDX) technique has been used greatly. It depends on the investigation of an interaction of some source of X-ray excitation and a sample. Its characterization capabilities are due in large part to the fundamental principle that each element has a unique atomic structure allowing unique set of peaks on its X-ray spectrum. A high energy beam of charged particles like electrons or protons or a beam of X-rays, is focused onto the studied sample to stimulate the emission of characteristic X-rays from a specimen. To understand the microstructural information of a material, different types of EM are available for use such as Scanning Electron Microscope (SEM), Field Emission Scanning Electron Microscopy (FESEM), Transmission Microscopy (TEM) etc. For elemental and compositional study of a sample EDAX is normally used associated with SEM, FESEM or TEM instrument.

#### **2.4.2.1. Field Emission Scanning Electron Microscopy:**

The emission of electrons under the influence of high electrostatic field from a metal or semiconductor into vacuum at the surface is termed as Field emission. Wood in 1987 [21] first reported this phenomenon. After that Schottky explained this phenomenon by a complete reduction of the height of a potential barrier at the surface down to the Fermi Level [22]. The phenomenon of field emission was used to develop a microscope on the basis of the difference in work-function of the various crystal planes on the surface. For producing intense electric field, the emitter is made in the form of a sharp “tip”. The electric field at the apex of the tip is

inversely proportional to the radius of the tip and the radius of the tip is of the order of 100nm. Its material is composed of a metal with a high melting point such as tungsten [23]. The Field emitted electrons travel along the field lines and producing bright and dark patches on the fluorescent screen giving a one-to-one correspondence with the crystal planes of the hemispherical emitter. The work-function anisotropy of the crystal planes is mapped onto the screen as intensity variations. This acts as a microscope without any lenses [24].

Actually, FESEM is a microscope that works with electrons (particles with a negative charge) instead of light. These electrons are liberated by a field emission source. Electrons scan the object according to a zig-zag pattern. The microscope possesses the magnification in the order of  $10^5$  and has a resolving power of 30Angstrom. The Energy-Dispersive Spectroscopy (EDS) system associated with it, can detect X-rays emitted from the sample as a result of the high-energy electron beam penetrating into the sample. X-ray spectra can be collected and analyzed, yielding quantitative elemental information about the sample.

A “standardless” routine is utilized, which yields an accuracy of 1-2% and sensitivities for some elements down to 0.1 weight percent. Line-scans and X-ray maps can also be generated. FESEM produces clearer, less electrostatically distorted images with spatial resolution down to 1-1/2 nm. That is almost 3 to 6 times better than conventional SEM. The FESEM is used to visualize and understand very small topographic details on the surface of entire or fractioned objects. This type of technique can be used to measure the coating thickness and structural uniformity of the prepared sample, characterization of size, distribution of size, shape and correlation of surface appearance and surface morphology and elemental identification and composition. We are using Field Emission Scanning Electron Microscope (Supra 35VP, Carl Zeiss) for our synthesized sample characterization and to understand the morphology of the sample, sensor coating microstructure including coating thickness of the prepared sensor.



### **2.4.2.2. Transmission Electron Microscopy:**

In transmission electron microscopy (TEM), a beam of electrons is transmitted through an ultra-thin specimen (or electron transparent solution), interacting with the specimen as it passes through. At the time of interaction of the electrons transmitted through the specimen, an image is formed in magnified nature and focused onto an imaging device. There are different types of imaging devices such as a fluorescent screen, a layer of photographic film or a sensor like CCD camera. The basic principle of operation of the transmission electron microscope (TEM) is similar to light microscope, but the difference is that it uses electrons instead of light. In this particular technique, a thin specimen is illuminated with electrons in which the electron intensity is uniform over the illuminated area [25]. As electrons travel through the specimen, they are either scattered by a variety of processes or they may remain unaffected by the specimen. The net result is that a non-uniform distribution of electrons emerges from the exit surface of the specimen that contains all the structural and chemical information about the specimen [26].

TEM produces normal as well as high-resolution micrographs (HRTEM), in the form of black and white image (known as dark and bright field images respectively) from the interaction that takes place between prepared samples and energetic electrons in the vacuum chamber [27]. A vacuum chamber is prepared by pumping the air out to create a space for the free movement of the electron. The beam passes through the solenoids, down the column, makes contact with the screen where the electrons are converted to light and form an image. The image can be manipulated by adjusting the voltage of the gun to accelerate or decrease the speed of electrons as well as changing the electromagnetic wavelength via the solenoids. The coils focus images onto a screen or photographic plate. During transmission, the speed of electrons directly correlates to electron wavelength; the faster electrons move, the shorter wavelength and the greater the quality and detail of the image. The lighter areas of the image represent the places

where a greater number of electrons were able to pass through the sample and the darker areas reflect the dense areas of the object. These differences provide information on the structure, texture, shape and size of the sample.

To obtain a TEM analysis, samples need to have certain properties, viz., sample should have electron transparency. Samples need to be able to withstand the vacuum chamber and often require special preparation before viewing. Angular distribution of scattering can be viewed in the form of scattering patterns, usually called diffraction patterns, commonly referred to as selected area electron diffraction (SAED). TEM is the technique of choice due to atomic-level resolution leading to direct visual morphological information like size, shape, dispersion and structure. Further, when coupled with selected area electron diffraction (SAED), the technique can provide important information on the crystallographic directions in the structures, helpful to understand the growth kinetics [28].

Energy dispersive analysis using X-rays (EDAX) has been used to determine the chemical composition, stoichiometry (including “hkl” planes and “d” value detection) or the impurity content in the compound. The particle size and morphology of the powder samples were examined by TEM analysis on a Technai G2 30ST unit. The calcined powders were dispersed in ethanol prior to the sample preparation required for the TEM examination. A small volume of dispersion using a micropipette was dropped onto the carbon coated copper grid for the final examination. The size of the particles in the TEM micrographs and their distributions were calculated using an ImageJ software.

### **2.4.3. Spectroscopic Techniques:**

#### **2.4.3.1. Fourier Transform Infrared Spectroscopy:**

Fourier-transform infrared spectroscopy (FTIR) is a workhorse technique collecting spectral data based on the measurements of the coherence of a radiative source, using time-domain or

space-domain measurements in a wide range for material analysis which corresponds to the infrared region of the electromagnetic spectrum [29]. Actually, the resulting spectrum represents absorption and transmission which correspond to the particular frequencies of the vibrations between the bonds of the atoms making up the material especially for identifying organic functional groups and in some cases inorganic materials.

The main criteria for a molecule to be IR active are that the dipole moment of the molecule must be changed during vibration [30]. The infrared (IR) region can be separated into three parts depending on their harmonic vibrations, fundamental vibrational, and rotational modes of atoms or molecule; NIR (14000-4000  $\text{cm}^{-1}$ ), Mid IR (4000-200  $\text{cm}^{-1}$ ) and Far IR (50-1000  $\text{cm}^{-1}$ ) region. FTIR spectrometer is commonly used for measuring in the Mid-IR region to study the fundamental vibrational and rotational structure.

The basic principle of FTIR technique relies on the absorption of incident infrared light by the sample at different wavelengths. The light passes through a beam splitter, which sends the light in two directions at right angles. One beam goes to a stationary mirror and the other goes to a moving mirror. When the two meet up again at the beam splitter, they recombine to create constructive and destructive interference. The detector now reports variation in energy versus time for all wavelengths simultaneously and a common algorithm Fourier transform turns those raw data into intensity vs. frequency spectrum with high signal to noise ratio. These are the major advantage of the FTIR spectrometer over a dispersive spectrometer.

All the FTIR spectra were collected on a Perkin Elmer FTIR Spectrometer in the range of 400-4000 $\text{cm}^{-1}$ . For each spectrum, 200 interferograms of 4 $\text{cm}^{-1}$  resolution were recorded. Potassium bromide (FTIR grade  $\geq 99\%$ , Sigma Aldrich (Germany)) was used to prepare pellets. The as-received KBr was oven-dried overnight at  $\sim 100^\circ\text{C}$  and then stored in a desiccator prior to use. For better measurement, the ratio of sample:KBr was varied to nullify the back ground signal.

**2.4.3.2. UV-Visible Spectroscopy:**

UV-Visible (UV-Vis) spectroscopy deals with the recording of absorption signals due to electronic transitions. In semiconductors, when the incident photon energy exceeds the band gap energy of the materials, absorption takes place and signal is recorded by the spectrometer whereas in metals when the surface free electrons vibrate coherently with the incident frequency then resonant absorption takes place. It measures the intensity of light passing through a sample (I), and compares it to the intensity of light before it passes through the sample (I<sub>0</sub>). The ratio of I/I<sub>0</sub> is determined as the transmittance, and is usually expressed as a percentage (%T). The absorbance (A) is based on the transmittance as [equation (2.4)],

$$A = -\log(\%T/100) \dots\dots\dots(2.4)$$

UV-Vis spectroscopic method is based on the Beer-Lambert law, mentioned in equation (2.5).

$$A = \epsilon cl \dots\dots\dots(2.5)$$

In the experimental part, the absorbance of the dispersions of the samples as well as the percentage of optical transmittance (%T) of the films was measured by UV-Vis-NIR spectrophotometer (Shimadzu UV-3600), using a Xe lamp, as a function of wavelength in the wavelength range of 200-800nm. The fundamental interest of measuring these spectra is to calculate the energy gap or band gap of synthesized samples. The band gap or energy gap (E<sub>g</sub>) can be estimated by assuming direct transition between conduction band and valance bands. Theory of optical absorption gives the relationship between the absorption coefficients  $\alpha$  and the photon energy,  $h\nu$  for direct allowed transition as [equation (2.6)], [31]

$$(\alpha h\nu)^2 = A(h\nu - E_g) \dots\dots\dots(2.6)$$

This is popularly known as Tauc's equation where, A is a function of index of refraction and hole/electron effective masses where  $\alpha$ ,  $\nu$ ,  $h$  corresponds to absorption coefficient, frequency and Planck's constant respectively. Extrapolation of linear part of the absorption edge leads to the axis interpretation, which corresponds to the band gap (E<sub>g</sub>) of the corresponding material.

### **2.4.3.3. Raman Spectroscopy:**

When a beam of visible light is passed through a transparent substance, a small amount of the radiation energy is scattered, the scattering persists even if all other extraneous matter is rigorously excluded from the substance. If monochromatic radiation is used and the scattered energy will consist almost entirely of radiation of the incident frequency then it is the so-called Rayleigh scattering but, in addition, certain discrete frequencies above and below that of the incident beam will be scattered, it is referred to as Raman scattering. When the frequency of incident radiation is higher than frequency of scattered radiation, Stokes lines appear in Raman spectrum. But when the frequency of incident radiation is lower than frequency of scattered radiation, anti-Stokes lines appear in Raman spectrum. Scattered radiation is usually measured at right angle to incident radiation. Stokes shifted Raman bands involve the transitions from lower to higher energy vibrational levels and therefore, Stokes bands are more intense than anti-Stokes bands and hence are measured in conventional Raman spectroscopy. Whereas, anti-Stokes bands are measured with fluorescing samples because fluorescence causes interference with Stokes bands, as schematically illustrated in Figure 2.4. The magnitude of Raman shifts does not depend on wavelength of incident radiation. Raman scattering depends on wavelength of incident radiation. A change in polarizability during molecular vibration is an essential requirement to obtain Raman spectrum of sample. Since Raman scattering of water is low, it is an ideal solvent for dissolving samples. Glass can be used for optical components (mirror, lens, sample cell) in Raman spectrophotometer. Raman shifts are typically in wave numbers, which have units of inverse length. In order to convert between spectral wavelength and wave numbers of shift in the Raman spectrum, following formula [equation (2.7)] can be used, [32]

$$\Delta w = (1/\lambda_0 - 1/\lambda_1) \dots \dots \dots (2.7)$$

Where,  $\Delta w$  is the Raman shift,  $\lambda_0$  is the excitation wavelength and  $\lambda_1$  is the Raman spectrum wavelength. Most common unit to express wave numbers in Raman spectrum is  $\text{cm}^{-1}$ . A typical

Raman spectrometer consists of laser beam (very narrow, monochromatic, coherent and powerful) which when passed through the cell, usually a narrow glass or quartz tube filled with the sample, light get scattered sideways from the sample, which is collected by a lens and passed into a grating monochromator. The signal is measured by a sensitive PMT and after amplification; it is usually processed by a computer which plots the Raman spectrum. Raman spectra of the samples were obtained using a Renishaw InVia Reflex micro-Raman spectrometer. The data were collected after with excitation of argon ion (514nm) lasers with a resolution of  $1\text{cm}^{-1}$  under line-focus mode and the laser power was adjusted to 0.5% which was about 1.25mW. Spectra were collected at room temperature in continuous mode with 10sec. exposure time and accumulated for one time using a grating of  $1200\text{mm}^{-1}$ . The intensity data were plotted against Raman frequency shift, in the range of  $50\text{-}1500\text{cm}^{-1}$ . We have used STR500, Cornes Technologies (formerly known as Seki Technotron) Raman spectrometer. A 514.5nm Ar<sup>+</sup> ion green laser was used with 50mW power. The Raman signals were taken over 10sec of exposure time using 1200 grating sizes and 50x objective lenses of the spectrometer.

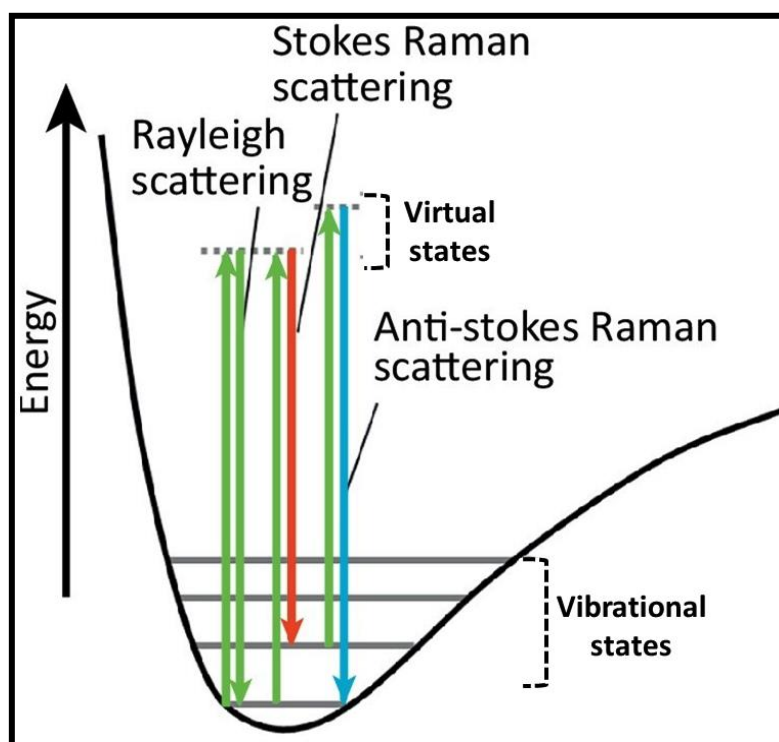


**Figure 2.4:** Jablonski diagram for Raman scattering.

#### **2.4.3.4. X-ray Photoelectron Spectroscopy:**

X-ray Photoelectron Spectroscopy (XPS) is a quantitative spectroscopic technique. It is a surface analytic technique where the spectra are obtained by irradiating a material with a beam of X-ray and while simultaneously measuring the kinetic energy (KE) and number of electrons that escapes from the top 1 to 10nm of the materials being analyzed. From this study we can get different surface related information like elemental composition, empirical formula, chemical state and electronic state of the elements present in the material. When a soft X-ray irradiates the surface, the core-level electrons are emitted from the surface. The binding energy ( $E_B$ ) of each of the emitted electron can be determined by using the equation,

$$E_B = E_{\text{Photon}} - (EK + \Phi) \dots\dots\dots(2.8)$$

Here,  $E_{\text{Photon}} = h\nu$  is the X-ray energy, which is being used. EK is the kinetic energy of the electron as measured by the instrument and  $\Phi$  is the work function of the spectrometer. Then the EB can be calculated from the above equation which is the main goal of the spectrometer. All the binding energies (BE) are referred to the C 1s peak (set at 284.6eV) arising from surface hydrocarbons (or adventitious hydrocarbon). In this thesis work, the X-ray photoemission spectroscopy measurements of the synthesized samples were carried out in a PHI 5000 Versa probe II scanning XPS microprobe (ULVAC-PHI, U.S.). The measurements were performed at room temperature and at a base pressure better than  $6 \times 10^{-10}$  mbar. All spectra were recorded with monochromatic Al K $\alpha$  ( $h\nu = 1486.6\text{eV}$ ) radiations with a total resolution of about 0.7eV and a beam size of 100 $\mu\text{m}$ .

#### **2.4.4. Specific Surface Area Analysis:**

Surface area of a solid sample can be best described as the external surface area of a solid object including surface attributable to pores. Brunauer-Emmett-Teller (BET) method is the standard technique for estimation of the mesoporous film porosity, pore size distribution and its surface

area per gram. BET theory is based on the physical adsorption/desorption of the gas molecules (N<sub>2</sub> inert gas as a standard for this method) and determines the sample surface area and pore volume. The surface area per gram of the material can be controlled by using different molar ratio of precursors in material's synthesis or by using different concentration of precipitation agent. BET has been used to characterize the special surface area per gram of as synthesized materials. BJH analysis can also be employed to determine pore area and specific pore volume using adsorption and desorption techniques. This technique characterizes pore size distribution independent of external area due to particle size of the sample. The concept of the BET theory is an extension of the Langmuir theory, which is a theory for monolayer molecular adsorption to multilayer adsorption [33]. The BET equation is expressed by equation (2.9),

$$1/[VP/(P_0-1)] = 1/V_m C + (C-1) P/V_m C P_0 \dots\dots\dots(2.9)$$

Where, c is a constant and V<sub>m</sub> is volume of mono layer formed at the boiling point of nitrogen. V is the volume of gas adsorbed and is measured at a constant temperature for various values of P/P<sub>0</sub> (usually in the range of 0.05-0.3).

From the nature of adsorption-desorption isotherm the materials are classified into five different porous types as shown in Figure 2.5. Nitrogen adsorption-desorption measurements were conducted at 77K with a Quantachrome (iQ3) instrument. The samples were out gassed in a vacuum at 200°C for 2h prior to the measurement. The surface area was obtained using the Brunauer-Emmet-Teller (BET) method within the relative pressure (P/P<sub>0</sub>) range of 0.05-0.20, and the pore size distribution was calculated by the Barret-Joyner-Halenda (BJH) method. The nitrogen adsorption volume at the relative pressure (P/P<sub>0</sub>) of 0.99 was used to determine the pore volume. The specific surface area and pore size distribution measurement was carried out for synthesized materials for sensor application by Brunauer-Emmett-Teller (BET) method on a Quantachrome Instrument (NOVA 4000 E series).



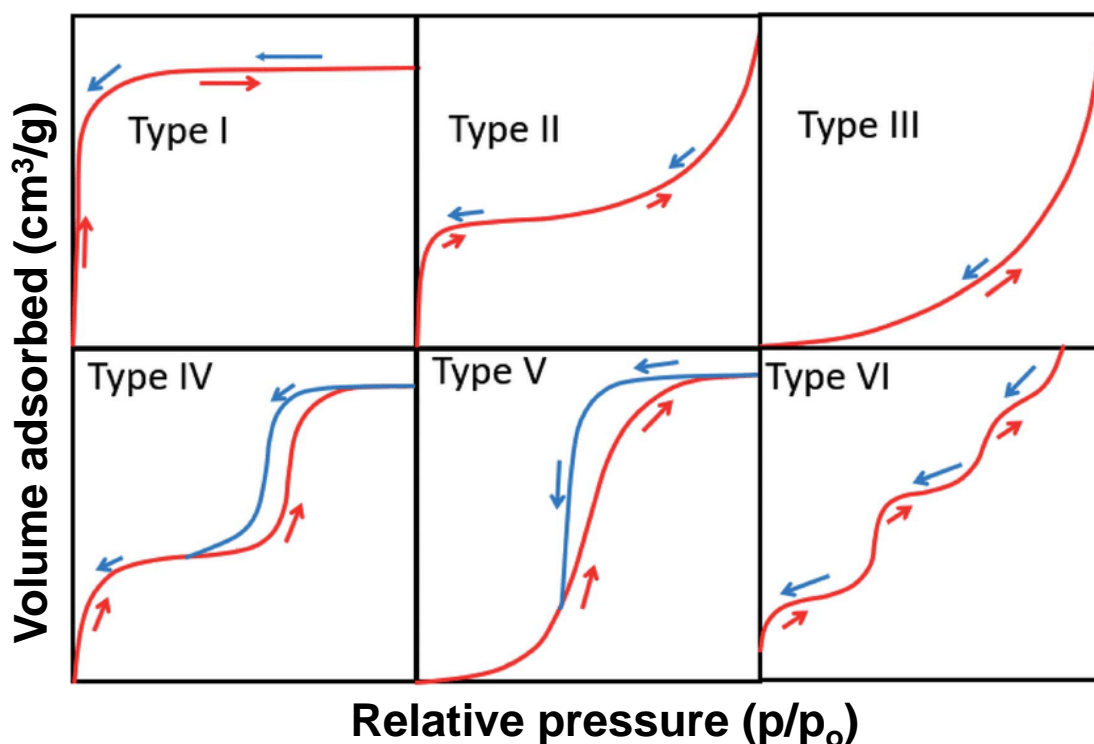


Figure 2.5: Different type of  $N_2$  adsorption-desorption isotherms.

#### 2.4.5. Zeta Potential Measurement and Particle Size Analysis:

Zeta potential is scientifically known as electro-kinetic potential in colloidal dispersions. Theoretically zeta potential is the electric potential in the interfacial double layer at the location of the slipping plane relative to a point in the bulk fluid away from the interface or the potential difference between the dispersion medium and the stationary layer of fluid attached to the dispersed particle. Thus, it is widely used for quantification of the magnitude of the charge. The zeta potential mainly justifies the stability of colloidal dispersions. The threshold of zeta potential value of  $\pm 30\text{mV}$  indicates the stability of solution. The zeta potential is often measured at different pH. The colloidal stability can be achieved by increasing the surface charge i.e., zeta potential.

Dynamic light scattering (DLS) technique has been used to measure the particle size in the dynamic range of  $0.3\text{nm}$ - $8\mu\text{m}$ . The lower limit is influenced by concentration, how strongly

the sample scatters light and the presence of large, unwanted particles. The upper limit is influenced by the density of the sample since DLS is modelled on all motion coming from Brownian motion, not from gravitational settling. The zeta potential and DLS measurements have been carried out on Horiba Nanoparticle Analyzer model- SZ100.

### **2.4.6. DC Current-Voltage (*I-V*) Characteristics Measurement:**

A current-voltage characteristic or *I-V* curve is a relationship, typically represented as a chart or graph, between the electric current through a circuit, device, or material, and the corresponding voltage, or potential difference across it. It is generally used to understand the basic parameters of a component or device which can also be used to mathematically model its behaviour within an electrical/electronic circuit. *I-V* characteristics curves can be used to plot the operation of any electrical or electronic component from resistors, to amplifiers, to semiconductor devices such as diodes, transistors and thyristors and solar cells. The simplest *I-V* characteristic involves a resistor, which according to Ohm's law exhibits a linear relationship between the applied voltage and the resulting electric current. The current voltage characteristics of an electronic component tells us much about its operation and can be a very useful tool in determining the operating characteristics of a particular device or component by showing its possible combinations of current and voltage, and as a graphical aid can help visually to understand better what is happening within a circuit.

Here, throughout the work, temperature dependent relationships between the direct current (DC) through a sensor device and the DC voltage characteristics across its terminals are shown. These were measured by using an Agilent made 2 channel precision source & measurement unit (model no. B2902A) along with a GW Instek made dual-range DC power supply (model no. SPD-3606) for -42V to +42V bias voltage ranges at different operating temperatures from 150°C to 350°C in air and in presence of acetone environment.

### **2.5. Sensor Fabrication Details**

#### **2.5.1. Fabrication of Sensors**

There are different types of device structures in conductometric sensors based on the heating mechanisms available in the device such as: directly and indirectly heated devices. A directly heated type structure means the heater is contacted with the sensing material, which generally lacks stability and anti-interference ability. So, most of the nanostructure-based gas sensors are indirectly heated types which are mainly fabricated in two different forms such as cylindrical and planar layouts. Alumina ceramics (wafers or tubes) are generally used as substrates to support the sensing films. In the ceramic tube-based device, a piece of heating wire is placed in the interior of the tube, while, in the ceramic wafer-based device, heating paste is placed on the backside of the wafer. For the planar sensor set-up, interdigital electrodes (IDE) are prepared as transducers with 50 $\mu\text{m}$  lines and 50 $\mu\text{m}$  spaces by laser patterning of fired Au thick-film layers. Usually, Au thick-film paste is printed on top of an alumina substrate and fired for nearly 10min at 850 $^{\circ}\text{C}$ . The fired dense film of  $\sim 10\mu\text{m}$  thickness is covered all over the substrate [34-36]. Maiti and co-workers fabricated Taguchi type thick film gas sensors of various materials for different gas sensing applications [37-40].

In this work, Taguchi type thick film tubular shaped sensors have been fabricated as shown in Figure 2.6 [41-44]. For making coating of the sensor materials, the thick paste of the calcined powders was made using very small amount (1 wt% with respect to the weight of powder) of alumina sol as binder and then coated (coating thickness 50-60 $\mu\text{m}$ ) on the outer surface of alumina tubes (length  $\sim 3\text{mm}$ , outer diameter  $\sim 1\text{mm}$  and thickness  $\sim 0.2\text{mm}$ ) as thick paste with gold electrodes and platinum lead wires already attached at the ends of the substrate. The as-prepared powders were calcined previously in a chamber furnace. The coated alumina tubes were cured at 300 $^{\circ}\text{C}$  to 600 $^{\circ}\text{C}$  for 45min, depending on the materials under investigation. Curing helped to evaporate the binders resulting in porous coating with increased effective

surface area for easier gas adsorption as well as diffusion. After curing, nichrome heating coils were placed inside the tubes for indirect heating of the sensing materials.

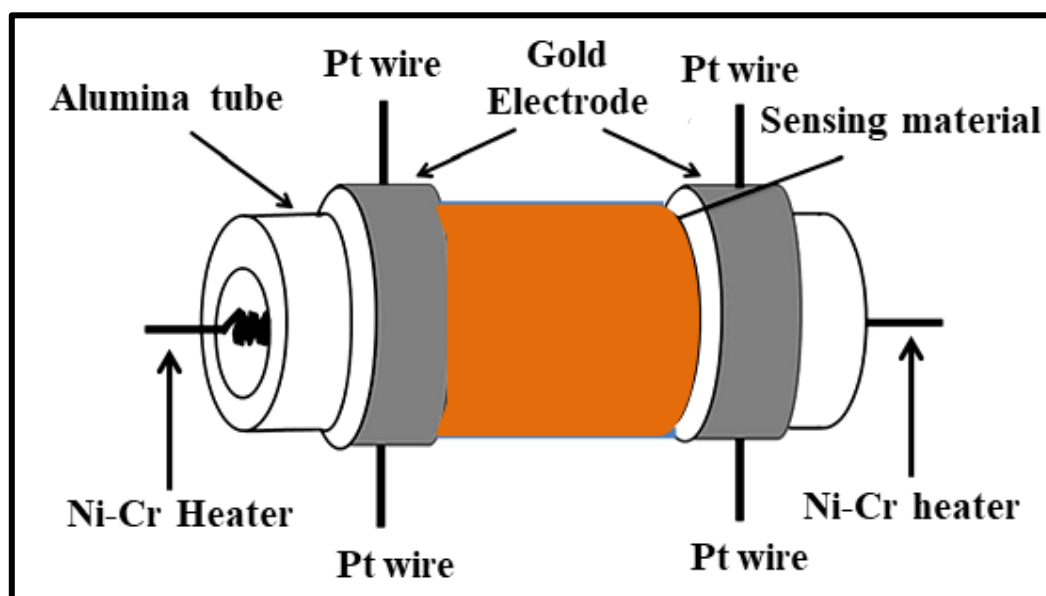


*Figure 2.6: Schematic diagram of sensor devices.*

### **2.5.2. Substrate Preparation, Coating on Substrate and Heat Treatment**

Thin alumina tubes were used for sensor fabrication whose outer diameter was 2mm and thickness ~0.2mm and length ~12mm. This type of hollow alumina tubes was cut in 3mm length and tubes were polished and properly cleaned through chemical etching by using dilute HCl. After that, the substrates were cleaned in distilled water under sonication in a sonication bath, kept for drying in an oven at nearly 70<sup>o</sup>-80<sup>o</sup>C for 45min to 60min. The substrates were then electroded with gold paste (made by Gwent Electronic Materials Ltd., United Kingdom, product no. C2070117D2) on both ends of the substrates. It introduces contact-electrodes on the alumina substrates. The distance between the two electroded parts was maintained at nearly 2mm. After that the pasted substrates were dried in an oven for 30min. Now on these substrates, on either side over gold paste electrode areas, platinum lead wires were attached at the both ends. The leaded substrates were again gold pasted over the platinum wires followed by curing in a tube furnace at 930<sup>o</sup>C for 1h with aerial environment which helps the pastes to stabilize by

means of full evaporation of the solvent part from gold paste with suitable contact between platinum lead to achieve the full requirement characteristics for electrical measurements. The electroded substrates are now fully prepared for coating. The important methods for fabricating thin and thick film based on metal oxides gas sensors are different coating techniques such as spin coating [45,46], dip coating [47], simple thermal vaporization process [48,49], surface chemical modification [50], sol-gel dip coating [51], deposition by e-beam evaporation [52], spray pyrolysis process [53], photochemical deposition and doping methods [54], lithographic technique [55] and sol-gel deposition [56].

Here, in this thesis work the thick film coating have been done by microposition-control coating unit for powder slurry coating on the outer surface of several leaded substrates through brush coating with repeated cycles to maintain the thickness of nearly 50-60 $\mu\text{m}$ . The consistency of the pastes and the processing variables were optimized to get final coatings of specified thickness. This coating practice for thick film is easy to perform and cost effective. For making coating of the sensor materials on the substrates, the thick paste or slurry of the calcined base material (semiconducting oxide) powders were made using very small amount (1 wt% with respect to the weight of powder) alumina sol as binder and then brush coated by micro-position-controlled coating unit as thick paste.

The amount of alumina present in the added sol was only 1 wt% and hence was expected not to affect the properties of the sensor material. However, it was observed from the response study of powder coating with and without alumina sol, that the sol had no adverse effect on the sensor performance. It basically helped to form strongly adhered coating on cylindrical alumina ( $\text{Al}_2\text{O}_3$ ) substrate's surface. Another advantage of using alumina sol is that it prevents cracking during sintering due to the difference in thermal expansion between the sensing material and the alumina substrate. This difference is nullified to some extent by alumina sol addition. The use of alumina sol made the sensor coating porous which can be seen from the FESEM of the

coating of sensor units in different chapters of this thesis, increased the overall effective surface area available for sensing activity and it basically helped to form strongly adhered coating on cylindrical alumina ( $\text{Al}_2\text{O}_3$ ) substrate's surface.

After coating, the curing of the coated alumina tubes was done at a tube furnace with heating and cooling rates of  $100^\circ\text{C}$  per minute at  $300^\circ\text{C}$  for 45min. Curing helped to evaporate the used coating binders and to perforate the surface of the coating which ultimately increases the effective surface area (porous coating) for easier gas adsorption as well as diffusion. Therefore, the mean free path for gas molecules was much higher than the average gas molecule diameter. It helped to avoid physisorption or chemisorption of gas on the  $\text{Al}_2\text{O}_3$  surface. It concludes that alumina sol had no adverse effect on the sensing properties. After curing, heating coils were placed inside the tubes for indirect heating of the semiconducting sensing material.

### **2.5.3. Stabilization of the Coated Sensing Material**

The sensor units painted of sensing materials were stabilized through prolonged heating by using a 220V-5A heating source i.e. a constant voltage/current source (GWINSTEK made Dual-Range DC Power Supply: model no. SPD-3606 and for few earlier samples with Aplab made regulated dual DC power supply: model no. LD3210) for continuous seven days (ageing for one week) at a constant sensor heater temperature of  $350^\circ\text{C}$ , to achieve the desired base-resistance stability required and finally used for the measurement.

The operating temperatures of the sensors were varied by changing the current driven through the nichrome or Kanthal wire (already inserted in hollow alumina tube substrate) by varying the voltage. The circuit representation of a metal oxide semiconductor gas sensor is shown in Figure 2.7.

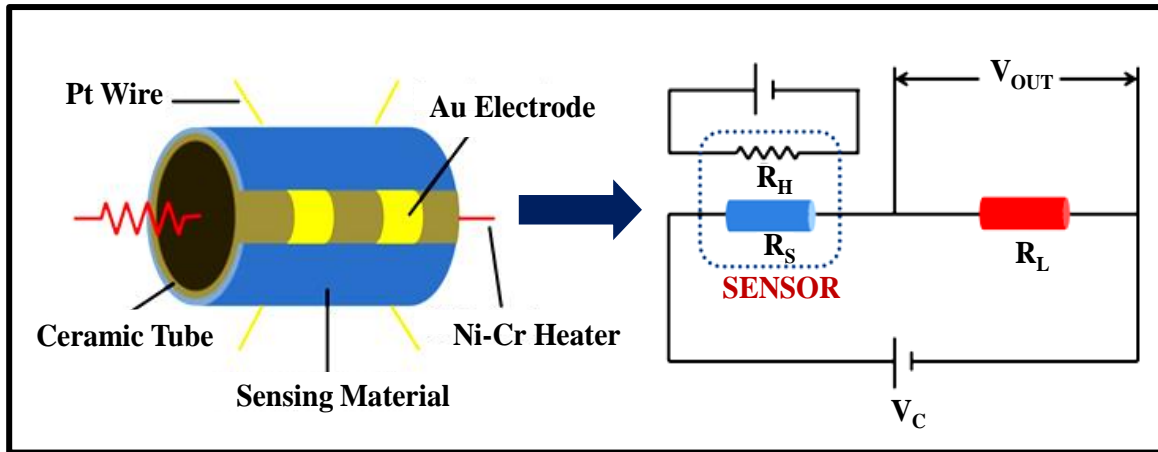


Figure 2.7: Circuit representation of a metal oxide semiconductor gas sensor.

A simple linear circuit, called as voltage divider is used for the measurement of MOS gas sensor resistance shown in Figure 2.8. Here,  $R_s$ : the resistance of sensor unit;  $R_L$ : load resistance;  $V_{OUT}$ : voltage drop against load,  $V_C$ : source voltage. Sensor resistance  $R_s$  which is a gas concentration dependent resistance measured as:

$$R_s = \left( \frac{V_C}{V_{OUT}} - 1 \right) \times R_L \dots \dots \dots (2.10)$$

There are detailed calibrated values of the voltages and the corresponding temperature generated at the cylindrical thick film coated sensor surface. For example; if it is required to maintain sensor surface temperature to be at 350°C steadily in an ambient, in that case 5V heating voltage is required and the current flows of nearly 200mA or 0.2A and 1W power is drawn from the system source. Similarly, for providing 150, 200, 250, 300, 400 and 450°C surface temperatures, 2.7, 3.5, 3.9, 4.4, 5.5 and 6V heating voltages were applied, respectively.

**2.6. Gas Sensing Measurement Details**

The performance of the hollow tube-shaped bulk sensors coated of semiconducting metal oxide powder and operate as a resistive element was studied by DC (direct current) measurements. The measurements were carried out with the sensor specimen placed inside the measurement setup facility with ambient environment and controlled temperature and gas delivery. The

electric contact was provided by the cylindrical gold-coated electrodes. The operating temperature of the sensors was controlled by varying the voltage and thereby the electric power consumed i.e., by changing the current driven through the kanthal or nichrome wire inserted within the hollow alumina tube. The gas environment inside the chamber was provided with inlet and outlet leads.

The sensor under test was exposed to the target gas at 1 atmospheric pressure and at a flow rate of 10sccm (standard cubic centimetre per minute) as the gas delivery system was based on three mass-flow controllers with green display unit (MKS Instruments: model no. PR4000) for desired concentration of the respective target gases exposure. The concentration was varied by applying different mixed gas cylinders where different target gases were diluted with carrier or reference gas  $N_2$ . The gas exposure time or response time was fixed at 15sec for each gas pulse and recovery time was calculated as the time taken for a sensor to come back to its original state of base resistance value when the target gas was removed. The electrical resistances in air ( $R_{Air}$ ) and in presence of analyte gas ( $R_{Gas}$ ) were measured at the same operating temperatures (from 150°C to 450°C) in an average ambient humidity of ~ 60% to 65% (aerial environment) by applying bias voltage of 2 to 5V across the sensing material. This change in resistance in presence of air and gas at different operating temperatures and also all the current-voltage measurements of the active metal oxide layer of every coated sensor unit were carried out using an Agilent B2902A precision measurement source-meter unit (100fA; 2ch, LXI) and was recorded as the experimental setup was equipped with custom-built Lab View-based control and data acquisition software using a graphical user interface (GUI) by interface cable with “IR to USB” connector facility. The AC measurements have been carried out on a precision impedance analyzer (6500 B Wayne Kerr) within a wide range of frequency from 100Hz to 1MHz. The sensing measurement arrangement setup of our laboratory is shown in Figure 2.8 below.



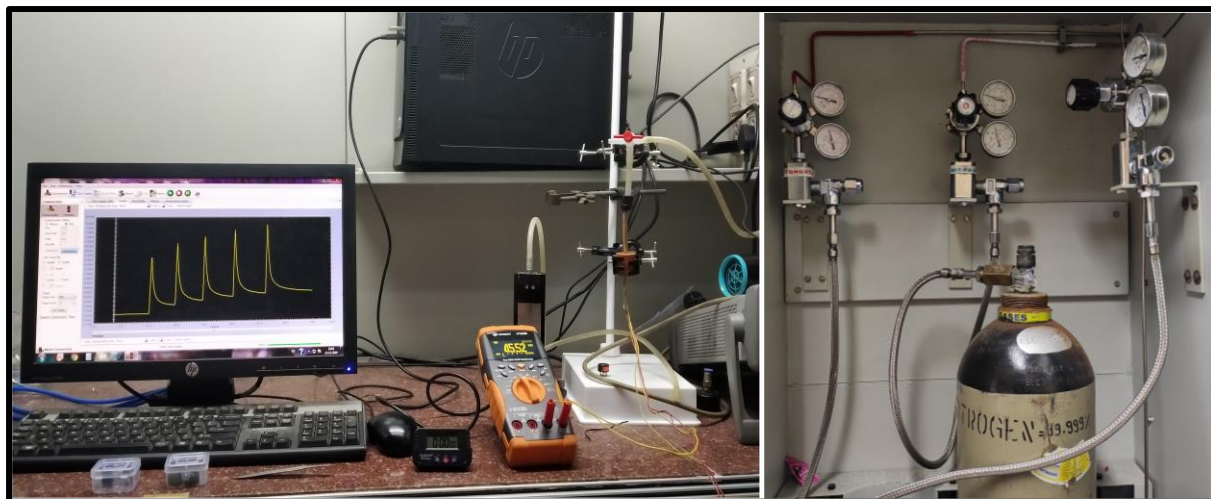


*Figure 2.8: Laboratory Gas Sensing measurement setup.*

### 2.6.1. Gas Selectivity Measurement

Gas selectivity was measured with the help of real-time combined dynamic response for different concentrations of different gases. For this purpose, in most of the cases 10ppm (for all the gases) was used. Response time apparatus is constructed in such a way that each gas is introduced serially one after another into the gas chamber so that the sensor can respond to each gas in order. Selectivity measurements could have been done for other different reducing gases also. As-purchased mixed gases with different concentrations were used in this purpose. The respective response was obtained using an 'Agilent B2901A' source-meter and was recorded using a Lab View-based graphical user interface (GUI) and plot the corresponding data to establish selectivity nature.

### 2.6.2. Measurement of Sensor Stability

Sensor stability was judged in air as well as in highly humid (of the order of ~90% relative humidity) environment. The presence of moisture in the ambient degrades the gas sensing ability of the SMO based gas sensors to some extent. It generally reduces the base resistance of n-type semiconducting oxide-based gas sensors thereby reducing the response and extending the recovery time. But these results vary as these parameters depend on working temperature,

initial and final moisture content, gas concentration applied as well as the material under consideration. To judge the influence of this moisture effect, sensor unit was placed within a sealed (airtight) desiccator. These sensor units were well connected with current source for sensor heating and also with gas source.

The dynamic base-resistance stability in air was measured first. Simultaneously, the base resistance stability was measured with the help of real-time dynamic response in this time period. After the passage of substantial amount of time say 8-10min, the base resistance became stable with lower base resistance value of the placed sensor unit and the introduction of gas was done with the necessary attachment to judge the extent of negative influence or ill effect of moisture on the response as well as recovery time of the sensor. After 15sec gas exposure, both the moisture and gas supply were cut and base resistance recovery process started. This recovery nature of the sensor was judged and the effect of the whole process described above recorded as real-time dynamic response. The moisture content (R.H.) present in the ambient air and closed environment of the desiccators was measured for all the thesis work by Fisher Scientific (Germany) made digital hygrometer, model no. 11-661-14.

### **2.6.3. Sensor Terminology**

The most important parameter is the response (some reports also have mentioned it as “sensitivity” interchangeably with “response”) and selectivity towards the particular target gas of interest. Usually, response or sensitivity can be simply calculated as  $R_{Air}/R_{Gas}$  for reducing gases or  $R_{Gas}/R_{Air}$  for oxidizing gases, where  $R_{Air}$ : Resistance of the sensor unit in air;  $R_{Gas}$ : Resistance of the sensor unit in presence of the target analyte gas, such as hydrogen, methane, butane or any other gas at the same operating temperature. Therefore, **Sensitivity** or **Response** of a sensor is defined in terms of the relationship between input physical signal and output electrical signal.

The sensitivity is generally the ratio between a small change in electrical signal and a small change in physical signal.

- **Selectivity** is the ability of a sensor to detect the target gas (without being affected) in presence of other interfering gases.
- **Response time** is the time it takes for a sensor to read 90% of the full-scale reading after being exposed to a target (analyte) gas.
- **Recovery time** is the time taken by a sensor to reach its initial state of base resistance (at least 90% of the original base resistance) when the target gas is removed.
- **Drift** is the slow time variation of metrological characteristics of a sensor. Material instabilities and ambient interactions as well as ageing affects are primarily responsible for the lack of stability.

### 2.7. Conclusion

Powder synthesis, characterization, sensor fabrication and sensor response measurement are the important steps in the whole process of sensor fabrication, characterization and performance evaluation. Powder has been synthesized by different cost-effective solution-based synthesis routes. In this chapter, the detailed powder characterization techniques for as-prepared and calcined samples have been provided briefly. The sensor fabrication process from sensor coating to final stable sensor fabrication has been touched upon thoroughly. The gas sensing measurement procedure also has been discussed in detail.

### 2.8. References

1. Kulkarni, S. K. Synthesis of Nanomaterials-I (Physical Methods). In: Nanotechnology: Principles and Practices, *Springer*, Cham, **2015**, 55.
2. Rao, C. N. R.; Cheetham, A. K. The Chemistry of Nanomaterials: Synthesis, Properties and Applications, Wiley-VCH: Weinheim, Germany, **2004**, Vols. 1 and 2.

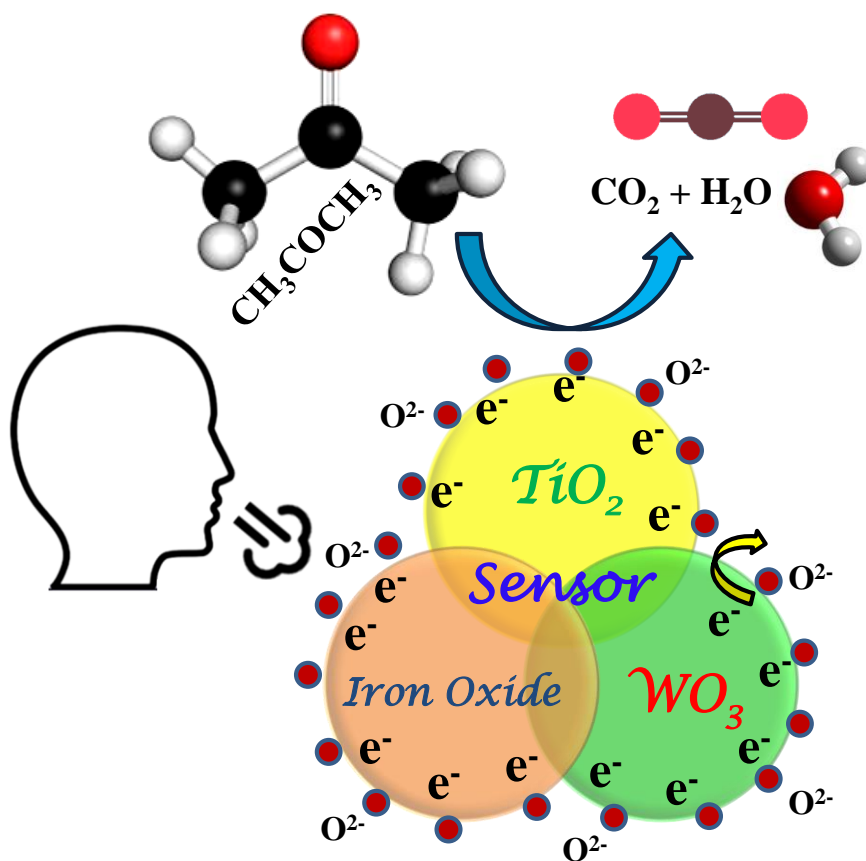
3. Chen, G.; Seo, J.; Yang, C.; Prasad, P. N. *Chem. Soc. Rev.* **2013**, *42*, 8304.
4. G. Cao and Y. Wang, *Nanostructures and Nanomaterials: Synthesis, Properties and Applications*, World Scientific Series, **2011**, Imperial College press.
5. Xu, H.; Zeiger, B.W.; Suslick, K.S. *Chem. Soc. Rev.* **2013**, *42*, 2555.
6. Gedanken, A. *Ultrasonics Sonochemistry* **2004**, *11*, 47.
7. Xu, H.; Zeiger, B. W.; Suslick, K. S. *Chem. Soc. Rev.* **2013**, *42*, 2555.
8. Anderson, P. S.; Kirk, C.A.; Knudsen, J.; Reaney, I. M.; West, A. R. *Solid State Sciences* **2005**, *7*, 1149.
9. Shi, W.; Song, S.; Zhang, H. *Chem. Soc. Rev.* **2013**, *42*, 5714.
10. Djurisic, A. B.; Xi, Y.Y.; Hsu, Y. F.; Chan, W. K. *Recent Pat. Nanotechnol.* **2007**, *1*, 121.
11. Hohman, M. M.; Shin, M.; Rutledge, G.; Brenner, M. P. *Phys. Fluids* **2001**, *13*, 2201.
12. Li, D.; Xia, Y. *Adv. Mater.* **2004**, *16*, 1151.
13. Mukhopadhyay, S.; Maiti, D.; Saha, A.; Devi, P.S. *Cryst. Growth Des.* **2016**, *16*, 6922.
14. Roy, A.; Mukhopadhyay, S.; Devi, P. S.; Sundaram, S. *ACS Omega* **2019**, *4*, 1130.
15. Ghosh, P.; Roy, A.; Mukhopadhyay, S.; Narjinary, M.; Sen, S.; Devi, P. S. *Adv. Electron. Mater.* **2021**, 2000785.
16. Maiti, D.; Mukhopadhyay, S.; Mohanta, S.; Saha, A.; Devi, P. S. *J. Alloys. Compd.* **2015**, *653*, 187.
17. Das, P. P.; Roy, A.; Das, S.; Devi, P. S. *Phys. Chem. Chem. Phys.* **2016**, *18*, 1429.
18. Das, P. P.; Devi, P. S. *Inorg. Chem.* **2014**, *53*, 10797.
19. Das, P. P.; Roy, A.; Agarkar, S.; Devi, P. S. *Dyes Pigm.* **2018**, *154*, 303.
20. Elton, L. R. B.; Jackson, D. F. *Am. J. Phys.* **1966**, *34*, 1036.
21. R. W. Wood, *Phys. Rev (Series I)*. **1987**, *5*, 1-10.
22. J. Tersoff, *Phys. Rev. Lett.*, **1984**, *52*, 465-468.

23. Stranks, D. R.; Heffernan, M. L.; Lee Dow, K. C., McTigue, P. T., Withers, G. R. A. *Melbourne University Press, Carlton, Victoria*, **1970**, 424.
24. Goodhew, P. J.; Humphreys, F. J.; Beanland, R. *Taylor & Francis*, **2001**, 42, 251.
25. Williams, D. B.; Carter, C. B. *Kluwer Academic/Plenum Publishers*, **1996**, 666.
26. Duan, J.; Yang, S.; Liu, H.; Gong, J.; Huang, H.; Zhao, X.; Zhang, R.; Du, Y. *J. Am. Chem. Soc.* **2005**, 127, 6180.
27. Reimer, L.; Kohl, H. *Springer* **2008**, 44.
28. Yao, N.; Wang, N. *Kluwer Academic Pub., Boston, USA*, **2005**, 554.
29. Szymanski, H. A. *Plenum Press*, **1964**.
30. Griffiths, P.; DeHaseth, J. A. *John Wiley & Sons*, **2007**.
31. Tauc, J. *Mater. Res. Bull.* **1968**, 3, 37.
32. Gardiner, D. J. *Springer-Verlag* **1989**, 89.
33. Thommes, M.; Kaneko, K.; Neimark, A.V.; Olivier, J. P.; Rodriguez-Reinoso, F.; Rouquerol, J.; Sing, K. S. W. *Pure Appl. Chem.* **2015**; 87, 1051.
34. Foner, S. *Rev. Sci. Instrum.* **1959**, 30, 548.
35. Yamazoe, N. *Sens. Actuators B* **1991**, 5, 7.
36. Yamazoe, N.; Sakai, G.; Shimanoe, K. *Catal. Surv. Asia*, **2003**, 7 63.
37. Barrett, E. P.; Joyner, L.G.; Halenda, P. P. *J. Am. Chem. Soc.* **1951**, 73, 373.
38. Aligizaki, K.K. *Taylor & Francis* **2005**.
39. Sing, K. S.W.; Everett, D. H.; Haul, R. A. W.; Moscou, L.; Pierotti, R. A.; Rouquérol, J.; Siemieniowska, T. *Pure Appl. Chem.* **1985**, 57, 603.
40. Rouquerol, F.; Rouquerol, J.; Sing, K. *Academic Press* **1999**.
41. Mukhopadhyay, A. K.; Mitra, P.; Chatterjee, A. P.; Maiti, H. S. *Ceram. Int.* **2000**, 26, 123.
42. Chatterjee, K.; Chatterjee, S.; Banerjee, A.; Raut, M.; Pal, N. C.; Sen, A.; Maiti, H. S. *Mater. Chem. Phys.* **2003**, 81, 33.

43. Saha, M.; Banerjee, A.; Halder, A. K.; Mondal, J.; Sen, A.; Maiti, H. S. *Sens. Actuators. B* **2001**, 79, 192.
44. Mukhopadhyay, A. K.; Mitra, P.; Chatterjee, A. P.; Maiti, H. S. *J. Mater. Sci. Lett.* **1998**, 17, 625.
45. Bamsaoud, S. F.; Rane, S. B.; Karekar, R. N.; Aiyer, R. C. *Mat. Chem. Phy.* **2012**, 133, 681.
46. Bamsaoud, S. F.; Rane, S. B.; Karekar, R. N.; Aiyer, R. C. *Sens. Actuators B* **2011**, 153, 382.
47. Bamsaoud, S. F.; Rane, S. B.; Karekar, R. N.; Aiyer, R. C. *Trans. Indian Ceram. Soc.* **2010**, 69, 193.
48. Jeong, S. H.; Kim, S.; Cha, J.; Son, M. S.; Park, S. H.; Kim, H. Y.; Cho, M. H.; Whangbo, M. H.; Yoo, K. H.; Kim, S. J. *Nano Lett.* **2013**, 13, 5938.
49. Shen, Y.; Yamazaki, T.; Liu, Z.; Meng, D.; Kikuta, T.; Nakatani, N.; Saito, M.; Mori, M. *Sens. Actuators B* **2009**, 135, 524.
50. Wada, K.; Egashira, M. *Sens. Actuators B* **1998**, 53, 147.
51. Kumar, A.; Zhang, P.; Vincent, A.; McCormack, R.; Kalyanaraman, R.; Cho, H. J.; Seal, S. *Sens. Actuators B* **2011**, 155, 884.
52. Adamyan, A. Z.; Adamyan, Z. N.; Aroutiounian, V. M.; Schierbaum, K. D.; Han, S. D. *Arm. J. Phy.* **2009**, 2, 200.
53. Zima, A.; Köck, A.; Maier, T. *Microelectron. Engg.* **2010**, 87, 1467.
54. Ito, D.; Ichimura, M. *Jpn. J. Appl. Phys.* **2006**, 45, 7094.
55. Shirahata, N.; Shin, W.; Murayama, N.; Hozumi, A.; Yokogawa, Y.; Kameyama, T.; Masuda, Y.; Koumoto, K. *Adv. Funct. Mater.* **2004**, 14, 580.
56. Shukla, S.; Zhang, P.; Cho, H. J.; Seal, S.; Ludwig, L. *Sens. Actuators B* **2007**, 120, 573.

# CHAPTER-III

## Performance of Single Component Metal Oxide-based Acetone Sensor



*In this chapter, we have put an effort to introduce single metal oxides as appropriate sensing material for device application. Various metal oxides such as Anatase, Rutile,  $\text{Na}_{0.23}\text{TiO}-\text{TiO}_2$  composite, different phases of Iron oxide and  $\text{WO}_3$  are showing better sensing response with higher stability, flexibility with comparatively lower operating temperature because of their better thermal and chemical stability and other physico-chemical properties leading to improve overall sensing performance. This chapter deals with the different chemical synthesis process to produce various morphology such as anatase cube, rutile rod,  $\text{TiO}_2$  composite nanorod, Iron oxide nanoparticle and fiber,  $\text{WO}_3$  particle and fiber and systematic structural characterization of the synthesized materials. With this, the composite nanorods were synthesized through a hydrothermal process with varying different synthesis parameters which exhibited a better sensing response towards acetone at room temperature. Fiber like structure by electrospun showed the capability for sensing lower concentration of acetone with higher sensitivity and stability than sonochemically prepared different phases of iron oxides nanoparticles. We have also observed the morphology depended sensing performance with  $\text{WO}_3$  particle and fiber-based material with comparatively lower range resistance limit. On the basis of our results, we are able to establish some of the single metal oxide-based material for sensor fabrication in the application field of acetone sensing development.*

### **3.1. Introduction:**

In the past few decades, research in the area of gas sensors has been growing extensively due to their application in fields such as environmental pollution protection, industrial processing monitoring, household's emergency detection, health quality checking, fire detection and breath analyzers. For many years, glucose monitoring technology has been used to manage diabetes. Traditional devices use a painful technique to take out the patient's blood and test glucose concentration and provide sample information. Nevertheless, recently research has been prompted towards a new horizon of a pain-free life by developing a new inexpensive platform like a breath analyzer. Breath analysis technology has received significant attention in clinical application because it is non-invasive, rapid, simple and a portable low-cost detection method. Of late human breath analysis has been considered as a non-invasive and rapid method for detecting various volatile organic compounds that are indicators for different diseases. Acetone in breath has been considered as a biomarker for non-invasive diagnosis of diabetes where a concentration of below 1ppm acetone is considered as a condition in normal people. An acetone concentration in breath of above 1ppm has been considered as condition in patients with diabetes. The gas sensor with low concentration detection limit has been developed to demonstrate non-invasive techniques for detecting acetone in the breath, which is considered as the biomarker for early diagnosis of diabetes. The concentration of acetone in breath for an average individuals is <1ppm, increasing to more than 3ppm for diabetic patients. The main focus of this thesis work was to explore various oxide materials for fabricating metal oxide-based sensors for acetone sensing. The exclusive surface properties, high catalytic activity, wide band gap energy, and chemical stability of metal oxide make them better candidates for improved gas sensing properties. The sensing mechanism of metal oxide-based gas sensor can be described as the reaction between the adsorbed oxygen species and target gas molecules. The electrical resistance of the semiconductor-based sensor is greatly influenced in



the presence of oxidizing and reducing gases. Recent efforts in this direction have been dedicated in search of new variety of semiconducting metal oxides (SMOs) with different nanostructures in pure phase or using any dopant to enhance the gas sensing performance. Various binary n-type oxides such as SnO<sub>2</sub>, ZnO, WO<sub>3</sub> and In<sub>2</sub>O<sub>3</sub> and p-type oxides such as CuO, PdO and Co<sub>3</sub>O<sub>4</sub> metal oxides have been manifested as chemiresistive gas sensor materials towards different target gases for better sensitivity and low operating temperature.

In this chapter our efforts in exploring single component oxides such as TiO<sub>2</sub>, Fe<sub>2</sub>O<sub>3</sub> and WO<sub>3</sub> in various size and shape and their performance in acetone sensing have been presented in detail. Here, the main focus was to understand the performance of various crystallographic modifications of TiO<sub>2</sub> and Fe<sub>2</sub>O<sub>3</sub> in sensing acetone and also to understand the effect of different shapes and their influence in the sensing mechanism. Finally, a modified composite materials has also been identified for enhanced acetone sensing at room temperature.

### **3.2. TiO<sub>2</sub> Based Oxides: Phase Dependence on Acetone Sensing (Anatase, Rutile, Anatase-Na<sub>0.23</sub>TiO<sub>2</sub> Composite)**

#### **3.2.1. Introduction:**

TiO<sub>2</sub> has been known to exist mainly in three primary crystallographic modifications such as anatase (tetragonal), rutile (tetragonal) and brookite (orthorhombic) forms at ambient conditions. During the past few decades, the above mentioned TiO<sub>2</sub> polymorphs have been widely investigated for diverse applications due to their well-accepted electronic and optical properties [1,2]. There have been many efforts to improve the electronic properties of titania and an effective way of further modifying the electronic properties of TiO<sub>2</sub> is doping, though ion-implant, shape control and surface modifications are also being explored to improve the properties of TiO<sub>2</sub>. In order to enhance the sensor performance, significant efforts have been devoted in improving the host TiO<sub>2</sub>, which acts as a framework for sensor. However, mixing different phases followed by a hetero-structure formation of TiO<sub>2</sub> has been found to result in

better sensing response performance than the sole usage of pure anatase and rutile phases. In order to improve the performance of TiO<sub>2</sub>, one-dimensional nanostructures of TiO<sub>2</sub>, such as nanorods, nanotubes and nanowires, have also been studied [3,4] which are expected to significantly improve the electronic properties due to directionally smooth electron mobility band lower inter-crystalline contacts [5-8]. As reported by others, Na<sub>0.23</sub>TiO<sub>2</sub> with a monoclinic crystal structure is expected to form a p-n junction with TiO<sub>2</sub> which allows faster electron-hole separation followed by mobility via synergistic effect [9,10]. In this part of the thesis chapter 3, the sensing performance of cube shaped anatase and rod-shaped rutile TiO<sub>2</sub> has been discussed towards different concentrations of acetone with different sensing parameters.

### 3.2.2. Structural and Optical Properties Analysis

The phase purity of the hydrothermally synthesized TiO<sub>2</sub> samples was investigated with powder X-ray diffraction (XRD) study shown in Figure 3.2.1a. The patterns show that the synthesized powder diffraction peaks resemble the crystal structure of anatase phase TiO<sub>2</sub> (JCPDS card number 21-1272) and rutile phase of TiO<sub>2</sub> (JCPDS card number 89-4920). Raman spectroscopic analysis was also evaluated to understand the different phase formation of synthesized anatase TiO<sub>2</sub> and rutile TiO<sub>2</sub>, as shown in Figure 3.2.1b.

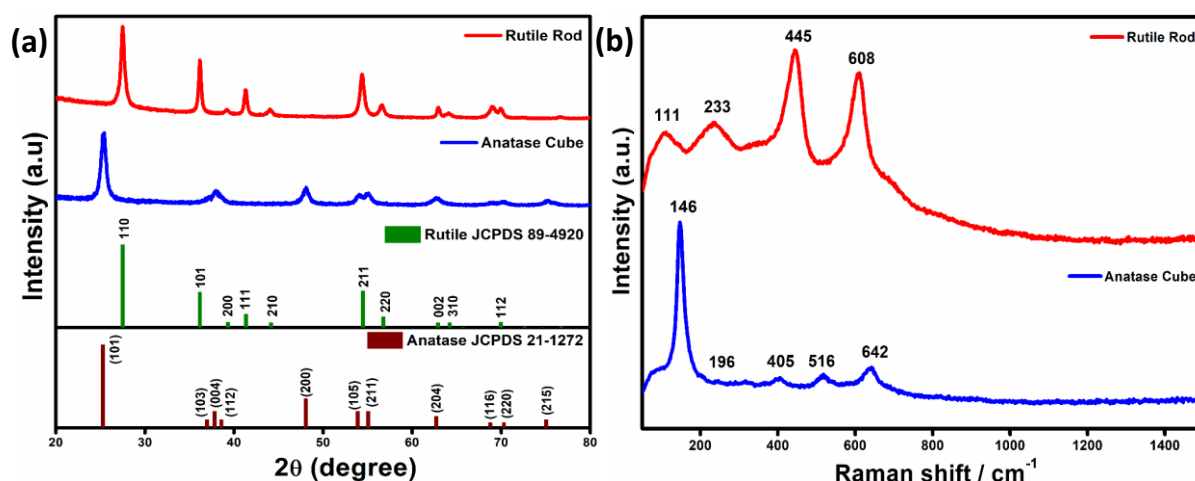


**Figure 3.2.1:** (a) X-ray diffraction pattern and (b) Raman spectra of synthesized anatase TiO<sub>2</sub> and rutile TiO<sub>2</sub>, respectively

The Raman spectra of anatase TiO<sub>2</sub> cube showing strong E<sub>g</sub> band at 146 and 642cm<sup>-1</sup>, the B<sub>1g</sub> band at 405cm<sup>-1</sup> and the (A<sub>1g</sub> + B<sub>1g</sub>) mode centered at 516cm<sup>-1</sup> have been reported by many researchers [7]. The characteristic sharp Raman bands of synthesized TiO<sub>2</sub> sample at 445 (E<sub>g</sub>) and 608cm<sup>-1</sup> (A<sub>1g</sub>) and a second order phonon band at 235cm<sup>-1</sup> confirms the presence of rutile phase of TiO<sub>2</sub> [11].

Further, from the interpretation of FTIR spectra it is also confirmed the successful synthesis of both anatase cube and rutile rod TiO<sub>2</sub> as shown in Figure. 3.2.2. The sharp and intense band appeared at 536 and 649cm<sup>-1</sup> corresponds to the symmetry stretching vibration band for Ti–O–Ti of the rutile and anatase structure of the bond vibration. The peaks at 3435 and 1638cm<sup>-1</sup> of rutile rod and 3418 and 1632cm<sup>-1</sup> of anatase cube samples were attributed to water molecules adsorbed or O-H stretching on the surface of the sample. Actually, the intense spectroscopic bands at around 3435 and 3418cm<sup>-1</sup> were attributed to both symmetric and asymmetric stretching vibrations of the hydroxyl group (Ti-OH). At lower frequencies, the characteristic peaks at 1638 and 1632cm<sup>-1</sup> correspond to the O-H bending vibrations of the surface adsorbed water molecules.

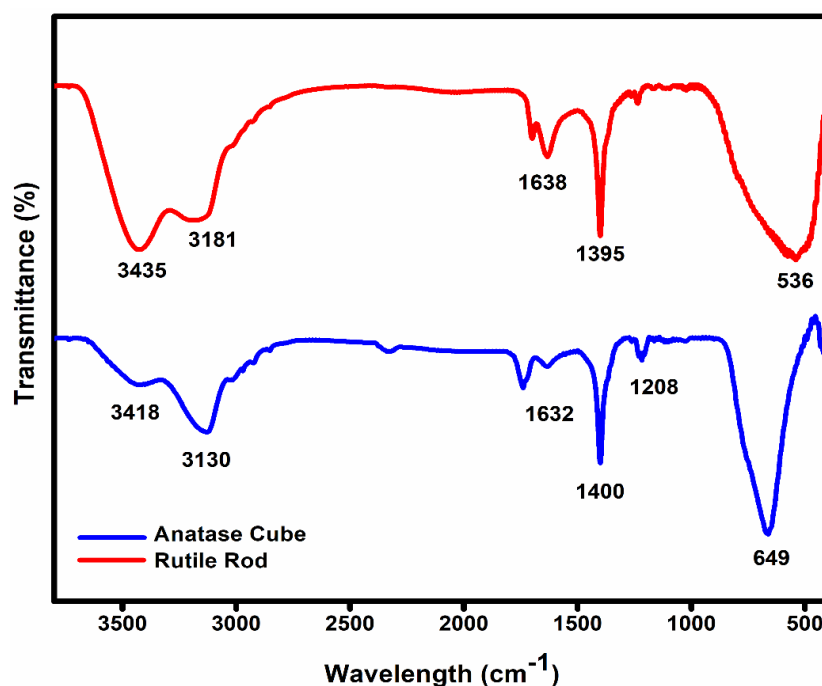


**Figure 3.2.2:** FTIR spectra of synthesized anatase cube and rutile rod TiO<sub>2</sub>, respectively.

### **3.2.3. Microstructural Study:**

The morphology, size and crystal orientation pattern of the anatase and rutile samples were investigated by transmission electron microscopy (TEM) and high-resolution transmission electron microscopy (HRTEM), respectively, as shown in Figure 3.2.3. The bright field image (Figure 3.2.3a and b) exhibits synthesized TiO<sub>2</sub> nanocubes with average size of 21nm. Corresponding HRTEM image (in Figure 3.2.3c) confirm the formation of anatase nanocube with *d*-spacings of ~0.35nm corresponding to (101) lattice planes. The bright-field image of as synthesized rutile TiO<sub>2</sub> exhibited densely packed elongated nanorods with a length of 300-350nm and an average width of 13nm, as shown in Figure 3.2.3d and e. It was observed that these rods are laterally self-assembled to form a bundle like pattern. In each bundle, similar type of nanorods is tightly held together. From the HRTEM images in Figure 3.2.3f, it is observed that the individual nanorods are arranged in highly crystalline nature. There are actually two sets of perpendicularly aliened lattice fringes with distances of 0.29 and 0.32nm corresponds to the inter layer *d* spacings of the (001) and (110) rutile TiO<sub>2</sub>. It was observed that the nanorods preferentially expose to the (110) low energy facets and grow along the (001) direction. In this case Cl<sup>-</sup> plays a vital role for the formation of TiO<sub>2</sub> grains into nanorods instead of nanoparticles.

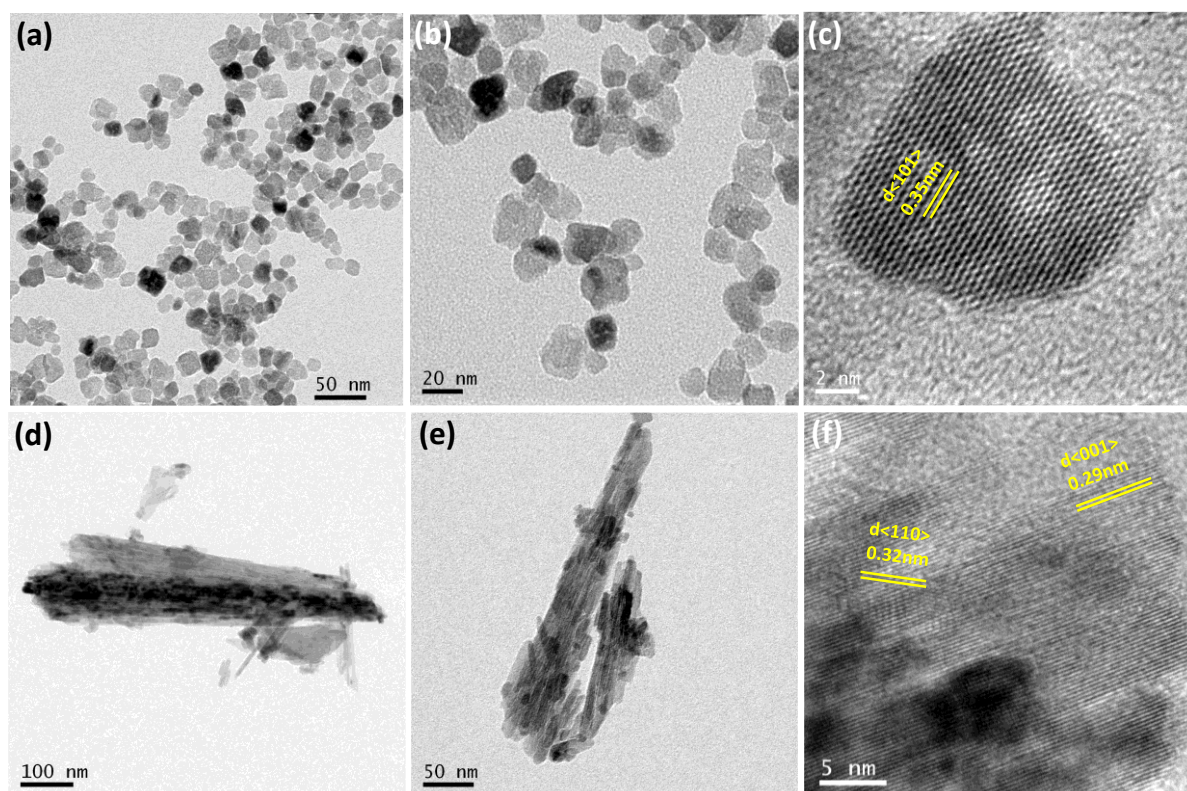


**Figure 3.2.3.** (a-b) and (d-e) Bright field TEM and (c) & (f) HRTEM images of Anatase Cube  $TiO_2$  and Rutile Rod  $TiO_2$  respectively.

### 3.2.4. Surface Area Analysis

In order to investigate the surface properties of the various nanostructures, surface area measurement was carried out after evacuation at  $150^{\circ}C$  for 4h.  $N_2$  adsorption-desorption isotherms is shown in Figure 3.2.4. Type IV sorption behaviour as evident from the isotherms typically assigned to the existence of mesoporosity for both samples. It is worth mentioning that high surface area of  $86.5m^2/g$  as observed for anatase cube compared to Rutile rod (surface area  $16.5m^2/g$ ), which is highly beneficial for sensing activities which will be discussed later in sensing measurements part.

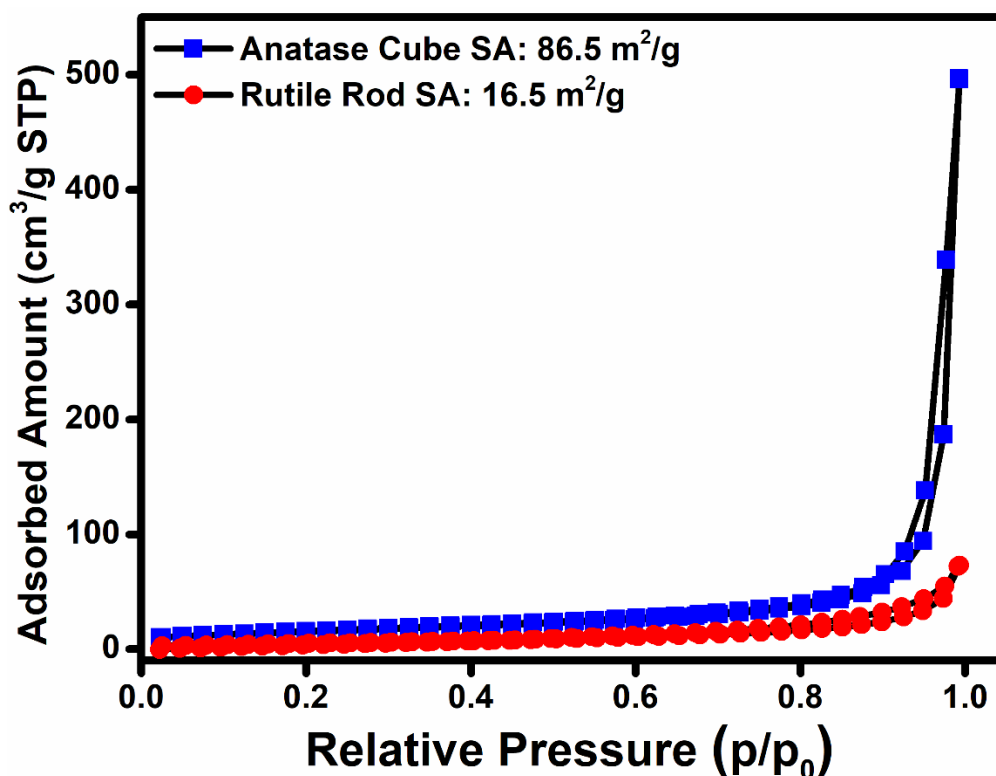


Figure 3.2.4. Surface area of anatase cube  $\text{TiO}_2$  and rutile rod  $\text{TiO}_2$ .

### 3.2.5. Acetone Sensing

The sensor under test was exposed to the target gas at one atmospheric pressure and at a flow rate of 10sccm by using mass flow controllers for using mass flow controllers for the desired quantity of the target gas (already diluted with carrier gas nitrogen) exposure. The stabilized fabricated sensor units coated with anatase cube and rutile rod were used for further measurements. The details of the measurement procedure have already been discussed in the previous section and the corresponding results related to gas response measurement are described below.

Figure 3.2.5a represents the variation of the resistance of the fabricated sensors as a function of operating temperature. As characteristic of the sample, the resistance in air initially decreases with temperature and then slowly varies. Both the samples showed a decrease in the resistance from 180°C temperature to around 380°C. The typical trends of the curves can be understood by considering the competitive adsorption of oxygen and moisture on sample

surface from the ambient. At the lower temperature zone, the adsorbed oxygen ions act as surface acceptors by binding conducting electrons and lower the effective surface conductivity. At the same time, physically adsorbed water on a sample can partially neutralize the surface charge by aligning their dipoles. With an increase in the temperature, desorption of physically adsorbed water should lead to a decrease in the resistance due to release of the carriers. Also, the migration of charged species like  $O_2$ ,  $O_2^-$ ,  $O^-$  and  $H_3O^+$  can contribute to low-temperature conductivity. Hence, in the low-temperature range, the sensor's resistance decreases with temperature, as shown in Figure 3.2.5a. The decrease in the resistance at higher temperatures is due to the desorption of the oxygen species and hydroxyl groups. Anatase cube-like sample showed the maximum sensing response ratio of 6.5 at 250°C towards 10ppm acetone with 15sec of exposure time. In case of rutile rod based sensor, it exhibited a sensitivity ratio of 4.9 at about 300°C operating temperature with 15sec of gas exposure. It is interesting to note that a desorption of metastable surface adsorbed charged oxygen species is occurred at higher operating temperature range.

To understand the selectivity nature of the fabricated sensor, both the sensors have been exposed to different target gases with same concentration of 10ppm such as CO, nitrogen, Methanol, Ethanol, and acetone. The selectivity co-efficient has been calculated by the equation:  $\beta = S_{\text{acetone}}/S_{\text{gas}}$  where  $S_{\text{acetone}}$  and  $S_{\text{gas}}$  are the response of the sensor towards acetone and any other gas of 10ppm concentration. The selectivity co-efficient ( $\beta$ ) calculated from Figure 3.2.5d varied in the order  $\beta_{\text{Nitrogen}} (5.4) > \beta_{\text{CO}} (5.1) > \beta_{\text{Methanol}} (5) > \beta_{\text{Ethanol}} (2.5)$  for anatase cube and for Rutile rod it is like  $\beta_{\text{Methanol}} (4.9) > \beta_{\text{CO}} (4.5) > \beta_{\text{Nitrogen}} (4.4) > \beta_{\text{Ethanol}} (2.2)$  and from the selectivity data it is confirmed that both the sensors have selective sensitivity towards acetone. The sensors showed a higher sensitivity response towards acetone comparatively other target gases.

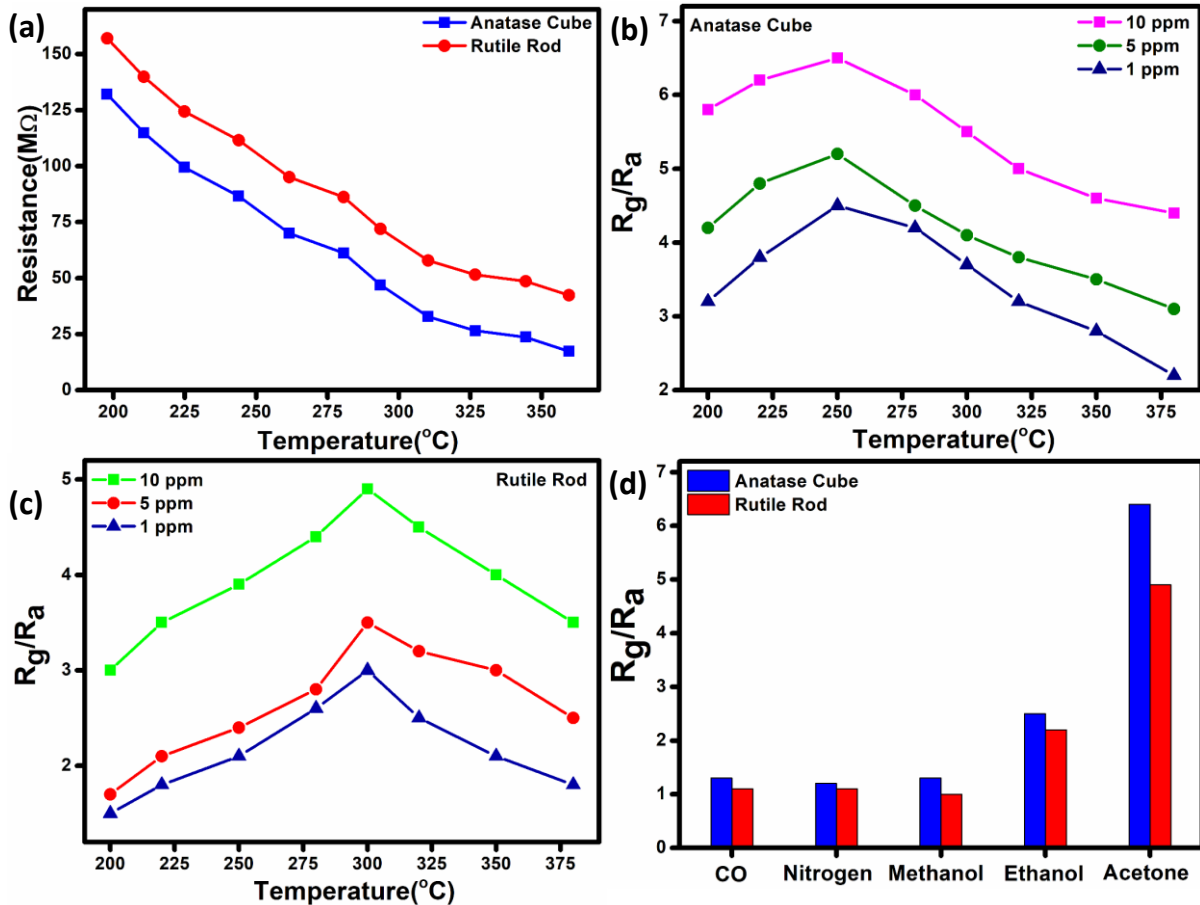


**Figure 3.2.5:** (a) Resistance monitoring as a function of operating temperature, Response ratio variation with temperature of (b) Anatase cube-based sensor and (c) Rutile rod-based sensor respectively (d) Selectivity study based on different target gas of same concentration of 10ppm.

The temperature dependent  $I$ - $V$  characteristics have been carried out to investigate the current-voltage relation for the fabricated sensor units coated with anatase cube and rutile rod. Figure 3.2.6a and b shows  $I$ - $V$  characteristics of anatase cube and rutile rod sample coated sensor, respectively, for  $-42V$  to  $+42V$  bias voltage range at different operating temperatures from  $200^{\circ}C$  to  $350^{\circ}C$  in presence of 10ppm acetone. The  $I$ - $V$  curve as Figures 3.2.6a and b shows semiconducting behaviour, as the resistance of the sensor unit decreases with the increase of operating temperature, which generates higher current flow to the sensor-system. For Figure 3.2.6a and b, it is basically following the same nature but some deviations are there due to the temperature dependent adsorption and desorption of metastable species like  $O^-$ ,  $O_2^-$  and  $O_2^{\cdot-}$  taking place on sensor surface as discussed in detail under gas sensor mechanism.



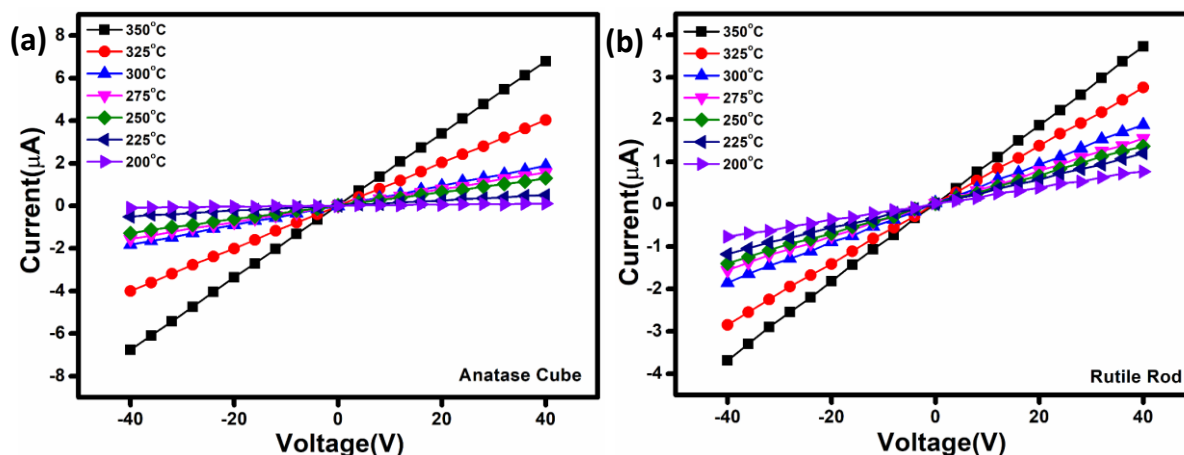


**Figure 3.2.6:** Current-Voltage ( $I$ - $V$ ) characteristics plot in the presence of 10ppm acetone as a function of different operating temperatures from 200°C to 350°C (a) Anatase Cube and (b) Rutile Rod based sensor, respectively.

It is obvious that the sensing response is greatly affected by the shape and size of the sensing material. The response of the anatase cube like structured  $\text{TiO}_2$  based-sensor is much higher with comparatively low operating temperature than rutile rod-based sensor. As the response of the  $\text{TiO}_2$  based sensors were very low, detailed studies on such systems were not carried out here.

### 3.2.6. Anatase- $\text{Na}_{0.23}\text{TiO}_2$ composite nanorod based Acetone Sensing

The above-mentioned studies on the acetone sensing characteristics of bare phase pure  $\text{TiO}_2$  samples (anatase cube and rutile rod) were not that interesting due to their lower sensitivity towards acetone and higher operating temperature. After that, attention has been focused on composite systems for better sensing characteristics. As our interest was to develop room temperature performing acetone sensor towards lower concentration of acetone gas, we have synthesized anatase- $\text{Na}_{0.23}\text{TiO}_2$  composite nanorod by hydrothermal synthesis process using sodium hydroxide ( $\text{NaOH}$ ). We have investigated the formation of anatase- $\text{Na}_{0.23}\text{TiO}_2$  composite nanorod and explored its performance in sensing application. An enhanced p-type semiconducting sensing response was achieved for different concentrations of acetone (10, 5, 3, 2 and 1ppm) along with strong selectivity, stability and reproducibility towards acetone at room temperature.

### 3.2.7. Thermal Analysis

The thermal decomposition nature of the as-prepared sample at pH 12 is shown in Figure 3.2.7, which exhibited an overall weight loss of ~9% within a temperature range from room temperature to 550°C. Initially, about 3% weight change between 30°C and 180°C was observed, followed by a change at 400°C corresponding to removing surface adsorbed and crystalline water molecules of the as prepared powder. Finally, the weight loss became negligible above 400°C. The corresponding DSC curve exhibited a broad exothermic change in the range of 150°C-400°C, corresponding to the decomposition of the as-prepared powder. The prepared powder was calcined at 500°C to get the phase pure material based on the TG-DTA analysis.

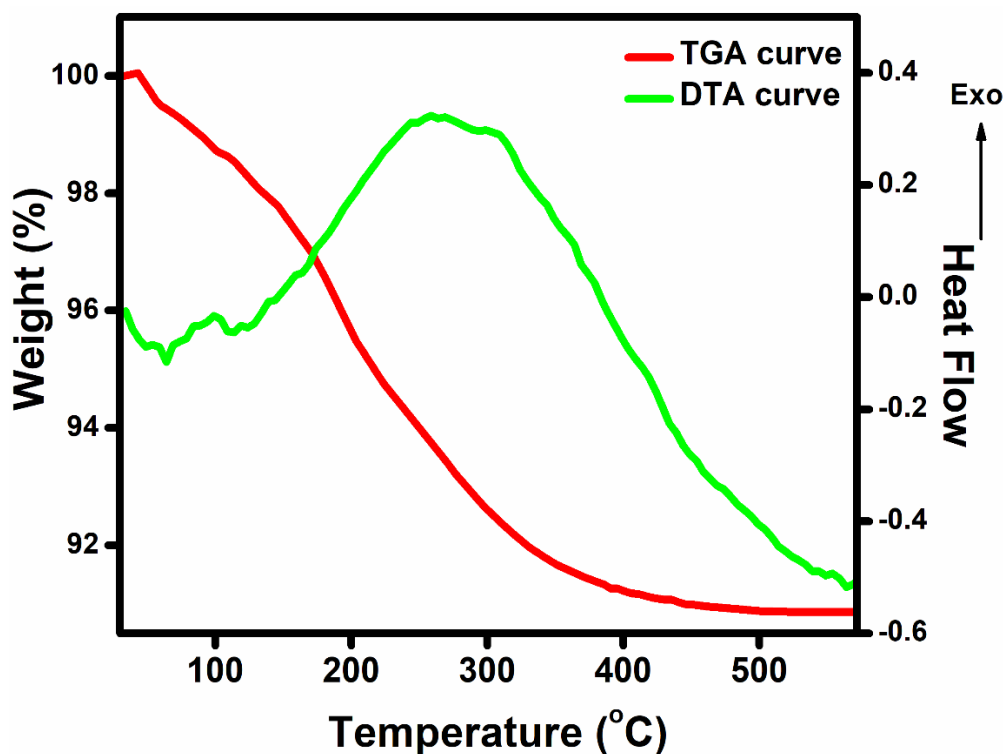


Figure 3.2.7: TG-DTA curve of the as prepared sample.

### 3.2.8. Effect of pH on Phase and Morphology Formation

The effects of pH on the synthesis and its effect on the phase transformation was investigated through systematic powder X-ray diffraction (XRD) and FESEM analysis (Figure 3.2.8).

Figure 3.2.8a depicts the XRD patterns of starting  $\text{TiO}_2$  powder and the subsequent prepared powder at pH 8, 10, 12 and 14, using NaOH under identical conditions. The XRD pattern confirmed the starting  $\text{TiO}_2$  powder in the anatase phase and the same phase retains up to pH 10 during the reaction. There is an indication of a second phase,  $\text{Na}_{0.23}\text{TiO}_2$  at pH 12. The growth of this phase continues at a higher pH of  $\sim 14$  also. And pH 12 has been fixed as the optimized condition to get  $\text{Na}_{0.23}\text{TiO}_2$  phase and the anatase phase.

Systematic microstructural analysis was also performed to understand the effect of pH if any on the morphology of the starting material. A change in the morphology of the starting material started to appear with change in pH and a distinct change in morphology was observed at a pH of 12. The transformation of particles and the formation of rod-shaped material are clear in Figure 3.2.8b. Further, at higher pH ( $\sim 14$ ), the rods get fused probably due to the extreme basic condition as shown in Figure 3.2.8b (iv). Thus, it is evident from Figure 3.2.8b that the starting anatase particles have transformed to rods during the hydrothermal reaction in the presence of NaOH and further annealing at  $500^\circ\text{C}$ .

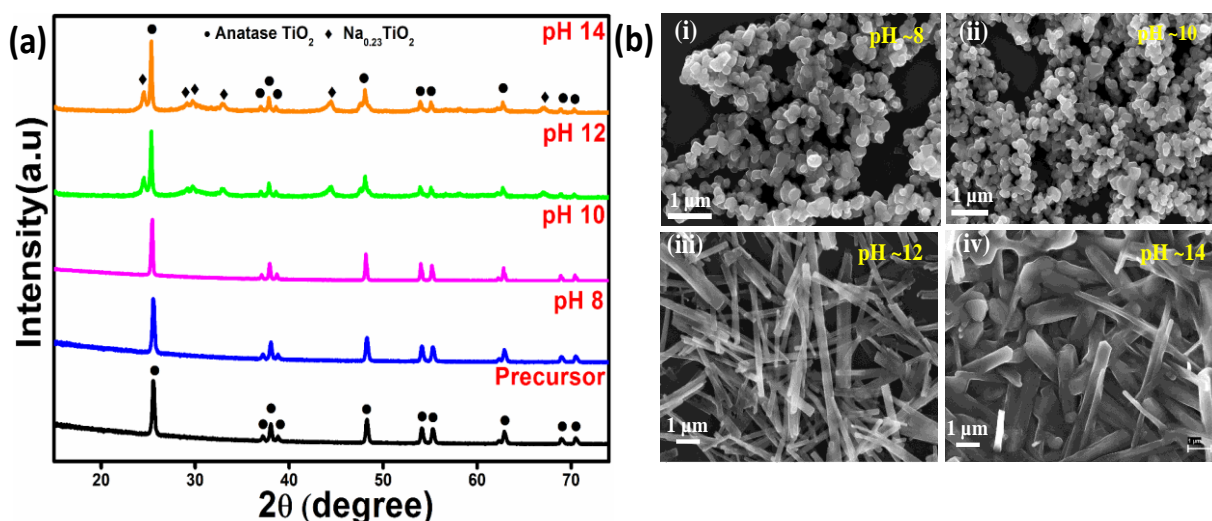


**Figure 3.2.8:** (a) XRD patterns of synthesized products obtained after hydrothermal treatment of anatase  $\text{TiO}_2$  nanoparticle at different pH and (b) FESEM microstructural images of hydrothermally prepared samples at different pH from 8 to 14.

### **3.2.9. Optimization of Hydrothermal Conditions**

In order to understand the formation of composite nanorods during hydrothermal synthesis, conditions were varied which led to the formation of anatase/ $\text{Na}_{0.23}\text{TiO}_2$  co-existed nanorods. This involved the structural transformation of the Na-titanate intermediate phase, which is of interest in the formation of anatase/ $\text{Na}_{0.23}\text{TiO}_2$  co-existed phases where  $\text{Na}^+$  ions have actively participated to form the new phase. It is clear from Figure 3.2.9 that the hydrothermal reaction duration has a strong effect on the phase formation and morphological changes of the resulting products, where it was found that the morphology of the product changed gradually from particles to rods along with the phase as observed from the XRD and FESEM analysis. Such a change was evident on increasing the hydrothermal duration at  $180^\circ\text{C}$  as shown in Figure 3.2.9. As observed from the XRD analysis, the anatase phase was retained up to 12h of hydrothermal treatment, which gets transformed to a mixed phase of anatase- $\text{Na}_{0.23}\text{TiO}_2$  after 36h. Finally, an optimum phase was achieved by minimizing the other phases after 48h of hydrothermal treatment at  $180^\circ\text{C}$  temperature. We have taken successive FESEM images under identical conditions as recorded for the XRD analysis to understand the rod formation. Initially, the precursor anatase  $\text{TiO}_2$  contains only particle form that gets successively transformed into nanorod on increasing the hydrothermal treatment duration from 12 to 48h.

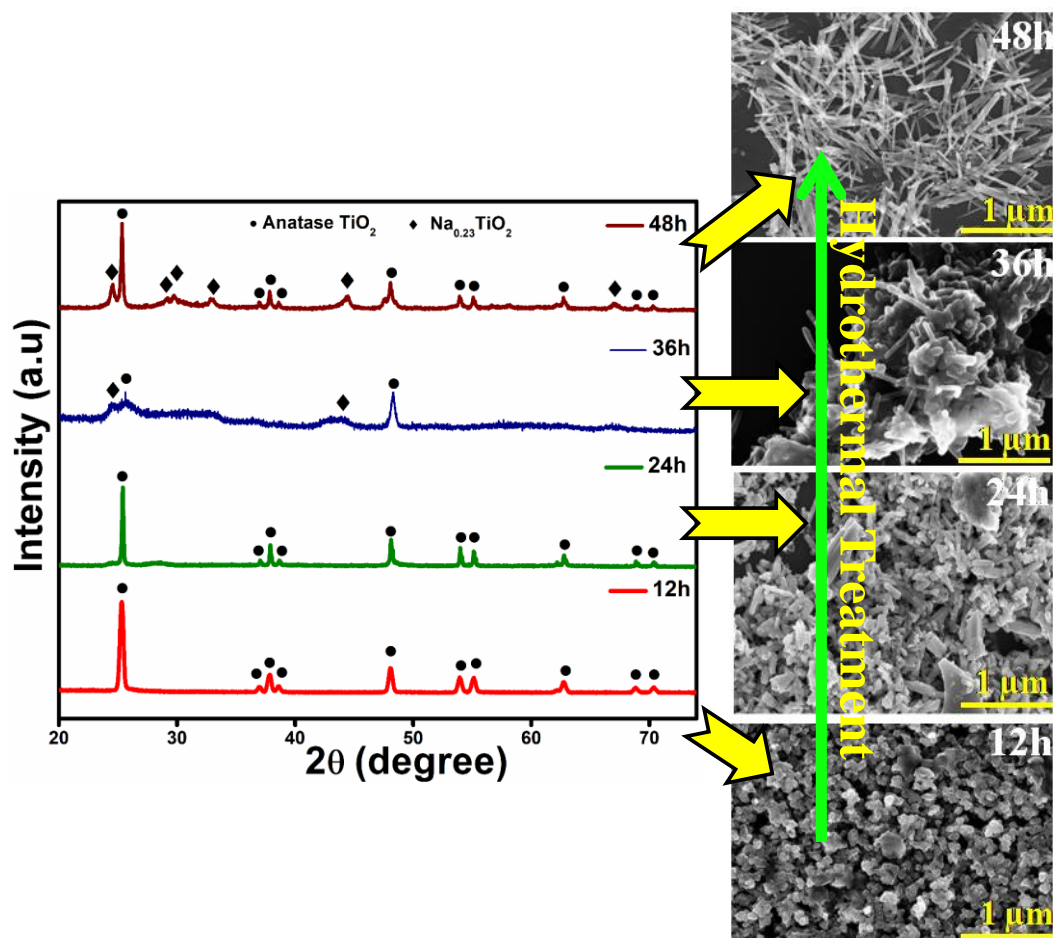


**Figure 3.2.9:** X-ray diffraction pattern along with the respective FESEM analysis of anatase  $\text{TiO}_2$  nanoparticle treated with  $\text{NaOH}$  under the hydrothermal reaction at a temperature of  $180^\circ\text{C}$  for different duration of reaction.

This phenomenon can be explained by Ostwald ripening. Many small crystals formed initially slowly disappear, except for a few that grow larger, at the expense of the small crystals, where the smaller crystals act as fuel for the growth of more giant crystals [12,13]. Kolen'ko et al. (2006) reported the synthesis of nanorods in one step by a hydrothermal treatment in a  $\text{NaOH}$  solution followed by an acid treatment, which helps to produce  $\text{Na}$ -free nanorods [14]. By following the work of Kolenko et al., we have followed acid washing to generate sodium-free samples. Figure 3.2.10, indicates the effect of acid washing on the as-prepared product.

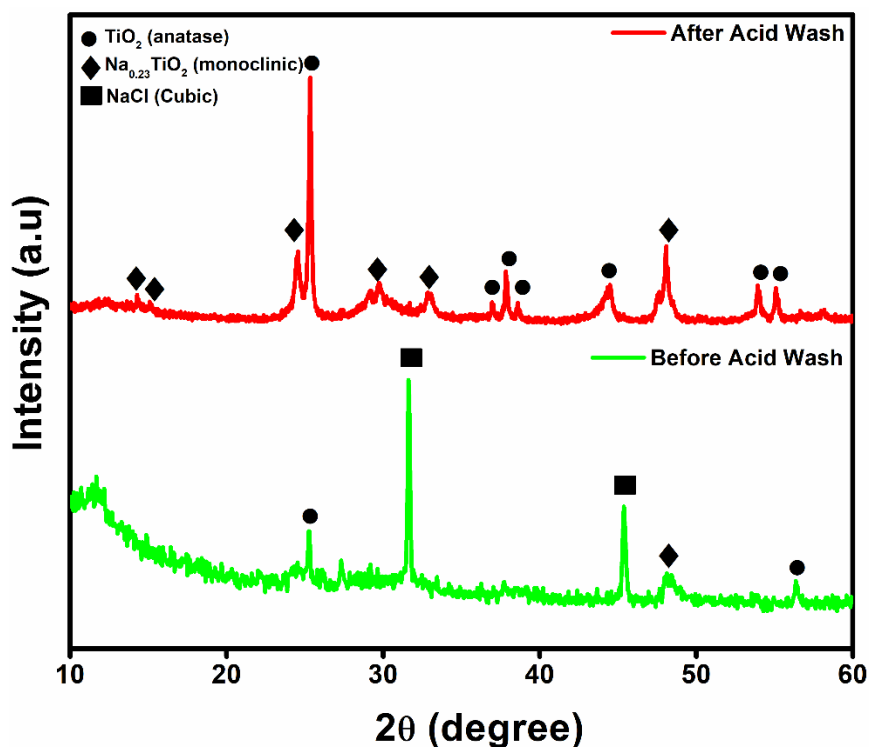


**Figure 3.2.10:** XRD pattern of as prepared sample before and after acid washing, respectively.

Formation of crystalline dominating NaCl phase and anatase TiO<sub>2</sub> and Na<sub>0.23</sub>TiO<sub>2</sub> phase was evident before acid wash. Similarly, the TEM and corresponding EDX result (Figure 3.2.11a) also shows NaCl phase in the as-prepared sample before acid wash. After controlled acid treatment, excess NaCl get completely dissolved and the synthesized rods exhibited only the mixed phase (Figure 3.2.11b). Therefore, acid treatment is important to obtain sodium free nanorods or to avoid titanate phases, which effectively help to remove excess Na ions. To check qualitative analysis of chloride ion in the sample after acid washing, a small amount of the composite sample was treated with 0.1M aqueous AgNO<sub>3</sub> solution. No white precipitate was formed, indicating chloride ion's absence as NaCl form in the sample solution. Thus, successive acid washing and AgNO<sub>3</sub> treatment indicates absence of excess Na<sup>+</sup> in the composite sample.

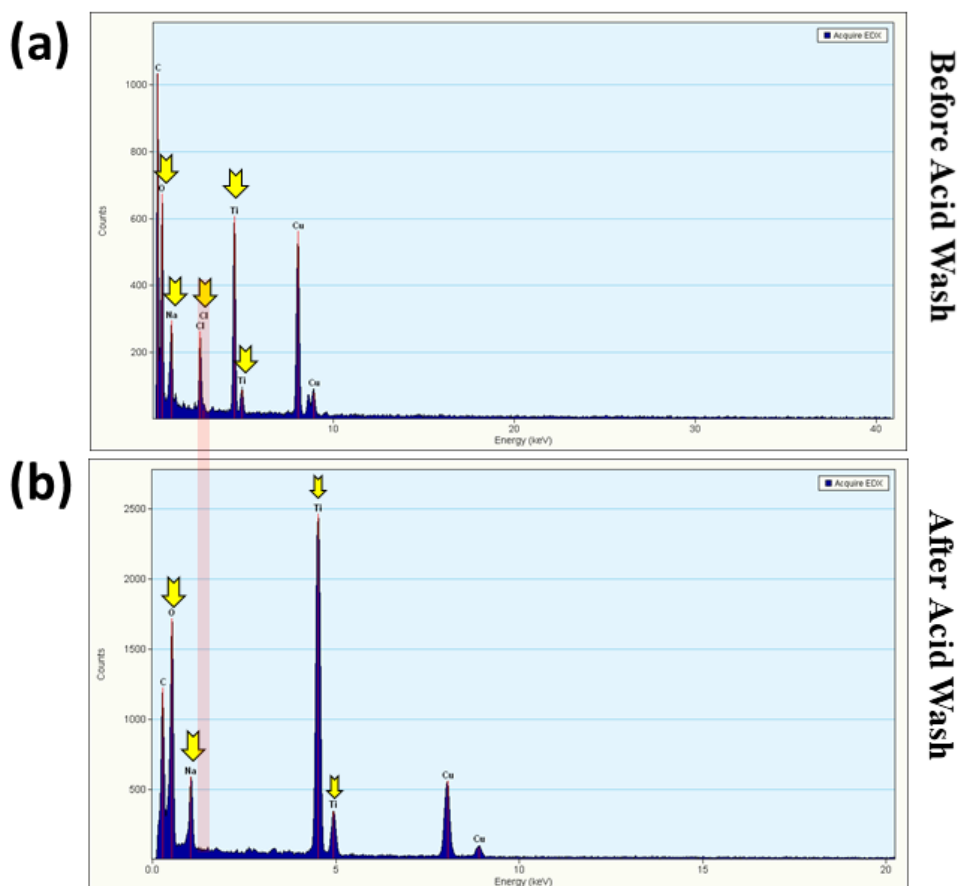


**Figure 3.2.11:** EDX spectrum of as prepared sample (a) before and (b) after acid washing, respectively. (Red zone indicate absence of chlorine after acid wash).

### 3.2.10. Phase Evaluation

In order to ascertain the phase change that occurred during the synthesis, X-ray powder diffraction has been successively recorded for the as prepared and calcined samples as shown in Figure 3.2.12. The XRD pattern of the starting commercial  $\text{TiO}_2$  powder confirmed the presence of anatase phase only (JCPDS No. 21-1272). After the hydrothermal treatment, the as prepared sample contains a small amount of another phase along with the anatase phase. The observed reflections of the new phase match well with the monoclinic  $\text{Na}_{0.23}\text{TiO}_2$  phase (JCPDS No. 22-1404). Thus, the final resultant product obtained from the hydrothermal treatment of commercial  $\text{TiO}_2$  anatase nanoparticle powder exhibits mainly anatase  $\text{TiO}_2$  phase with a minor amount of  $\text{Na}_{0.23}\text{TiO}_2$  as the co-existed phase. Further, on calcination at  $500^\circ\text{C}$ , as such no significant change was observed in the XRD pattern other than an enhanced

crystallinity. Therefore, based on TG-DTA and XRD results, the 500°C calcined sample was selected for further studies.

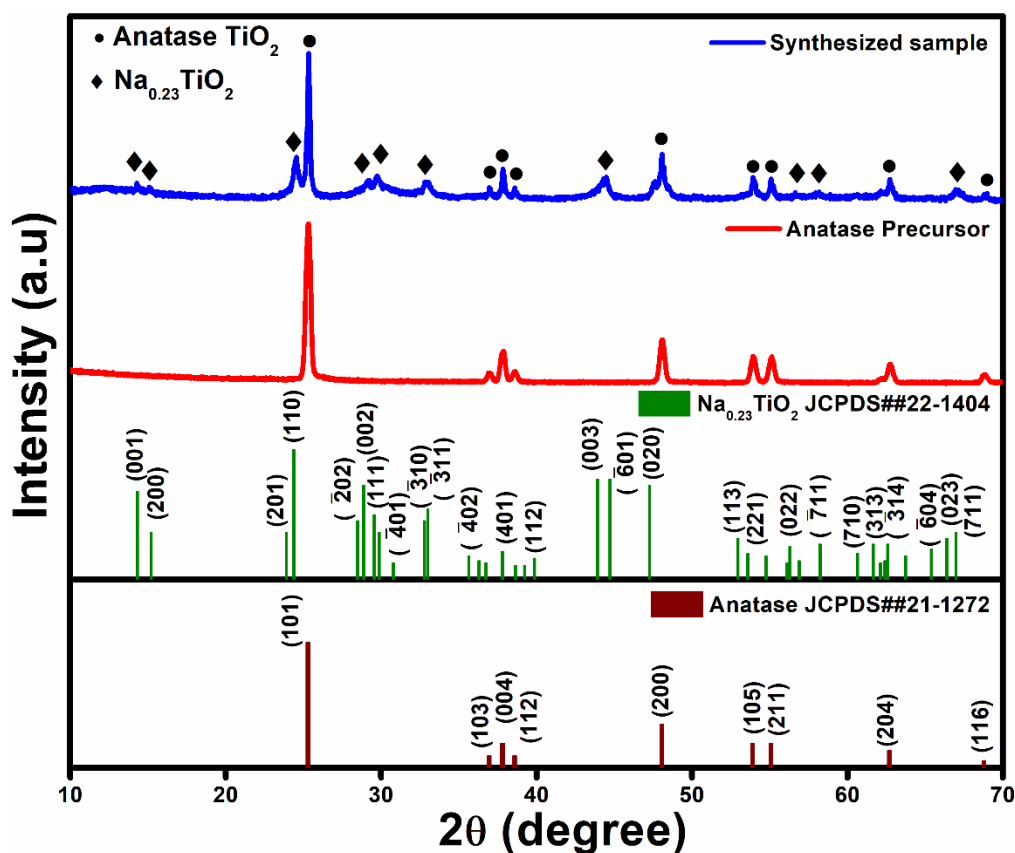


**Figure 3.2.12:** The X-ray diffraction pattern of the standard JCPDS data, precursor sample and as prepared sample calcined at 500°C.

Raman studies were also carried out to further understand the presence of mixed phase in the final product. Figure 3.2.13 depicts the characteristic  $E_g$  band at  $143.4$  and  $639\text{cm}^{-1}$ , the  $B_{1g}$  band at  $397\text{cm}^{-1}$ , and the  $(A_{1g} + B_{1g})$  mode centred at  $516\text{cm}^{-1}$  of anatase phase of  $\text{TiO}_2$ . After the hydrothermal treatment, the characteristic  $E_g$  mode becomes narrower and slightly blue-shifted from  $143.4$  to  $148\text{cm}^{-1}$ . This may be due to the phonon-confinement effect developed strain owing to the change in size and shape of  $\text{TiO}_2$  during the hydrothermal synthesis process. Also,  $202.4$ ,  $285.3$  and  $449.6\text{cm}^{-1}$  confirms the presence of sodium titanate phase (NT) in the sample besides the anatase  $\text{TiO}_2$ .



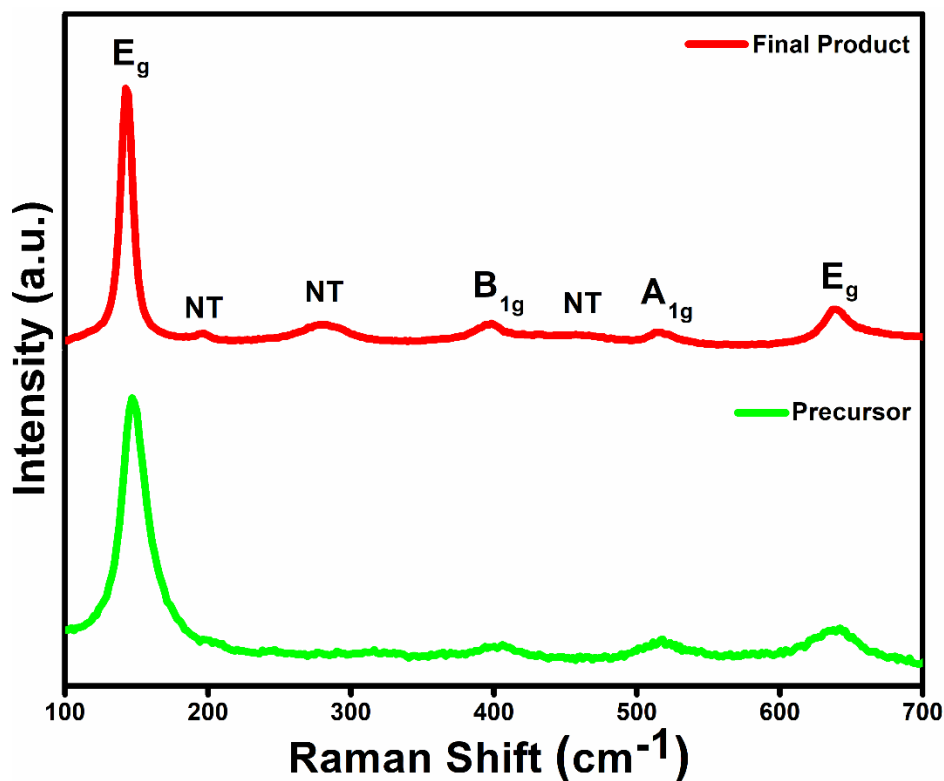


**Figure 3.2.13:** Raman spectra of anatase  $\text{TiO}_2$  precursor and after the hydrothermal treatment product which is calcined at  $500^\circ\text{C}$ .

### 3.2.11. Mechanism of Phase and Morphology Transformation

According to many reports, the phase and morphology transformation during hydrothermal synthesis strongly depends on the NaOH content [15]. Hydrothermal reaction of  $\text{TiO}_2$  nanoparticles in high pH condition with NaOH might have helped in the formation of sodium tri-titanate ( $\text{Na}_2\text{Ti}_3\text{O}_7$ ) particles with a rod like morphology. The  $\text{TiO}_2$  nanoparticles in NaOH could lead to the formation of lamellar sheets due to the breakage of Ti-O-Ti bonds and form O-Ti, Ti-OH bonding and the loose O-Ti could bind to  $\text{Na}^+$ . For instance, for protonated  $\text{TiO}_2$  nanorods, pure anatase phase is usually formed, whereas for  $\text{Na}^+$  rich nanorods, post-annealing leads to a mixed phase. The ion exchange of  $\text{Na}^+$  by  $\text{H}^+$  is a well-known mechanism reported in the literature [12,16,17]. The measured zeta potential of the precursor anatase nanoparticle was  $-49.2\text{mV}$ , indicating highly water-soluble colloidal solution whereas in case of the synthesized nanorod, the zeta potential value gets reduced to  $-12.6\text{mV}$ .

### **3.2.12. Transmission Electron Microscopic (TEM) Analysis**

Clearer evidence for the formation of nanorod morphology can be found in Figure 3.2.14(a-i), from the detailed TEM investigation of anatase/ $\text{Na}_{0.23}\text{TiO}_2$  co-existed  $\text{TiO}_2$  nanorod. Figure 3.2.14a and b represents the TEM bright field image of the precursor  $\text{TiO}_2$  nanoparticles having an average particle size of 30nm at different magnifications. The high-resolution TEM (HRTEM) image (Figure 3.2.15c) clearly shows an interlayer spacing value of 0.352nm corresponding to crystalline (101) plane of anatase  $\text{TiO}_2$  phase. On the other hand, TEM bright field images of the as-prepared anatase/ $\text{Na}_{0.23}\text{TiO}_2$  co-existed sample exhibited rod like structure having an average diameter of 22nm as shown in Figure 3.2.14d and e at different magnifications. The corresponding HRTEM shown in Figure 3.2.14f, indicates the co-existence of (001) plane of  $\text{Na}_{0.23}\text{TiO}_2$  and (101) plane of anatase  $\text{TiO}_2$ . Further, the TEM bright field images of calcined sample exhibit randomly distributed fine thinner rod like structure having an average diameter of ~10nm and an aspect ratio of 25:1 as shown in Figure 3.2.14g and h at different magnifications. The good crystallinity of the synthesized nanorods is clear from the HRTEM image as shown in Figure 3.2.14i. Further, the interlayer spacing of the most intense (101) peak is found 0.352nm along with (004) plane (0.237nm) corresponding to anatase  $\text{TiO}_2$  phase which corroborates with the XRD and Raman analysis.

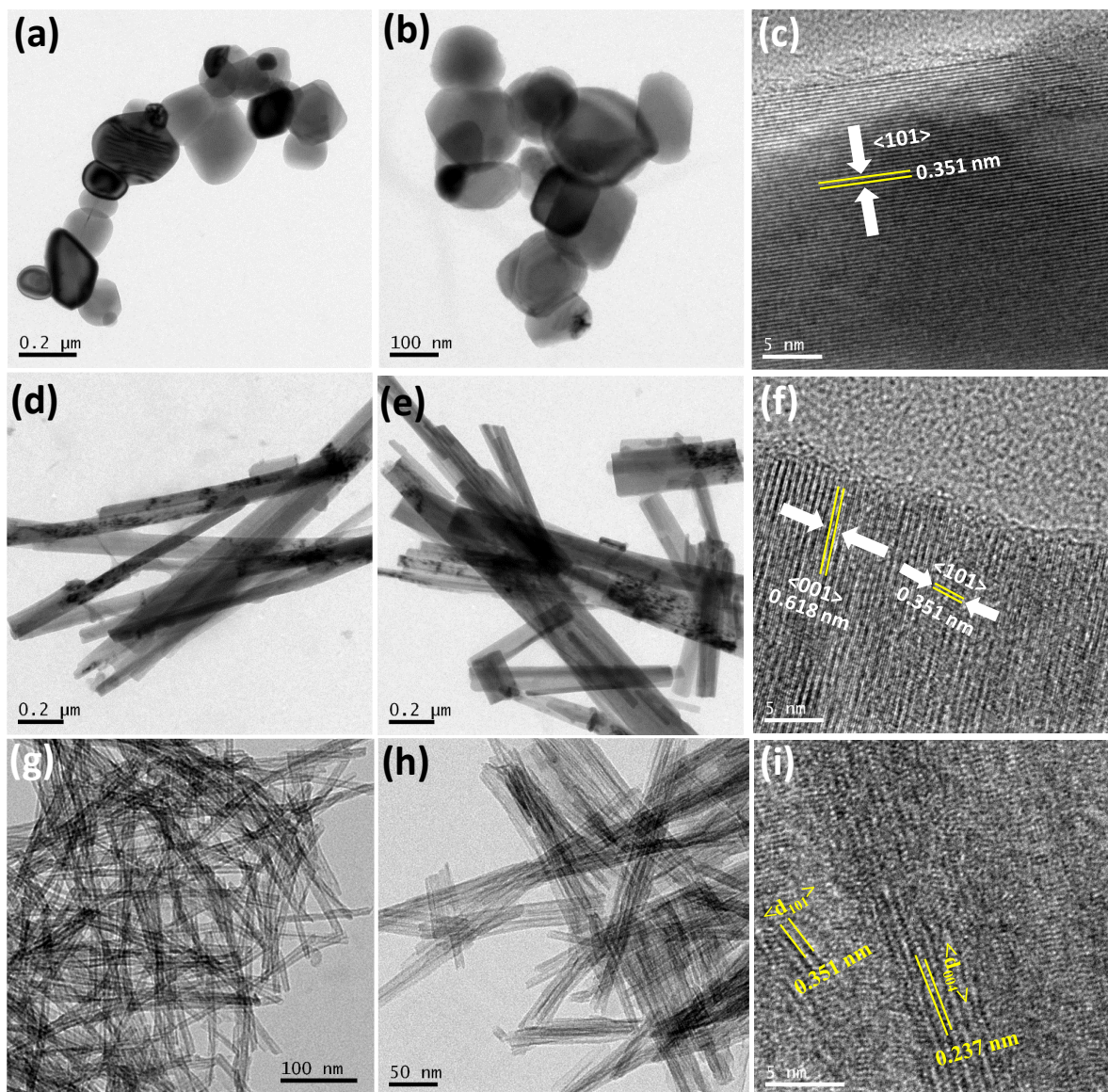


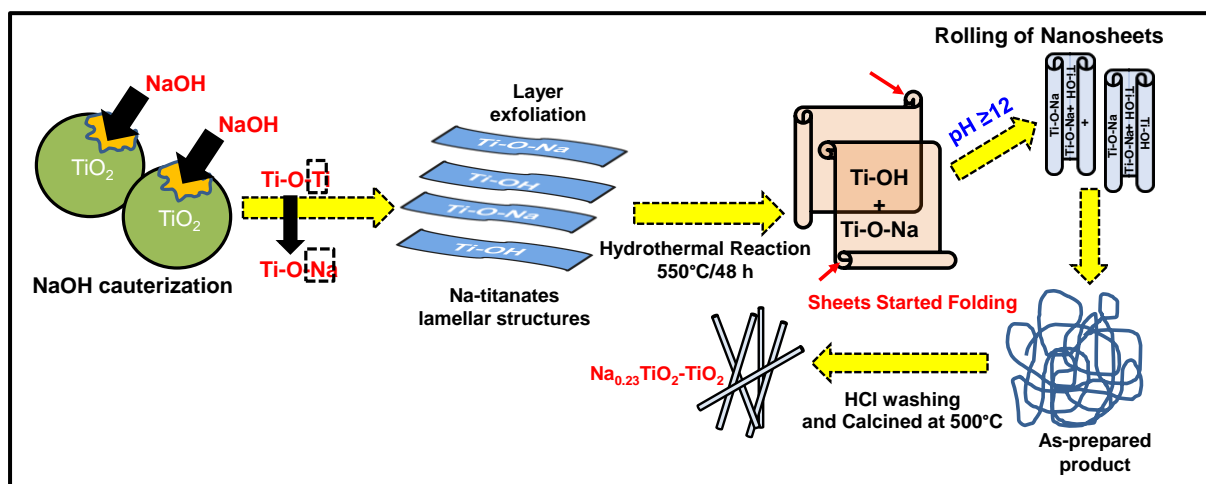
**Figure 3.2.14:** (a)-(b) TEM bright field images of starting anatase  $\text{TiO}_2$  powder at different magnifications, (c) corresponding HRTEM image, (d)-(e) TEM bright field images at different magnifications and (f) corresponding HRTEM image of as-prepared nanorod, (g)-(h) TEM bright field images at different magnifications and (i) corresponding HRTEM image of composite nanorod prepared at  $500^\circ\text{C}$ .

As described in other reports, the formation of layered nanosheets might be the initial step for the formation of rods which then become seeds for an oriented crystal growth process leading to thinner titanate nano rods [5,6]. In addition, the period of hydrothermal treatment determines the formation of this 1D morphology.

According to many reports, the phase and morphology transformation during hydrothermal synthesis strongly depended on the NaOH content [13,15]. The  $\text{TiO}_2$  nanoparticles in highly

basic medium in NaOH could lead to the formation of lamellar sheets due to the breakage of Ti-O-Ti bonds and form O-Ti, Ti-OH bonding and the loose O-Ti could bind to Na<sup>+</sup> forming Ti-O-Na. The intermediates such as Ti-OH would proceed with rearrangement to form sheets of edge-sharing TiO<sub>6</sub> octahedra with Na<sup>+</sup> and OH<sup>-</sup> intercalated between the sheets. These two longer Ti-O bonds in the TiO<sub>6</sub> octahedra were broken, partially the anatase TiO<sub>2</sub> would transform into the layered titanate [16]. The hydrothermal reaction of TiO<sub>2</sub> nanoparticles in high pH condition with NaOH might have helped in the formation of sodium tri-titanate (Na<sub>2</sub>Ti<sub>3</sub>O<sub>7</sub>) particles with a rod-like morphology [17].

For instance, for protonated TiO<sub>2</sub> nanorods, pure anatase phase is usually formed, whereas, for Na<sup>+</sup> rich nanorods, post-annealing leads to a mixed phase. The ion exchange of Na<sup>+</sup> by H<sup>+</sup> is a well-known mechanism reported in the literature [18,19]. The measured zeta potential of the precursor anatase nanoparticle was -49.2mV, indicating highly water-soluble colloidal solution whereas, in case of the synthesized nanorod, the zeta potential value gets reduced to -12.6mV.



*Scheme 3.2.1: Schematic representation of the growth mechanism of composite nanorods.*

### 3.2.13. X-ray Photoelectron Spectroscopic (XPS) and Surface Area Analysis

To understand the chemical and binding states of the elements present in TiO<sub>2</sub> nanoparticle (TP) and composite nanorod (CR), X-ray photoelectron spectroscopy (XPS) studies were carried out as shown in (Figure 3.2.15a-e). It is evident that both samples contain Ti and O, as

shown in the XPS survey spectra in Figure 3.2.15a. The appearance of metallic Na specifies the existence of Na in CR sample. The core-level binding energy peaks at 493.2 and 1070.1eV indicates Na KLL and Na 1s states, respectively (Figure 3.2.15b). The XPS peaks at 464.42eV and 458.62eV correspond to binding energies of the Ti 2p<sub>3/2</sub> and 2p<sub>1/2</sub> states, respectively of TP sample. The binding energy of CR exhibited a significant stokes shift, i.e. 463.75 and 457.95eV of the Ti 2p<sub>3/2</sub> and 2p<sub>1/2</sub> states, respectively, as shown in Figure 3.2.15c. This may be due to the co-existence of tetragonal-monoclinic phase [7,20]. Besides, the peak shifting sometimes may be attributed to the lower electronegativity of Na (0.93) than that of Ti (1.52), which confirms the substitutional incorporation of Na<sup>+</sup> at Ti<sup>4+</sup> site [21]. For both the samples, the spin-orbit splitting energy of 5.8eV is characteristic of Ti<sup>4+</sup> in the TiO<sub>2</sub> form. At the same time, the O1s binding energy gets decreased for CR than TP. By deconvolution, the observed three peaks of O1s shown in Figure 3.2.15d and e represents the high-resolution O1s spectrum of TP and CR samples, respectively. The observed two different binding energies are attributed to Ti-O-Ti for both the samples as O1 component and Ti-O-H as O2 component for both the samples (Figure 3.2.15d and e). Table 3.2.1, indicates the individual core level binding energies and their difference for both the samples. Interestingly, TP exhibits an additional component of O3 at 531.16eV is associated with the O<sup>2-</sup> ions in oxygen-deficient regions within the TiO<sub>2</sub> matrix. Moreover, the absence of any signal of Cl as an element or relative derivatives in the survey spectrum (Figure 3.2.15a) indicates the nanorods are free of NaCl and its derivatives.

**Table 3.2.1: XPS binding energies of Ti and O core level spectrum of different TiO<sub>2</sub> samples, respectively\***

Sample	Ti <sub>1/2</sub> (eV)	Ti <sub>3/2</sub> (eV)	Difference (eV)	O 1s (eV)		
				O1	O2	O3
TP	458.62	464.42	5.8	529.92	530.54	531.16
CR	457.95	463.75	5.8	529.51	530.16	-

\* The binding energies calculated from Figure 3.2.15 (c)-(e)

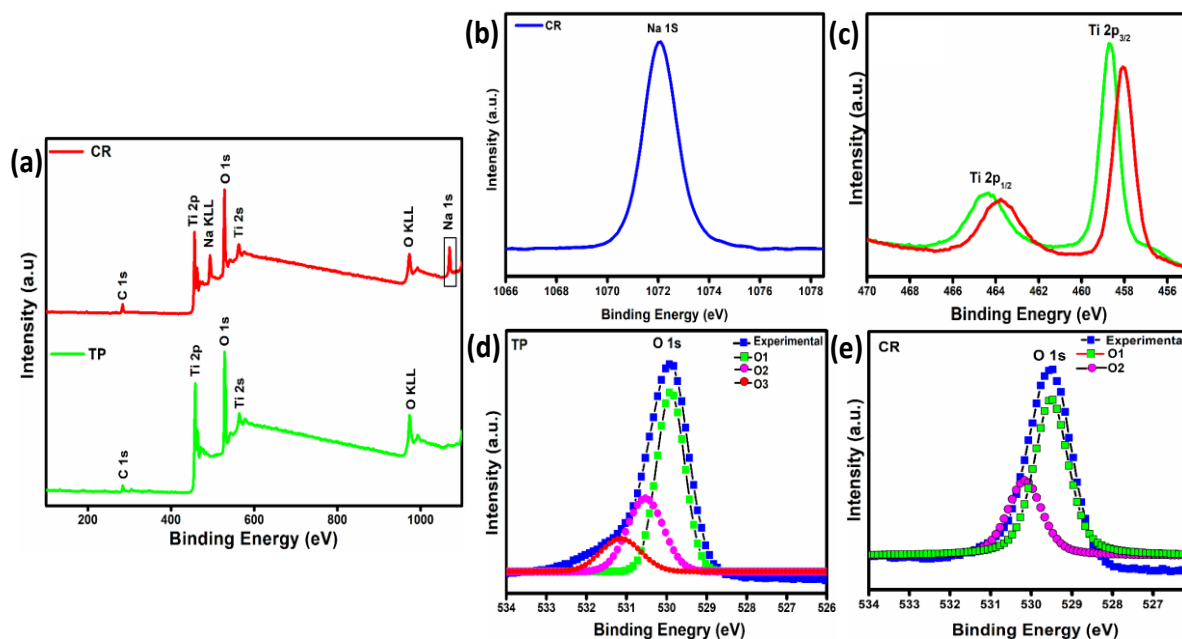


**Figure 3.2.15:** XPS (a) survey, core level spectra of (b) Na-spectrum of CR sample, (c) Ti spectrum of TP and CR sample, respectively, corresponding deconvoluted O 1s spectrum of (d) TP and (e) CR samples.

In order to unravel the distinction in morphology and sensing performance, the BET surface area of composite rod based, sample was measured by nitrogen isothermal adsorption process (Figure 3.2.16). The corresponding pore size was calculated by the BJH method, as shown in Figure 3.2.16b. As evident from Figure 3.2.16, the type *IV* isotherm was observed for the composite morphology. The composite rod exhibited an enhanced BET specific surface area of  $90.03\text{m}^2.\text{g}^{-1}$ , mainly attributed to the thinner rod-based structure. Whereas, the pore size for nanorods was  $> 50\text{ nm}$  mainly originated from the interlayer space of nanorods, as shown in Figure 3.2.16b.

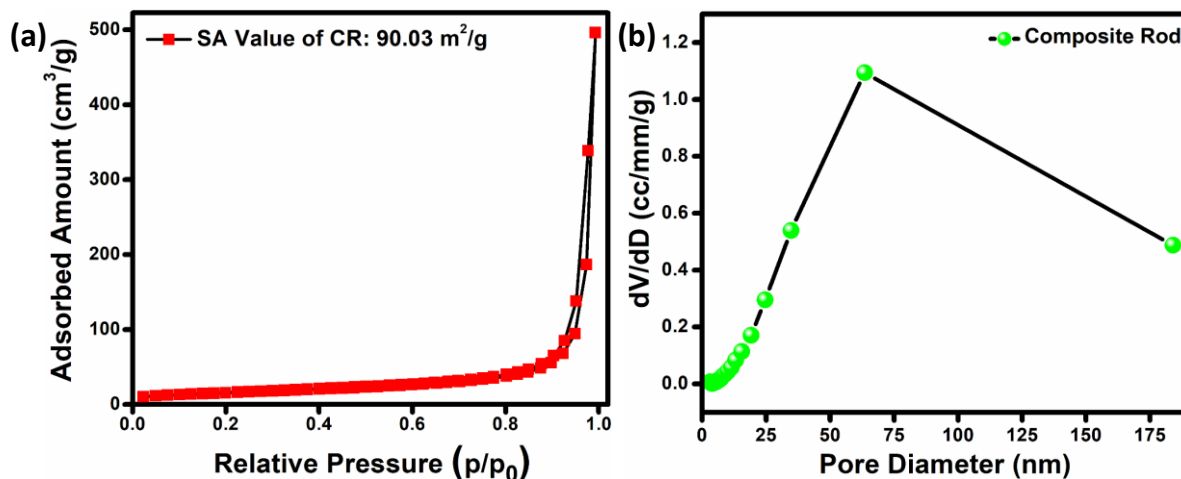


**Figure 3.2.16.** (a) Nitrogen adsorption-desorption isotherm (b) Corresponding BJH pore size distribution curves of Composite Rod based samples.

### 3.2.14. Acetone Sensor Application

As an initiative to eventually develop self-powered gas sensor, we have utilized the synthesized powder for gas sensor fabrication. As a preliminary drive to develop the self-powered gas sensor, we have also utilized the synthesized powder for gas sensor fabrication. An attempt has been taken with the sensor fabricated using the synthesized composite nanorod (CR) powder for the detection of acetone which is considered as the biomarker to detect blood glucose level from breath non-invasively. The acetone concentration for diabetic patients in breath lies in the range from 1.7ppm to 3.7ppm, whereas for a healthy person, the concentration range should be below 1ppm [22,23]. After fabrication of the sensor with CR, the change of resistance was monitored at different acetone concentrations. The sensor was exposed to 10, 5, 3, 2 and 1 ppm acetone at room temperature. The CR based sensor exhibited the response ( $R_g/R_a$ ) signal as 7.1, 4.7, 4.1, 3.8 and 3.6 for 10, 5, 3, 2 and 1ppm acetone respectively, at room temperature with 15 sec of exposure time, as shown in Figure 3.2.17a. The dynamic response curve of the sensor towards 10, 3 and 1ppm acetone is presented in Figure 3.2.17(b-d). The single cycle of the dynamic response curve of the CR-based sensor for 3 ppm of acetone showing the response and recovery time as 12sec and 20sec, respectively, as shown in Figure 3.2.17c.

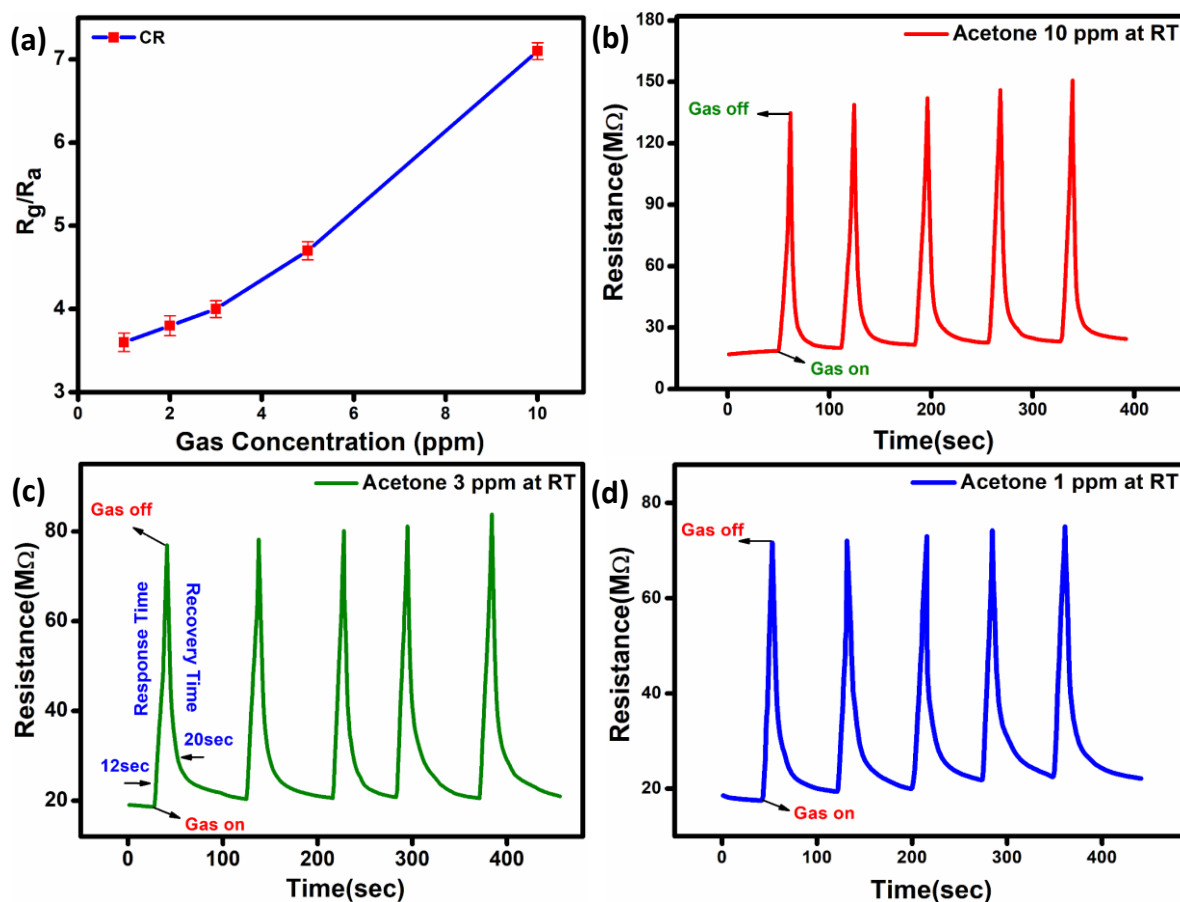


**Figure 3.2.17:** (a) The response of the sensor towards different concentrations of acetone at room temperature and dynamic response curve towards (b) 10ppm (c) 3ppm and (d) 1ppm acetone, respectively.

Besides, the CR-based gas sensor exhibits enhanced acetone response compared to methanol, nitrogen, ethanol and CO gases, which are considered as the interfering gases, as shown in Figure 3.2.18a. The selectivity co-efficient ( $\beta$ ) has been calculated to find out the cross sensitivity from Figure 3.2.18a which is varied in the order  $\beta_{\text{Ethanol}} (5.9) > \beta_{\text{Nitrogen}} (5.1) > \beta_{\text{CO}} (4.7) > \beta_{\text{Methanol}} (4.5)$  for composite rod-based sensor and the nature of co-efficient confirmed the selectivity sensing performance towards acetone.

Along with the direct current (DC) measurements, we have also used the alternating current (AC) method by using a precision impedance analyzer in the 100Hz to 1MHz frequency range to understand the conduction process and the sensing mechanism where  $Z'$  indicates the real part and  $Z''$  represents the imaginary part of the complex impedance data. The variation of



Nyquist diagram of CR based sensor is presented in Figure 3.2.18b in presence of air and acetone at room temperature. An attempt has been executed to understand the sensing response with TP-based sensor. However, it showed meagre sensing response ( $R_g/R_a$ ) about 1.2 towards 10ppm acetone at 350°C operating temperature.

Interestingly, the composite exhibited a p-type sensing behaviour compared to  $TiO_2$ , which is an n-type semiconducting material. However, further studies are in progress to understand the acetone sensing behaviour of the composite powder.

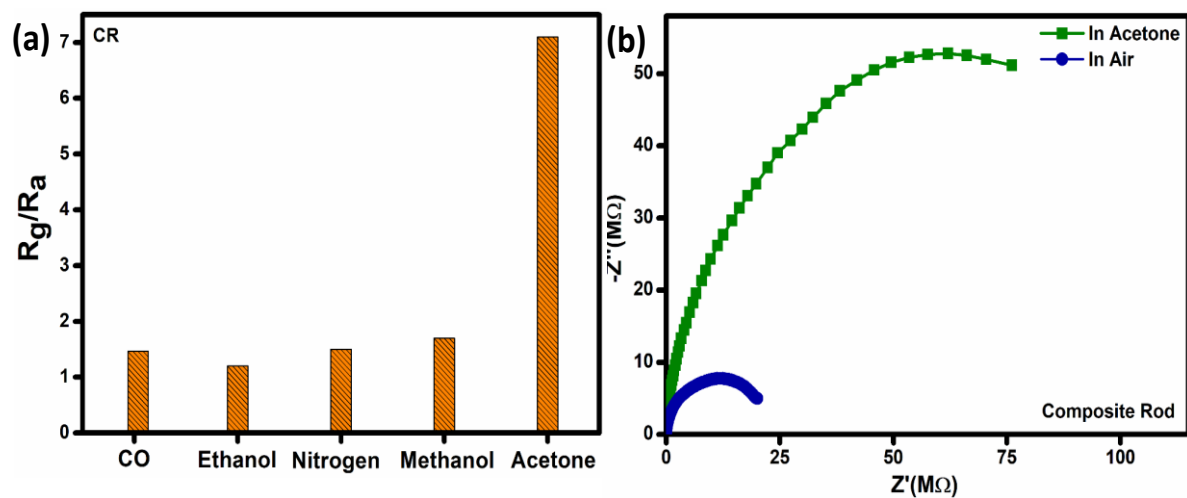


**Figure 3.2.18:** (a) selectivity of CR-based sensor towards different gases (b) Nyquist plot of CR-based sensor in air and in presence of acetone.

Figure 3.2.19a shows the comparison current-voltage ( $I$ - $V$ ) characteristics of composite rod-based sensor towards  $-42V$  to  $+42V$  bias voltage range at room temperature in air and in 10ppm acetone (balanced by  $N_2$ ) respectively. In this figures, good ohmic (linear) type metal-semiconductor contact is shown for the composite rod-based sensor without applying any operating temperatures. Although, in Figure 3.2.19a, the  $I$ - $V$  characteristics in presence of 15sec gas exposure of 10ppm acetone gas exhibits semiconducting behaviour, as the resistance of sensor unit is increasing with applying acetone gas and it results in higher current flow to the sensor-system [24,25].

It is very difficult to prepare a sensor having good sensing stability at room temperature. Generally, after some days of fabrication the sensing response of the sensor is going to decrease at room temperature. But here in our work we have fabricated a composite metal oxide-based sensor with higher sensing response stability up to 90 days without applying any operating temperature. The good stability of our prepared sensor is shown in Figure 3.2.19b for composite rod-based sensor towards 10ppm of acetone gas at completely room temperature.

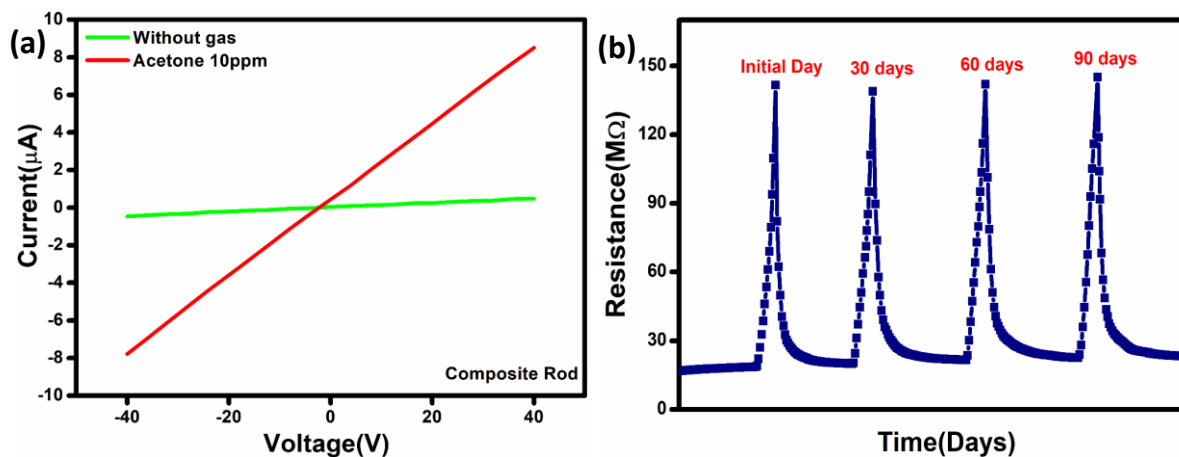


**Figure 3.2.19:** (a) Current-Voltage (I-V) characteristic plot in presence of 10ppm acetone and air and (b) Sensitivity stability towards 10ppm of Acetone at Room Temperature of Composite Rod based Sensor.

The study about sensor's surface coating and its surface topography is very much essential to understand the gas-sensing properties. For this purpose, the microstructure of the coated sensor surface was monitored through FESEM on a field emission scanning electron microscope. EDAX of the surface coating of the sensor device in Figure 3.2.20 shows the purity of the material. The presence of Al arise from the substrate of the sensor device. The presence of open cracks can be clearly seen that certainly helps in the gas adsorption and desorption process by means of increasing the overall effective specific surface-active sites and increasing acetone gas diffusion pathways towards interior surface portions of the coating.

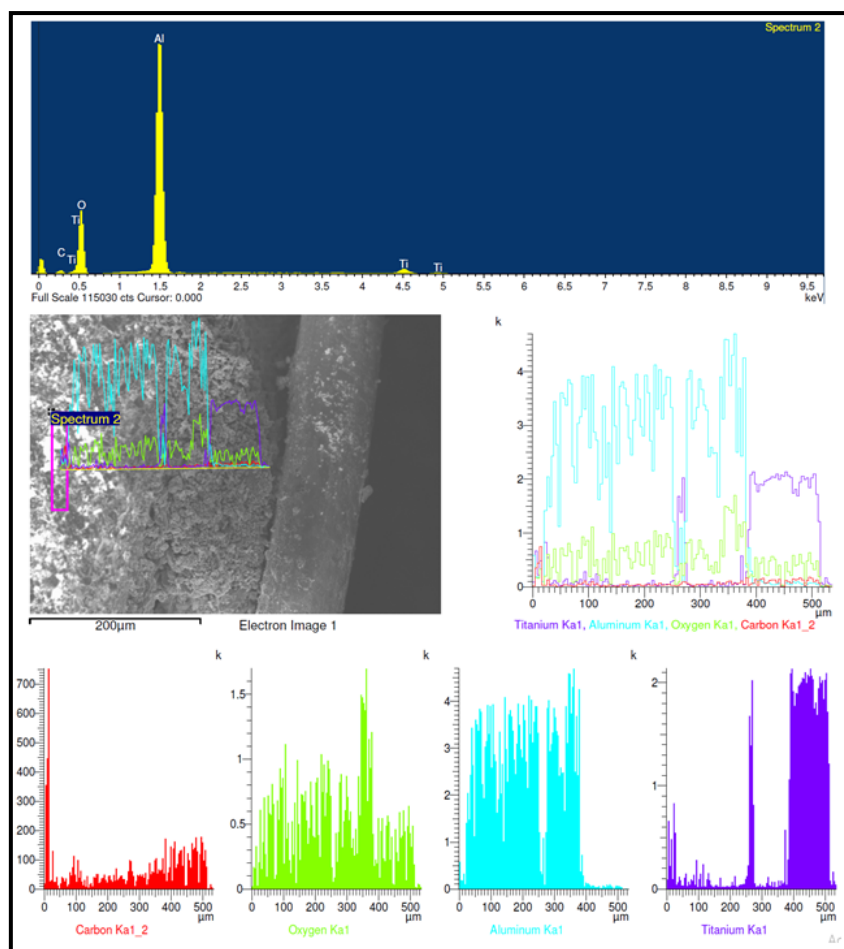


**Figure 3.2.20:** The EDAX of the sensor surface coating and thickness measurement with colour mapping of TiO<sub>2</sub> composite rod-based sensor.

After exploring all the sensing performance with different parameters, the comparative sensing performance of Anatase cube, Rutile rod and Composite nanorod based sensor has been tabulated in Table 3.2.2.

Table 3.2.2: Sensing Parameters obtained from TiO <sub>2</sub> based study			
Sensor Material	Surface Area (m <sup>2</sup> .g <sup>-1</sup> )	Operating Temperature (°C)	Response Ratio
Anatase Cube	86.5	250	6.5
Rutile Rod	16.5	300	4.9
Na <sub>0.23</sub> TiO <sub>2</sub> - Anatase Nanorod	90.03	Room Temperature	7.1

### **3.2.15. Conclusion:**

In this chapter, interesting shapes of TiO<sub>2</sub> in the anatase and rutile forms have been synthesized and tubular gas sensors have been fabricated with the nanostructures. The anatase cube-based sensor exhibited better sensitivity towards acetone than the rod-shaped rutile system with sensing ratios of 6.5 and 4.9, respectively. The corresponding operating temperature for anatase cube and rutile rod-based gas sensor was found to be 250°C and 300°C, respectively. As the performance of single phase TiO<sub>2</sub> was not satisfactory, composite nanorods of Anatase TiO<sub>2</sub> with Na<sub>0.23</sub>TiO<sub>2</sub> have been synthesized by hydrothermal treatment of the commercially available anatase TiO<sub>2</sub> nanoparticle with NaOH solution at pH 12. An enhanced p-type semiconducting sensing response was achieved for different concentrations of acetone (10, 5, 2, 3 and 1ppm) followed by strong selectivity and reproducibility towards acetone at room temperature for composite nanorod based gas sensor. The experimental results thus indicate that this simple and cost-effective synthesis process can be used as a promising tool to synthesize RT sensing materials for fabricating acetone sensors for diagnostic application.

### **3.3. Fe<sub>2</sub>O<sub>3</sub> Based Oxides: Phase and Shape Dependence on Acetone Sensing**

#### **3.3.1. Introduction:**

Similar to TiO<sub>2</sub>, oxides of iron have also been explored extensively for gas sensing application because of their good sensing response, easy synthesis process, low cost, higher stability and fast response-recovery time [26-30]. Oxides of iron such as Fe<sub>3</sub>O<sub>4</sub> and  $\gamma$ -Fe<sub>2</sub>O<sub>3</sub> have been reported to be ideal for acetone sensing applications compared to other volatile gases [31-34]. Our interest, here was to understand the effect of two different crystallographic modification of iron oxide in acetone sensing. For this study, we have synthesized  $\gamma$ -Fe<sub>2</sub>O<sub>3</sub> and Fe<sub>3</sub>O<sub>4</sub> iron oxides by sonochemical process and utilized the resulting nanostructured materials for acetone sensing. The synthesized  $\gamma$ -Fe<sub>2</sub>O<sub>3</sub> based gas sensor exhibited a higher sensing response with fast response and recovery time compared to Fe<sub>3</sub>O<sub>4</sub>. To understand the conduction mechanism and electrical properties followed by sensing mechanism, we have also carried out impedance study using alternating current (AC) method for in the presence of air and acetone.

#### **3.3.2. Results and Discussion:**

##### **3.3.2.1. Nanoparticles of $\gamma$ -Fe<sub>2</sub>O<sub>3</sub> and Fe<sub>3</sub>O<sub>4</sub> and their sensing behaviour**

The synthesized nanostructured materials have been characterized by different analytical techniques including power X-ray diffraction. The highly crystalline phase formation of the synthesized sample was confirmed from the XRD pattern as show in Figure 3.3.1, and the diffraction peaks of  $\gamma$ -Fe<sub>2</sub>O<sub>3</sub> and Fe<sub>3</sub>O<sub>4</sub> are well indexed and matched with standard cubic  $\gamma$ -Fe<sub>2</sub>O<sub>3</sub> (JCPDS No.39-1346) and Fe<sub>3</sub>O<sub>4</sub> (JCPDS No.19-0629) [35-36].

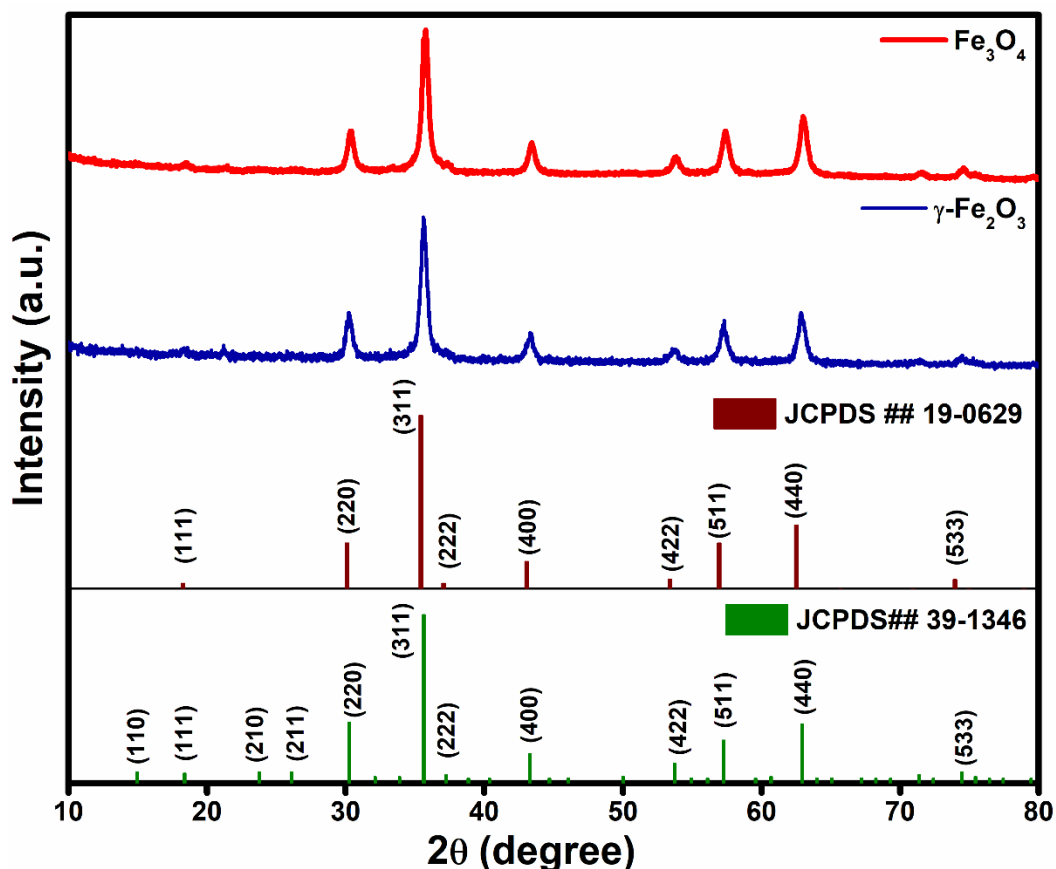


**Figure 3.3.1:** X-ray diffraction pattern of  $\gamma\text{-Fe}_2\text{O}_3$  and  $\text{Fe}_3\text{O}_4$  matched with standard JCPDS card number 39-1346 and 19-0629 respectively.

For further analysis the X-ray diffraction patterns of the Iron Oxide samples were recorded in ULTIMA IV X-Ray Diffractometer (Rigaku) operating at 45kV and 40 mA using  $\text{CuK}_\alpha$  radiation. The XRD data were recorded with step size of 0.02 ( $2\theta$ ) and step time 1sec from  $10^\circ$  to  $80^\circ$  for these samples. The XRD patterns of the sample confirm that  $\gamma\text{-Fe}_2\text{O}_3$  sample contains cubic Iron Oxide ( $\text{Fe}_2\text{O}_3$ ) phase having space group P4132 (space group no:213). The  $\text{Fe}_3\text{O}_4$  sample contains cubic Iron Oxide ( $\text{Fe}_3\text{O}_4$ ) phase having space group Fd-3m (space group no:227) shown in Figure 3.3.2. Values of cell parameters, unit cell volume, average crystallite size and average lattice strain of Iron oxide phase were estimated for these samples from X-ray diffraction (XRD) line profile analysis using Rietveld analysis [37,38] by X'pert high score plus software (PANalytical) and the values are shown in the Table 3.3.1.

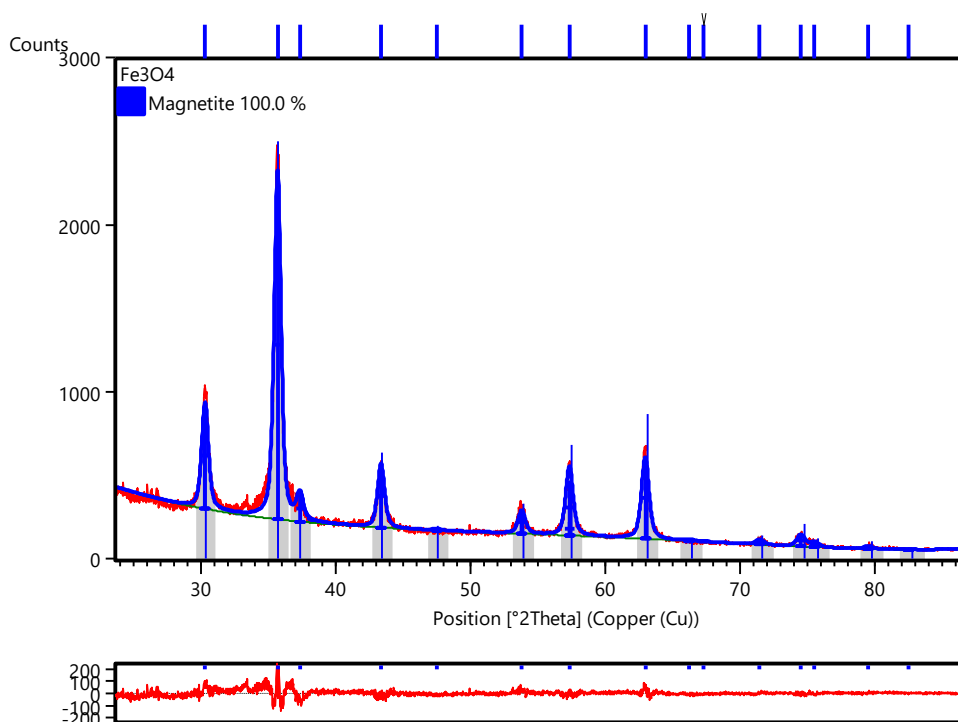
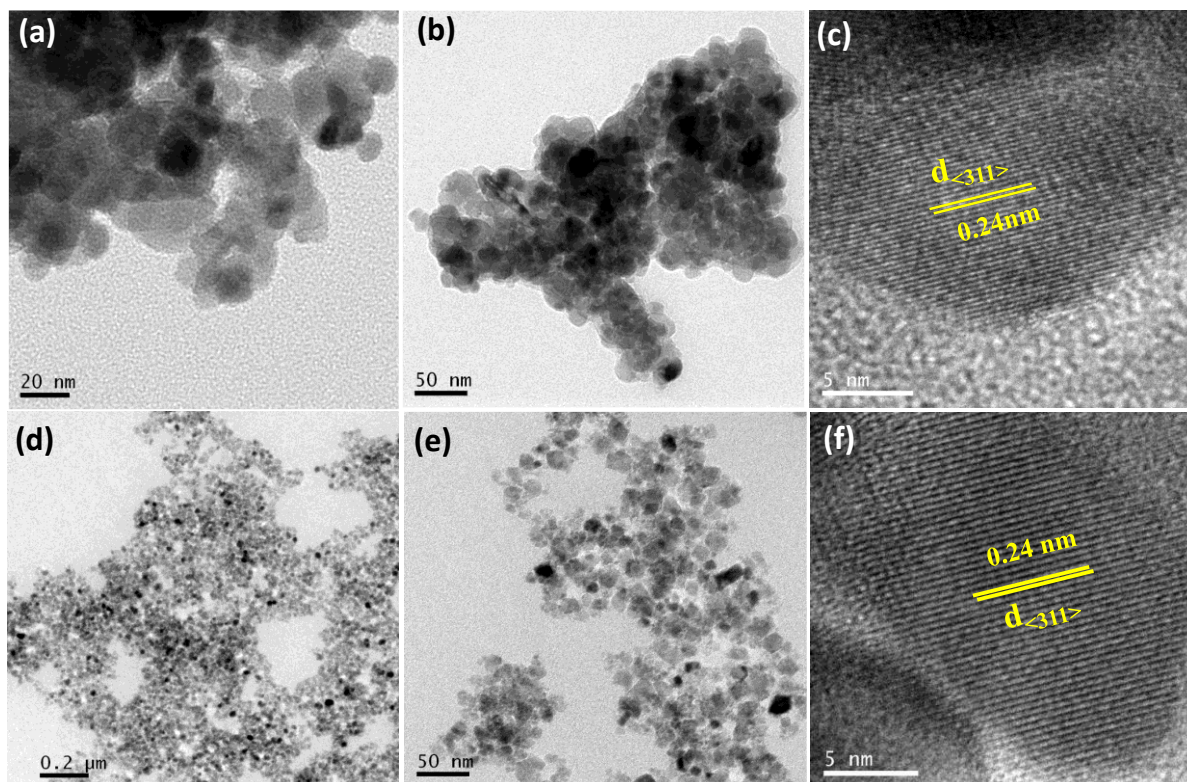


Figure 3.3.2: XRD pattern and difference plot of  $Fe_3O_4$  powders as obtained by Rietveld technique.

Table 3.3.1: Different Parameters Calculation from XRD Data					
Sample	Wt. % of Phases	Cell parameters (Å)	Unit Cell volume (Å) <sup>3</sup>	Average crystallite Size & Lattice strain	
				Crystallite Size (nm)	Lattice strain (%)
$\gamma$ - $Fe_2O_3$	Maghemite Iron Oxide (Cubic) ( $Fe_2O_3$ ): 100 %	a= b =c= 8.36	584.47	15.82	0.033
$Fe_3O_4$	Magnetite Iron Oxide (Cubic) ( $Fe_3O_4$ ): 100%	a= b =c= 8.35	582.98	15.87	0.034

The transmission electron microscopy images of  $\gamma$ - $Fe_2O_3$  and  $Fe_3O_4$  are presented in Figure 3.3.3(a & b) and (d & e). The corresponding HR-TEM image is shown in Figure 3.3.3(c & f)

and the lattice interplanar spacings calculated for  $\gamma\text{-Fe}_2\text{O}_3$  and  $\text{Fe}_3\text{O}_4$  are assigned to 0.24nm corresponding to the (311) plane [39,40]. The HR-TEM image shows high crystallinity of the synthesized samples.



**Figure 3.3.3:** (a-b) & (d-e) Transmission electron micrographs bright field image and (c) & (f) HRTEM image of  $\gamma\text{-Fe}_2\text{O}_3$  and  $\text{Fe}_3\text{O}_4$ , respectively.

The metal oxygen functional groups and the vibrational peaks of the synthesized samples were further studied by FTIR spectra. Figure 3.3.4a shows the FTIR spectra of the synthesized  $\gamma\text{-Fe}_2\text{O}_3$  and  $\text{Fe}_3\text{O}_4$  samples. The band at the position of  $\sim 3435\text{cm}^{-1}$  represents the stretching vibration in OH group. The absorption peak at  $1626\text{cm}^{-1}$  can be attributed to the COO-Fe bond and the peaks at  $1379$  and  $1013\text{cm}^{-1}$  can be represented as  $\text{COO}^-$  bonds [41]. The absorption bands were found at  $447$ ,  $576$  and  $633\text{cm}^{-1}$  due to Fe-O stretching bond [42]. Raman spectroscopic study is very delicate characterization for investigation of nanostructured material and has been carried out for identification of structural properties and phase configuration. The well distribution of the peaks in Raman spectrum shown in Figure 3.3.4b confirms the crystalline phase formation of the sonochemically synthesized sample  $\gamma\text{-Fe}_2\text{O}_3$  and  $\text{Fe}_3\text{O}_4$ . The



transversal optical (TO) modes of maghemite ( $\gamma\text{-Fe}_2\text{O}_3$ ) are located at 222, 289, 408, 502 and 608 $\text{cm}^{-1}$  peak position. The intense peak observed at 222 $\text{cm}^{-1}$  can be assigned to the  $A_{1g}$  mode and the other peaks are attributed to the  $E_g$  mode [43]. On the other side, the vibration mode of Fe-O bonds of magnetite ( $\text{Fe}_3\text{O}_4$ ) can be observed at peak position 395, 492 and 585 $\text{cm}^{-1}$ . The broad raman  $E_g$  band is located at 284 $\text{cm}^{-1}$ , whereas the intense  $T_{2g}$  band is observed at 216 $\text{cm}^{-1}$  [44].

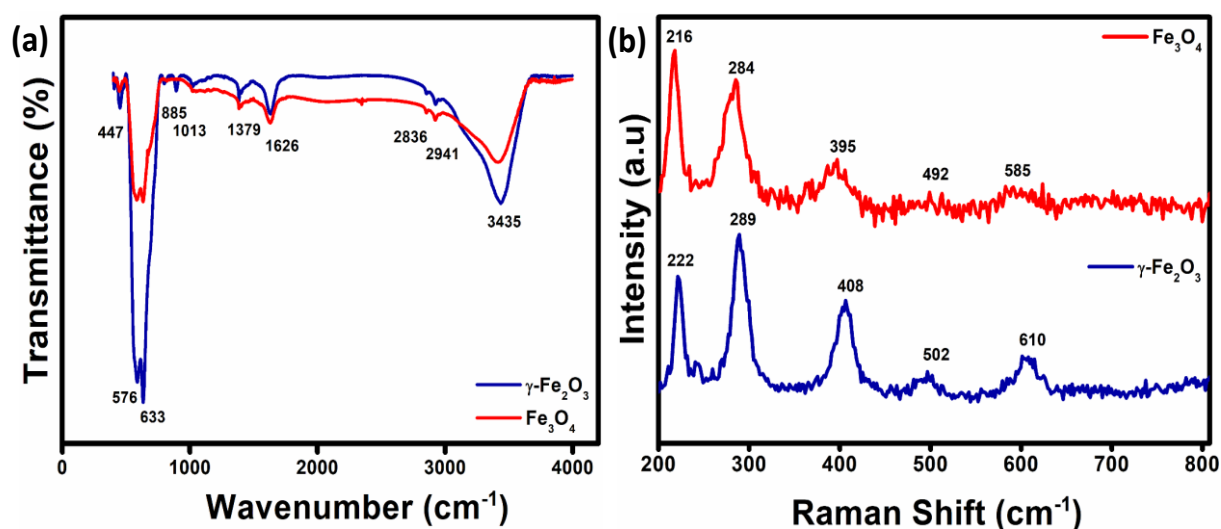


**Figure 3.3.4:** (a) Fourier transformed-infrared (FT-IR) spectrum and (b) Raman spectrum of  $\gamma\text{-Fe}_2\text{O}_3$  and  $\text{Fe}_3\text{O}_4$ , respectively.

The synthesized sample has been further analyzed by XPS study to investigate the chemical composition and oxidation state of the elements present in  $\gamma\text{-Fe}_2\text{O}_3$  and  $\text{Fe}_3\text{O}_4$ . The high resolution XPS spectra of Fe2P core level can be fitted with two spin orbit doublets characteristic of the peak of  $\text{Fe}^{2+}$  and  $\text{Fe}^{3+}$  and with satellite peaks. The core level spectra of Fe2P corresponding to  $\text{Fe}2\text{P}_{3/2}$  peaks at binding energy 710.40eV and  $\text{Fe}2\text{P}_{1/2}$  peak is located at binding energy 723.91eV for  $\gamma\text{-Fe}_2\text{O}_3$  sample is presented in Figure 3.3.5a. The expected signal for  $\text{Fe}^{2+}$  at binding energy 709.5eV is absent in this Fe2P core level spectra which is the clear evidence of the existence of only  $\text{Fe}^{3+}$  in  $\gamma\text{-Fe}_2\text{O}_3$  sample. The satellite peaks are observed at the binding energy 718.25eV for  $2\text{P}_{3/2}$  and  $2\text{P}_{1/2}$  satellite peak at 732.37eV. The binding energy difference between the  $\text{Fe}2\text{P}_{3/2}$  and  $\text{Fe}2\text{P}_{1/2}$  and their corresponding satellite peak is

found to present in between 8 and 8.5eV. This result supports the presence of +3 valency of Fe ions in the sample. For another sample the core level spectra of Fe2P are appeared at binding energy 709.93eV and 723.24eV corresponds to Fe2P<sub>3/2</sub> and Fe2P<sub>1/2</sub> respectively in Figure 3.3.5b. In addition, the satellite peaks are observed at 716.33 eV for 2P<sub>3/2</sub> and another at binding energy 729.55eV for 2P<sub>1/2</sub>. This result is good evidence for the formation of Fe<sub>3</sub>O<sub>4</sub>.

Therefore, the core level O1S spectra of  $\gamma$ -Fe<sub>2</sub>O<sub>3</sub> and Fe<sub>3</sub>O<sub>4</sub> can be resolved into three Gaussian components in Figure 3.3.5c and d indicating the significant differences in oxygen states of the samples [45,46]. The peak centered at about 529.72eV (O<sub>L</sub>), 530.88eV (O<sub>V</sub>) and 531.54eV (O<sub>ads</sub>) for  $\gamma$ -Fe<sub>2</sub>O<sub>3</sub> and for Fe<sub>3</sub>O<sub>4</sub> the O<sub>L</sub> component attributed with energy 529.34eV, O<sub>V</sub> component at 530.80eV and O<sub>ads</sub> identified at 531.72eV. Here O<sub>L</sub>, O<sub>V</sub> and O<sub>ads</sub> components are described as lattice oxygen species, oxygen vacancy and adsorbed oxygen species respectively [47]. The relative percentage of the components of  $\gamma$ -Fe<sub>2</sub>O<sub>3</sub> and Fe<sub>3</sub>O<sub>4</sub> are listed in Table 3.3.2. The relative percentage of O<sub>ads</sub> component of  $\gamma$ -Fe<sub>2</sub>O<sub>3</sub> was approximately 19.24% which is much higher than Fe<sub>3</sub>O<sub>4</sub> (7.48%) which can strongly influence the capacity of oxygen adsorption of  $\gamma$ -Fe<sub>2</sub>O<sub>3</sub>. The excellent ability of chemisorbing oxygen species can be considered in the enhancement of gas sensing performance towards the target gas.

**Table 3.3.2: Relative Percentage of the Components of  $\gamma$ -Fe<sub>2</sub>O<sub>3</sub> and Fe<sub>3</sub>O<sub>4</sub>**

Sample	Oxygen Species	Binding Energy (eV)	Relative Percentage (%)
<b><math>\gamma</math>-Fe<sub>2</sub>O<sub>3</sub></b>	O <sub>Lattice</sub>	529.72	68.33
	O <sub>V</sub>	530.88	12.42
	O <sub>ads</sub>	531.54	19.24
<b>Fe<sub>3</sub>O<sub>4</sub></b>	O <sub>Lattice</sub>	529.34	81.49
	O <sub>V</sub>	530.80	11.01
	O <sub>ads</sub>	531.72	7.48

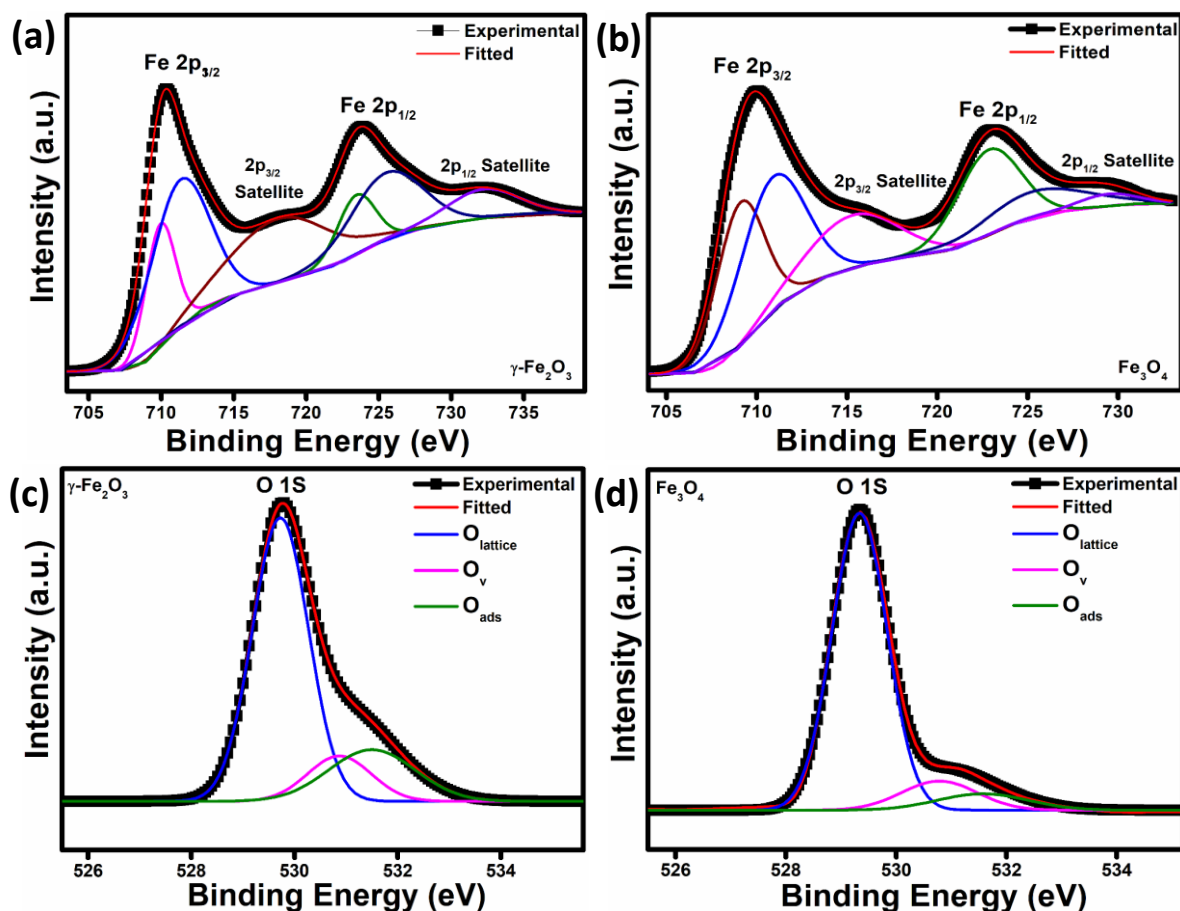


Figure 3.3.5: Core level spectra of (a) Fe 2P and (b) O 1S for  $\gamma$ -Fe<sub>2</sub>O<sub>3</sub> and Fe<sub>3</sub>O<sub>4</sub> respectively.

### 3.3.2.2. Surface Area:

The Brunauer–Emmett–Teller (BET) surface area curves of synthesized  $\gamma$ -Fe<sub>2</sub>O<sub>3</sub> and Fe<sub>3</sub>O<sub>4</sub> are shown in Figure 3.3.6. It is observed that  $\gamma$ -Fe<sub>2</sub>O<sub>3</sub> nanoparticles have a surface area around 56 m<sup>2</sup>/g and it increases drastically than Fe<sub>3</sub>O<sub>4</sub> nanoparticle which is about 38 m<sup>2</sup>/g. This increase of surface area for  $\gamma$ -Fe<sub>2</sub>O<sub>3</sub> nanoparticle may be due to the crystallographic structure and phase formation. It is clear from the sensing performance of both nanoparticle-based sensor that the high surface area is more beneficial and suitable for achieving enhanced response than parameters. Actually, the sufficiently high specific surface area and porous structure is always in the favour of gas absorption and desorption which exhibits the higher sensing performance.

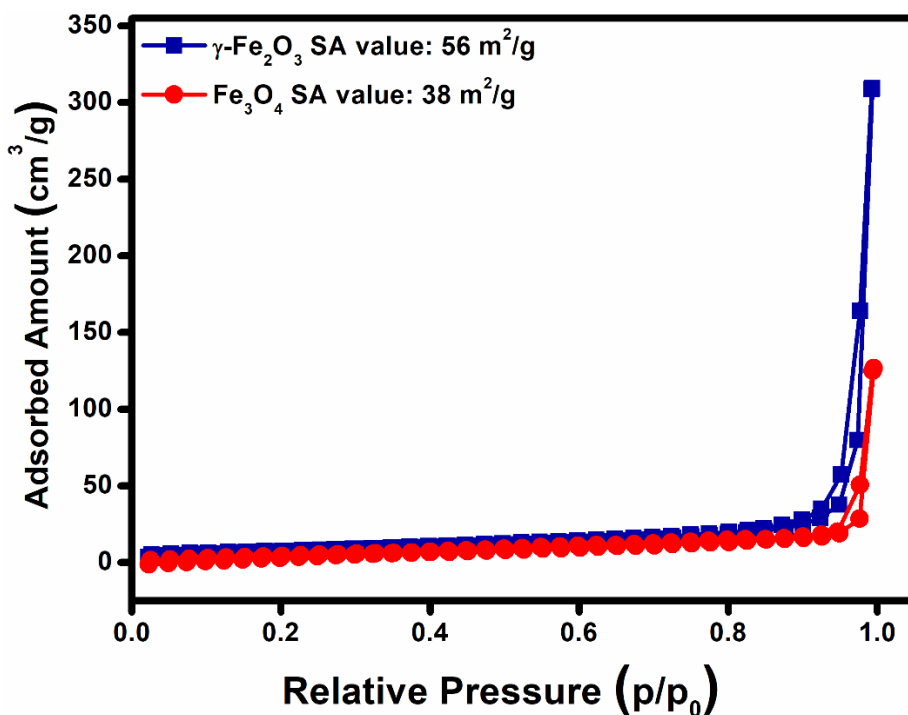


Figure 3.3.6: Nitrogen adsorption-desorption isotherms of  $\gamma\text{-Fe}_2\text{O}_3$  and  $\text{Fe}_3\text{O}_4$  nanoparticles.

### 3.3.2.3. Magnetic Study:

Measurements of magnetization (M) vs. magnetic field (H) is plotted in Figure 3.3.7a and b for  $\gamma\text{-Fe}_2\text{O}_3$  and  $\text{Fe}_3\text{O}_4$  nanoparticles, respectively [48-50]. The saturation magnetization values are 70emu/g for  $\gamma\text{-Fe}_2\text{O}_3$  nanoparticle and 112emu/g for  $\text{Fe}_3\text{O}_4$  nanoparticle at 300 K, respectively, as shown in Figure 3.3.7. It is clear from the magnetization study that  $\text{Fe}_3\text{O}_4$  is ferromagnetic and  $\text{Fe}_2\text{O}_3$  is superparamagnetic.

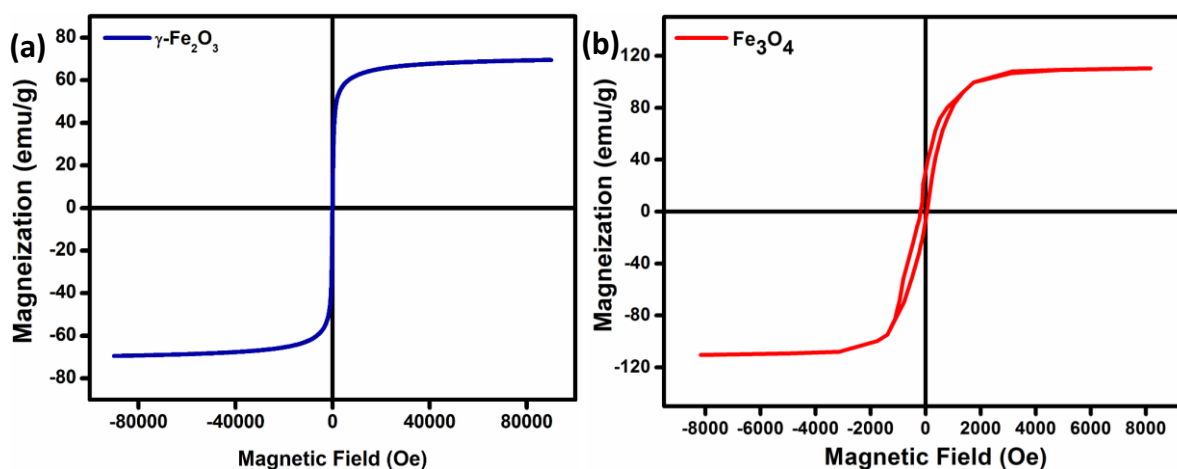
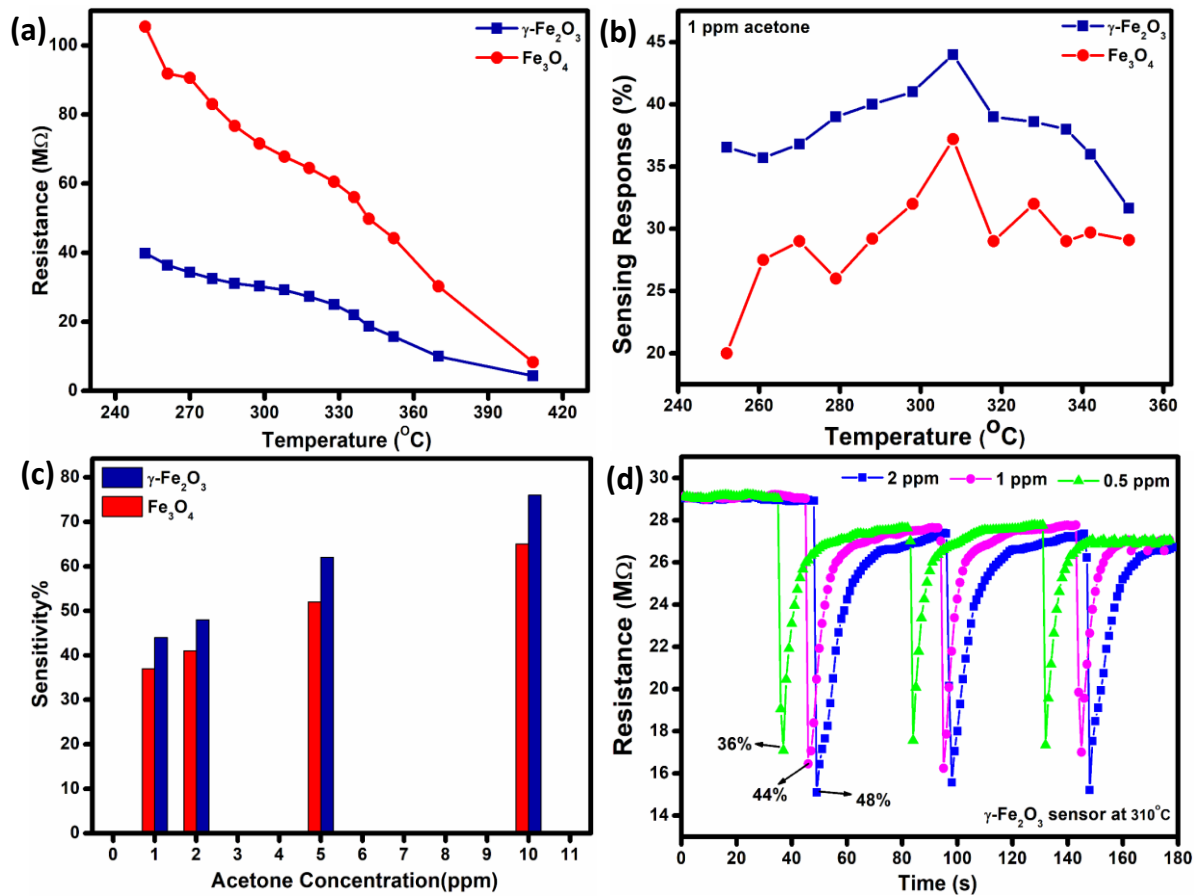


Figure 3.3.7: Magnetization vs field of  $\gamma\text{-Fe}_2\text{O}_3$  and  $\text{Fe}_3\text{O}_4$  nanoparticles.

#### **3.3.2.4. Sensing Properties:**

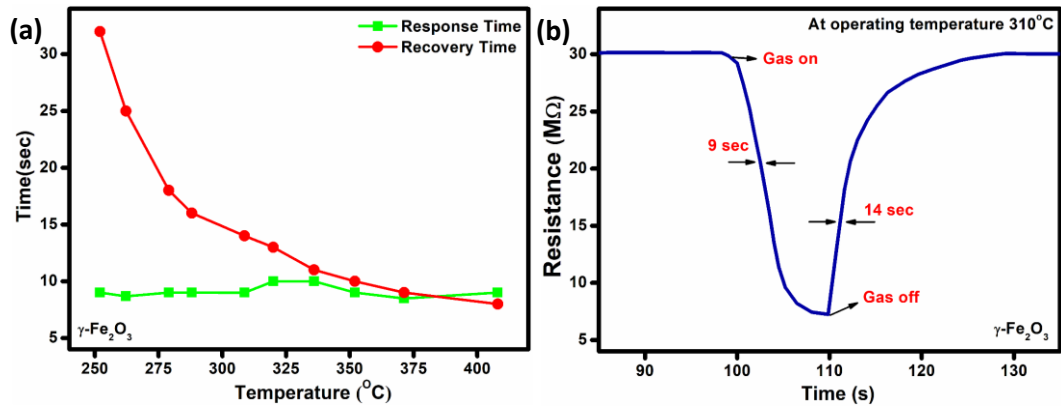
In Figure 3.3.8a, the variation of base-resistance of the fabricated  $\gamma$ -Fe<sub>2</sub>O<sub>3</sub> and Fe<sub>3</sub>O<sub>4</sub> based sensors in air as a function of temperature is plotted. The resistance variation with operating temperature ranging from 250°C to 410°C is shown in Figure 3.3.8a. At first a sharp decrease in resistance of the fabricated sensors was observed with increasing of operating temperature in the lower range of temperature due to the physisorption of the oxygen molecules. Above 340°C operating temperature the resistance decreased with increasing temperature due to the increase in concentration of electrons in intrinsic process of excitation. After stabilization of the base resistance the sensors were exposed towards acetone for different sensor characteristic study. In Figure 3.3.8b the sensing response of both types of sensors with different operating temperature towards 1ppm acetone is presented. In both cases the maximum operating temperature appeared at 310°C. After reaching at this operating temperature the sensing response decreases with increasing temperature due to the desorption of the adsorbed species from the sensor surface. Therefore, 310°C has been optimized for the detailed analysis of gas sensing study. The bar diagram of sensitivity vs different concentration of acetone of  $\gamma$ -Fe<sub>2</sub>O<sub>3</sub> and Fe<sub>3</sub>O<sub>4</sub> based sensor is presented in Figure 3.3.8c. It is obvious from the graph that  $\gamma$ -Fe<sub>2</sub>O<sub>3</sub> shows higher sensitivity response towards different concentrations of acetone than Fe<sub>3</sub>O<sub>4</sub> based sensor. The maximum sensing response of  $\gamma$ -Fe<sub>2</sub>O<sub>3</sub> based sensor has been calculated to be about 76%, 62%, 48% and 44%, respectively towards 10, 5, 2 and 1ppm acetone at 310°C operating temperature. The response of the Fe<sub>3</sub>O<sub>4</sub> based sensor on the other hand was much lower like 65%, 52%, 41% and 37% towards 10, 5, 2 and 1ppm acetone at 310°C operating temperature. The response of the sensors at lower concentration of acetone was also investigated. The  $\gamma$ -Fe<sub>2</sub>O<sub>3</sub> based sensor exhibited increased sensing response of 48%, 44% and 36% towards 2, 1 and 0.5ppm acetone respectively. The corresponding dynamic response curve

of  $\gamma\text{-Fe}_2\text{O}_3$  based sensor at  $310^\circ\text{C}$  operating temperature towards lower concentration of acetone is shown in Figure 3.3.8d.



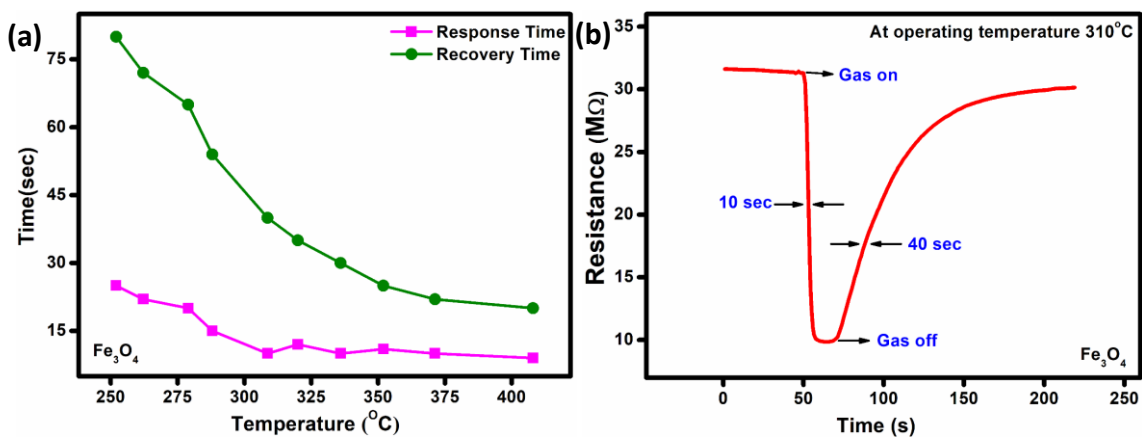
**Figure 3.3.8:** (a) Variation of sensor resistance with operating temperature for  $\gamma\text{-Fe}_2\text{O}_3$  and  $\text{Fe}_3\text{O}_4$  nanoparticle-based sensor (b) Response vs operating temperature curve of both sensor towards 1ppm acetone (c) Bar diagram presents the sensitivity response variation with different concentration of acetone for  $\gamma\text{-Fe}_2\text{O}_3$  and  $\text{Fe}_3\text{O}_4$  based sensor (d) The dynamic response curve of  $\gamma\text{-Fe}_2\text{O}_3$  based sensor toward very lower concentration of acetone (2, 1 and 0.5ppm) at  $310^\circ\text{C}$  operating temperature.

Figure 3.3.9a exhibits the variation of response-recovery time of  $\gamma\text{-Fe}_2\text{O}_3$  based sensor towards 10ppm acetone with different operating temperature. The particle size of the sensor material, structural properties and the thickness of the film are the main controlling parameters of the response and recovery time of the gas sensor. For example,  $\gamma\text{-Fe}_2\text{O}_3$  nanoparticle-based gas sensor shows rapid response and recovery time about 9sec and 14sec, respectively, at  $310^\circ\text{C}$  operating temperature was calculated from the dynamic response curve represented in Figure 3.3.9b.



**Figure 3.3.9:** (a) Variation of response-recovery time with operating temperature (b) Dynamic response curve of  $\gamma\text{-Fe}_2\text{O}_3$  nanoparticle-based gas sensor representing the response and recovery time.

For comparison  $\text{Fe}_3\text{O}_4$  based sensor also explored towards 10ppm acetone with different operating temperature to understand the response recovery time management. The response time and recovery time have been plotted as a function of operating temperature and shown in Figure 3.3.10a. From the single dynamic curve in Figure 3.3.10b the response and recovery time was calculated which is about 10sec and 40sec respectively at optimum operating temperature. But it is very obvious that the response nature of  $\text{Fe}_3\text{O}_4$  based sensor is more or less compatible with  $\gamma\text{-Fe}_2\text{O}_3$  based sensor but the recovery nature of  $\gamma\text{-Fe}_2\text{O}_3$  based sensor is better than other sensor which is more acceptable in the technology development of gas sensor application field.



**Figure 3.3.10:** (a) Variation of response-recovery time with operating temperature (b) Dynamic response curve of  $\text{Fe}_3\text{O}_4$  nanoparticle-based gas sensor representing the response and recovery time.

The most important feature of a good sensor for application purpose is to have the ability to discriminate the target gas molecule from the interference molecules with higher sensing response. To check the selectivity of our prepared sensor towards acetone, we have tested the sensing response towards different target gases like methanol, formaldehyde, CO, ethanol, nitrogen, acetone etc. at 10 ppm of concentration level at optimum operating temperature. The selectivity co-efficient was calculated from the Figure 3.3.11 by using the equation  $\beta = S_{\text{acetone}}/S_{\text{gas}}$  where  $S_{\text{acetone}}$  and  $S_{\text{gas}}$  are the response of the sensor towards acetone and any other gas of 10ppm concentration. The selectivity co-efficient ( $\beta$ ) for  $\gamma\text{-Fe}_2\text{O}_3$  based sensor is varied like  $\beta_{\text{Methanol}} (6.5) > \beta_{\text{formaldehyde}} (5.2) > \beta_{\text{CO}} (4.3) > \beta_{\text{Ethanol}} (3.9) > \beta_{\text{Nitrogen}} (3.1)$  and for  $\text{Fe}_3\text{O}_4$  based gas sensor is like  $\beta_{\text{Methanol}} (5.9) > \beta_{\text{formaldehyde}} (4.6) > \beta_{\text{CO}} (4) > \beta_{\text{Ethanol}} (3.4) > \beta_{\text{Nitrogen}} (2.9)$ . It is clear from Figure 3.3.11 below and the selectivity co-efficient data that both the fabricated sensors are more sensitive for acetone gas sensing compared to other target gases.

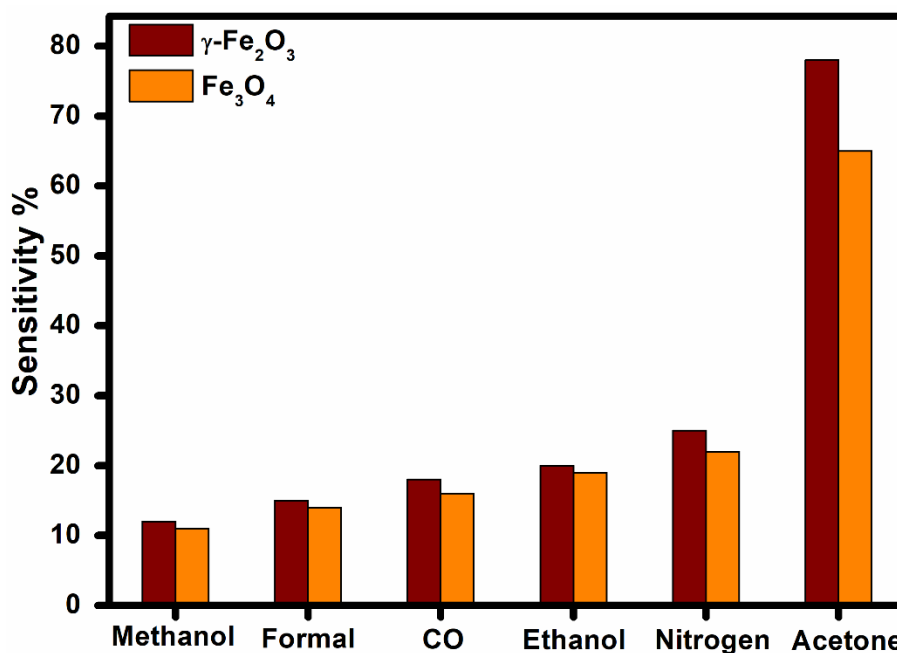
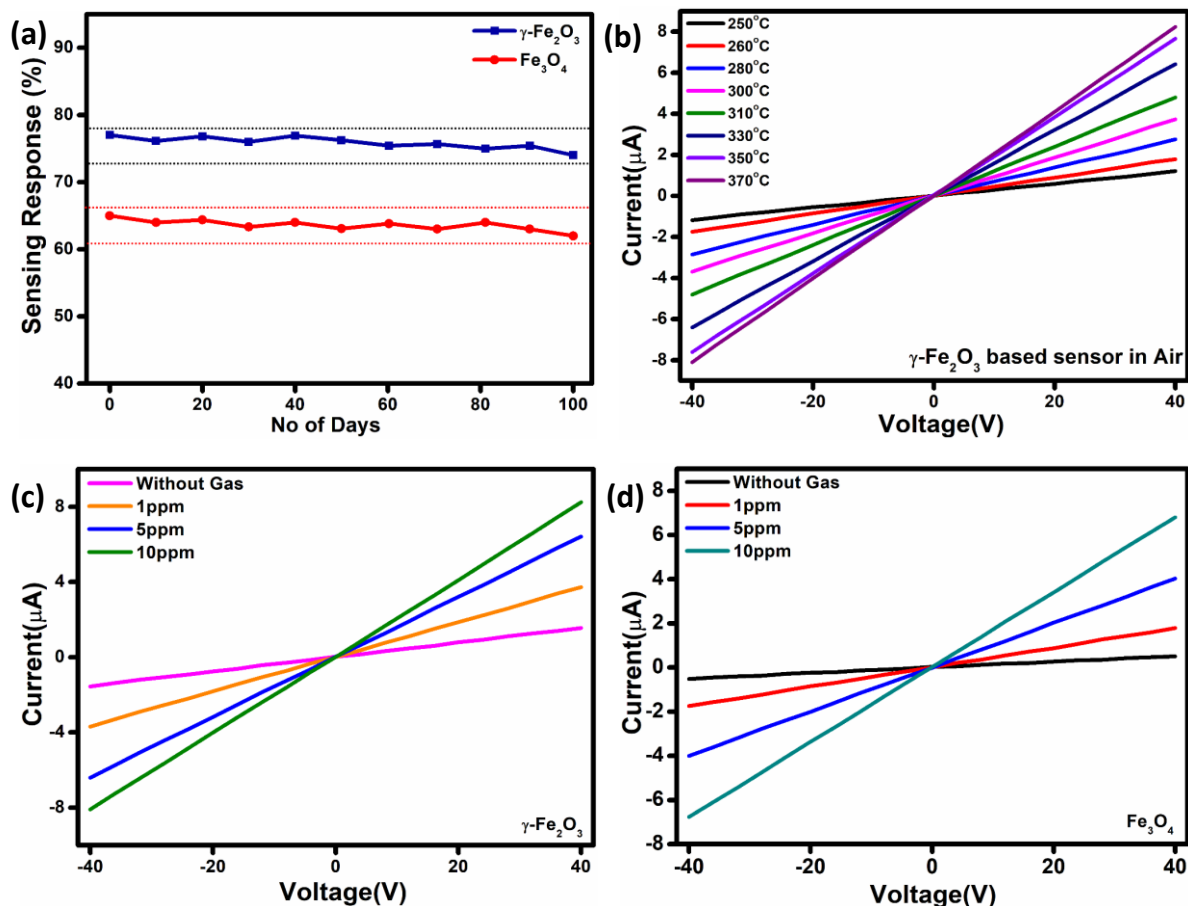


Figure 3.3.11: Selectivity response bar diagram of  $\gamma\text{-Fe}_2\text{O}_3$  and  $\text{Fe}_3\text{O}_4$  based sensor.

Besides higher sensing response and fast response-recovery time, the stability of response is an important characteristic for establishing a good sensing material. A long-term stability of both  $\gamma\text{-Fe}_2\text{O}_3$  and  $\text{Fe}_3\text{O}_4$  based sensor was measured towards 10ppm acetone within 100 days



shown in Figure 3.3.12a. The response result signifies that the sensitivity of the synthesized material-based gas sensor suggested near about 4% decrease in response which can indicate the long-term stability of our sensor. The current-voltage (*I-V*) characteristics curves measured at the bias voltage ranges increased from -42V to +42V at different operating temperature from 250°C to 370°C shown in Figure 3.3.12b. For  $\gamma\text{-Fe}_2\text{O}_3$  based sensor showed the linearity behaviour of all the current with increasing the bias voltage in presence of air. This linear behaviour of *I-V* characteristics of iron oxides-based gas sensor reveals a good ohmic contact between the iron oxide-based material layer and Au electrodes. It is clear from Figure 3.3.12b that the conductivity of  $\gamma\text{-Fe}_2\text{O}_3$  nanoparticle is increased with increasing operating temperature which proves the standard conduction nature of a semiconductor. The comparison study of *I-V* characteristic in presence of air and acetone (towards different concentration of acetone 10, 5 and 1ppm) environment is represented in Figure 3.3.12c and d of  $\gamma\text{-Fe}_2\text{O}_3$  and  $\text{Fe}_3\text{O}_4$  nanoparticles-based sensor respectively.



**Figure 3.3.12:** (a) Sensing response stability checking of  $\gamma\text{-Fe}_2\text{O}_3$  and  $\text{Fe}_3\text{O}_4$  based sensor (b) I-V characteristics of  $\gamma\text{-Fe}_2\text{O}_3$  sensor at different operating temperature in air (c) & (d) Comparison study of I-V characteristics in presence of air and acetone (10, 5 and 1ppm) of  $\gamma\text{-Fe}_2\text{O}_3$  and  $\text{Fe}_3\text{O}_4$  coated gas sensor respectively.

To get insight into the coating surface topography, the distribution of the sintered coated particles on the surface and the pores, FESEM-EDAX study of the coated sensor was done which is presented in Figure 3.3.13. It is clear from EDAX (qualitative) that the sensor unit is coated with purely  $\gamma\text{-Fe}_2\text{O}_3$  material-based powder. The non-porous nature of the surface is evident from the figure but there is very little number of cracks present on the surface that also help to increase the overall effective surface area taking part in the gas sensing activity. The peaks of Al arise from the cylindrical substrate material over which the coating was done.

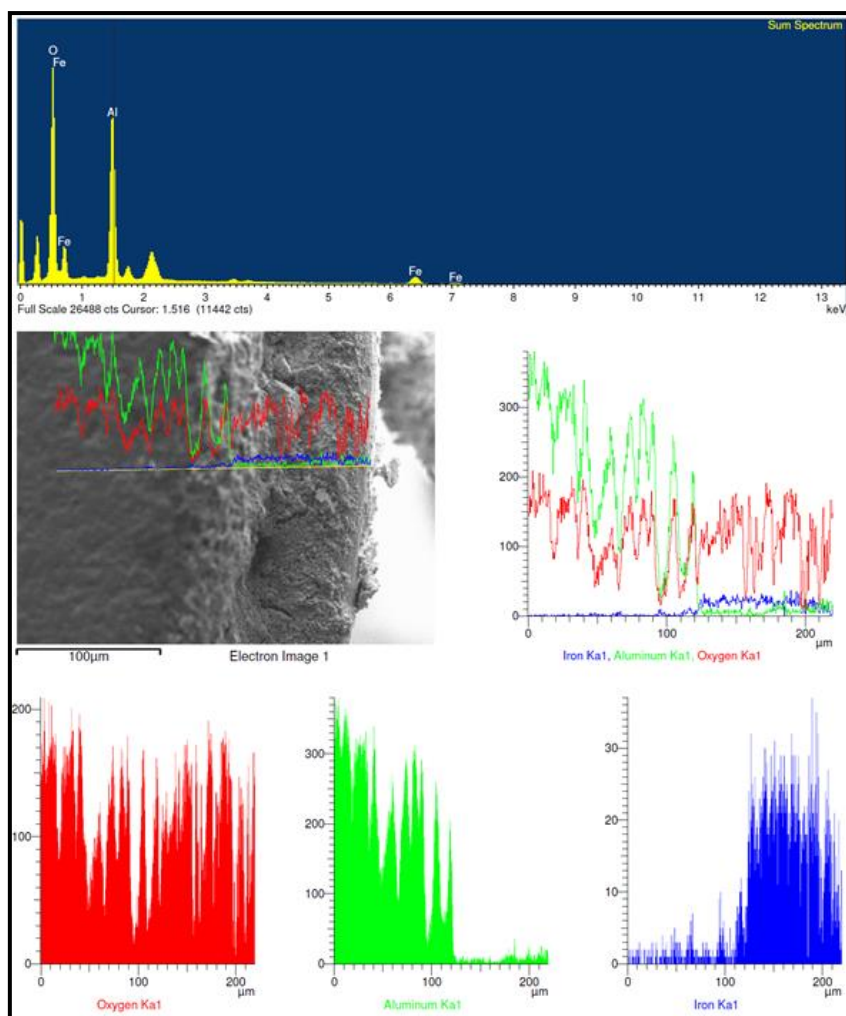


**Figure 3.3.13:** EDAX (qualitative) of  $\gamma\text{-Fe}_2\text{O}_3$  coated sensor surface and FESEM image of sensor device with elemental colour mapping.

### 3.3.2.5. Gas sensing mechanism:

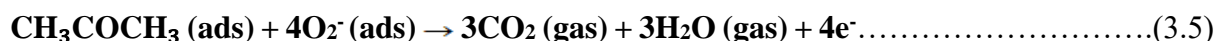
Iron oxide is known as n-type metal oxide semiconductor. The gas sensing mechanism and sensing response of semiconductor metal oxide based gas sensor is mainly depend on the resistance variation which is based on the adsorption-desorption techniques between oxygen molecules present in air and target gas molecules. When the sensors are exposed in air, large amount of oxygen molecules in air contacts with iron oxide nanoparticles and trap the electrons from the conduction band of the material and ionized into adsorbed oxygen species. In this adsorption process the electron concentration on the surface of the material is decreased which increases the resistance of the sensor in air. Due to this process, an electron depletion layer will

be formed resulting in a reduction in conductivity due to the loss of electrons on the surface of the sensor material [51,52].



When the iron oxide-based sensor is exposed towards acetone which is a reducing gas, the target gas molecules react with adsorbed oxygen species which was produced on the surface of the sensor material and release the free electrons back to the conduction band of  $\gamma\text{-Fe}_2\text{O}_3$  and  $\text{Fe}_3\text{O}_4$  materials. As mentioned above due to the electron transfer process and related mechanisms, the electrical resistance of the sensing material decreases. Thus, from the dynamic response curve the sensitivity can be calculated with the change of resistance [53,54].

Overall reaction that is expected to occur on the sensor surface could be:



### **3.3.2.6. Electrical Impedance Spectroscopy (EIS) Measurements:**

The impedance of a semiconducting metal oxide is highly influenced by the adsorbed oxygen species in presence of oxidizing and reducing gas. It is necessary to understand the bulk and grain boundary transport properties to optimize the gas sensing behaviour of the sensor material. The conduction process, electrical properties and the mechanism of interaction between the gas molecules and the adsorbed oxygen species have been further analyzed by AC impedance spectroscopic by varying the frequency. Most of the previous studies on iron oxide-based sensor have been on dc measurements, here we have also characterized the sensor properties towards different target gas based on impedance study. In this thesis work, the change of complex impedance of the iron oxide was investigated in presence of air and acetone at different operating temperature. The frequency dependent complex impedance of iron oxide

is described by the  $Z'$  and  $Z''$  which are calculated from the mod value of  $Z$  and phase angle  $\theta$  by using the following equation.

$$Z' = |Z| \cos\theta \dots \dots \dots (3.6)$$

$$Z'' = |Z| \sin\theta \dots \dots \dots (3.7)$$

The nyquist diagram from AC impedance spectroscopic measurement for  $\gamma\text{-Fe}_2\text{O}_3$  and  $\text{Fe}_3\text{O}_4$  based sensor is shown in Figure 3.3.14 (a & b) and (c & d) in presence of air and acetone, respectively at different operating temperature represents a smooth semi-circle nature.

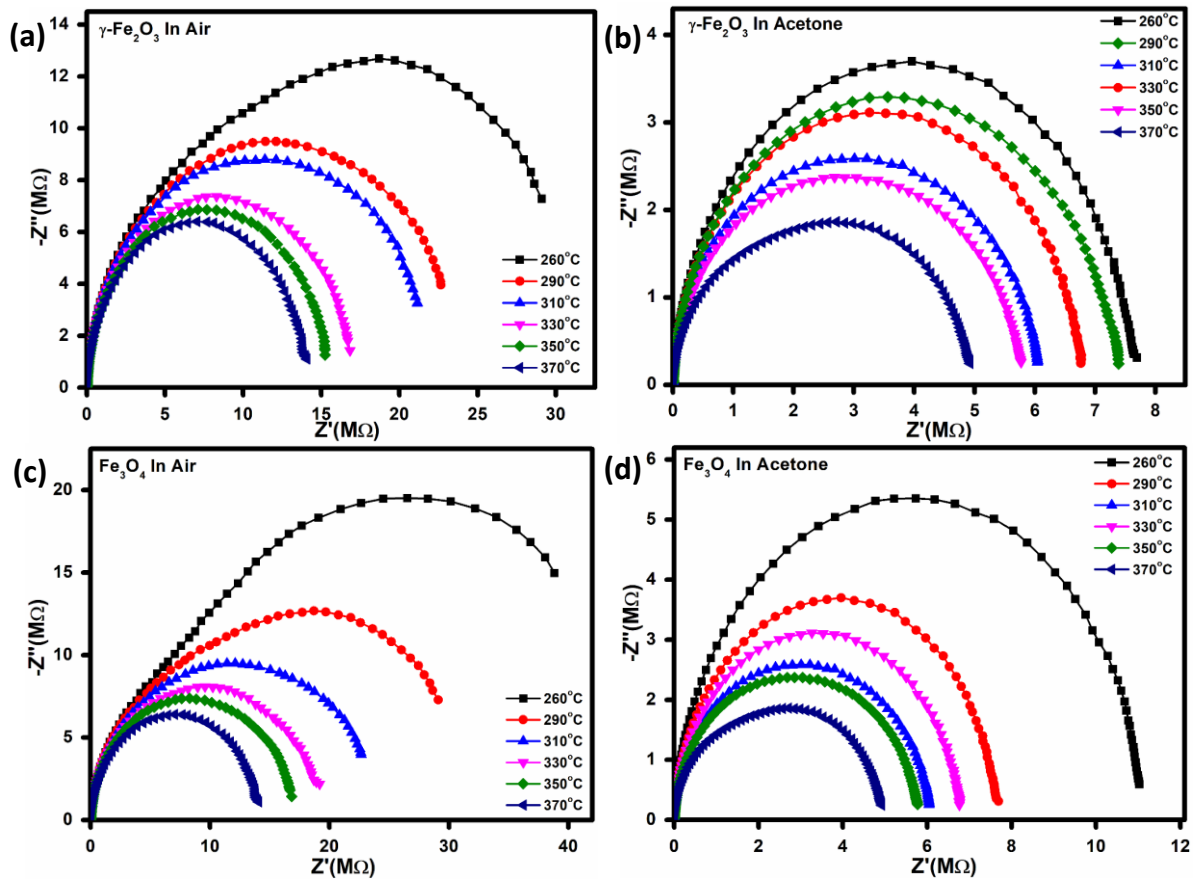


**Figure 3.3.14:** Nyquist diagram of  $\gamma\text{-Fe}_2\text{O}_3$  and  $\text{Fe}_3\text{O}_4$  based sensor at different operating temperature from 260°C to 370°C in presence of (a) air and (b) acetone.

Figure 3.3.15a represents the variation in Nyquist diagram of  $\gamma\text{-Fe}_2\text{O}_3$  sensor in presence of air and acetone. After injecting the target gas the grain resistance ( $R_g$ ) of  $\gamma\text{-Fe}_2\text{O}_3$  based sensor decreases and the capacitance ( $C_g$ ) increases. The adsorbed oxygen species trap the electron

from the grains of  $\gamma\text{-Fe}_2\text{O}_3$  and create a depletion region and decrease the electron transport and as a result the grain resistance ( $R_g$ ) will be high. After interacting with acetone, the depletion layer has been reduced by removing the electron from the adsorbed oxygen ions and the grain resistance  $R_g$  will be decreased. The capacitance will be increased after injecting the gas due to reduction of the depletion region in  $\gamma\text{-Fe}_2\text{O}_3$  film. As a result, when the space charge capacitance will increase then at grain boundaries of  $\gamma\text{-Fe}_2\text{O}_3$ , the space charge region will decrease and electron transport will be high.

Here  $n$  is the electron concentration and  $L_D$  is the effective Debye length.

$$L_D = \sqrt{\frac{\epsilon_0 \epsilon_r K T}{q^2 n}} \approx n^{-1/2} \dots \dots \dots (3.8)$$

$$C_g = \frac{\epsilon_0 \epsilon_r}{L_D} \approx n^{1/2} \dots \dots \dots (3.9)$$

By using Z view software (version 2.70), the measured impedance data has been fitted to a R-C parallel circuit for  $\gamma\text{-Fe}_2\text{O}_3$  and  $\text{Fe}_3\text{O}_4$  based sensor in presence of air and 10 ppm of acetone and shown in Figure 3.3.15 (a&b) suggests the effect of grain resistance to control the adsorption mechanism.

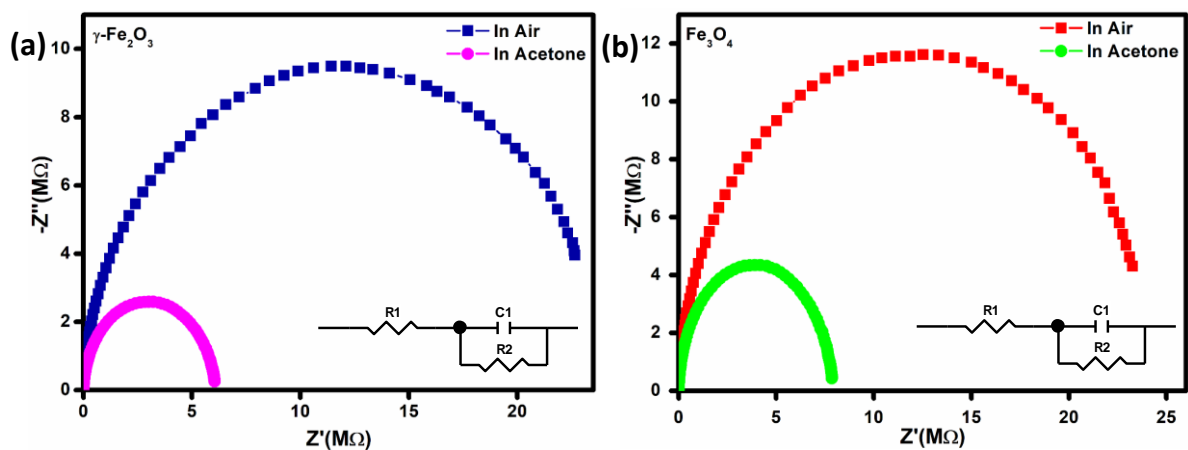


**Figure 3.3.15:** Variation in Nyquist diagram and Equivalent R-C parallel circuit of (a)  $\gamma\text{-Fe}_2\text{O}_3$  (b)  $\text{Fe}_3\text{O}_4$  based sensor in presence of air and acetone.

In this work, sonochemically synthesized  $\gamma\text{-Fe}_2\text{O}_3$  and  $\text{Fe}_3\text{O}_4$  nanoparticles have been used as sensing material for fabricating tubular thick film solid state gas sensors for acetone sensing.

The results demonstrated the enhanced acetone sensing of  $\gamma$ -Fe<sub>2</sub>O<sub>3</sub> based sensor towards 10ppm acetone at 310°C. The fabricated sensor exhibited around 76% response 10 ppm acetone towards with better stability compared to Fe<sub>3</sub>O<sub>4</sub> based sensor which exhibited 65% response only.

### 3.3.3. Nanoparticles and Nanofibers of $\alpha$ -Fe<sub>2</sub>O<sub>3</sub>

#### 3.3.3.1. Structural and Morphological Analysis

In order to have a comparison on properties of various shapes of iron oxide,  $\alpha$ -Fe<sub>2</sub>O<sub>3</sub> nanoparticles and fibers have also been made and properties have been evaluated. To investigate the crystallinity and phase purity, the synthesized sample was characterized by using XRD technique as shown in Figure 3.3.16a. According to the JCPDS card no. 33-0664, the XRD pattern for  $\alpha$ -Fe<sub>2</sub>O<sub>3</sub> confirms the formation of phase pure sample with highly crystalline nature of the diffraction pattern. Raman spectroscopic study has been carried out for the electrospun fiber and nanoparticle samples to monitor and confirmation of further phase purity. The raman spectrum shown in Figure 3.3.16b represents the well distribution of crystalline phase formation followed by different transversal optical modes and vibration mode of Fe-O bonds positioned at 216, 283, 394, 684 and 1304 cm<sup>-1</sup> peak position.

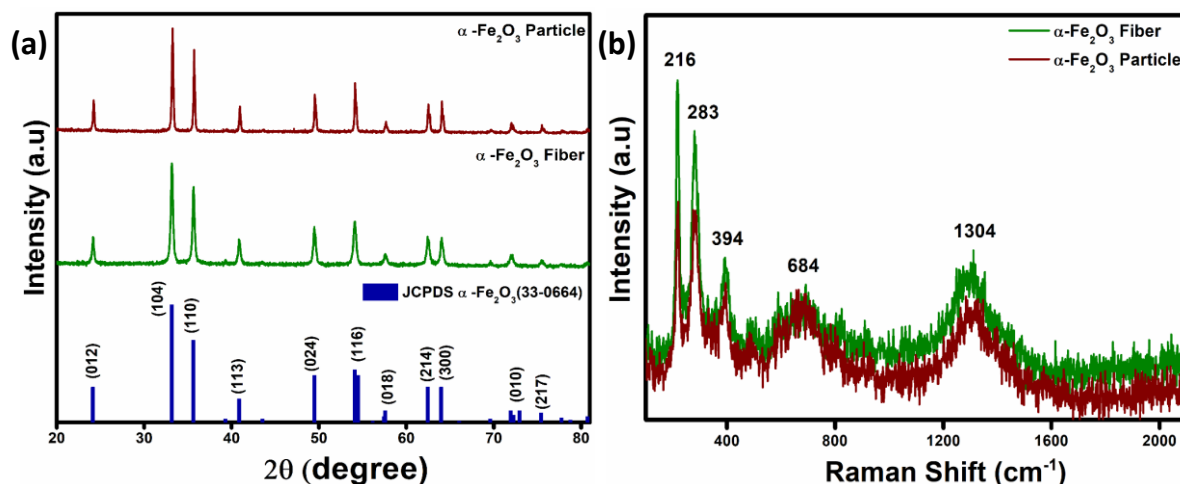


**Figure 3.3.16:** (a) XRD pattern and difference plot (b) Raman spectrum of synthesized  $\alpha$ -Fe<sub>2</sub>O<sub>3</sub> fiber and nanoparticle powders.

Figure 3.3.17 (a&b) and (d&e) represent TEM bright field images of the synthesized  $\alpha$ -Fe<sub>2</sub>O<sub>3</sub> fiber and nanoparticle at different magnifications. As it is clear from the Figure that fiber-based morphology has been formed for the  $\alpha$ -Fe<sub>2</sub>O<sub>3</sub> phase with a range of diameters of 220-250 nm and for  $\alpha$ -Fe<sub>2</sub>O<sub>3</sub> nanoparticle the size has been calculated from the bright field image is around 95-100nm in range. The HR-TEM image in Figure 3.3.1c and f shows good crystallinity of the synthesized fiber and nanoparticle based sample as evident from the interlayer spacing of the most intense (104) peak as 0.28nm.

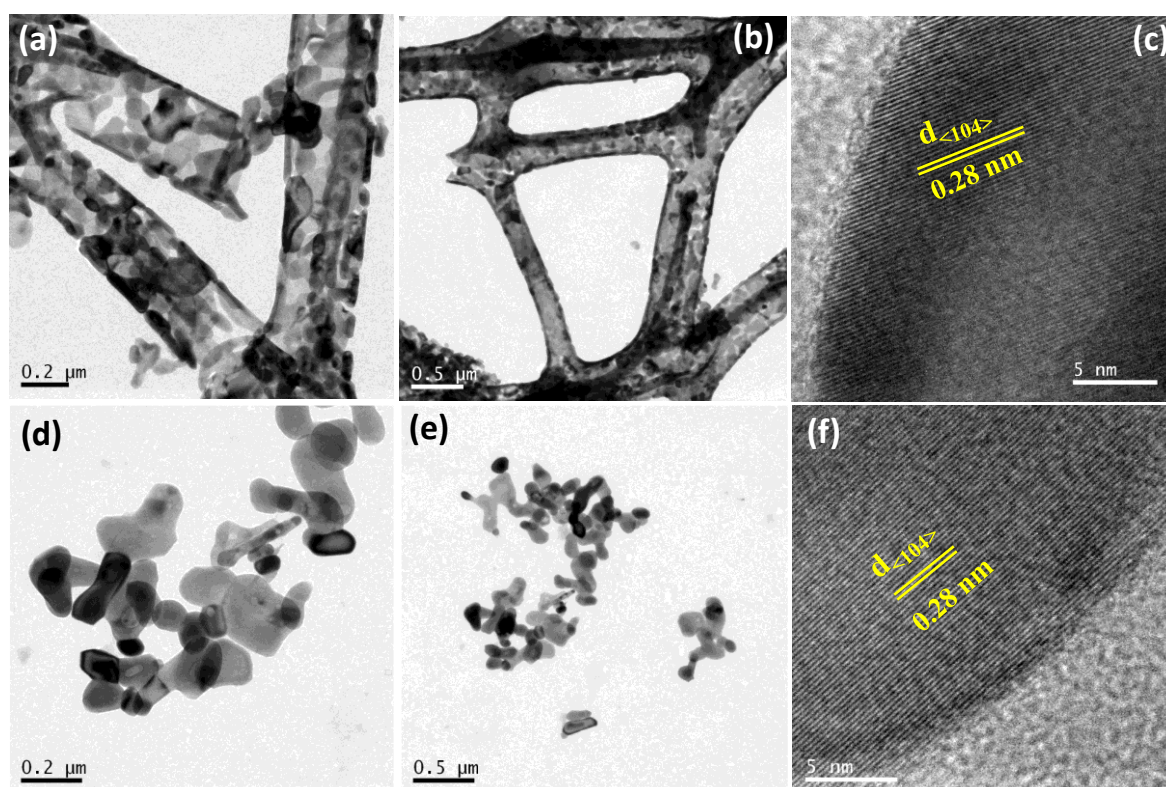


**Figure 3.3.17:** (a)-(c) Transmission electron micrographs bright field image and (d) HRTEM image of  $\alpha$ -Fe<sub>2</sub>O<sub>3</sub>.

A comparatively higher surface area of  $\sim 86.2\text{m}^2/\text{g}$  was exhibited by BET multipoint isotherm of  $\alpha$ -Fe<sub>2</sub>O<sub>3</sub> fiber compared with nanoparticle with surface area of  $30.2\text{m}^2/\text{g}$  as shown in Figure 3.3.18a. As the specific surface area is a beneficial parameter for absorption and desorption of the gas is expected to be more required for achieving higher sensing response with good stability. The saturation magnetization value calculated from the magnetization (M) vs.



magnetic field (H) plot is 5.2 and 5.6 emu/g for  $\alpha$ -Fe<sub>2</sub>O<sub>3</sub> fiber and nanoparticle based sample as shown in Figure 3.3.18b.

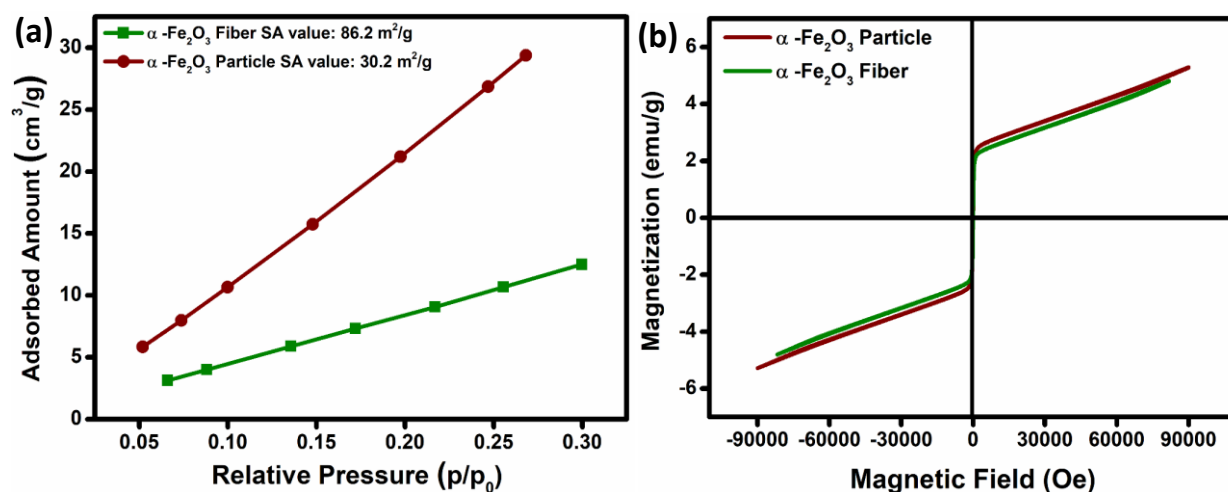


Figure 3.3.18: (a) BET surface area isotherm and (b) Magnetic plot of  $\alpha$ -Fe<sub>2</sub>O<sub>3</sub> based sample.

### 3.3.3.2. Sensing Measurements:

The base resistance of the  $\alpha$ -Fe<sub>2</sub>O<sub>3</sub> fiber and nanoparticle-based sensor was monitored at different temperature for understanding the stabilization of the fabricated sensor performance. The sensing response of  $\alpha$ -Fe<sub>2</sub>O<sub>3</sub> fiber and nanoparticle-based sensor is plotted in Figure 3.3.19a towards different concentration of acetone in a wide range with 15sec of exposure time and the sensors have the ability to sense upto 0.5ppm acetone with good stability. This performance is acceptable and highly demanding in the application field of breath analysis. The sensitivity for fiber and nanoparticle-based sensor has been calculated from the response curve is about 94.5%, 91.4%, 85.5%, 80.2%, 70.1%, 64.2% and 62%, 58%, 50%, 45%, 40%, 32% towards 10, 5, 3, 2, 1 and 0.5ppm at optimum operating temperature of 150°C and 300°C, respectively and it is clearly noticeable that the fiber like structure-based sensor has higher sensitivity with comparatively lower operating temperature towards very lower concentration of acetone. After that, the change in sensitivity of fiber-based sensor was measured throughout

a wide range of operating temperature ranging from 100°C to 350°C towards different concentration of acetone.

It is clear from the plot shown in Figure 3.3.19b that the fiber-based sensor is more sensitive at 150°C operating temperature for all the concentration of acetone as this temperature is considered as optimum operating temperature for further sensing measurements. The response and recovery time of fiber and nanoparticle based sensor is monitored as a function of operating temperature shown in Figure 3.3.19c and it is clear from the plot that fiber based sensor exhibits fast response and recovery time 8sec and 12sec respectively at 150°C operating temperature which is useful for further application-based study. It is very much important to focus on the selectivity activity of both fabricated sensors to compare its performance with the sensing result obtained from the previous studied nanoparticle-based sensor.

The selectivity co-efficient ( $\beta$ ) for fiber-based sensor is varied like  $\beta_{\text{Methanol}}$  (9.4) >  $\beta_{\text{formaldehyde}}$  (7.8) >  $\beta_{\text{CO}}$  (6.3) >  $\beta_{\text{Ethanol}}$  (5.5) >  $\beta_{\text{Nitrogen}}$  (4.7) and for nanoparticle-based sensor is like  $\beta_{\text{Methanol}}$  (7.7) >  $\beta_{\text{formaldehyde}}$  (6.2) >  $\beta_{\text{CO}}$  (5.2) >  $\beta_{\text{Ethanol}}$  (4.1) >  $\beta_{\text{Nitrogen}}$  (3.4) respectively, it is confirmed from Figure 3.3.19d that the fiber-based sensor is higher sensitive for acetone gas compared to other target gases.

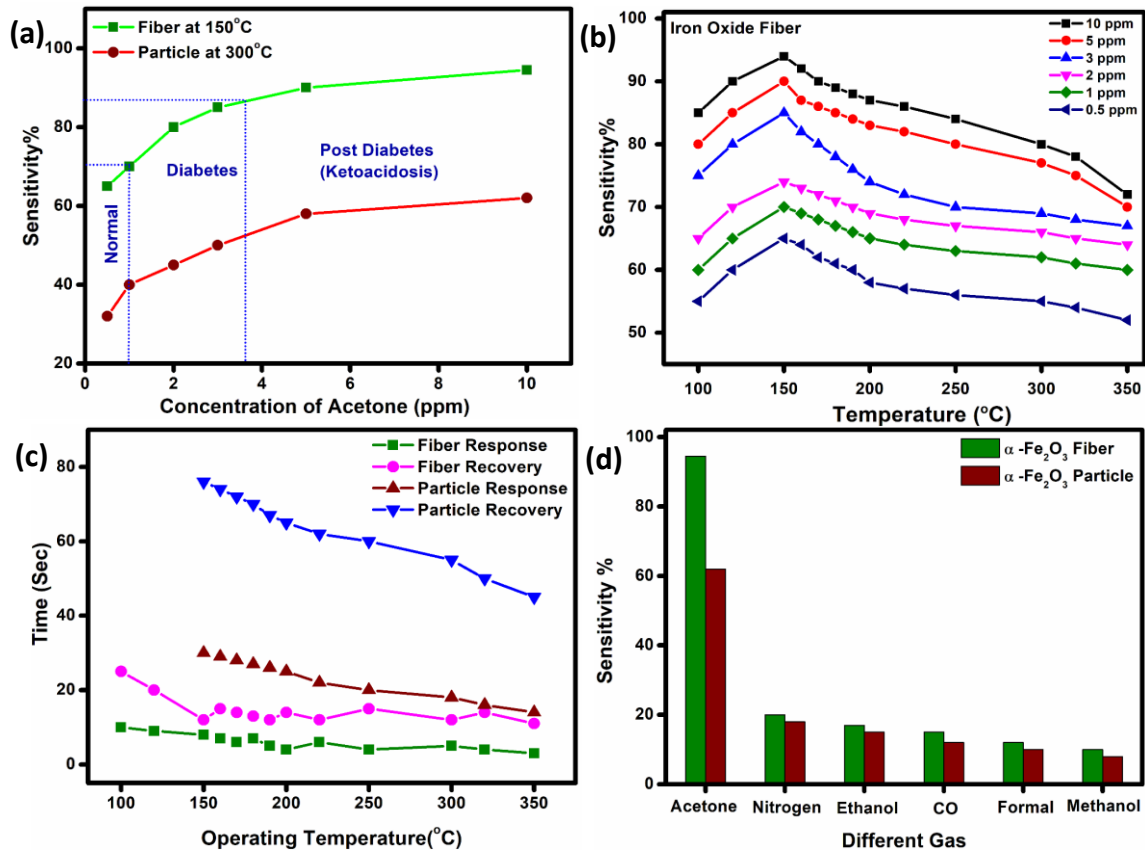


**Figure 3.3.19:** (a) Sensitivity plot of  $\alpha\text{-Fe}_2\text{O}_3$  fiber and nanoparticle-based sensor towards different concentration of gases (0.5, 1, 2, 3, 5 and 10ppm) (b) Response vs operating temperature curve towards different concentration of acetone for fiber-based sensor (c) Variation of response and recovery time with operating temperature (d) Selectivity nature of  $\alpha\text{-Fe}_2\text{O}_3$  fiber and nanoparticle-based sensor towards acetone compared with other tested gases of 10ppm concentration each.

The electrical properties have been further analyzed by AC impedance spectroscopic of  $\alpha\text{-Fe}_2\text{O}_3$  fiber and nanoparticle-based sensor as a function of frequency. The recorded impedance data has been plotted Figure 3.3.20a and c for both fiber and nanoparticle based sensor in presence of acetone with varying the operating temperature. The change in impedance for fiber and nanoparticle-based sensor has been implemented in Figure 3.3.20b and d respectively in presence of air and acetone to understand the influence of electrical properties of the sensor surface at the time of reaction after injecting acetone.

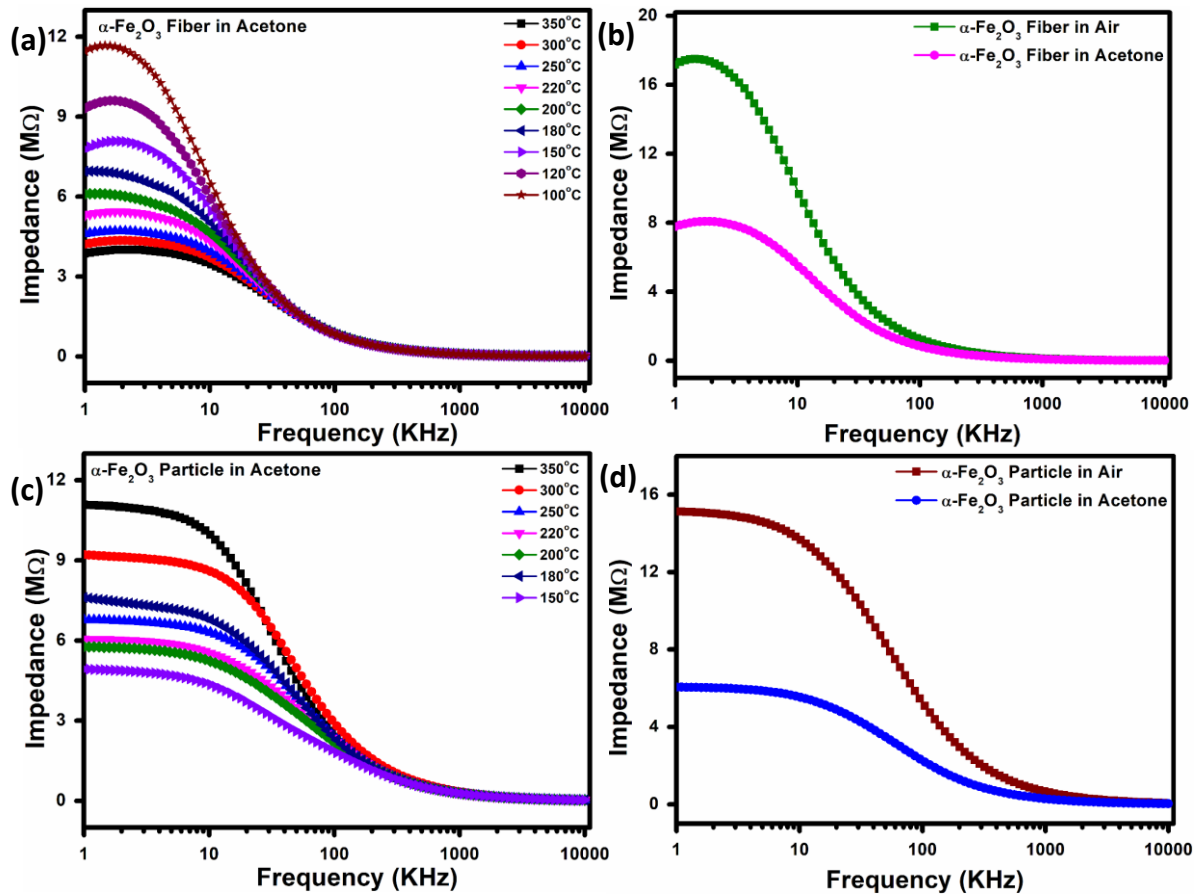


**Figure 3.3.20:** (a) & (c) Impedance diagram in presence of acetone varying the operating temperature in presence of acetone (b) & (d) Impedance difference in presence of air and acetone of  $\alpha\text{-Fe}_2\text{O}_3$  fiber and nanoparticle-based sensor, respectively.

Figure 3.3.21a and c shows the nyquist diagram from AC impedance spectroscopic measurement in presence of acetone at wide range of operating temperature and Figure 3.3.20b and d represents the change in nyquist in air and after injecting acetone for  $\alpha\text{-Fe}_2\text{O}_3$  fiber and nanoparticle-based sensor respectively. As both the nyquist plot have only one semicircle in nature for the synthesized fiber and nanoparticle based sensor, which signifies that in this system the gas sensing property depends on the grain size only and there is no grain boundary effect on the sensor performance.

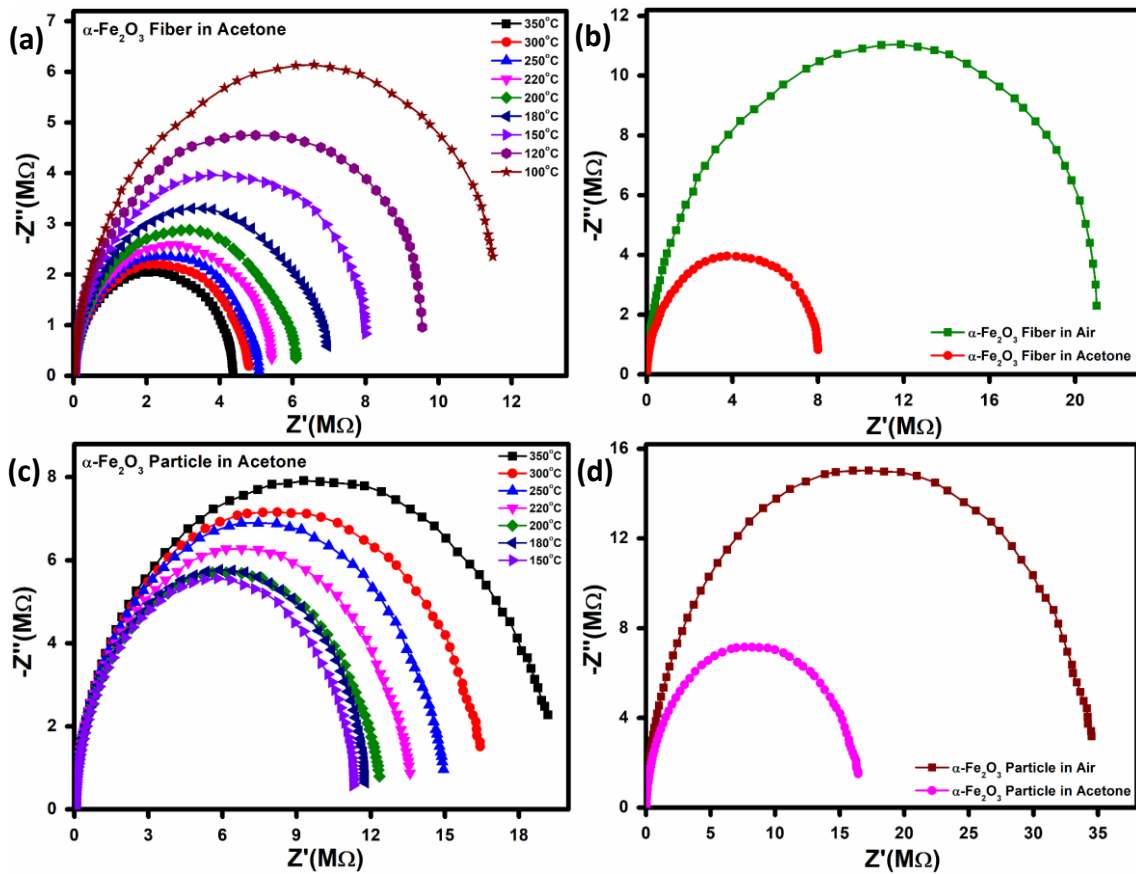


**Figure 3.3.21:** (a) Nyquist diagram at different operating temperature in a wide range in presence of acetone (b) Nyquist plot difference in presence of air and acetone for  $\alpha\text{-Fe}_2\text{O}_3$  fiber and nanoparticle-based sensor.

In conclusion the obtained result from the phase and size depended iron oxide-based work has been summarized in Table 3.3.3 below.

Table 3.3.3: Sensing Results obtained from the above work					
Sensing Materials	Surface Area (m <sup>2</sup> /g)	Operating Temperature (°C)	Response and recovery Time (sec)	Concentration of acetone (ppm)	Sensitivity %
$\gamma\text{-Fe}_2\text{O}_3$ Nanoparticles	56	310	9/14	10	76
				0.5	36
$\text{Fe}_3\text{O}_4$ Nanoparticles	38	310	10/40	10	65
				0.5	30
$\alpha\text{-Fe}_2\text{O}_3$ Nanoparticles	30.2	300	18/50	10	62
				0.5	32
$\alpha\text{-Fe}_2\text{O}_3$ Fiber	86.2	150	8/12	10	94.5
				0.5	64.2

#### **3.3.4. Conclusion:**

In this part of the work, various oxides of iron such as  $\gamma$ -Fe<sub>2</sub>O<sub>3</sub>, and Fe<sub>3</sub>O<sub>4</sub> have been prepared by sonochemical process and  $\alpha$ -Fe<sub>2</sub>O<sub>3</sub> fiber and nanoparticle synthesized by electrospinning and sonochemically synthesis method and used these powders as thick film solid state gas sensing materials to understand the acetone sensing performance. Among all the nanoparticles,  $\gamma$ -Fe<sub>2</sub>O<sub>3</sub> exhibited better response compared to Fe<sub>3</sub>O<sub>4</sub> and  $\alpha$ -Fe<sub>2</sub>O<sub>3</sub> nanoparticle-based sensor. Interestingly,  $\alpha$ -Fe<sub>2</sub>O<sub>3</sub> fiber-based sensor was found to be very effective for sensing in a wide range of concentration of acetone from high concentration corresponding to a diabetic stage to concentration below 1ppm corresponding to normal condition. The enhanced performance of  $\alpha$ -Fe<sub>2</sub>O<sub>3</sub> fiber-based sensor could be due to its higher surface area and it can easily increase the electron transport by improving the effect of electron depletion region through adsorption and desorption process. The higher sensitivity, stability and lower concentration detection level of  $\alpha$ -Fe<sub>2</sub>O<sub>3</sub> fiber-based sensor could be a good platform for developing new generation non-invasive, rapid and simple diagnosis device for breath analyzing.

### **3.4. Fiber and Particle Based WO<sub>3</sub> for Acetone Sensing**

#### **3.4.1. Introduction**

Tungsten trioxide (WO<sub>3</sub>) is a widely studied n-type semiconducting oxide with band gap ranging from 2.4 to 3.2eV with interesting visible light harvesting properties below 500nm, which makes it a very interesting candidate for photocatalytic and electrochromic applications. In search of new oxides for next-generation gas sensing materials with higher response, lower operating temperature and faster response-recovery time, tungsten oxide has been established as a promising material compared to other conventional materials to develop sensor devices for various flammable and toxic gases. Interestingly, response of WO<sub>3</sub> towards volatile organic vapours like acetone has drawn renewed attention in the area of developing sensors for breath analysis [55-59].

Among the existing oxide materials exhibiting acetone sensing, WO<sub>3</sub> is one system exhibiting polymorphism which led to intense R&D in identifying the right structure for acetone sensing. As reported earlier by many investigators, WO<sub>3</sub> exists in five different crystallographic phases at different temperatures such as a low temperature monoclinic  $\epsilon$ -WO<sub>3</sub>, a triclinic WO<sub>3</sub>, a room temperature monoclinic  $\gamma$ -WO<sub>3</sub>, an orthorhombic WO<sub>3</sub> and a tetragonal WO<sub>3</sub> phases. Among these, the monoclinic phase has been reported to be the most stable phase at RT. There are interesting reports on the acetone sensing performance of few of the WO<sub>3</sub> polymorphs. S. Sun *et.al.* in 2019 reported an integrated acetone monitoring system for low power consumption with Graphene-Tungsten oxide nanocomposites exhibiting higher sensitivity and fast response time [60]. Systems offering acetone detection for breath analysis with Si doped WO<sub>3</sub> based sensor material with increasing thermal stability and selectivity has also been reported for the application of diabetic detection [61]. A possible sensing mechanism towards the sensing of acetone vapour was proposed in 2013 by Yidong Zhang *et.al.* using WO<sub>3</sub> microspheres synthesized via hydrothermal reaction [62]. Most of the reports on WO<sub>3</sub> sensors are based on

monoclinic  $\gamma$ -WO<sub>3</sub> phases. However, there are also reports highlighting the selective detection of acetone by the unstable  $\varepsilon$ -WO<sub>3</sub> and faceted hexagonal phases [63,64]. In addition, there are also reports on the effect of various morphologies, crystal orientation and grain effects on the acetone sensing characteristics of WO<sub>3</sub> [65-69]. The importance of this semiconducting material in fabricating acetone sensors for the non-invasive diagnosing of diabetes, has thrown critical issues in understanding the actual reasons behind the diverse and interesting acetone sensing behaviour of WO<sub>3</sub> nanomaterials. To find a solution for our quest to understand the effect of particle morphology, crystallographic modifications and impedance behavior to address the acetone sensing characteristics of WO<sub>3</sub>, we have synthesized WO<sub>3</sub> nanoparticles by hydrothermal technique and WO<sub>3</sub> with fiber-like morphology by electrospinning technique. Our major interest was to understand the above factors which basically are important in fabricating acetone sensors which can differentiate various concentrations of acetone at lower temperature than the commonly reported 350°C [70-72].

### **3.4.2. Results and discussions:**

The X-ray diffraction analysis was performed on synthesized WO<sub>3</sub> particles (WP) and fibers (WF) to understand the structure and crystal phase of the material after calcination at 500°C as shown in Figure 3.4.1a. The XRD peaks of both WP and WF are sharp and clear, which could be attributed to the high-quality crystalline WO<sub>3</sub> phase formed during the annealing process (500°C). All the diffraction peaks are indexed and well-matched with the JCPDS data card (No. 83-0950) for standard monoclinic crystal structure of WO<sub>3</sub>. The three most intense reflections in the  $2\theta$  range of 22°-26° could be indexed to the 002, 020 and 200 reflections of a monoclinic  $\gamma$ -WO<sub>3</sub> phase. The lattice parameters calculated from the respective XRD patterns were  $a = 7.290\text{\AA}$ ,  $b = 7.534\text{\AA}$  and  $c = 7.667\text{\AA}$  for WF samples, and  $a = 7.299\text{\AA}$ ,  $b = 7.524\text{\AA}$  and  $c = 7.673\text{\AA}$  for WP samples. It is also clear from the XRD patterns shown in Figure 3.4.1b that the (002) reflections for both samples are significantly stronger than the standard pattern



confirming a preferred orientation in the 002 direction. From equation (3.10) the relative texture coefficient of the crystal facet ( $TC_{002}$ ) has been calculated [73,74].

$$TC_{002} = \frac{I_{002}/I^0_{002}}{I_{002}/I^0_{002} + I_{200}/I^0_{200}} \dots\dots\dots (3.10)$$

Where,  $I_{002}$  and  $I_{200}$  are the intensities of the (002) and (200) diffraction facets, respectively and  $I^0_{002}$  and  $I^0_{200}$  are the corresponding intensities of the standard XRD patterns. Here, the relative texture coefficient of (002) diffraction peak has been calculated over (200) for both fiber and particle sample. The calculated texture coefficient values are 0.552 and 0.521 for WF and WP sample, respectively. It is clear from the magnified image of Figure 3.4.1b in the range of 20° to 30° and the texture coefficient value calculated that (002) plane is more exposed for  $WO_3$  fiber (WF) sample than particle (WP) and standard  $WO_3$  indicating a preferred growth of the fibers in (002) direction.

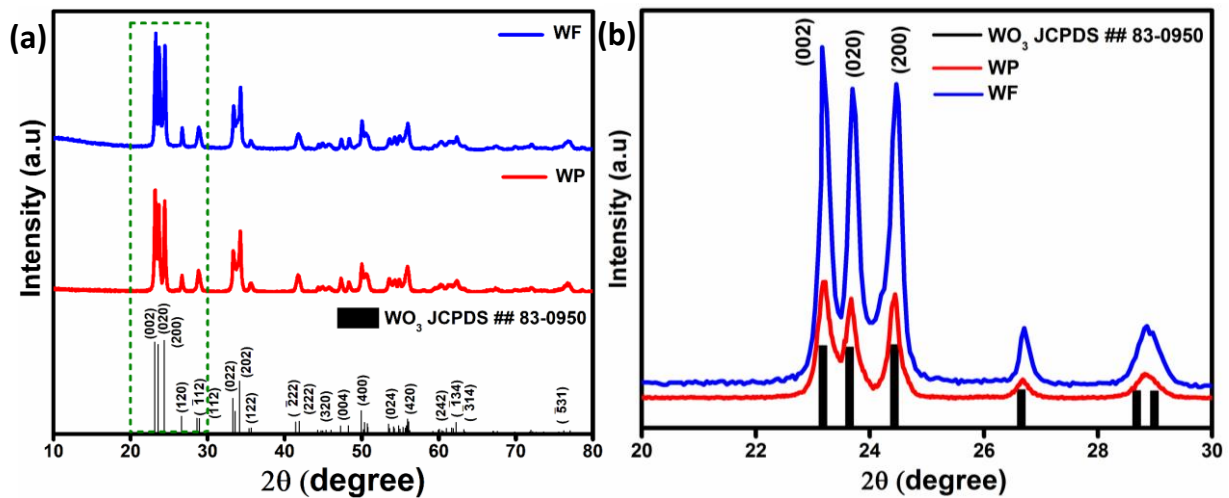


**Figure 3.4.1:** (a) X-ray diffraction pattern of WP and WF samples (b) Magnified image of the highlighted area showing the preferred orientation of 002 reflections.

For further confirming the phase formation, Raman spectroscopic study has been done for the WP and WF samples (Figure 3.4.2a). Figure 3.4.2a represents the W-O-W bending mode at  $272.43\text{cm}^{-1}$  and W-O-W stretching mode at  $718.41\text{cm}^{-1}$  and  $806.94\text{cm}^{-1}$  which further confirms the formation of monoclinic  $WO_3$ . The broad peak at  $760\text{cm}^{-1}$  is attributed to the W-O-W vibrational bond of  $WO_6$  octahedron in the crystal structure of  $WO_3$ . The peak at  $815.17\text{cm}^{-1}$

corresponds to W-O-W stretching vibration bond. The Fourier-transform infrared spectroscopy analysis of both the samples shown in Figure 3.4.2b confirms the complete removal of polymer from the fiber sample as the spectra shows only O-W-O and W-O-W modes [75].

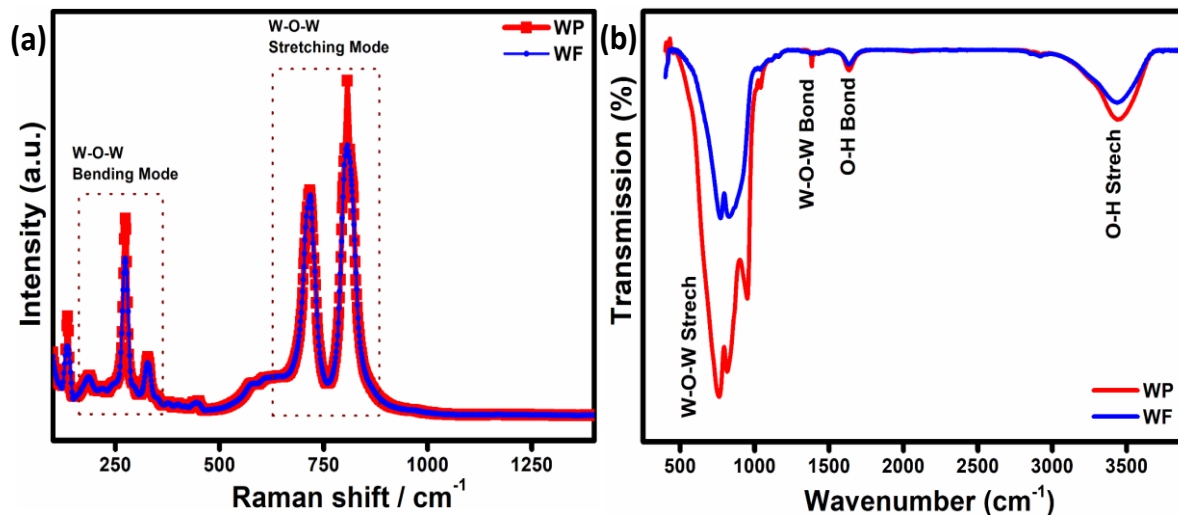
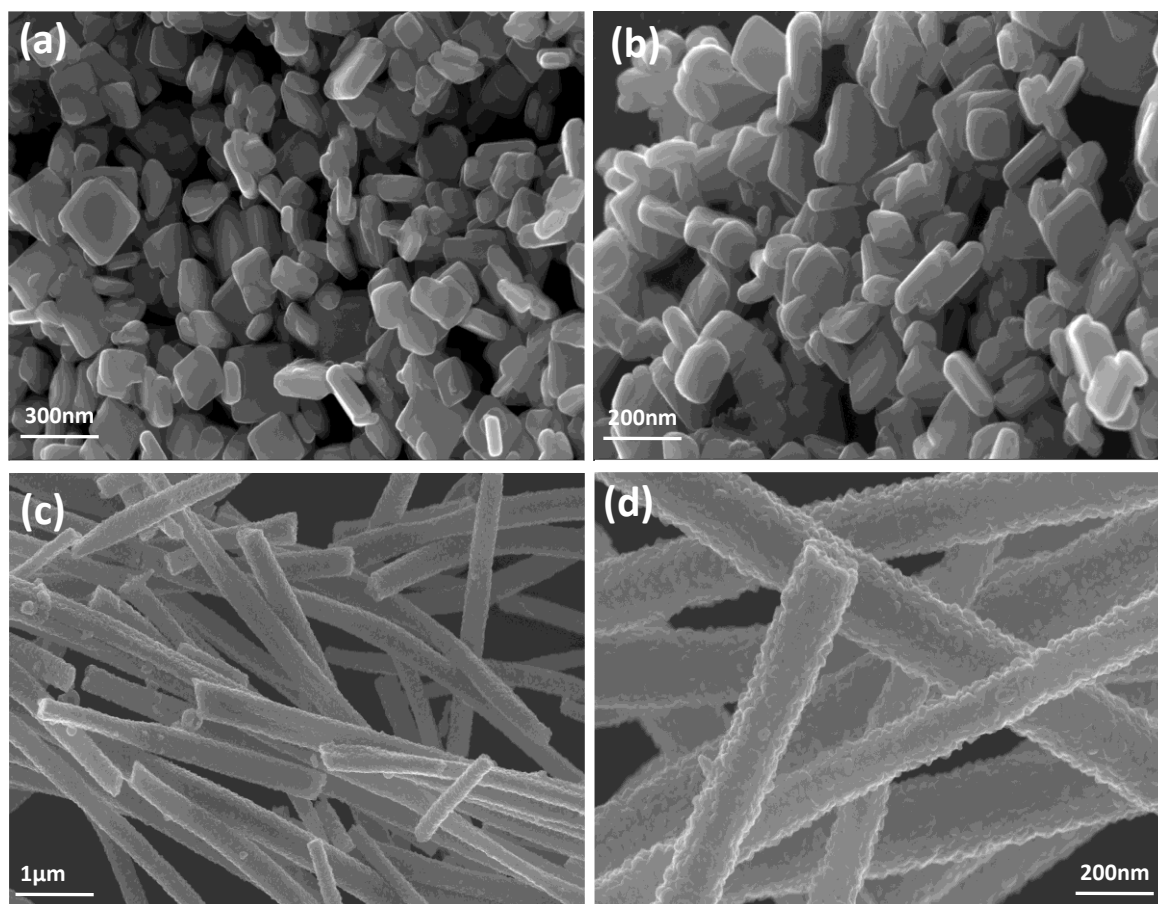


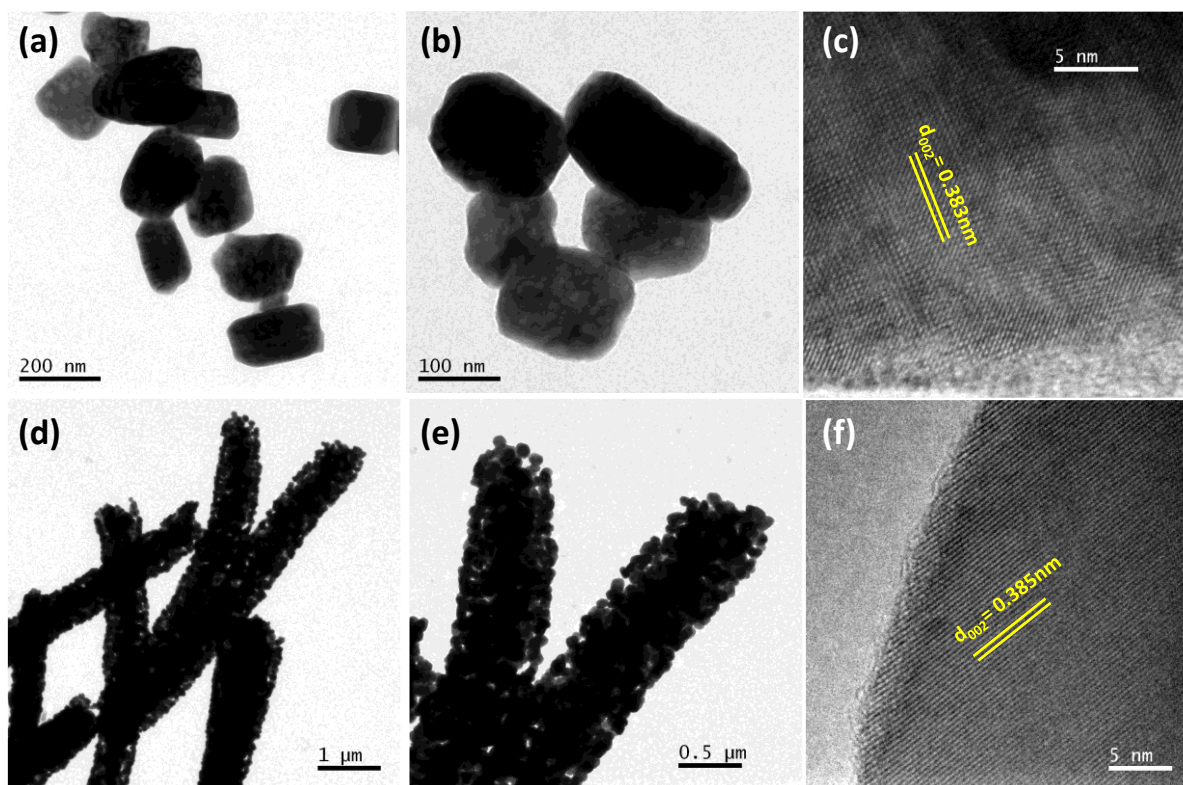
Figure 3.4.2: (a) Raman spectra and (b) FTIR spectra of WP and WF, respectively.

Figure 3.4.3 (a & b) and (c & d) represent the field emission scanning electron microscopic (FESEM) images of  $\text{WO}_3$  samples, having well developed granular particles and fiber morphologies, respectively. Single fiber having an overall length varying in the range of 1-2  $\mu\text{m}$  and an average diameter of 550nm is clearly visible in Figure 3.4.3c. In comparison, the particles are more homogeneous with granular disk-like structure with an average size of 200nm.



**Figure 3.4.3:** The FESEM images of calcined samples (a) & (b) WP and (c) & (d) WF, respectively.

The corresponding bright-field images are also depicted in Figure 3.4.4 (a & b) and Figure 3.4.4 (d & e) as obtained from the transmission electron microscopic observations. The clear disc like structures of well separated large  $\text{WO}_3$  grains is evident for particles whereas the fibers are formed of well interconnected smaller grains forming highly porous structure. The lattice structure of both WP and WF samples are distinguished in high-resolution transmission electron microscope (HRTEM) images which are shown in Figure 3.4.4 (c & f), respectively. Very clear two-dimensional ordered lattice structures shown in Figure 3.4.4 (c & f) indicates the single crystalline nature of the samples. From the HRTEM image, the interlayer spacing was calculated as 0.383nm and 0.385nm for WP and WF sample respectively, corresponding to the (002) crystal plane of the monoclinic  $\text{WO}_3$  structure.



**Figure 3.4.4:** TEM bright field images of WP (a) & (b) and WF (d) & (e) and Corresponding HRTEM images of WP (c) and WF (f), respectively.

BET specific surface area analysis of synthesized  $\text{WO}_3$  particle and fiber sample revealed a surface area of  $15.5\text{m}^2/\text{g}$  and  $85.6\text{m}^2/\text{g}$ , respectively, from the BET isotherm shown in Figure 3.4.5 (a & b), respectively. Surface area is a crucial parameter, which enables a material to be suitable for sensing performance. It is expected that the comparatively higher surface area of fiber-based sample has a tendency to attach more gas molecules than particle and show good sensing response under identical condition.

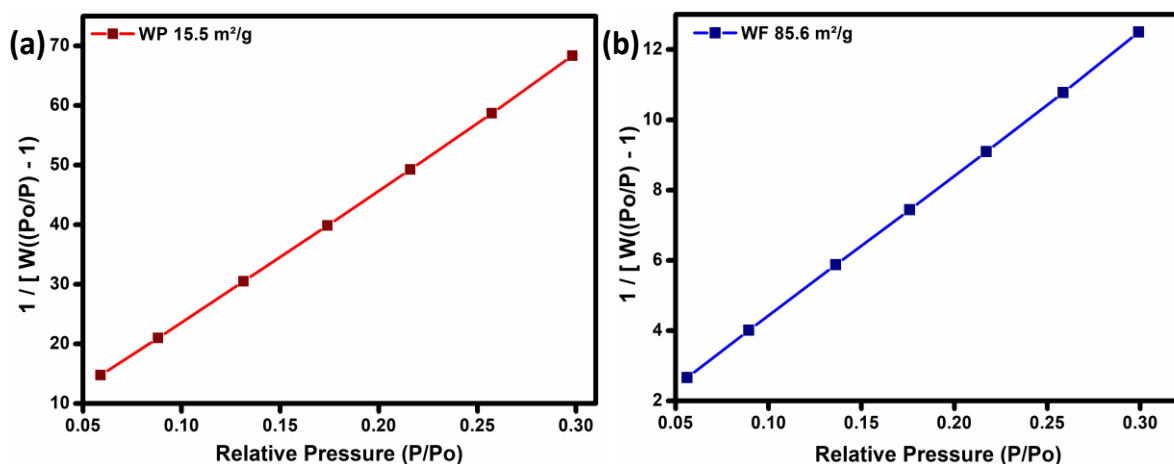


Figure 3.4.5: BET surface area plot of (a) WP and (b) WF, respectively.

### 3.4.3: Sensing Measurements Data

The fully characterised calcined  $WO_3$  particle and electrospun fiber have been used as the acetone sensing material for fabricating sensor films on alumina tubes. Hereafter, the data corresponding particle-based sensor will be designated as WPS and that of fiber will be designated as WFS. The resistance changes of both WPS and WFS sensors at different temperatures before measuring the changes on exposure to different concentrations of acetone gas has been measured. The sensing response as a function of change of resistance is measured at different operating temperatures for both WPS and WFS are shown in Figure 3.4.6a. Both the sensors have been exposed towards different concentrations of acetone for 15sec of exposure time, and the change of resistance was monitored. The particle-based sensor (WPS), exhibited a response of about 84% at 200°C, and fiber-based sensor (WFS) showed a higher sensitivity of around 90% at a comparatively lower operating temperature of 150°C (Figure 4a). In Figure 3.4.6b response of WPS and WFS at the optimum operating temperature towards different acetone concentrations (0.5, 0.8, 1, 2, 5 and 10ppm) are shown which signifies the lower concentration acetone sensing ability of both the sensors under comparatively lower operating temperatures. From the data shown in Figure 3.4.6b, it is very clear that the fabricated sensors could be used for differentiating acetone in the breath of normal people and diabetic

patients. Based on the highest responses exhibited, 200°C and 150°C have been considered as the optimum operating temperatures for WPS and WFS sensors. As per the surface-controlled mechanism of sensing, a maximum number of gas molecules are expected to react with adsorbed oxygen species at the highest operating temperature leading to a higher resistance change [76,77]. To understand the quality of a sensor in terms of its response and recovery time on exposure to any analyte gas, same has also been measured on exposure to 10ppm acetone. Response time has been calculated as the time taken for a fabricated sensor to reach 90% of the final signal after exposing the same to the target gas concentration (response time). Conversely, recovery time can be measured by the time taken for a sensor to reach 10% of the previous response (recovery time). Fast response towards a target gas composition is one of the key properties of a good sensor. On comparison of the response and recovery times of the two sensors (Figure 3.4.6c), it is very clear about the very fast response and recovery of fiber based sensors compared to WPS. The higher surface area and the porous morphological nature of the fiber-based sensor could be one of the reasons for this improved response towards acetone.

To examine the cross response of the fabricated sensors towards different gases of equal concentration by volume and thereby determine its selectivity to any particular gas, we checked the dynamic response behaviour of the fabricated sensors towards 10ppm of different gases and the optimized results are plotted in Figure 3.4.6d. To analyze the cross-sensitivity, the selectivity co-efficient has been calculated by the equation:  $\beta = S_{\text{acetone}}/S_{\text{gas}}$  where  $S_{\text{acetone}}$  and  $S_{\text{gas}}$  are the response of the sensor towards acetone and any other gas of 10ppm concentration [78]. The selectivity co-efficient ( $\beta$ ) calculated from Figure 3.4.6d varied in the order  $\beta_{\text{Formaldehyde}}$  (12.85) >  $\beta_{\text{CO}}$  (11.25) >  $\beta_{\text{NO}_x}$  (9) >  $\beta_{\text{Ethanol}}$  (7.5) >  $\beta_{\text{Ammonia}}$  (6) for WFS and for WPS it is like  $\beta_{\text{Formaldehyde}}$  (16.8) >  $\beta_{\text{CO}}$  (14) >  $\beta_{\text{NO}_x}$  (10.5) >  $\beta_{\text{Ethanol}}$  (8.4) >  $\beta_{\text{Ammonia}}$  (7) and from the low

selectivity data it is confirmed that both the sensors have selective sensitivity towards acetone which is highly interesting for fabricating hand-held devices based on our systems.

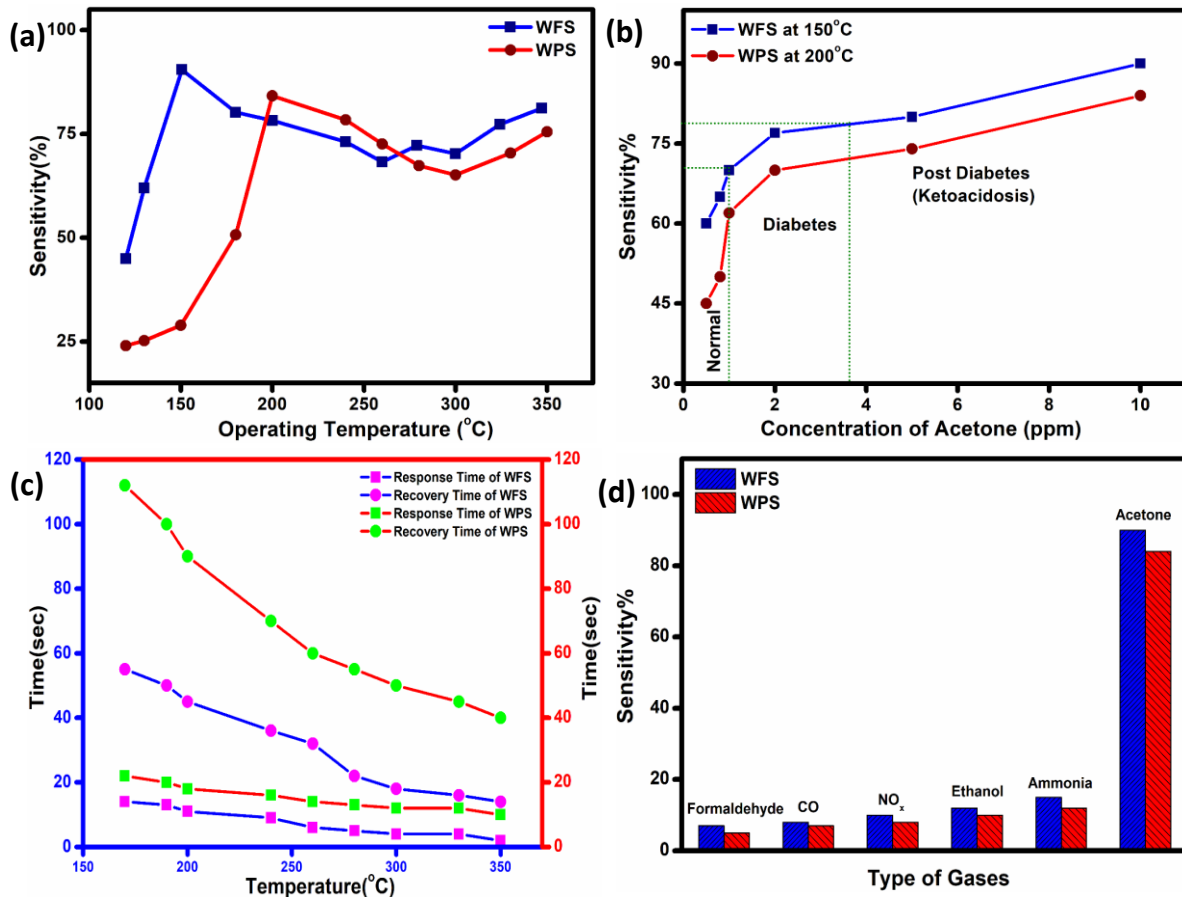


**Figure 3.4.6:** (a) Variation of the sensitivity of WPS and WFS based sensors with operating temperature (b) Change in sensing response with different acetone concentrations (0.5, 0.8, 1, 2, 5 and 10ppm) (c) Response and Recovery time variation with operating temperature (d) Selectivity measurement plot towards different type of gases with 10ppm concentration.

The dynamic response of WPS and WFS modules measured on exposure to 10ppm acetone gas for 15sec. are shown in Figure 3.4.7 (a & b), at the optimum operating temperature of 200°C and 150°C, respectively. The calculated response and recovery times are 18sec. and 90sec. for WPS and 10sec. and 40sec. for WFS, respectively. The sharp nature of the dynamic curve indicates the fast response of the sensor with high sensing capability. For better understanding of interaction between sensor material surface and target gas molecules the sensitivity of the sensors can be explained by Freundlich absorption isotherm equation [79] as given in equation (3.11).

$$S \propto aC^b / (1+aC^b) \dots\dots\dots (3.11)$$

Here C is the concentration of acetone, a is the proportionality factor and b is the exponent [80]. In our work the lower concentration of acetone used was below 1 and hence  $aC^b \rightarrow 0$ , the equation (3.11) is thus modified as:

$$S \propto aC^b \dots\dots\dots (3.12)$$

The above equation (iii) can be converted as:

$$\log(S) = \log a + b \log C \dots\dots\dots (3.13)$$

In Figure 3.4.7c, the power law relation between the responses of particle (WPS) and fiber (WFS) based sensor and the concentration of acetone is presented. The value of b calculated from slope of log S vs. log C plot is lower than 1 and the linear fitting of the experimental data shows the ability of the sensor in detecting lower concentration range of acetone which is more desirable for sensing application. Figure 3.4.7d show *I-V* characteristics measured at -40V to +40V bias voltage ranges at an operating temperature of 150°C for WFS and 200°C for WPS, respectively, in air and in 10ppm acetone indicating a linear ohmic response for both particle and fiber based sensor. The ohmic behavior of the *I-V* plot of the fabricated sensors is in fact an ideal situation to achieve optimized response from a semiconductor device.



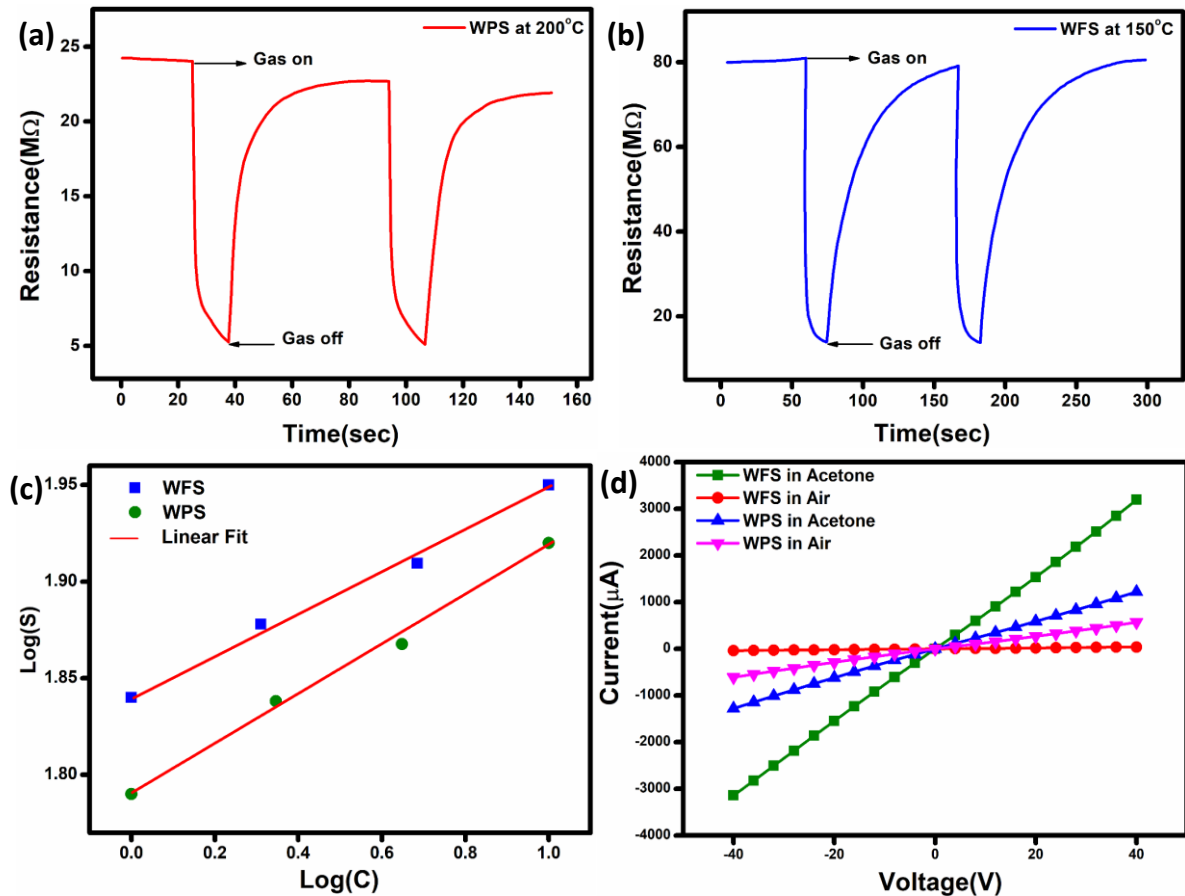


**Figure 3.4.7:** Dynamic response curve of (a) WPS and (b) WFS (c)  $\text{Log}(C)$  vs  $\text{Log}(S)$  plot (d)  $I$ - $V$  diagram for WPS and WFS sample in presence of acetone and air.

In order to monitor the stability, the response nature of both fabricated sensors has been monitored for more than three months and a high stability was exhibited by both the sensors as there was no observable change in resistance within the studied time period. Such an impressive stability is favourable for making devices as the material used appears to be stable in the ambient conditions.

In addition to the DC measurements discussed above, AC electrical measurements were also performed to correlate the response parameters in presence of acetone within the frequency range 100Hz to 1MHz. From Impedance spectroscopy studies it is easy to clearly interpret the contribution from bulk, inter grain and electrode towards the response of a sensor device. As we are trying to understand the sensing mechanism, the impedance characteristics were carried

out for better understanding of the contribution of intra-grain, grain boundary and electrode interfaces of the material under investigation.

The Nyquist diagram in Figure 3.4.8 (a & b) represent an explicit semi-circle nature of WPS and WFS in presence of acetone at different operating temperatures from 100°C to 350°C. The impedance plot is one of the major techniques for calculating the electrical parameters of the active region of a sensor material by plotting  $Z''$  (the reactive imaginary part) against  $Z'$  (resistive real part). In the case of a defect free homogeneous sensor material, a clear semicircle will be evident in the Nyquist plot with its origin lying exactly on the real axis [81,82]. The bulk grain contribution including that of surface and grain appears as a first semicircle, whereas contribution of grain boundary and electrode interface appears as subsequent semi circles [83]. In our case, only a single semicircle was seen in the impedance graph measured in air. In addition, the impedance of both the sensors decreases when exposed to acetone. Since this semicircle is mainly due to bulk contribution, the influence of grain boundary is expected to be negligible in the acetone detection process of the above samples.

By using the ZView2 software the  $Z'$  and  $Z''$  calculation from the impedance data have been analyzed in a wide range of frequency (100Hz – 1MHz) and temperature (100°C – 350°C) for both the particle and fiber based sensor in presence of acetone as shown in Figure 3.4.8 (a &b), all the electrical parameters are calculated for 10ppm acetone. The relationship between grain resistance and temperature can be shown by the Arrhenius equation:

$$R = R_0 \exp(E_a/KT) \dots\dots\dots (3.14)$$

Here  $E_a$  is the activation energy and  $K$  is the Boltzmann's constant,  $T$  is the temperature in Kelvin (K) and  $R_0$  can be described as pre-exponential factor. The activation energy has been calculated from the slope of  $\ln(R)$  vs  $1/KT$  graph as shown in Figure 3.4.8 (c & d) for both the sensors. The linear data shown in Figure 3.4.8 (c & d) suggests a single rate limiting step that could govern the acetone sensing behavior within this temperature regime. The calculated

activation energy is 0.356 eV and 0.226 eV for WPS and WFS, respectively. This high activation energy confirms chemisorption as the rate limiting activation process which is responsible for the acetone detection mechanism in both the cases.

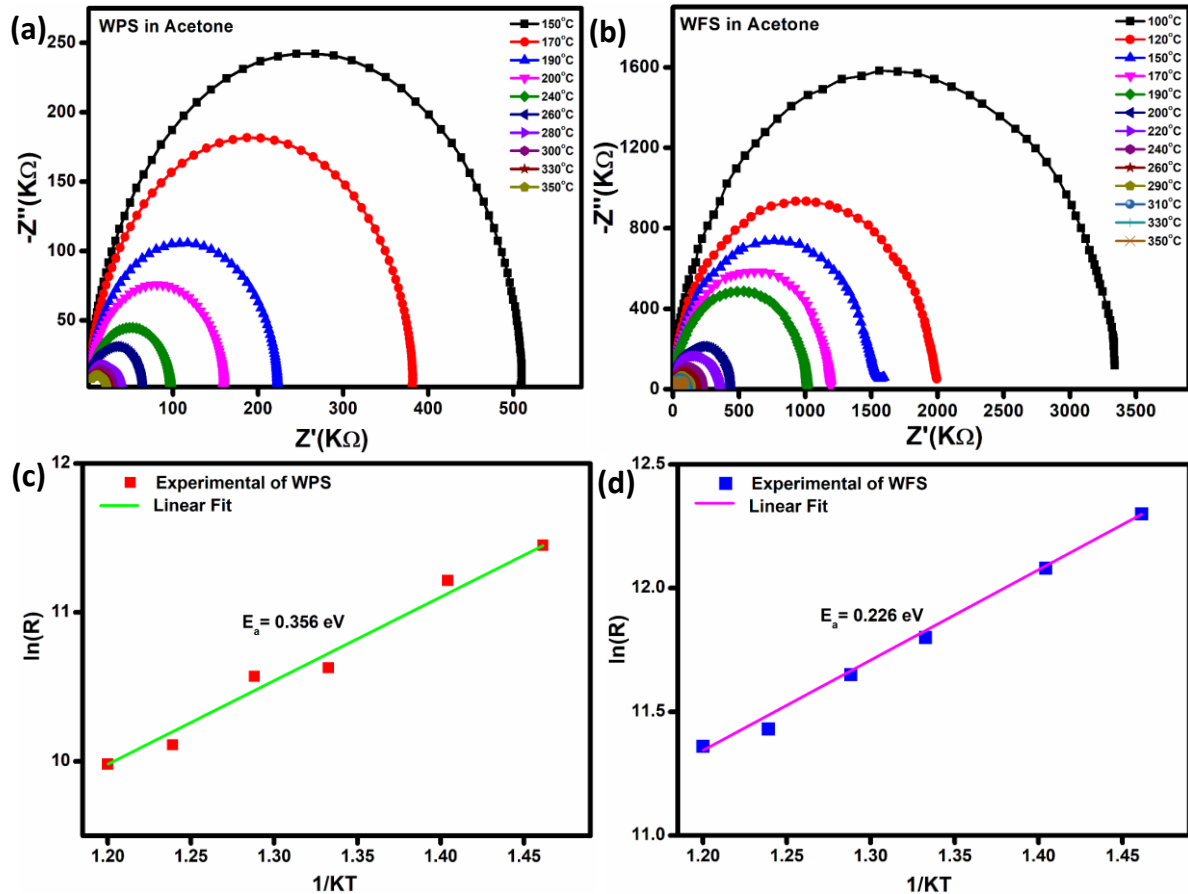


**Figure 3.4.8:** (a) & (b) Nyquist plot in the presence of acetone (c) & (d) Calculated activation energy of WPS and WFS, respectively.

The impedance data for both particle and fiber-based sensors are modelled by a parallel RC circuit. The Nyquist diagram of WPS and WFS in presence of air and 10 ppm of acetone has been plotted in Figure 3.4.9 (a & b), respectively. The RC parameters has been calculated from the RC model circuit and it is noticed that the data can be fitted with only one symmetric semicircle in case of  $WO_3$  particle-based sensor (WPS) and an asymmetric semicircle for the  $WO_3$  fiber-based sensor (WFS), probably due to a mild overlap of grain and grain boundary due to the nano crystalline nature of the fiber with large number of grains as evident from the microstructural studies shown in Figure 3.4.4. It is clear from the AC analysis that the response

of  $\text{WO}_3$  particle completely depends on contribution from the grains because the second semicircle is completely absent here. For the fiber-based sample there is an indication of an overlapped second semicircle in the main semicircle indicating mild evidence of the influence of grain boundaries on sensing response [84-86]. The equivalent circuit along with the Nyquist diagram of WPS and WFS in presence of 10ppm acetone is presented inset of Figure 3.4.9 (c & d).

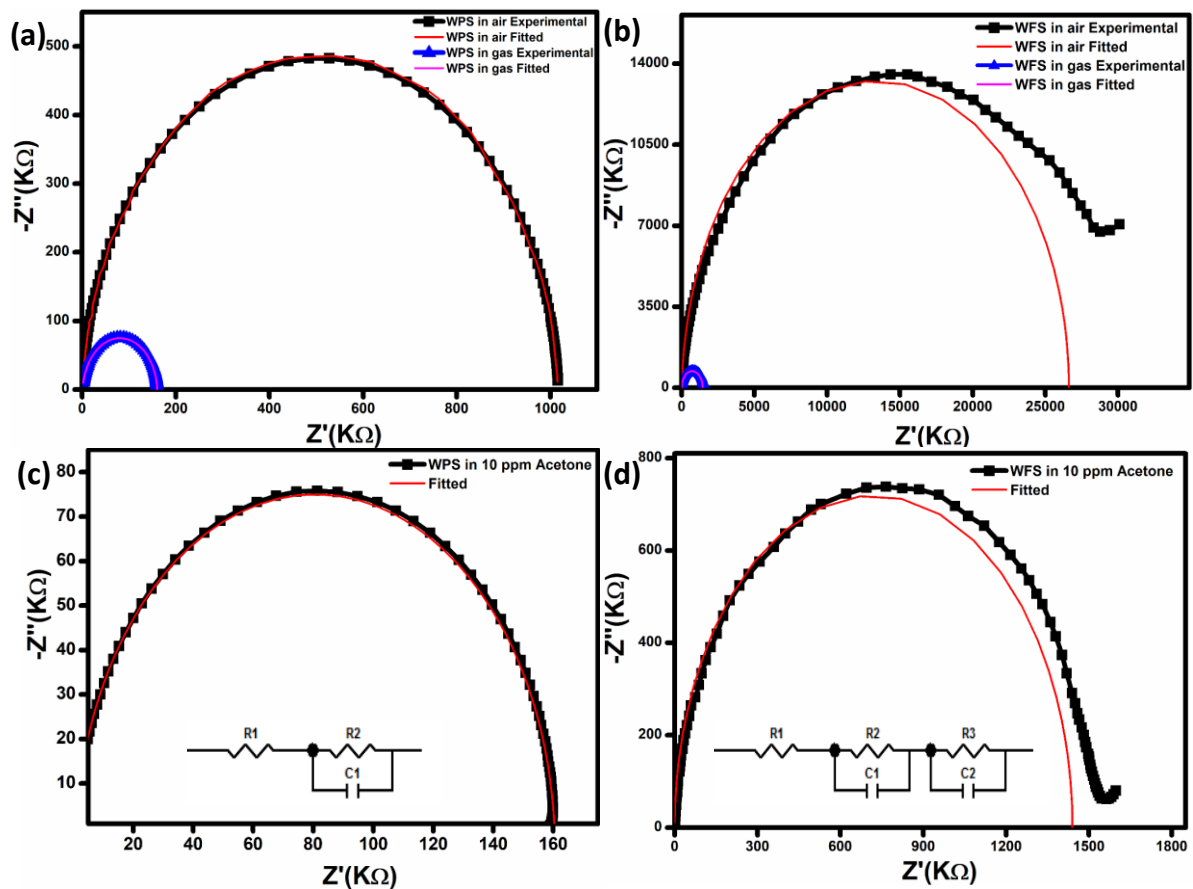


**Figure 3.4.9:** (a) & (b) Nyquist diagram in presence of air and 10ppm acetone with fitted plot (c) & (d) Nyquist plot with equivalent circuit at optimum operating temperature in presence of 10ppm acetone only of WPS and WFS, respectively.

It can be optimized that the impedance decreases after exposure to acetone at constant operating temperature and the sensitivity of the sensor can also be calculated from the impedance data as

$S \% = \frac{Z''_{Air} - Z''_{Acetone}}{Z''_{Air}}$  which correspond to maximum impedance imaginary part in presence of acetone and air under relaxation frequency in the Nyquist diagrams. From the data the sensitivity was calculated and it is nearly 82.5% and 93.1%, respectively, for WO<sub>3</sub> particle and fiber-based sensor respectively, which is very close to the results calculated from the DC measurements, comparison is represented in Table 3.4.1.

**Table 3.4.1: Comparison Sensitivity Response calculated from both AC and DC method.**

<b>Sensor Material</b>	<b>Surface Area (m<sup>2</sup>/g)</b>	<b>Activation Energy (eV)</b>	<b>Sensitivity from AC Impedance</b>	<b>Sensitivity from DC Resistance</b>
<b>Particle</b>	15.5	0.356	82.5%	84%
<b>Fiber</b>	85.6	0.226	93.1%	90%

#### **3.4.4. Gas Sensing Mechanism**

The gas sensing mechanism and sensing response of a semiconductor metal oxide based gas sensor mainly depend on the resistance variation due to the adsorption-desorption phenomenon occurring on the sensor surface. The surface resistance of the sensor decreases with increase in the operating temperature, in the range of 100°C-120°C for fiber and 130°C- 160°C for particle, which is mainly due to the physisorption of the oxygen molecule in air. With increase in temperature, the electrons from the conduction band of the material gets trapped into the surface resulting in ionization of the physisorbed oxygen molecules into adsorbed oxygen species like O<sup>2-</sup>, O<sub>2</sub><sup>-</sup> and or O<sup>-</sup>. During this process due to various reactions, the concentration of electrons on the surface of the material decreases resulting in an electron depletion layer leading to an increase in the resistance of the sensor in air as evident in Figure 3.4.10.

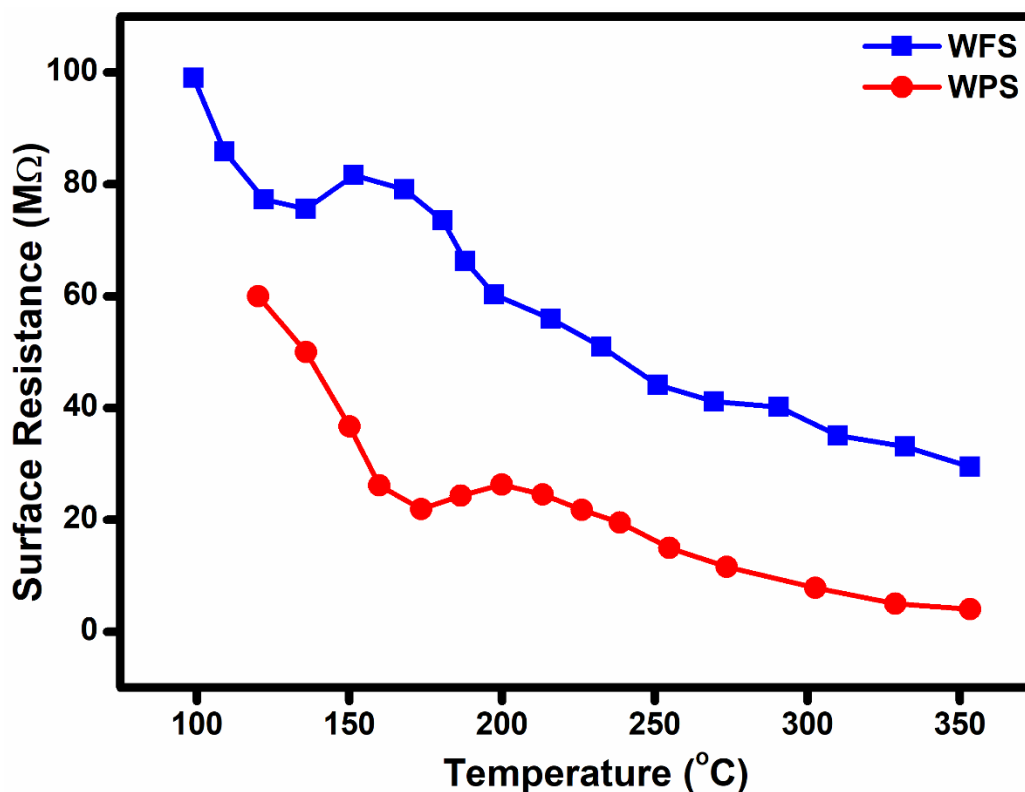
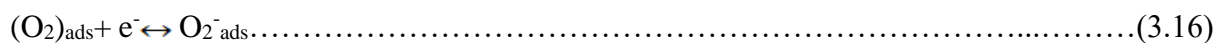
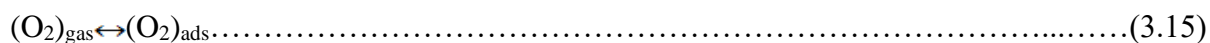


Figure 3.4.10: Resistance change with operating temperature in presence of air of WFS and WPS.

When the  $WO_3$  based sensor is exposed to the analyte gas acetone which is a reducing gas, the target gas molecules react with adsorbed oxygen species ( $O^-$  and  $O^{2-}$ ) which was produced on the surface of the sensor material and release the free electrons back to the conduction band of the  $WO_3$  leading to a further decrease in the electron depletion layer. As a result, the electrical resistance of the material also decreases [87-89]. The overall mechanism that has been described above is shown in the following equations,



We have compared the sensing characteristics of  $WO_3$  based sensors reported in the literature towards below 50ppm acetone (Figure 3.4.11) with our work. In most of the cases, both the

concentration and the operating temperatures have been high compared to the performance of the present sensors.

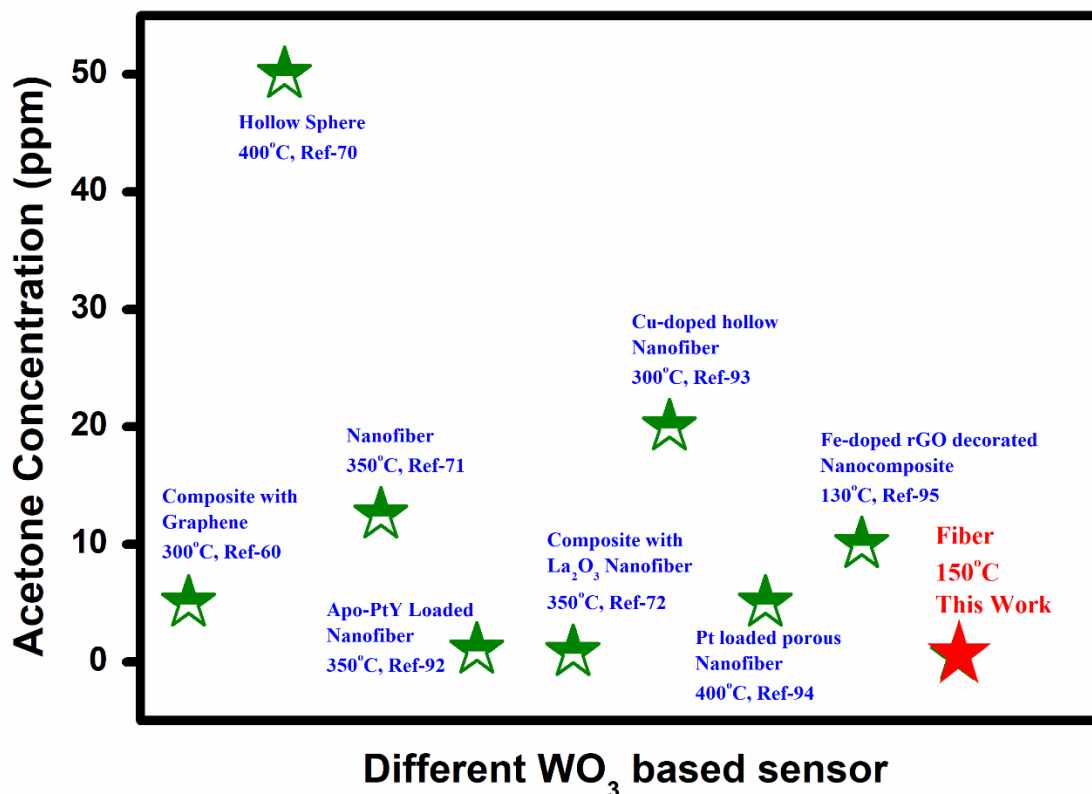


Figure 3.4.11: Comparative study on WO<sub>3</sub> based sensor materials towards acetone detection.

The WO<sub>3</sub> fiber-based sensor fabricated by us exhibited high performance at a lower operating temperature of 150°C with almost 90% response is highly encouraging. In order to explore the origin of the enhanced response of WO<sub>3</sub> fiber-based sensor towards acetone we have also looked into the preferred orientation of the facets as discussed under X-ray characterization. It has been reported that the surface energies of the crystal planes of WO<sub>3</sub> nanostructures follows an order of (002) (1.56 J m<sup>-2</sup>) > (020) (1.54 J m<sup>-2</sup>) > (200) (1.43 J m<sup>-2</sup>). They further reported that the (002) facets are the most active ones among the three facets of WO<sub>3</sub> and considered to have a superior reactivity in nanoparticulate form [90,91]. Therefore it could be confirmed that the preferential orientation of (002) planes of WO<sub>3</sub> could possibly be

more favourable in absorption-desorption of gas molecules leading to an enhanced response towards acetone at a lower temperature.

The factors responsible for the improved acetone sensing characteristics of WO<sub>3</sub> fiber can thus be summarized as (1) presence of 002 faceted structure (2) high surface area and porosity leading to better adsorption and desorption of oxygen at a lower temperature (3) lower activation energy.

### **3.4.5. Conclusion:**

In conclusion, the  $\gamma$ -monoclinic WO<sub>3</sub> fibers with highly reactive exposed (002) facets have been synthesized by electrospinning technique for sensor application. Through various characterization techniques, it has been demonstrated that by modifying the crystal facets of WO<sub>3</sub> it is possible to fabricate sensors exhibiting preferred response towards different concentrations of acetone which will be useful for developing acetone sensors for diagnosis of acetone from breath. A comparative study between WO<sub>3</sub> particles and fiber were undertaken to understand the various factors including shape of the oxide particles on acetone sensing. Based on various studies it has been confirmed that the morphological changes did not have any dramatic effect on the sensing properties. We also compared the response of the sensors using both AC and DC measurements which are complimentary techniques in understanding the sensing mechanism. Moreover, ac measurements and modelling confirmed that it is mainly the grains and the grain surfaces that are involved in the detection of acetone in both cases. The fabricated WFS sensor demonstrated an excellent ~90% sensing response in presence of 10ppm acetone at a low temperature (~150°C) with a fast response (~20s) and recovery (~40s) time. The enhanced performance of WO<sub>3</sub> fiber towards acetone sensing has been demonstrated here through various characterization study and thorough electrical properties investigation through AC and DC measurements. In conclusion, an outstanding response to low ppm acetone gas with improved selectivity, excellent reproducibility and stability projects WO<sub>3</sub> fiber as a



promising material to fabricate acetone sensors for non-invasive diagnosis of diabetes through breath analysis.

### **3.5. References:**

1. Zhang, H.; Banfield, J. F. *Chem. Rev.* **2014**, *114*, 9613.
2. Verma, R.; Gangwar, J.; Srivastava, A. K. *RSC Adv.* **2017**, *7*, 44199.
3. Roy, A.; Das, P. P.; Selvaraj, P.; Sundaram, S.; Devi, P. S. *ACS Sustain. Chem. Eng.* **2018**, *6*, 3299.
4. Lee, K.; Mazare, A.; Schmuki, P. *Chem. Rev.* **2014**, *114*, 9385.
5. Bai, Y.; Mora-Sero, I.; Angelis, F. D.; Bisquert, J.; Wang, P. *Chem. Rev.* **2014**, *114*, 10095.
6. Sagawa, T.; Yoshikawa, S.; Imahori, H. *J. Phys. Chem. Lett.* **2010**, *1*, 1020.
7. Mukhopadhyay, S.; Maiti, D.; Saha, A.; Devi, P. S. *Cryst. Growth Des.* **2016**, *16*, 6922.
8. Gouma, P. I.; Mills, M. J. *J. Am. Ceram. Soc.* **2001**, *84*, 619.
9. Evain, M.; Whangbo, M. H.; Brohan, L.; Marchand, R. *Inorg. Chem.* **1990**, *29*, 1413.
10. Guo, Z. Q.; Zhou, J. P.; An, L. L.; Jiang, J. X.; Zhu, G. Q.; Deng, C. Y. *J. Mater. Chem. A* **2014**, *2*, 20358.
11. Roy, A.; Mukhopadhyay, S.; Devi, P. S.; Sundaram, S. *ACS Omega* **2019**, *4*, 1130.
12. NoéDíaz de León, J.; Rodríguez, J. R.; Rojas, J.; Barrón, Y. E.; Cardenas, L.; Kumar, C. R.; Nuñez, G. A.; Moyado, S. F. *Front. Chem.* **2019**, *7*, 750.
13. Tsai, C. C.; Teng, H. *Chem. Mater.* **2006**, *18*, 367.
14. Shalini, S.; Prabavathy, N.; Balasundaraprabhu, R.; Kumar, T. S.; Walke, P.; Prasanna, S.; Velayuthapillai, D. *J Mater Sci: Mater Electron* **2017**, *28*, 3500.
15. Morais da Silva, D.; Canuto de Menezes, B. S.; Bezzon, V. D. N.; Montanheiro, T. L. A.; Macedo, E. F.; Tada, D. B.; Petraconi, G.; Thim, G. P. *SN Applied Sciences* **2019**, *1*, 945.
16. Ramakrishnan, V. M.; Muthukumarasamy, N.; Balraju, P.; Pitchaiya, S.; Velauthapillai, D.; Pugazhendhi, A. *Int. J. Hydrog. Energy*, **2020**, *45*, 15441.

17. Lan, L.; Yichao, Z.; Yanzhong, L.; Kaiqiang, Z.; Jinxian, H.; Zhigao, H.; Sanjay, M.; Zhensheng, H. *Nanoscale*, **2020**, *12*, 230.
18. Eom, J. Y.; Lim, S. J.; Lee, S. M.; Ryu, W. H.; Kwon, H. S. *J. Mater. Chem. A* **2015**, *3*, 11183.
19. Li, M-N.; Chi, Z-Y.; Yu, Y-C. *J. Am. Ceram. Soc.* **2012**, *95*, 3297.
20. Nassoko, D.; Li, Y. F.; Li, J. L.; Li, X.; Yu, Y. *Int. J. Photoenergy* **2012**, *1*.
21. Singh, I.; Birajdar, B. *RSC Adv.* **2017**, *7*, 54053.
22. Staerz, A.; Weimar, U.; Barsan, N. *Sensor*, **2016**, *16*, 1815.
23. Zhang, N.; Ruan, S.; Yin, Y.; Wen, S.; Chen, Y. *ACS Appl. Nano Mater.* **2018**, *1*, 4671.
24. Nag, P.; Banerjee, S.; Lee, Y.; Bumajdad, A.; Lee, Y.; Devi, P. S. *Inorg. Chem.* **2012**, *51*, 844.
25. Nag, P.; Majumdar, S.; Bumajdad, A.; Devi, P. S. *RSC Adv.* **2014**, *4*, 18512.
26. Capone, S.; Manera, M. G.; Taurino, A.; Siciliano, P.; Rella, R.; Luby, S.; Benkovicova, M.; Siffalovic, P.; Majkova, E. *Langmuir* **2014**, *30*, 1190.
27. Mohapatra, M.; Anand, S. *Int. J. Eng. Sci. Technol.* **2010**, *2*, 127.
28. Wang, G.; Gou, X.; Horvat, J.; Park, J. *J. Phys. Chem. C* **2008**, *112*, 15220.
29. Pawar, N. K.; Kajale, D. D.; Patil, G. E.; Wagh, V. G.; Gaikwad, V. B.; Deore, M. K.; Jain, G. H. *Int. J. Smart Sens. Intell. Syst.* **2012**, *5*, 441.
30. Lim, I.-S.; Jang, G.-E.; Kim, C.; Yoon, D. H. *Sens. Actuators B* **2001**, *77*, 215.
31. Gurlo, A.; Sahm, M.; Oprea, A.; Barsan, N.; Weimar, U. *Sens. Actuators B* **2004**, *102*, 291.
32. Gurlo, A.; Barsan, N.; Oprea, A.; Sahm, M.; Sahm, T.; Weimar, U. *Appl. Phys. Lett.* **2004**, *85*, 2280.
33. Lee, Y.-C.; Chueh, Y. L.; Hsieh, C.-H.; Chang, M.-T.; Chou, L.-J.; Wang, Z. L.; Lan, Y.-W.; Chen, C.-D.; Kurata, H.; Isoda, S. *Small* **2007**, *3*, 1356.
34. Hao, Q.; Li, L.; Yin, X.; Liu, S.; Li, Q.; Wang, T. *Mater. Sci. Eng. B* **2001**, *176*, 600.

35. Ziolo, R. F.; Giannelis, E. P.; Weinstein, B. A.; O'Horo, M. P.; Ganguly, B. N.; Mehrotra, V.; Russel, M. W.; Huffman, D. R. *Science* **1992**, *257*, 219.
36. Zheng, Y.; Cheng, Y.; Bao, F.; Wang, Y. *Mater. Res. Bull.* **2006**, *41*, 525.
37. Rietveld, H. M. *J. Appl. Cryst.* **1969**, *2*, 65.
38. Young, R. A. *The Rietveld Method*, Oxford University Press, **1993**.
39. N. Zhang, H.Y. Peng, B. Hu, *Talanta* **94**, **2012**, 278–283.
40. Barbieri, A.; Weiss, W.; Van Hove, M.; Somorjai, G. *Surf. Sci.* **1994**, *302*, 259.
41. Liu, S.; Yao, k.; Fu, L. H.; Ma. M. G. *RSC Adv.* **2016**, *6*, 2135.
42. Fu, R.; Wang, W.; Han, R.; Chen, K.; *Mater. Lett.* **2008**, *62*, 4066.
43. Kumar, P.; No-Lee, H.; Kumar, R. *J Mater Sci: Mater Electron*, **2014**, *25*, 4553.
44. Varadwaja, K. S. K.; Panigrahib, M. K.; Ghose. J. J. *Solid State Chem*, **2004**, *177*, 4286.
45. Lu, W.; Shen, Y.; Xie, A.; Zhang, W. *J. Magn. Magn. Mater.* **2010**, *322*, 1828.
46. Wu, H.; Wu, G.; Wang, L. *Powder Technol.* **2015**, *269*, 443.
47. Li, G.; Li, R.; Zhou, W. *Nano-Micro Lett.* **2017**, *9*, 46.
48. Wu, W.; Xiao, X. H.; Zhang, S. F.; Peng, T. C.; Zhou, J.; Ren, F.; Jiang, C. Z. *Nanoscale Res. Lett.* **2010**, *5*,1474.
49. Singh, A. K.; Srivastava, O. N., Singh, K. *Nanoscale Res. Lett.* **2017**, *12*, 298.
50. Nguyen, M. D.; Tran, H.-V.; Xu, S.; Lee, T. R. *Appl. Sci.* **2021**, *11*, 11301.
51. Liu, B.; Cai, D.; Liu, Y.; Wang, D.; Wang, L.; Wang, Y.; Li, H.; Li, Q.; Wang, T. *Sens. Actuators B* **2014**, *193*, 28.
52. Kim, T. H.; Hasani, A.; Quyet, L. V.; Kim, Y.; Park, S. Y.; Lee, M. G.; Sohn, W.; Nguyen, T. P.; Choi, K. S.; Kim, S. Y.; Jang, H. W. *Sens. Actuators B*, **2019**, *286*, 512.
53. Jeon, J.; Shim, Y.; Han, S. D.; Kim, D. H.; Kim, Y. H.; Kang, C.; Kim, J.; Kim, M.; Jang, H. W. *J. Mater. Chem. A*, **2015**, *3*, 17939.

54. Zhang, Y.; Liu, Y.; Zhou, L.; Liu, D.; Liu, F.; Liu, F.; Liang, X.; Yan, X.; Gao, Y.; Lu, G. *Sens. Actuators B*, **2018**, 273, 991.
55. Wei, S.; Zhao, G.; Du, W.; Tian, Q. *Vacuum*, **2016**, 124, 32-39.
56. Jiang, R.; Li, B.; Fang, C.; Wang, J. *Adv. Mater.* **2014**, 26, 5274-5309.
57. Dong, C.; Zhao, R.; Yao, L.; Ran, Y.; Zhang, X.; Wang, Y. *J. Alloys Compd.* **2020**, 820, 153194.
58. Broza, Y.; Haick, H. *Nanomedicine*, **2013**, 8, 785–806.
59. Righettoni, M.; Amann, A.; Pratsinis, S. E. *Materials Today*, **2015**, 18.
60. Sun, S.; Xiong, X.; Han, J.; Chang, X.; Wang, N.; Wang, M.; Zhu, Y. *ACS Appl. Nano Mater.* **2019**, 2, 1313-1324.
61. Righettoni, M.; Tricoli, A.; Pratsinis, S. E. *Anal. Chem.* **2010**, 82, 3581-3587.
62. Zhang, Y.; He, W.; Zhao, H.; Li, P. *Vacuum* **2013**, 95, 30-34.
63. Wang, L.; Teleki, A.; Pratsinis, S. E.; Gouma, P. I. *Chem. Mater.* **2008**, 20, 4794-4796.
64. Abe, O. O.; Qiu, Z.; Jinschek, J. R.; Gouma, P. I. *Sensors* **2021**, 21, 1690.
65. Choi, S. J.; Chattopadhyay, S.; Kim, J. J.; Kim, S. J.; Tuller, H. L.; Rutledge, G. C.; Kim, I. D. *Nanoscale* **2016**, 8, 9159-9166.
66. Leng, J. Y.; Xu, X. J.; Lv, N.; Fan, H. T.; Zhang, T. *J. Colloid Interface Sci.* **2011**, 356, 54-57.
67. Lu, X.; Liu, X.; Zhang, W.; Wang, C.; Wei, Y. *J. Colloid Interface Sci.* **2006**, 298, 996-999.
68. Nguyen, T. A.; Jun, T. S.; Rashid, M.; Kim, Y. S. *Mater. Lett.* **2011**, 65, 2823-2825.
69. Chen, D.; Hou, X.; Li, T.; Yin, L.; Fan, B.; Wng, H.; Li, X.; Xu, H.; Lu, H.; Zhang, R.; Sun, J. *Sens. Actuators B Chem.* **2011**, 153, 373-381.
70. Li, X. L.; Lou, T. J.; Sun, X. M.; Li, Y. D. *Inorganic Chemistry* **2004**, 43, 5442-5449.

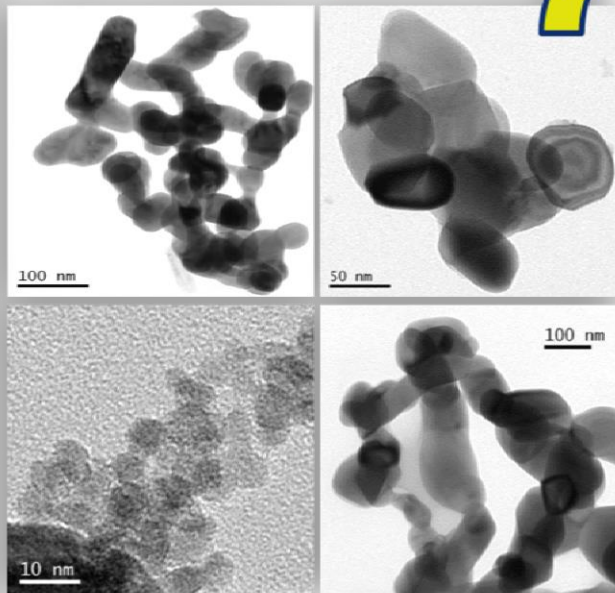
71. Imran, M.; Rashid, S. S. A. A. H.; Sabri, Y.; Motta, N.; Tesfamichael, T.; Sonar, P.; Shafiei, M. *J Mater. Chem. C* **2019**, *7*, 2961-2970.
72. Feng, C.; Wang, C.; Cheng, P.; Li, X.; Wang, B.; Guan, Y.; Ma, J.; Zhang, H.; Sun, Y.; Sun, P.; Zheng, J.; Lu, G. *Sens. Actuators B* **2015**, *221*, 434-442.
73. Wei, S.; Li, S.; Wei, R.; Liu, S.; Du, W. *Sens. Actuators B Chem.* **2020**, *329*, 129188.
74. Jia, Q.; Ji, H.; Wang, D.; Bai, X.; Sun, X.; Jin, Z. *J. Mater. Chem. A* **2014**, *2*, 13602.
75. Ramkumar, S.; Rajarajan, G. *Appl. Phys. A* **2017**, *123*, 401.
76. Jia, Q. Q.; Ji, H. M.; Wang, D. H.; Bai, X.; Sun, X. H.; Jin, Z. G. *J. Mater. Chem. A* **2014**, *2*, 13602–13611.
77. Amrehn, S.; Wu, X.; Wagner, T. *ACS Sens.* **2018**, *3*, 191–199.
78. Banerjee, S.; Bumajdad, A.; Devi, P. S. *Nanotechnology* **2011**, *22*, 275506.
79. Johnson, J. L.; Behnam, A.; An, Y.; Pearton, S. J.; Ural, A. *J. Appl. Phys.* **2011**, *109*, 124301.
80. Dan, Y.; Lu, Y.; Kybert, N. J.; Luo, Z.; Johnson, A. T. C. *Nano Lett.* **2009**, *9*, 1472–5.
81. Labidi, A.; Jacolin, C.; Bendahan, M.; Abdelghani, A.; Guerin, J. *Sens. Actuator B* **2005**, *106*, 713-718.
82. Ling, Z.; Leach, C.; Freer, R. *Sens. Actuator B* **2002**, *87*, 215-221.
83. Aguir, K.; Labidi, A.; Mauriat, C. L. *IEEE Sensors* **2006**, 267-270.
84. Wang, X.; Yee, S. S.; Carey, W. P. *Sens. Actuators B Chem.* **1995**, *25*, 454-457.
85. Tamaki, J.; Zhang, Z.; Fujimori, K.; Akiyama, M.; Harada, T.; Miura, N.; Yamazoe, N. *J Electrochem. Soc.* **1994**, *141*, 2207.
86. Labidi, A.; Lambert-Mauriat, C.; Jacolin, C.; Bendahan, M.; Maaref, M.; Aguir, K. *Sens. Actuators B Chem.* **2006**, *119*, 374-379.
87. Kadir, R. A.; Li, Z.; Sadek, A. Z.; Rani, R. A.; Zoolfakar, A. S.; Field, M. R.; Ou, J. Z.; Chrimes, A. F.; Kalantar-zadeh, K. *J. Phys. Chem. C* **2014**, *118*, 3129–3139.

88. Chen, Y.; Qin, H.; Cao, Y.; Zhang, H.; Hu, J. *Sensors* **2018**, *18*, 3425.
89. Xu, S.; Shi, Y. *Sens. Actuators B* **2009**, *143*, 71–75.
90. Guo, Y.; Quan, X.; Lu, N.; Zhao, H.; Chen, S. *Environ. Sci. Technol.* **2007**, *41*, 4422–4427.
91. Xie, Y. P.; Liu, G.; Yin, L.; Cheng, H. M. *J. Mater. Chem.* **2012**, *22*, 6746.
92. Kim, S. J.; Choi, S. J.; Jang, J. S.; Cho, H. J.; Kim, I. D. *Acc. Chem. Res.* **2017**, *50*, 1587-1596.
93. Bai, X.; Ji, H.; Gao, P.; Zhang, Y.; Sun, X. *Sens. Actuators B Chem.* **2014**, *193*, 100-106
94. Choi, S. J.; Kim, S. J.; Cho, H. J.; Jang, J. S.; Lin, Y. M.; Tuller, H. L.; Rutledge, G. C.; Kim, I. D. *Small* **2016**, *12*, 911-920.
95. Sen, S.; Maity, S.; Kundu, S. *Sens. Actuators B Chem.* **2022**, *361*, 131706.

# CHAPTER-IV

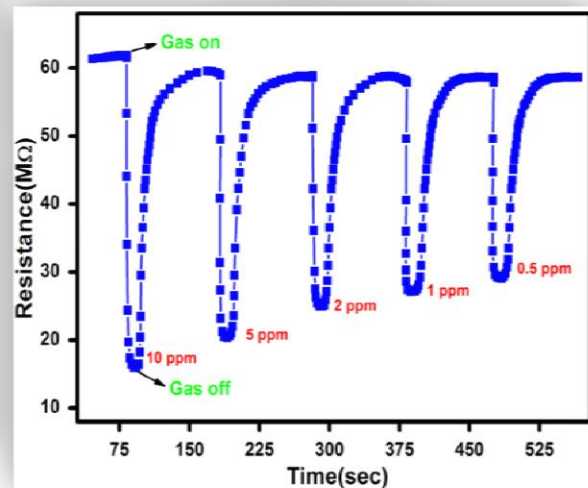
## Ternary Metal Oxide-based Acetone Sensor

### Materials Synthesis



### Evaluate Performance

### Improved Sensing Property



*This chapter describes  $\text{BiFeO}_3$  and  $\text{Zn}_2\text{SnO}_4$  nanoparticles as ternary metal oxide-based materials for acetone sensor fabrication. The sensing mechanism study of ternary metal oxide based materials has been implemented with and explored their performance in the field of acetone sensing application. The ternary metal oxide semiconductor material has been attracted enormous attention in current research field with enhanced sensitivity, selectivity and stability over normal binary oxide material due to their good electrical conductivity and optical properties with higher thermodynamic stability. At the same time we have developed different grain size sensing materials with higher surface area via different synthesis procedures for the enhancement of various sensing parameters. Also trying to explore vacancy induced acetone sensing property and on the other side grain size effect on sensing performance has been established for futuristic acetone development study.*

## **4.1. Background**

Interest in the design and development of nanocrystalline metal oxide-based gas sensor (MOS) has grown considerably from fundamental and applied perspectives to devices. In Chapter 3, synthesis, characterization and acetone sensing performance of single component metal oxides such as  $\text{TiO}_2$ ,  $\text{Fe}_2\text{O}_3$  and  $\text{WO}_3$  have been presented in detail. In this Chapter, acetone sensing characteristics of multicomponent oxides such as  $\text{BiFeO}_3$  and  $\text{Zn}_2\text{SnO}_4$  are presented. In this work the interest was to explore newer compositions in the area of gas sensors that could exhibit better sensing characteristics at lower operating temperature.

## **4.2. $\text{BiFeO}_3$ (BFO) Nanoparticles for Acetone Sensing: Synthesis, Characterization and Performance evaluation**

### **4.2.1. Introduction**

MOS gas sensors based on n-type semiconductor metal oxides such as  $\text{In}_2\text{O}_3$ ,  $\text{WO}_3$ ,  $\text{TiO}_2$ ,  $\text{ZnO}$ ,  $\text{SnO}_2$ ,  $\text{Fe}_2\text{O}_3$  etc. have been widely studied to detect various gases [1-6]. In addition, many multicomponent oxides have also been explored for gas sensor applications [7,8]. Among various multicomponent oxides,  $\text{BiFeO}_3$ , (BFO) has been established as a well-accepted multiferroic material possessing simultaneous ferroelectricity and ferromagnetism [9,10]. Of late, this rhombohedrally distorted p-type perovskite oxide having a direct band gap of 2.2-2.8 eV with high electron mobility [11-12] has also been explored for gas sensor applications [2,13]. It is worth mentioning the remarkable reports published in the recent years on the gas sensing properties of BFO and the increased attention the material received due to its high electron mobility, high electrical conductivity, good response and recovery time, long term stability and reproducibility compared to other binary oxides such as  $\text{ZnO}$ ,  $\text{SnO}_2$  and  $\text{Fe}_2\text{O}_3$ . Different morphological structures of  $\text{BiFeO}_3$  have been synthesized by techniques such as sol-gel, hydrothermal, microwave-assisted, and electrospinning [14,15]. Some interesting reports



on the gas sensing characteristics of BFO nanoparticles refer to its response towards ethanol and ammonia [16-19]. Very recently, the gas sensing properties of BFO crystallites towards acetone gas has also been reported by a few researchers [20,21]. Acetone is known as a highly volatile and reactive colourless compound and is vital for detecting the concentration of acetone in various industrial and biological environments. When the acetone concentration is higher in the environment (more than 150ppm), it can cause damage to the eyes, noses, and central nervous system. Acetone is also known as an essential biomarker for the non-invasive detection of diabetes. Therefore, the necessity to identify newer materials to develop acetone sensors, which can detect higher concentrations of acetone in the environment and lower concentrations of acetone in breath, has been of high priority in recent times.

Though there are more than a dozen reports on the sensing characteristics of BFO towards various gases, there are still many lacunae to understand its performance as a sensing material towards acetone. Interestingly, depending on the purity of the resultant material, in some cases, BFO exhibited ferromagnetic behaviour and, in other cases, antiferromagnetic behaviour. It is also not very clear from the existing reports the actual role of ferromagnetic  $\text{BiFeO}_3$  or the presence of  $\text{Bi}_2\text{Fe}_4\text{O}_9$  along with  $\text{BiFeO}_3$  as an acetone sensing material. In this study, we have synthesized multifunctional  $\text{BiFeO}_3$  by sonochemical synthesis process using hydrazine hydrate as a precipitating cum complexing agent and demonstrated the response of the ferromagnetic  $\text{BiFeO}_3$  as a gas sensing material towards different concentrations of acetone. In addition, along with the DC (Direct Current) measurements, we have also carried out AC (Alternating Current) impedance measurements to correlate the sensing mechanism.

### **4.2.2. Thermogravimetric analysis**

The thermal decomposition behaviour of as-prepared sample of BFO was investigated by the thermogravimetric analysis (TGA) and differential scanning calorimetry (DSC) analysis. The

initial weight loss of the precursor is indicative of dehydration within the temperature range of 50°C to 260°C. A sharp exothermic peak situated at around 424°C indicates the crystallization of the phase. The as-prepared powder sample calcined at > 450°C consists of a mixed phase of  $\text{Bi}_2\text{Fe}_4\text{O}_9$  and  $\text{BiFeO}_3$  as confirmed with XRD results. The TG-DSC analysis shown in Figure 4.2.1 indicates complete removal of all the organics below 500°C and the total weight loss observed is around 15%. The TG curve also confirms complete decomposition of the starting material as evident from the insignificant weight change after 500°C. Based on the phase change the as-prepared material was calcined at 500°C to obtain crystalline nanomaterials.

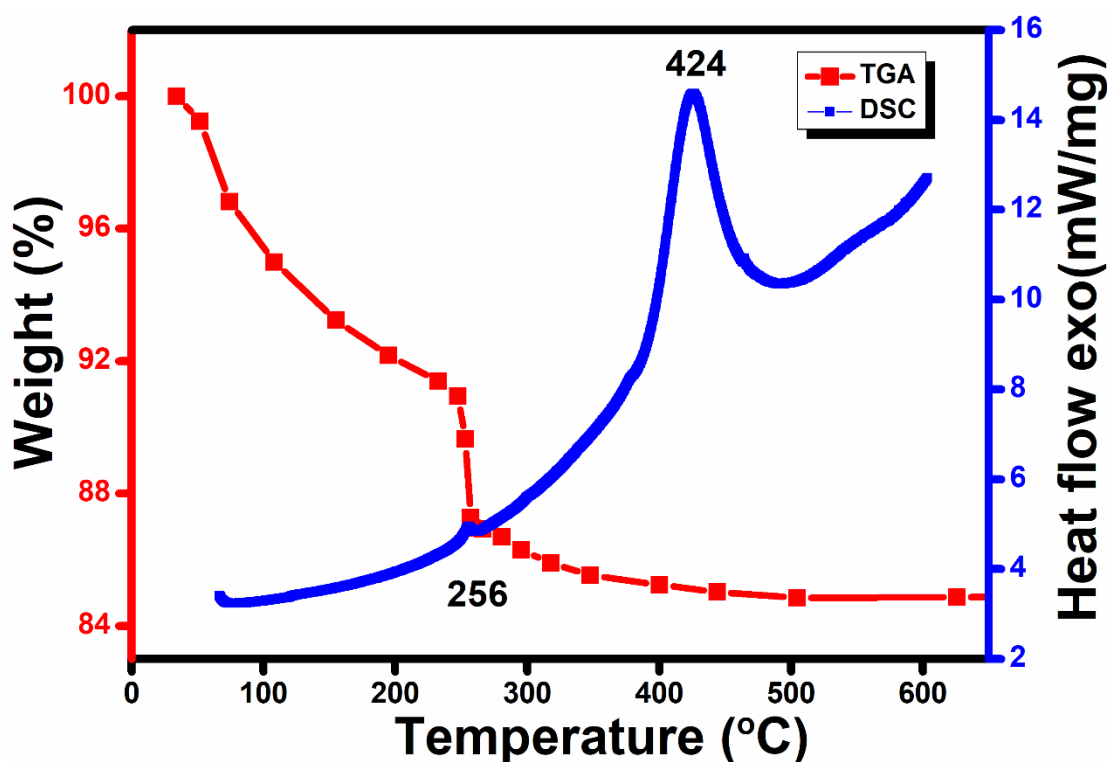


Figure 4.2.1: TGA-DSC plots of the as-prepared powder sample of  $\text{BiFeO}_3$ .

#### 4.2.3. Structural and Optical Analysis

The X-ray diffraction technique was used to examine the structure and purity of the as-prepared and calcined materials. In Figure 4.2.2a the XRD patterns of the as-prepared  $\text{BiFeO}_3$  precursor powder and the products calcined at 300°C and 500°C, for 4h, respectively, are presented. The

as-prepared powder is almost amorphous, followed by nucleation of BiFeO<sub>3</sub> and a secondary phase at 300°C. The XRD pattern of the 500°C calcined powder reflected well-resolved diffraction peaks for (010), (110), (111), (020), (120) and (121) planes corresponding to the rhombohedral crystal structure of the BiFeO<sub>3</sub> phase. All the peaks matched well with the reported XRD pattern of BiFeO<sub>3</sub> in JCPDS card number 72-2035. The patterns collected have been further refined by FULLPROF version 3.4.0 using the space group R3c. The structure refinement confirmed the presence of a minor impurity (<3%) phase of Bi<sub>2</sub>Fe<sub>4</sub>O<sub>9</sub> in the system. The rhombohedral crystal lattice structure derived from Vesta software from the XRD pattern is shown in the inset of Figure 4.2.2b. The information from the structure analysis confirms that the synthesized powder is a mixture of BiFeO<sub>3</sub> and Bi<sub>2</sub>Fe<sub>4</sub>O<sub>9</sub>.

The FTIR spectrum of the BiFeO<sub>3</sub> nanoparticles has been presented in Figure 4.2.2c. The bands observed around 400-600cm<sup>-1</sup> are the bending vibrations of Fe-O-Fe, the asymmetrical stretching of Fe-O-Fe bonds, and the deformation of FeO<sub>6</sub> octahedral perovskite structure, respectively. The two vibrational peaks observed ~551 and 457cm<sup>-1</sup> are due to the octahedral structure of BiO<sub>6</sub> and the latter one is also due to the bending vibration of Fe-O bond in FeO<sub>6</sub> octahedral unit. The absorption bands positioned at 813cm<sup>-1</sup> indicated the symmetric stretching of Bi-O bonds in BiO<sub>3</sub> pyramidal and BiO<sub>6</sub> octahedral units, respectively. The peak placed at 450-495cm<sup>-1</sup> is also due to Bi-O bonds in the BiO<sub>6</sub> structural unit. The broad absorption band centred at ~3437 and 1647cm<sup>-1</sup> corresponds to the stretching vibration of O-H bonds of adsorbed water onto the BiFeO<sub>3</sub> surface. In addition to FTIR, the Raman scattering measurement of the same is also important information for identifying different bond vibrations in BiFeO<sub>3</sub> lattice. Figure 4.2.2d represented several identified transverse optical (TO) phonon modes at 138 and 170cm<sup>-1</sup> responsible for A<sub>1</sub>, whereas 261, 275 and 522cm<sup>-1</sup> was responsible for E symmetry modes. The significant modes are responsible for rhombohedral BiFeO<sub>3</sub> structure.

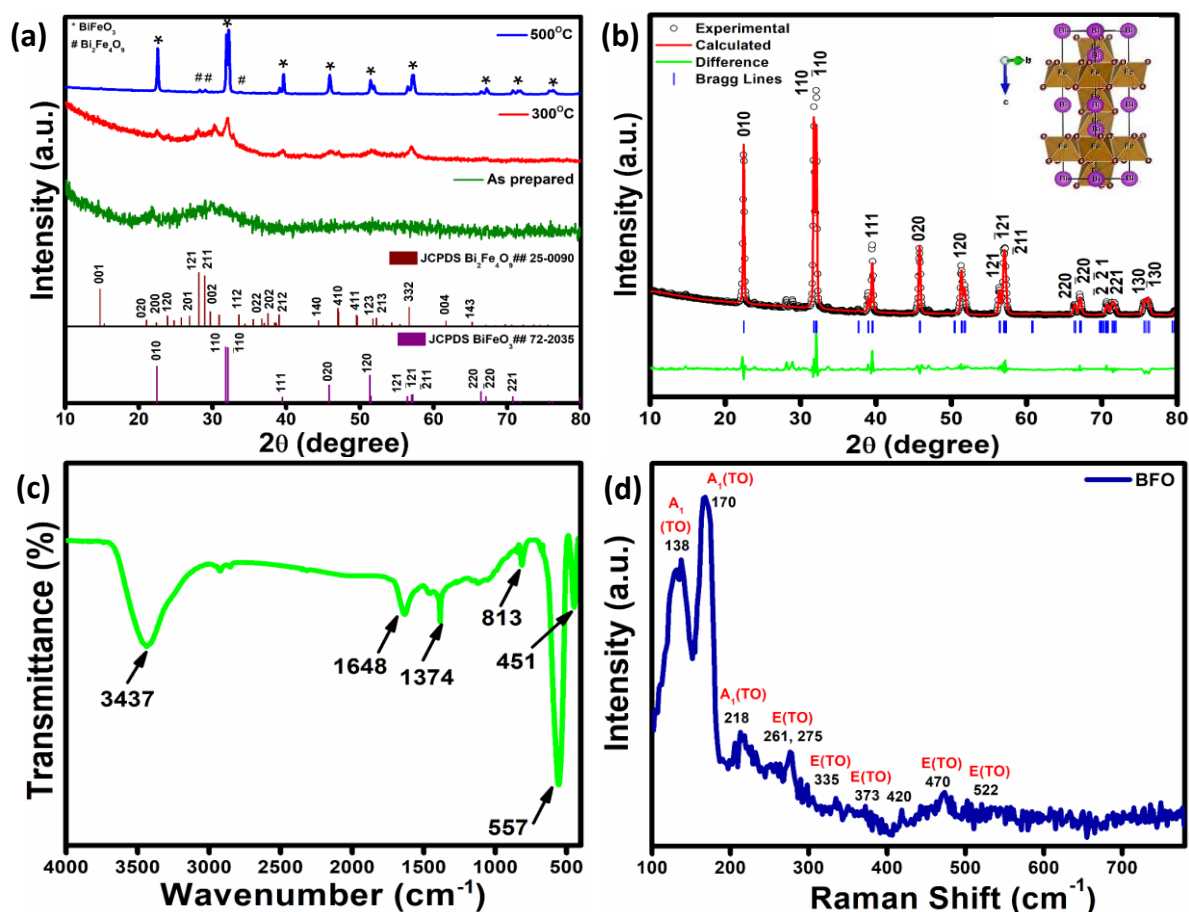


**Figure 4.2.2:** (a) X-ray diffraction pattern of the as-prepared sample followed by 300°C and 500°C calcined sample with the standard JCPDS card number (b) Experimental and FullProf refined X-ray diffraction pattern and Rhombohedral lattice structure (inset) (c) FTIR spectrum and (d) Raman spectrum of BiFeO<sub>3</sub>, respectively.

#### 4.2.4. Transmission Electron Microscopy Study

Transmission Electron Microscopic (TEM) investigations have been carried out, as shown in the representative TEM micrographs in Figure 4.2.3a-d. The bright-field images at different magnification, shown in Figure 4.2.3a-c, confirm the crystalline nature of the nanoparticle like grains, having an average size of 80-150nm in range. The distinct lattice fringes in high-resolution TEM image (Figure 4.2.3d) correspond to the (110) reflection of BiFeO<sub>3</sub> with a “d” spacing of 2.88Å and (121) plane of Bi<sub>2</sub>Fe<sub>4</sub>O<sub>9</sub> with an inter lattice spacing of 3.19Å respectively, which confirms the highly crystalline nature of the sample.

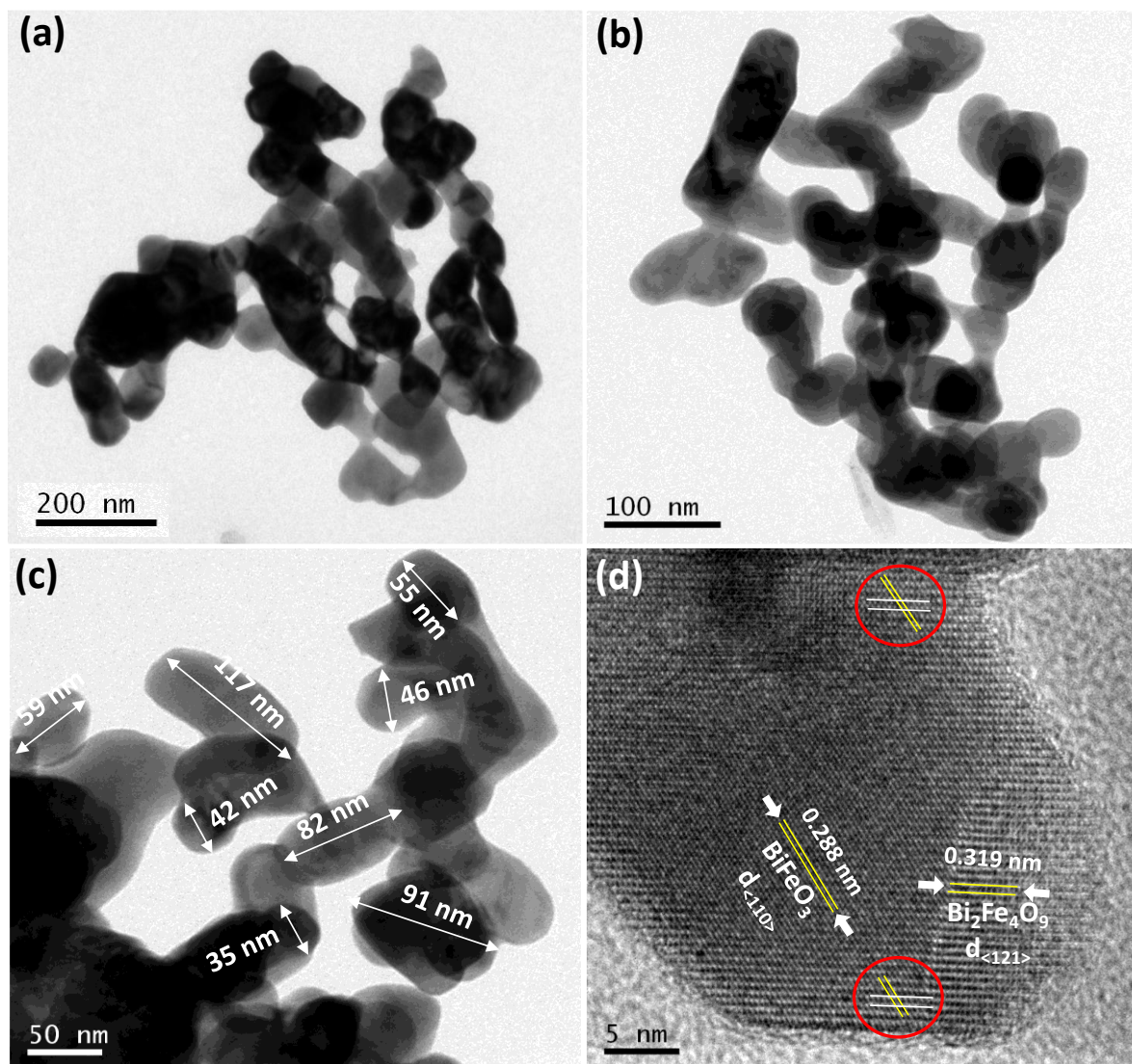


**Figure 4.2.3:** (a)-(c) TEM bright field image of  $\text{BiFeO}_3$  nanoparticle at different magnifications (d) HRTEM image.

#### 4.2.5. X-ray Photoelectron Spectroscopy Study

To find the valence state of Iron and Bismuth in BFO sample, photoelectron spectroscopic (XPS) measurements were carried out. In Figure 4.2.4a, the typical survey spectrum of BFO nanoparticles depicting  $\text{Bi}4f$ ,  $\text{Fe}2p$  and  $\text{O}1s$  is presented. In Figure 4.2.4b, the core-level XPS spectrum of  $\text{Bi}4f_{7/2}$  and  $\text{Bi}4f_{5/2}$  were observed at 158.9 and 164.2eV, respectively, which matches well with the  $\text{Bi}^{3+}$  energy levels in stoichiometric  $\text{BiFeO}_3$  [16].  $\text{Fe}2P$  spectrum in Figure 4.2.4c exhibits the features mostly of  $\text{Fe}^{3+}$  oxidation state as discerned from the binding energy of  $\text{Fe}2P$  for the sample. The core level  $\text{Fe}2P$  spectra of the BFO sample are present at

binding energies of 710.01eV for Fe2P<sub>3/2</sub>, and 723.56eV for Fe2P<sub>1/2</sub>. The satellite peak is present at 718.27eV for Fe2P<sub>3/2</sub>, and 731.80eV for Fe2P<sub>1/2</sub>. The presence of satellite peaks observed at the position of 8eV above the main peaks confirms the presence of Fe<sup>3+</sup> ions in the sample [18]. The peak at 711.1eV combined with two satellite peaks at 719.2 and 724.5eV confirms that the valence state of Fe is Fe<sup>3+</sup>, and there is no evidence for Fe<sup>2+</sup> existence within a few atomic percent resolutions. On deconvolution, the asymmetric O1s spectrum evolves into two components; a low binding energy (LBE) peak centered at 529.1eV (O<sub>L</sub> component) and a high binding energy (HBE) peak at 530.6eV (O<sub>V</sub> component), as shown in Figure 4.2.4d. The dominant O1 component is characteristics of O<sup>2-</sup> ions in the FeO<sub>6</sub> perovskite oxide lattice framework, whereas the O2 component at the higher binding side may be associated with the presence of chemisorbed oxygen in the grain boundaries or the existence of hydroxyl group (-OH) due to adsorption of water (H<sub>2</sub>O) onto the surface of the BiFeO<sub>3</sub> during synthesis through aqueous medium route which admittedly supports the FTIR data.

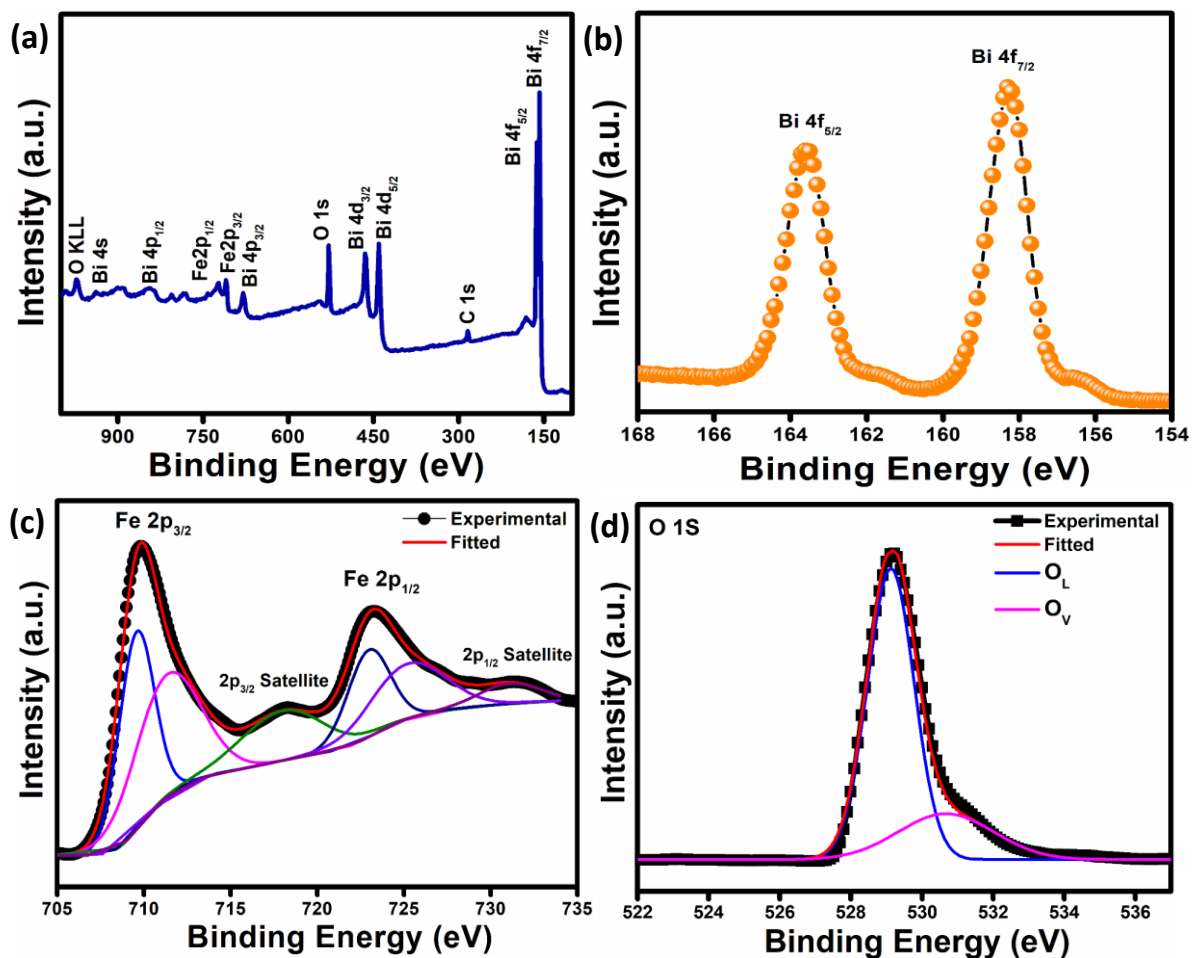


**Figure 4.2.4:** XPS of  $\text{BiFeO}_3$  nanoparticles (a) survey spectrum, (b) spin-orbit split peaks of Bi 4f, (c) Fe2P core level and (d) spectral decomposition of the O1s spectrum results in two different types of oxygen environment denoted as  $O_L$  and  $O_V$  fitted component in the  $\text{BiFeO}_3$  nanoparticle.

The symmetry in the O1s binding energy peak has been anticipated to be due to oxygen vacancy in the sample. In order to confirm the presence of oxygen vacancies, we have carried out fluorescence measurements of the calcined samples. Interestingly, the synthesized BFO sample exhibited a blue emission with a  $\lambda_{\text{max}}$  of 420nm, shown in Figure 4.2.5a which is probably due to the presence of oxygen vacancies. The calculated surface area of the BFO nanoparticle was found to be about  $32.3\text{m}^2/\text{g}$ , shown in Figure 4.2.5b which in turn can provide more surface-active sites for adsorption of oxygen species for reacting with gas molecules.

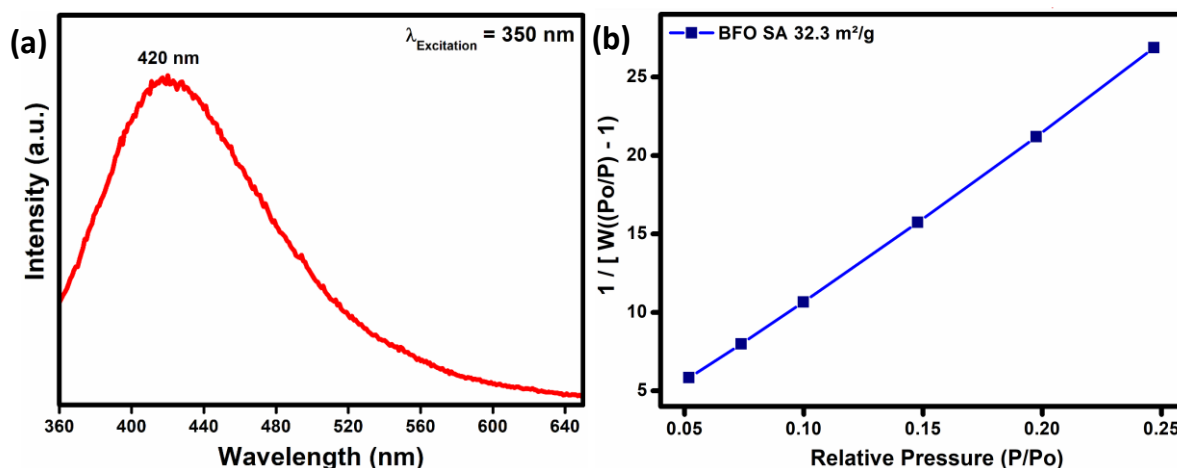


**Figure 4.2.5:** (a) Fluorescence Spectra of BFO nanoparticle (b) Surface area of BFO nanoparticle-based sensor.

#### 4.2.6. Magnetic Study

The DC magnetization hysteresis loop of BiFeO<sub>3</sub> nanoparticles as measured at room temperature has been presented in Figure 4.2.6. From the recorded M-H loop, the as-prepared particles' ferromagnetic nature is exhibiting a straight forward ferromagnetic ordering at 300K with coercivity ( $H_C$ ) of 528G saturation magnetization ( $M_s$ ) of 0.0828emu/g under the magnetization field of 1.2 Tesla. The remanent magnetization value of 0.0097emu/g indicates the ferromagnetic nature of the sample. The magnetic hysteresis loops exhibit exchange bias and vertical asymmetry because of spin pinning at the boundaries between ferromagnetic and antiferromagnetic domains [22].



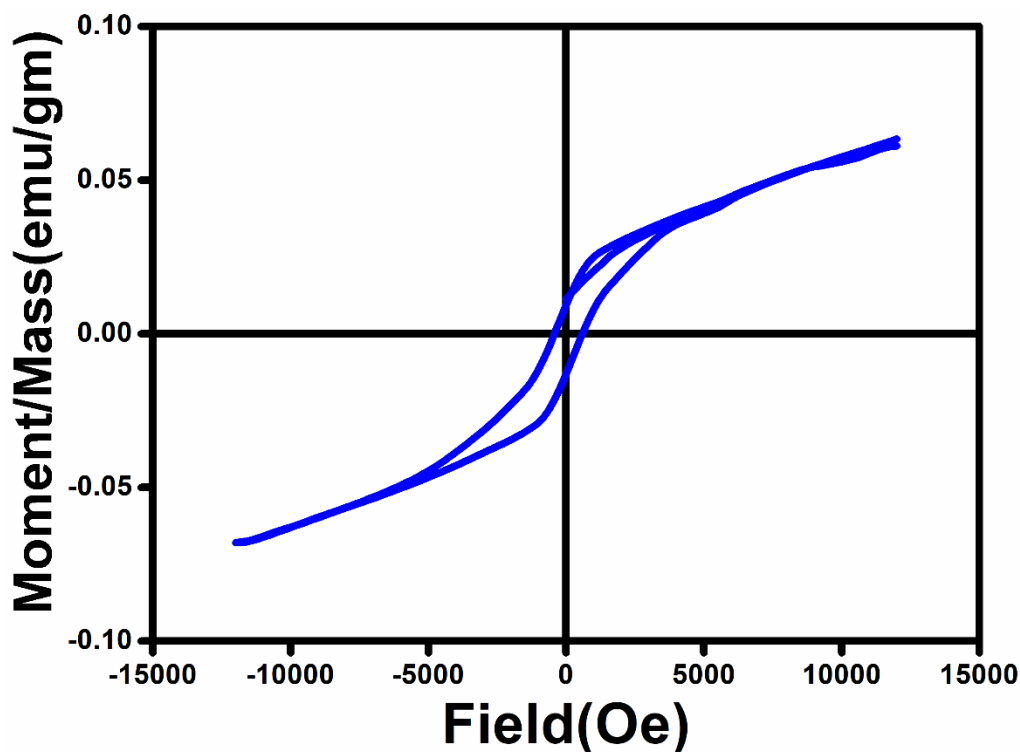
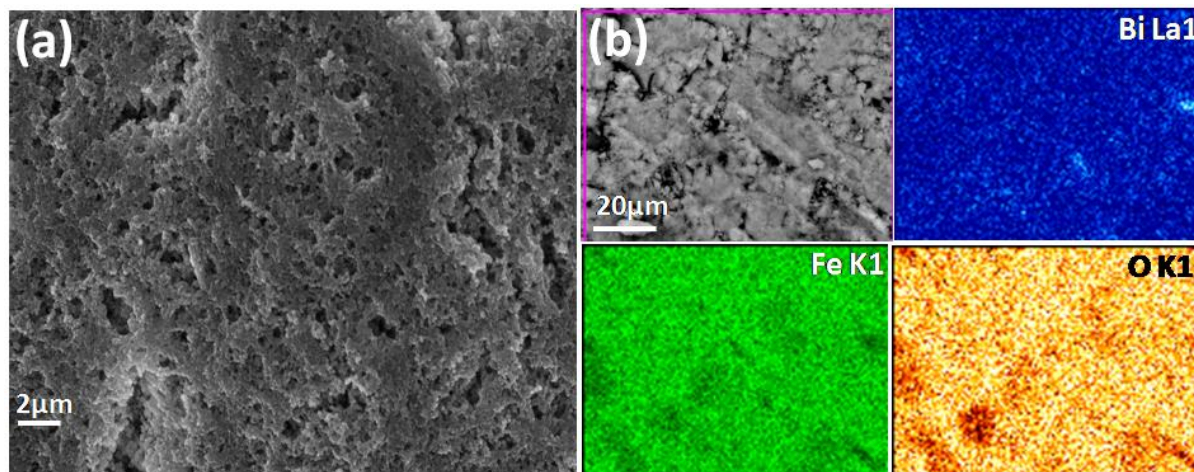


Figure 4.2.6: M-H curve of the BiFeO<sub>3</sub> nanoparticle

#### 4.2.7. Microstructural Analysis of fabricated BiFeO<sub>3</sub> Nanoparticles based Film

In order to investigate the microstructural properties of synthesized BiFeO<sub>3</sub>, films were fabricated on top of FTO electrodes, and the microstructural analysis of the fabricated film is shown in Figure 4.2.7a. The surface of the fabricated film indicates agglomeration of BiFeO<sub>3</sub> nanoparticles and formed dense porous layer throughout the film. The film's colour elemental mapping was executed as shown in Figure 4.2.7b EDAX analysis. The extensive area mapping ensures homogeneous distribution of Bi, Fe and O as the only element present in the BiFeO<sub>3</sub> film. The colour mapping analysis also indicates insufficient amount of O in BiFeO<sub>3</sub> compared to that observed from XPS analysis for O1s spectrum as well and further corroborates the quantitative TEM-EDAX data.



**Figure 4.2.7:** (a) Surface microstructure (b) Corresponding colour elemental mapping through EDX analysis.

#### 4.2.8. Acetone Sensor Application

As there are only a few reports on the acetone sensing characteristics of pure  $\text{BiFeO}_3$  samples, we have tested the acetone sensing characteristics of the synthesized powder. After fabrication, the variation of resistance of BFO based sensor with operating temperature has been monitored as shown in Figure 4.2.8a. The resistance of the BFO based sensor asymptotically decreases with increase in the operating temperature. This is probably due to more electrons entering into the conduction band from the valence band of BFO with physisorption of oxygen molecules resulting in a sharp decrease in the resistance with increasing the operating temperature [23]. Besides, Figure 4.2.8b exhibits the dynamic response of synthesized BFO based gas sensors towards different acetone concentrations (10, 5, 2 and 1ppm) at the operating temperature of  $260^\circ\text{C}$ . The response curve as a function of operating temperature is further recorded, as shown in Figure 4.2.8c. The sensor was exposed towards 10, 5, 2 and 1ppm of acetone, varying the operating temperature from  $170^\circ\text{C}$  to  $350^\circ\text{C}$ . The maximum sensitivity was observed at an operating temperature of  $260^\circ\text{C}$  ( $R_g/R_a$  about 12.1, 9.2, 8.2 and 7.5 for 10, 5, 2 and 1ppm of acetone, respectively) with 15sec of exposure time. At first the sensitivity of the sensor increases along with the increment of operating temperature which resulted to reach a maximum value at  $260^\circ\text{C}$  and above this temperature the response decreases with increasing

temperature. The first thing observed here was that under exposure to acetone, the sensor resistance increased, indicating the fabricated sensor's typical p-type behaviour. This also fits a mechanism in which adsorbed oxygen plays the role of the surface acceptor. The response ratio (S) of the sensor toward the different acetone concentrations (C) can be empirically given by the following equation [24]:

$$S \propto \frac{aC^b}{1+aC^b} \dots\dots\dots(4.1)$$

Here C is the acetone concentration, a is the proportionality factor and b is the exponent [24, 25]. But the concentration of acetone was very low for our current work so,  $aC^b \rightarrow 0$ , hence the equation (4.1) is modified and represented as [26]:

$$S \propto aC^b \dots\dots\dots(4.2)$$

The above equation (4.2) can be rewritten as a relation:

$$\log(S) = \log a + b \log C \dots\dots\dots(4.3)$$

And the power-law relation between the responses of BFO based sensor and the acetone concentration was represented in Figure 4.2.8d. The linear fitting of the experimental data shown in Figure 4.2.8d confirms the lower concentration sensing ability of the BFO based sensor.

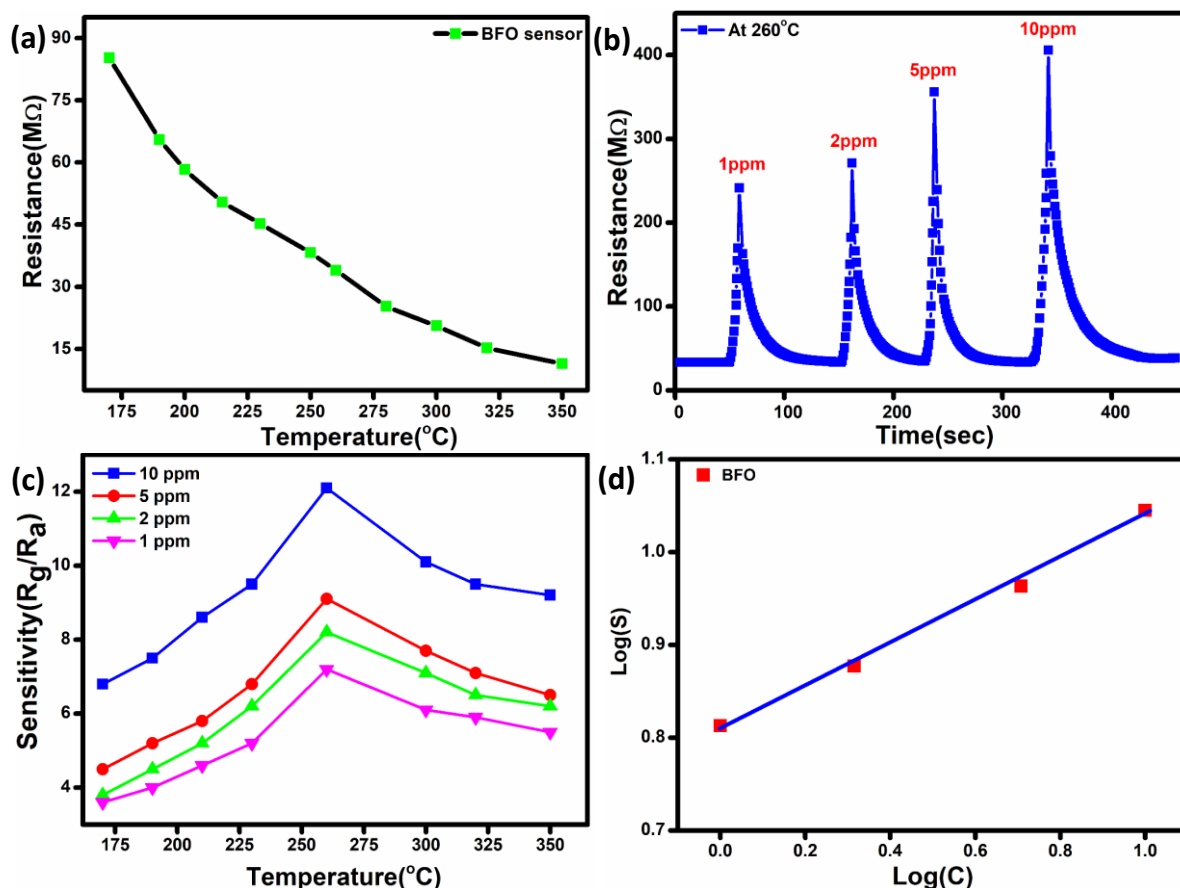


**Figure 4.2.8:** (a) Variation of resistance of the sensor with operating temperature, (b) Dynamic response curve of the sensor towards different concentrations of acetone at 260 $^{\circ}C$  operating temperature (c) Response of different concentrations of acetone as a function of operating temperature, and (d) Linear correlation between the  $\log(S)$  vs.  $\log(C)$  for the BFO based sensor.

The two essential parameters of sensitivity study as the sensor's response and recovery time were calculated from the dynamic response curve towards 10ppm acetone at the optimized operating temperature 260 $^{\circ}C$  is presented in Figure 4.2.9a. It is well indicated that the response and recovery time of the sensor is rapid, about 12sec and 25sec < respectively, which makes the BFO based sensor as an upcoming material for acetone detection. The variation of the recovery time as a function of operating temperature is presented in Figure 4.2.9b for different concentrations of acetone. The respective recovery time calculated from the plot is about 25sec, 17sec and 15sec towards 10ppm, 5ppm and 1ppm acetone, respectively. Besides, the  $I$ - $V$  characterization is measured at the voltage bias range of -40V to +40V. Figure 4.2.9c shows a

linear ohmic response at different temperatures in a wide range from 170°C-350°C in the presence of 10ppm acetone gas. The comparison of *I-V* measurement study has been presented in Figure 4.2.9d in the presence of air and acetone. In both Figure 4.2.9c and d, the *I-V* characteristics of a Schottky type metal-semiconductor contact were evident for all the operating temperatures. The *I-V* curve of the as-fabricated gas sensor showed a symmetric behaviour, from which we could conclude that not only the metal-semiconductor junction but also the semiconductor–semiconductor junction between the networked SnO<sub>2</sub> nanoparticles is also ohmic. This ohmic behaviour is very important to the sensing properties, because the sensitivity of the gas sensor or the ratio of electrical resistance in acetone gas to dry air can be maximized when the metal-semiconductor junction is ohmic or has a negligible junction resistance. Figure 4.2.9d shows the comparison of *I-V* characteristics in air and in presence of 10ppm acetone at 260°C operating temperature.

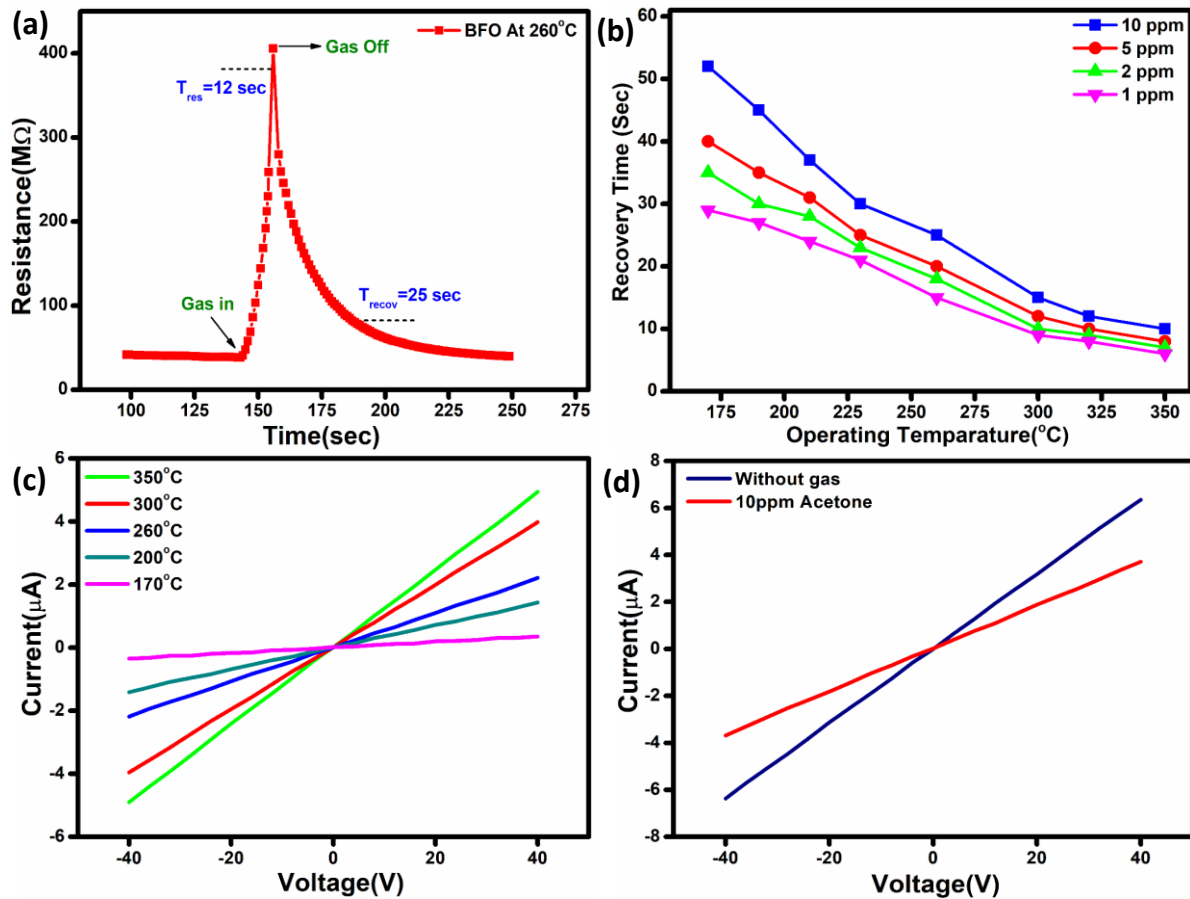


**Figure 4.2.9:** (a) Dynamic response curve towards 10ppm acetone showing the response and recovery time (b) Variation of recovery time with an operating temperature towards different concentrations of acetone (1, 5 and 10ppm) (c) I-V characterization BFO based sensor in different operating temperature, (d) Comparison of I-V characterization in air and acetone gas of BFO based sensor.

Besides stability and reproducibility, selectivity is the crucial indicator for metal oxides-based gas sensor. We have checked the response behaviour of BFO based sensor under expose of different gas to understand the selectivity. To examine the cross response or selectivity of the sensor towards different gases of equal concentration by volume and thereby determine its selectivity to any particular gas, the dynamic response behaviour of the fabricated sensor towards 10ppm of different gases were monitored. The BFO based gas sensor exhibited higher selectivity towards acetone than ammonia, nitrogen, methanol and ethanol, as observed from Figure 4.2.10. For better understanding, the cross-sensitivity of BFO based sensor towards acetone was evaluated by a selectivity co-efficient that can be defined as [27],  $\beta = S_{acetone}/S_{gas}$ . Here  $S_{acetone}$  and  $S_{gas}$  are the sensor's response towards acetone and any other gas. From Figure

10 the calculated selectivity co-efficient ( $\beta$ ) is varied like  $\beta_{\text{ammonia}} (9.7) > \beta_{\text{ethanol}} (4.8) > \beta_{\text{methanol}} (3.8) > \beta_{\text{nitrogen}} (3.2)$ , all of which are more than one and confirm the acetone n-selective nature of the sensing material.

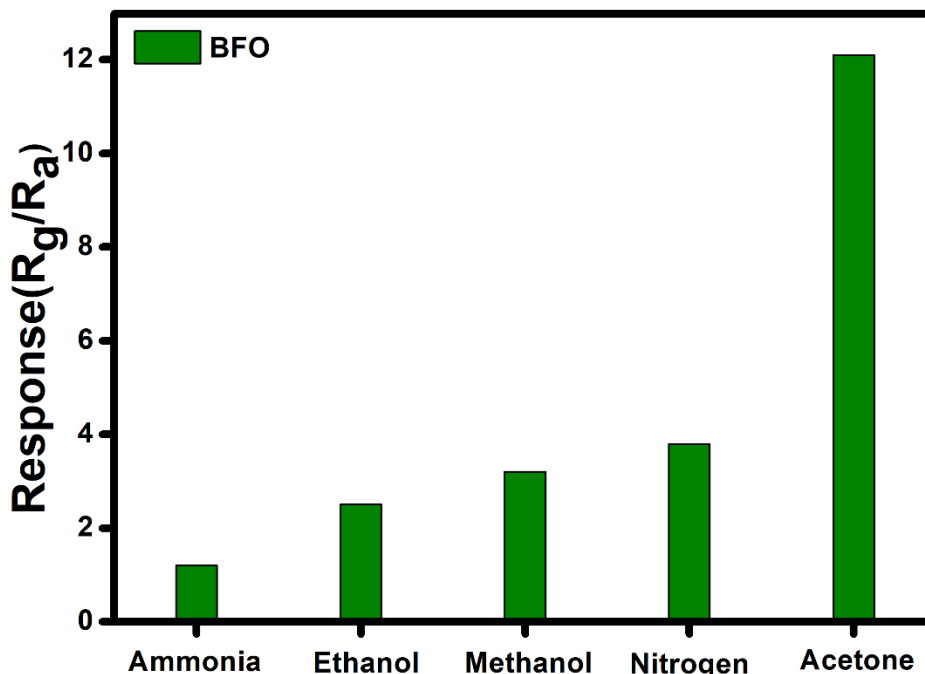


Figure 4.2.10: Selectivity of  $\text{BiFeO}_3$  nanoparticle-based sensor towards different gases.

#### 4.2.9. Impedance behaviour under dry air and acetone:

The mechanism of gas sensing response can be distinguished with an applied AC signal with the frequency. The sensor's conductivity can be determined by employing AC signal in presence of dry air and acetone to understand the contribution of the bulk, grain boundary and electrode. The impedance study was carried out to figure out the sensing mechanism of BFO based sensors. In the presence of air and acetone, the fabricated sensor's complex impedance data was measured using a precision impedance analyzer in the 100Hz to 1MHz frequency range with varying operating temperature where  $Z'$  indicates the fundamental part and  $Z''$  represents the imaginary part of the complex impedance [28-30]. To understand the effect of the operating temperature of the sensor, the AC impedance of the BFO based sensor was further

monitored by varying the temperature from 170°C to 350°C at different frequencies. We plotted the Nyquist diagram from the impedance measurements in the presence of dry air and acetone, shown in Figures 4.2.11 (a & b). The impedance variation of BFO based sensor in the presence of acetone and air is indicated in Nyquist diagram Figure 4.2.11c. From the Arrhenius equation, the relationship between resistance and temperature can be explained like that:

$$R = R_0 \exp(E_a/KT) \dots\dots\dots(4.4)$$

Here  $E_a$  can be described as activation energy and  $K$  is the Boltzmann's constant,  $T$  is the temperature in Kelvin (K) and  $R_0$  is pre-exponential factor. The activation energy calculated from the electrical parameter has been well plotted in Figure 4.2.11d from the slope of  $\ln(R)$  vs  $1/KT$  graph with the value 0.444 eV for BFO based sensor.

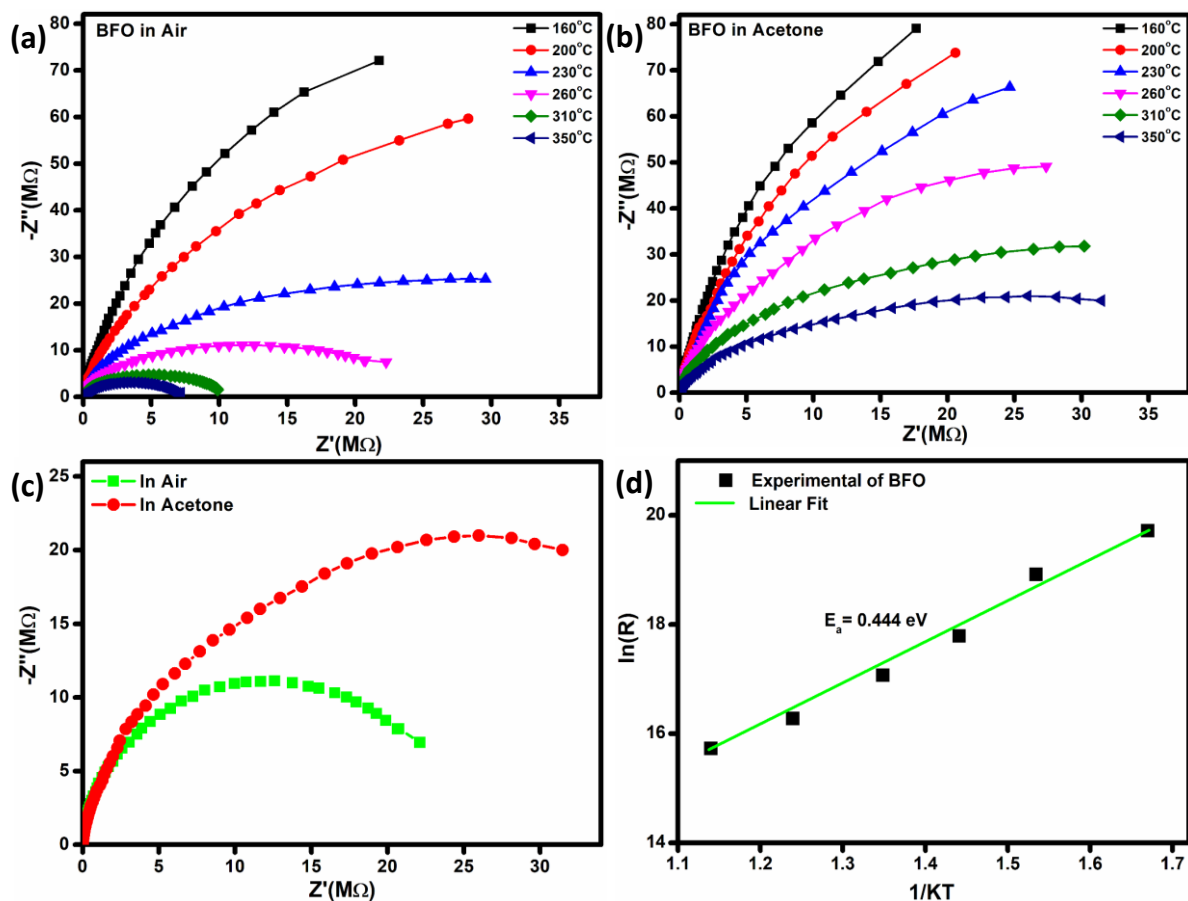


**Figure 4.2.11:** Nyquist plot of BFO based sensor (a) in air and (b) in the presence of acetone at different operating temperature (c) Difference in Nyquist plot in presence of air and acetone (d) Activation energy calculated from impedance data of BFO based sensor.



Regardless of the measured temperatures, the impedance data showed a single semicircle. It means that the electrical properties of samples are dominated by one electrical component corresponding to grain contribution. It could be observed that the diameter of the semicircle decreases monotonously with operating temperature, which means the resistance decreases as the temperature increases.

The Nyquist plot interprets about the effect of adsorption and desorption of the oxygen molecules with operating temperature under air and acetone. This phenomenon could be understood from the Lennard-Jones equation: [31]

$$\frac{d\theta}{dt} = K_{ads}e^{-\Delta E_A/KT} - K_{des}e^{-(\Delta E_A + \Delta H_{chem})/KT} \dots\dots\dots(4.5)$$

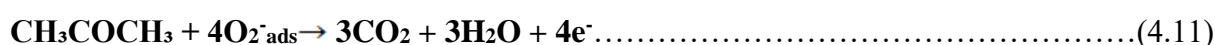
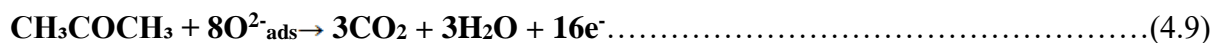
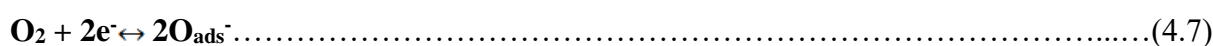
Where  $\theta$  is the fraction of available surface sites covered,  $K_{ads}$  and  $K_{des}$  are the rate constants for adsorption and desorption reaction, respectively,  $\Delta E_A$  is the activation energy of chemisorptions and  $\Delta H_{chem}$  is the heat of chemisorptions. From this equation we can easily interpret how the chemisorptions of molecules depend on the operating temperature. It has been observed that at the lower operating temperature, only physisorption process may occur, which decreases with increasing the operating temperature and at a higher operating temperature such as  $KT \geq \Delta E_A$ , the chemisorptions process will occur and the desorption rate became negligible at higher operating temperatures. In this study, the operating temperature varied between 170°C to 350°C and the expected chemisorption mechanism. At 260°C, the rate of adsorption and desorption led to a maximum equilibrium state, resulting in the sensor's maximum sensitivity. The sensitivity further reduces on increasing the operating temperature above 260°C. Then 260°C was found as the optimal operating temperature for acetone detection using BFO sensor.

#### **4.2.10. Gas Sensing Mechanism**

Based on the adsorption and desorption of the gas molecules on the surface of the particles, the mechanism of the sensing property mainly depending on the change of resistance of the

semiconductor with temperature and analyte gas concentration. Perovskite BFO nanoparticles are reported to be a p-type semiconductor with the hole as the majority carrier. By monitoring the response of the BFO based sensor in air and in presence of acetone, it has also been confirmed that the sensor shows a p-type sensing behaviour which means the resistance increases on exposure to acetone gas. The oxygen vacancies and defect states in the sample help the oxygen molecule to get adsorbed on the surface. The oxygen adsorbed by the BFO surface produces  $O^{2-}$ ,  $O_2^-$  and  $O^-$  species by capturing the electrons from the conduction band of the BFO surface when BFO sensor is exposed to the air. When the sensor is exposed to acetone gas, it gets adsorbed on the surface which interacts with the oxygen ions, release carbon dioxide, water vapour, and electron to the conduction band [23].

During such surface reactions, electron concentration of the semiconductor is increased which recombine with the holes present in the valence band, resulting in a reduction in the hole concentration of BFO nanoparticles. Since BFO nanoparticles is a p-type semiconductor so a decrease in the number of holes concentrations means an increase in resistance which is has been evident in the response curve [32, 33]. The overall mechanism as described has been shown in the following equations,



#### **4.2.11. Conclusions**

In conclusion, the ferromagnetic BiFeO<sub>3</sub> nanoparticles have been prepared through hydrazine assisted co-precipitation method. Various structural and optical characterizations emphasize

the formation of rhombohedral BiFeO<sub>3</sub> nanoparticles. Besides, X-ray photoelectron spectroscopic study established the phase purity of Bi, Fe and O in the BiFeO<sub>3</sub> nanoparticles with an indication of oxygen deficiency. In this work, particular attention has been given to vacancy-induced sensing properties of p-type BFO nanoparticles exhibiting rapid response, fast recovery, and good selectivity for acetone, a well-accepted biomarker in breath for diabetes detection. Further, the BiFeO<sub>3</sub> nanoparticles exhibited significant sensing response towards different concentration of acetone (10, 5, 2 and 1ppm). Considerable enhancement in gas sensing properties is achieved, the response up to 12.1 towards 10ppm acetone gas at operating temperature 260°C followed by reasonably good stability up to three months. The BiFeO<sub>3</sub> based sensor exhibited higher stability, selectivity, rapid response, recovery time and reproducibility for acetone sensing. Notably, the impedance analysis correlates the sensing mechanism with acetone. The results obtained series of studies suggest the enhanced performance of the synthesized BiFeO<sub>3</sub> nanoparticles compared to the other reports. The experimental results thus indicate that this simple and cost-effective sonochemical process can be used to prepare BiFeO<sub>3</sub> nanoparticles to use them as a promising tool for fabricating acetone sensor for futuristic applications.

### **4.3. Zn<sub>2</sub>SnO<sub>4</sub> based material for Acetone Sensing**

#### **4.3.1. Background**

Interest in design and development of alternate metal oxides for gas sensor (MOS) has grown considerably in recent years to replace commonly used semiconducting oxides materials such as SnO<sub>2</sub>, ZnO, Iron Oxide and WO<sub>3</sub>. For achieving improved sensitivity at lower operating temperatures along with faster response-recovery time, the research focus has been directed to establish newer ternary semiconducting oxides [34-36]. Among the many known ternary oxide semiconductor materials, we have chosen zinc stannate (Zn<sub>2</sub>SnO<sub>4</sub>) due to its higher electron mobility, good electrical conductivity with higher thermodynamic stability. In one of our recent studies, we have demonstrated the application of Zn<sub>2</sub>SnO<sub>4</sub> in DSSC as a photoanode material. In this thesis work, we have explored a newer application of Zn<sub>2</sub>SnO<sub>4</sub> in acetone sensing.

Reports on gas sensing characteristics of Zn<sub>2</sub>SnO<sub>4</sub> have been scarce compared to regular binary oxides. Excellent sensing property was demonstrated with Zn<sub>2</sub>SnO<sub>4</sub> nanostructures towards ethanol by Chen et al. (2011) [37]. They further reported one-step synthesis of flower like Zn<sub>2</sub>SnO<sub>4</sub> and explained the gas sensing properties of ethanol with high response [38]. There are also many reports on the sensing performance of various structures of Zn<sub>2</sub>SnO<sub>4</sub> towards ethanol [39-42]. In this work, Zn<sub>2</sub>SnO<sub>4</sub> synthesized by three different synthesis techniques such as sonochemical, hydrothermal and solid-state process have been used for fabricating acetone sensing thereby understanding the particle size effect and surface characteristics of this multicomponent oxide in the sensing mechanism. By employing these three synthesis techniques, the particle size has varied from 5-10nm in hydrothermal synthesis technique, 50-100nm in the solid-state process and for sonochemical synthesis process it varied like 100-125nm. The sensing response of the fabricated sensor was monitored towards acetone by varying different concentrations under a wide range of operating temperatures ranging from 200°C to 350°C. AC impedance study was carried out in presence of acetone to understand the

electrical properties and its effect on sensing mechanism. Through this investigation, we could propose  $Zn_2SnO_4$  as a new type of ternary metal oxide higher sensing response towards very low ppm of acetone with higher sensitivity and stability.

#### 4.3.2. Results and Discussion:

After annealing, the samples were characterized with an X-ray diffraction (XRD) study to understand the phase purity. All the diffraction peaks have been indexed and well-matched with the reported standard  $Zn_2SnO_4$  (JCPDS card no: 74-2184, lattice parameter: 8.650 Å). The XRD pattern of ZTO-Hydro, ZTO-Solid and ZTO-Sono is shown in Figure 4.3.1 indicating the well crystalline nature of the synthesized materials [43,44]. The diffraction peaks such as (311), (222), (400) and (440) signify the phase formation of  $Zn_2SnO_4$ . No extra peaks of ZnO and  $SnO_2$  in the XRD pattern were the evidence of the pure phase of  $Zn_2SnO_4$ .

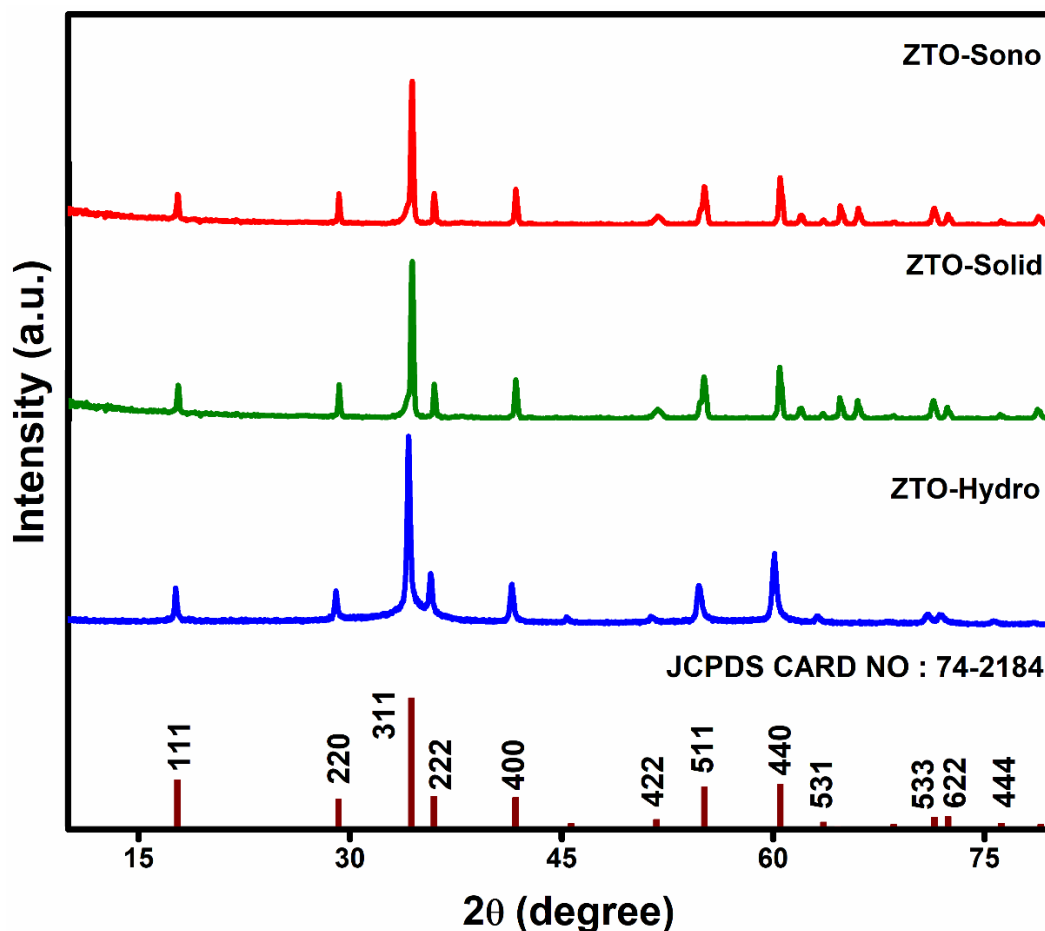
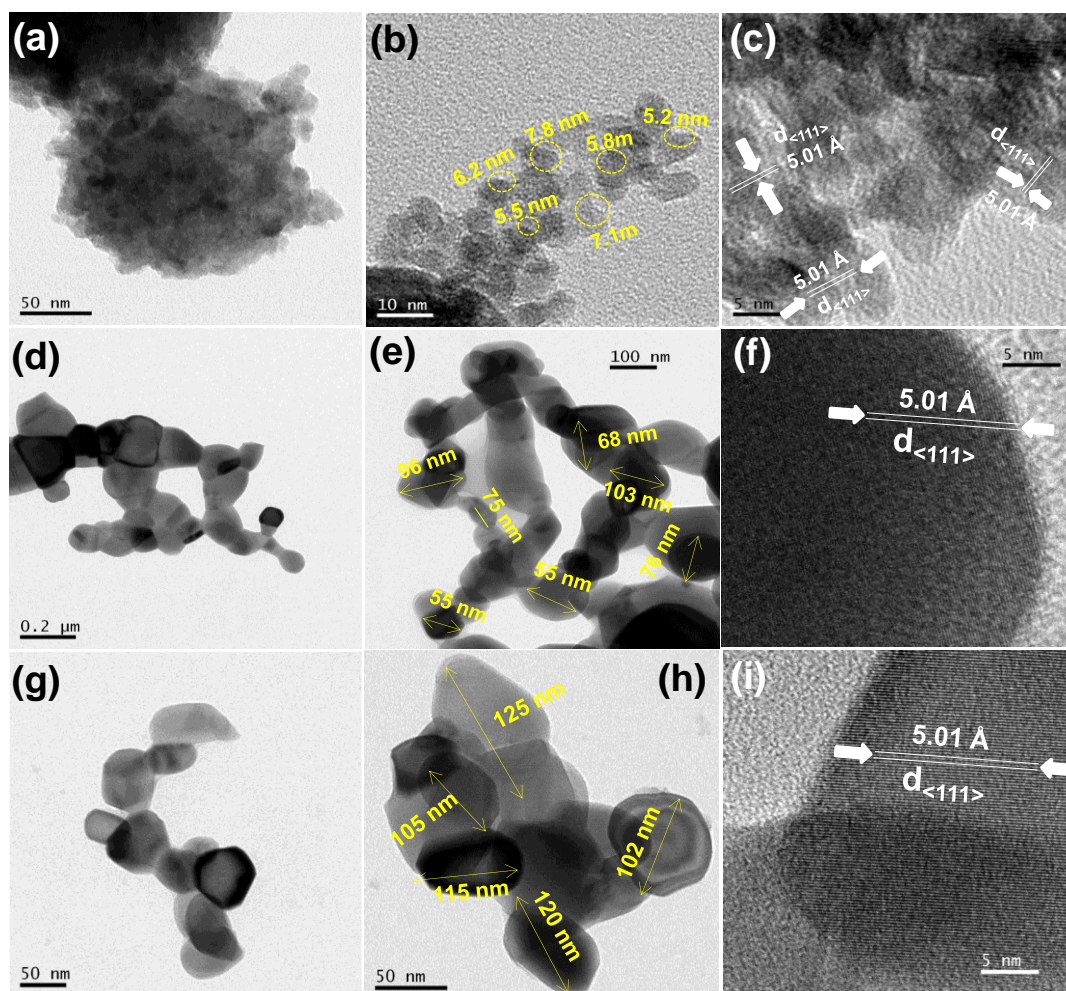


Figure 4.3.1. X-ray diffraction pattern of ZTO-Hydro, ZTO-Solid and ZTO-Sono.

The size and morphology of the synthesized samples ZTO-Hydro, ZTO-Solid and ZTO-Sono were examined by Transmission electron microscope bright-field images shown in Figure 4.3.2 (a, d, g). The uniform spherical morphology of the ZTO nanoparticles is clearly displayed, and the particle size distribution is calculated from the bright field image of Figure 4.3.2 (b, e, h). The figure represents that the sample is spherical in shape and the average particle size of ZTO-Hydro is 5nm and 50-100nm for ZTO-Solid and for ZTO-Sono it is 100-125nm. The lattice structure of the ZTO nanoparticles is clearly shown in the typical HRTEM image in Figure 4.3.2 (c, f, i). The crystallographic planes of ZTO sample were measured to be 5.01Å corresponding to the (111) plane of  $Zn_2SnO_4$  [45].



**Figure 4.3.2.** Transmission electron micrographs bright field image and HRTEM image of (a-c) of ZTO-Hydro (d-f) ZTO- Solid and (g-i) ZTO-Sono, respectively.

The Brunauer-Emmett-Teller (BET) surface area of ZTO-Hydro, Solid and Sono based samples was measured by nitrogen isothermal adsorption process (Figure 4.3.3). The ZTO-Hydro exhibited an enhanced BET specific surface area of 86.2m<sup>2</sup>/g than ZTO-Solid (16.9m<sup>2</sup>/g) and ZTO-Sono (10.3m<sup>2</sup>/g). The comparatively higher surface area of hydrothermally synthesized based sample is more attractive and useful for gas sensor fabrication as more surface-active sites are required for a large amount of surface adsorbed oxygen species.

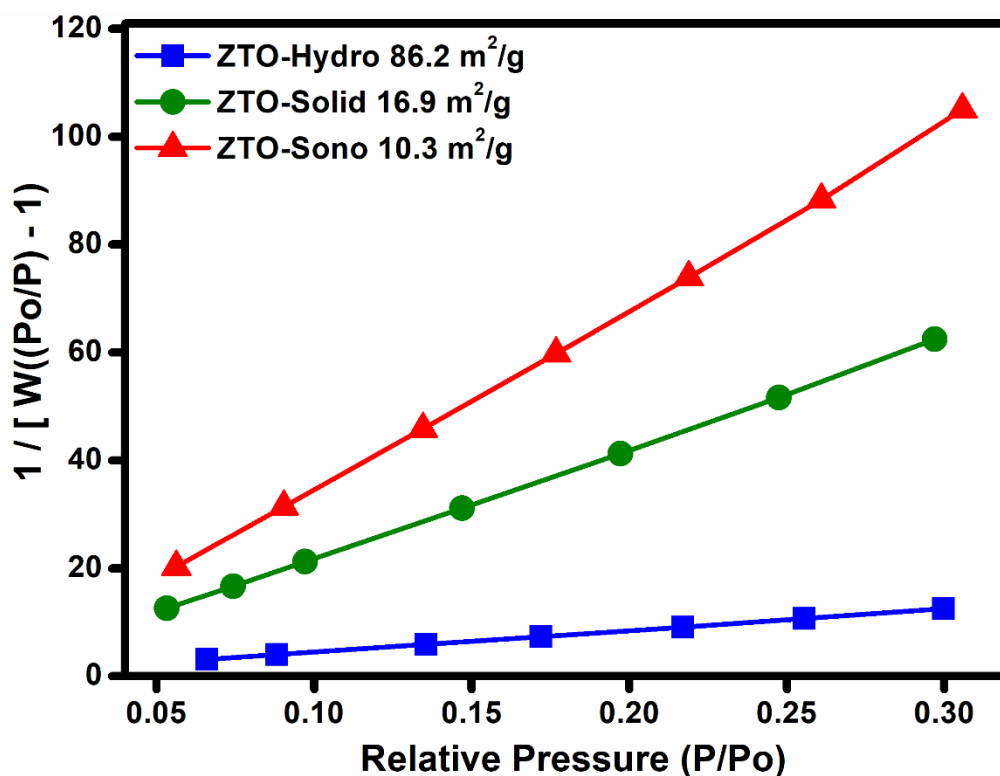
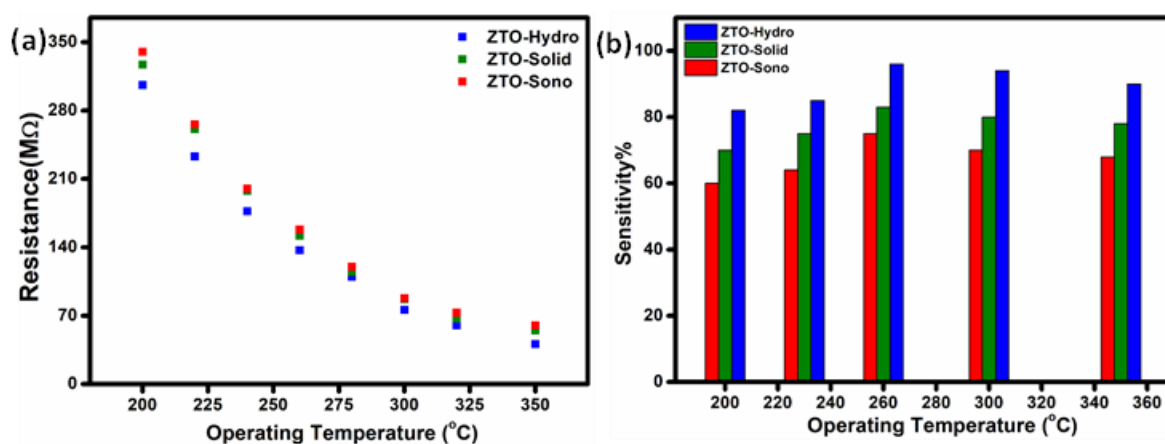


Figure 4.3.3: Surface area of ZTO based samples synthesized by Hydrothermal, Solid-State and Sonochemically Synthesis Process.

#### 4.3.3. Sensor Measurements:

It is well established that operating temperature plays an important role to understand the relation with the sensing responses performance of the sensors [46-49]. Initially, we have monitored the change of base resistance as a function of the operating temperature of the fabricated sensors in a wide range of temperatures varying from 200°C to 350°C. The sharp

change in resistance of all the sensors in air fabricated by ZTO-Hydro, ZTO-Solid and ZTO-Sono with temperature is plotted in Figure 4.3.4a. The comparison between the three synthesis processes was also implemented in the given diagram. The hydrothermal based sensor showed comparatively lower resistance in  $K\Omega$  range than another synthesis-based sensor. The fundamental properties of the fabricated sensor have been investigated and the sensing response is shown in Figure 4.3.4b with different operating temperatures. The three synthesized sample-based sensor responds to 10ppm acetone at various operating temperatures from 160°C to 350°C. It is clear from the plot that 260°C is considered the optimum operating temperature because the sensor material gets sufficient thermal energy for the reaction between the adsorbed oxygen species the target gas molecules. At the lower operating temperature, for the lack of energy, the acetone molecules cannot overcome the energy barrier and cannot react with the surface oxygen species, resulting in lower sensing response. As we increase the operating temperature the sensing response decreases because of the reduction in the gas adsorption capacity. As a result, the hydrothermal synthesis-based sensor shows a higher sensing response about 96% at 260°C towards 10ppm acetone, which is much higher than the other two samples synthesized by sonochemical and solid-state process. They showed sensing response 85% and 80% towards 10ppm acetone, respectively.



**Figure 4.3.4.** (a) Variation of base resistance with operating temperature of the (b) Sensing response variation towards 10ppm acetone as a function of operating temperature.



For better understanding of the cross-sensitivity of ZTO based sensor towards acetone, selectivity co-efficient which can be defined as,  $\beta = S_{\text{acetone}}/S_{\text{gas}}$  where  $S_{\text{acetone}}$  and  $S_{\text{gas}}$  are the response of the sensor towards acetone and any other gas in same concentration range has been calculated [27]. The selectivity co-efficient ( $\beta$ ) calculated from Figure 4.3.5 (a, b, c) is varied in the order  $\beta_{\text{NOx}} (6.4) > \beta_{\text{ammonia}} (5.6) > \beta_{\text{formaldehyde}} (4.8) > \beta_{\text{Ethanol}} (4.3) > \beta_{\text{CO}} (3.8)$  for ZTO-Hydro and it is in the order  $\beta_{\text{NOx}} (5.6) > \beta_{\text{ammonia}} (4.9) > \beta_{\text{CO}} (4.6) > \beta_{\text{formaldehyde}} (4.2) > \beta_{\text{Ethanol}} (3.8)$  for ZTO-Solid and the selectivity co-efficient is varied like  $\beta_{\text{ammonia}} (5.2) > \beta_{\text{formaldehyde}} (3.9) > \beta_{\text{Ethanol}} (2.8) > \beta_{\text{CO}} (2.7)$  for ZTO-Sono which further confirms a good selective nature of the sensor towards acetone. Figure 4.3.5d suggests the superior selectivity nature of the ZTO based sensing material, which is the most desirable feature for acetone sensing application.

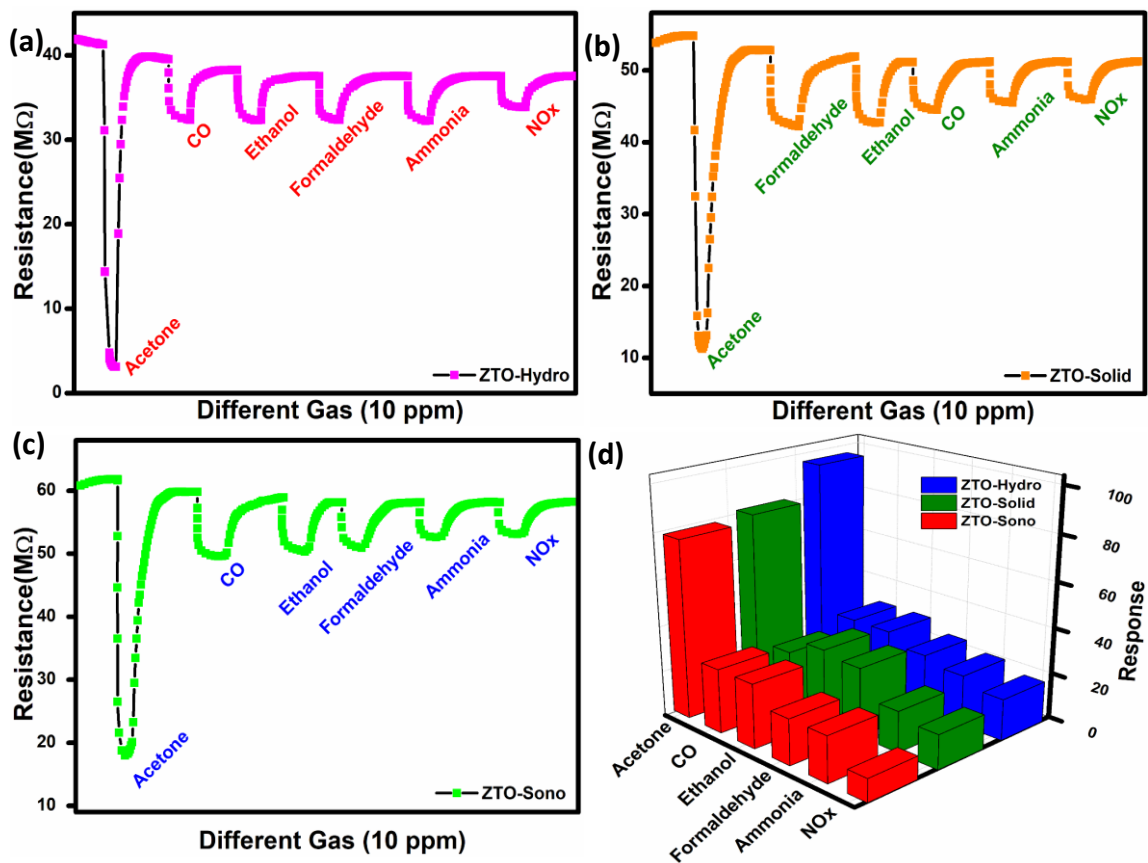


**Figure 4.3.5.** Selectivity diagram with different target gas such as Acetone, CO, Ethanol, Formaldehyde, Ammonia, NOx at the same concentration (10ppm) at operating temperature 260°C (a) ZTO-Hydro (b) ZTO-Solid and (c) ZTO-Sono, respectively (d) Selectivity diagram of all ZTO based sensor.

The other two critical properties for gas sensing measurements are response time and recovery time, which has been defined as the time required for reaching 90% of maximum response after the injecting gas and 10% when gas is out, respectively. The cycle of the dynamic response curve of ZTO-Hydro, ZTO-Solid and ZTO-Sono sample-based sensor is presented in Figure 4.3.6 (a, b, c) towards different concentration of acetone (10, 5, 2, 1 and 0.5ppm) respectively at 260°C showing the response and recovery time. The response nature increases sharply in presence of acetone and returns to its original position after removing acetone. According to the above definition the calculated response time is 4sec, 7sec and 8sec and the recovery time is 6sec, 18sec and 22sec for ZTO-Hydro, ZTO-Solid and ZTO-Sono based sensor, respectively. The very fast response and excellent recovery nature of the sensor makes  $Zn_2SnO_4$  material more suitable for acetone sensing application. Further, Figure 4.3.6d shows the sensing response of all the sensor synthesized by three different techniques (Hydrothermal, Solid-State and Sonochemical) towards different concentrations of acetone (10, 8, 5, 2, 1 and 0.5ppm) at optimized operating temperature of 260°C. The result also indicates the excellent sensitivity towards a lower concentration of acetone.

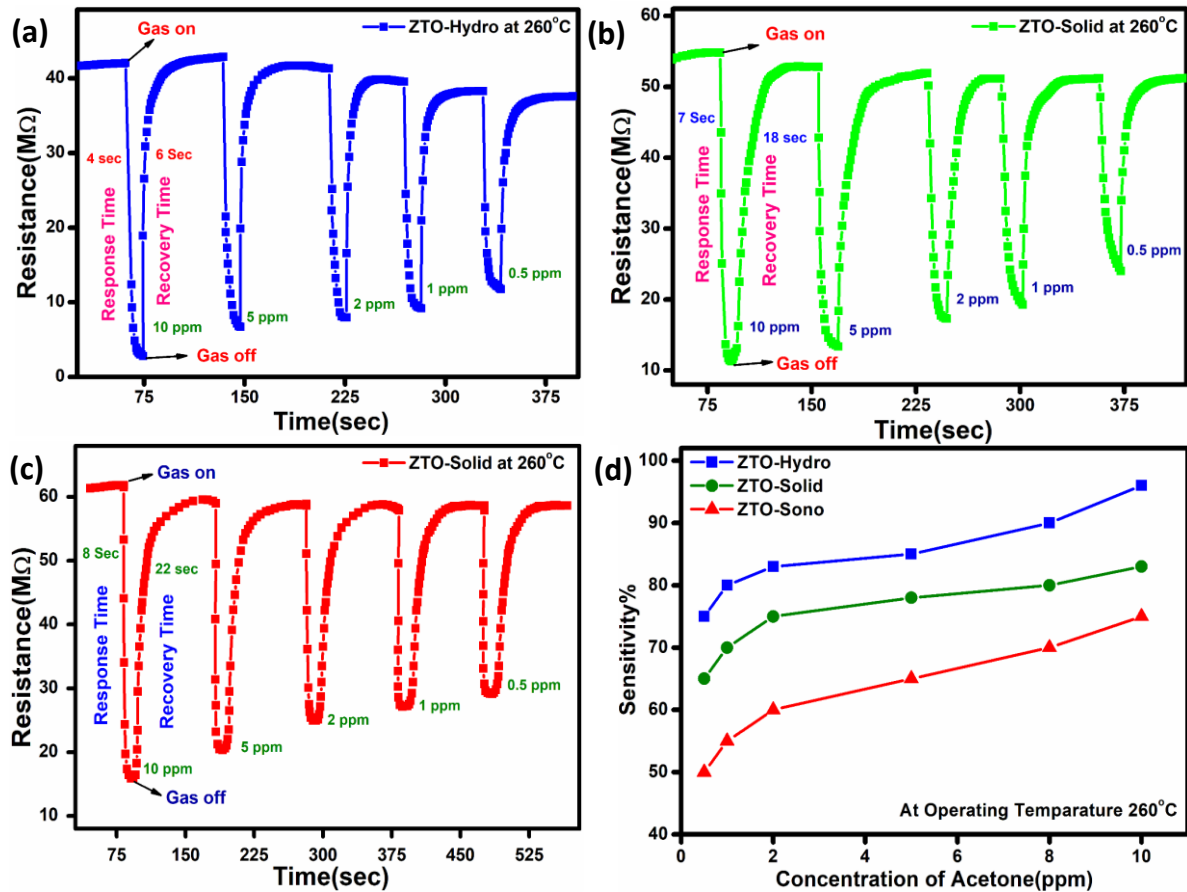


**Figure 4.3.6:** Dynamic response curve at different concentration of acetone at 260°C operating temperature showing response and recovery time of (a) ZTO-Hydro, (b) ZTO-Solid and (c) ZTO-Sono, respectively (d) Sensitivity of the synthesized sample towards different concentration acetone (10, 8, 5, 2, 1 and 0.5ppm) at 260°C operating temperature.

The sensitivity (S) calculated from the dynamic curve in different concentration of acetone (C) can be empirically explained by the following equation [24]:

$$S \propto aC^b / (1+aC^b) \dots\dots\dots (4.12)$$

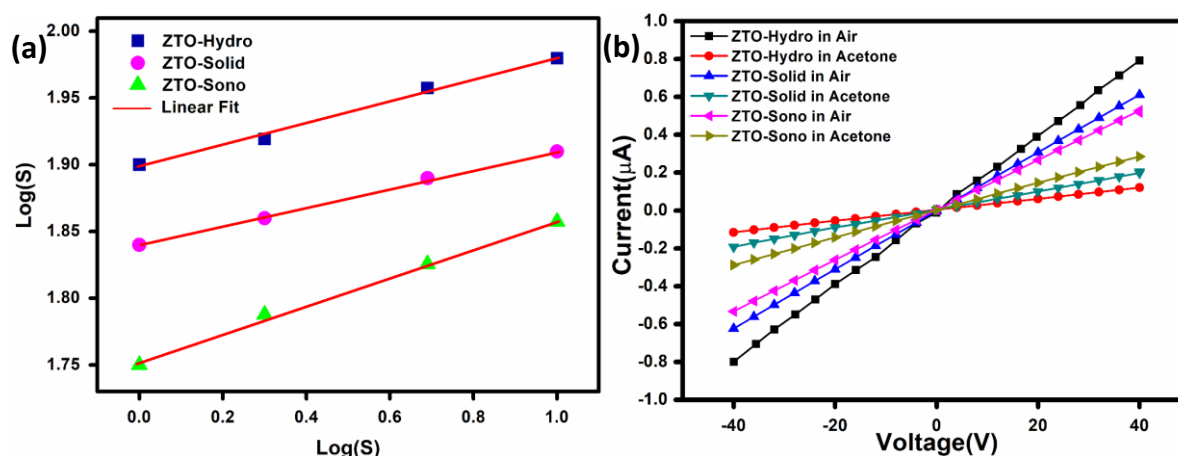
C can be described as the concentration of acetone, a is the proportionality factor and b is the exponent. As we have checked the sensitivity at very lower concentration of acetone,  $aC^b \rightarrow 0$ , hence the equation (4.12) can be modified as [25]:

$$S \propto aC^b \dots\dots\dots (4.13)$$

Further the equation (4.13) can be rewritten as a relation:

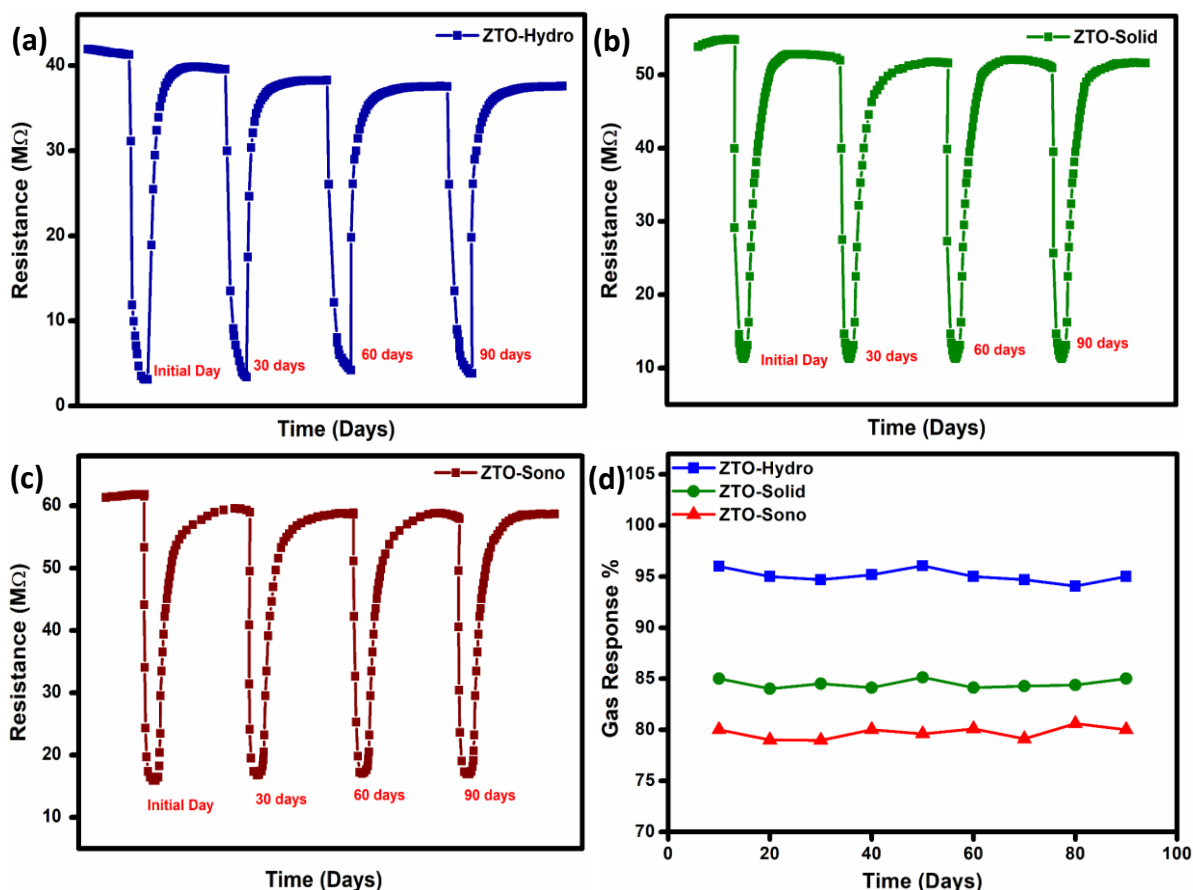
$$\text{Log}(S) = \text{log } a + \text{blog } C \dots\dots\dots (4.14)$$

Figure 4.3.7a represents the power law relationship between the sensing response and the concentration of acetone of ZTO-Hydro, ZTO-Solid and ZTO-Sono based sensor, respectively. The linear nature of the fitted plot shown in Figure 4.3.7a indicates about the ability of sensing in lower concentration of acetone of ZTO based sensor. The current-voltage (I-V) characteristics curve of ZTO samples are plotted in Figure 4.3.7b at the voltage bias range of -40V to +40V for ZTO-Hydro, ZTO-Solid and ZTO-Sono, respectively. The measured I-V curve shows excellent linearity within the experimental range indicating the formation of ohmic contact between the nanoparticles and the Au electrodes in air and also in presence of Acetone.



**Figure 4.3.7:** (a) Linear correlation between  $\log(S)$  vs  $\log(C)$  and (b) Comparison of I-V characterization in presence of air and acetone of ZTO-Hydro, ZTO-Solid and ZTO-Sono, respectively.

For further investigation, the stability of the sensor towards acetone gas was studied at their optimum operating temperature as shown in Figure 4.3.8. The gas response of the all-prepared sensors has been changed slightly after complete study for three months, proving the good long term stability of the prepared ZTO based gas sensor and providing reproducible sensing results for a certain period more suitable for further application study.



**Figure 4.3.8:** The long-term stability and reproducibility of (a) ZTO-Hydro (b) ZTO-Solid and (c) ZTO-Sono, respectively (d) Long-term stability plot of all ZTO based sensor.

The gas sensing mechanism concentrated on different parameters such as grain size, grain growth direction and surface area. Many reports claim that the surface of the sensing materials mainly determines the sensing property of semiconductor materials. In this work, along with the DC measurements, impedance measurements also have been carried out to understand the electrical properties of the sensor devices in presence of acetone at different operating temperatures. Generally, impedance spectroscopy study suggests the electrical behaviour of different components such as grain, grain boundary and electrode interface of a sensing material and can clearly differentiate the contribution on the electrical properties of the sensing material [50-52].

It is a combination of two terms of Complex impedance ( $Z$ ) such as the resistive real part ( $Z'$ ) and the reactive imaginary part ( $Z''$ ). To calculate the electrical parameters of the active region

of a sensor material, Nyquist plot is a better technique and here  $Z''$  is plotted against  $Z'$ . For the case of a defect free homogeneous sensor material, a clear semicircle has been shown from the Nyquist plot with its origin lying exactly on the real axis [53].

The exact semicircle can be modelled by a parallel RC circuit which is a reflection of the characteristic of perfect Debye type relaxation nature. And the all semicircles can be modelled by parallel RC circuit joined in series. Each semicircle represents different contributions such as at high frequency region the first semicircle from the Nyquist plot is represented for the grain contribution whereas inter grain boundary contribution comes from the second semicircle. Relations describing these semi-circular arcs are given by Equation (4.15) and Equation (4.16).

$$Z' = \frac{R_g}{(1+R_g \omega_g C_g)^2} + \frac{R_{gb}}{(1+R_{gb} \omega_{gb} C_{gb})^2} \dots\dots\dots(4.15)$$

$$Z'' = \frac{R_g^2}{1+(R_g \omega_g C_g)^2} + \frac{R_{gb}^2}{1+(R_{gb} \omega_{gb} C_{gb})^2} \dots\dots\dots(4.16)$$

Here  $g$  and  $gb$  signifies the grain and grain boundary, respectively. To understand these contributions,  $Z'$  and  $Z''$  from the impedance data in a wide range of frequency (100Hz – 1MHz) and temperature (200°C – 350°C) have been analysed. In the Nyquist plot, the point of intersections at the  $Z'$  axis (X axis) are the origin (0, 0), ( $R_g$ , 0) and ( $R_g + R_{gb}$ , 0) and the resistance of the grain and grain boundary can be evaluated from the measured point [54]. The Nyquist plots of all the synthesized sample-based sensors are shown in Figure below at all the experimental operating temperatures range. From the figures it is clear that Nyquist plot represents only one semicircle clearly which suggests the presence of only grain contribution. By using the ZView2 software, all the plots are fitted at all temperature ranges in presence of air and acetone for ZTO-Hydro, ZTO-Solid and ZTO-Sono, respectively. As expected with increase in temperature the radius of the semi-circle gets reduced indicating an enhancement in the electrical properties.

The complex impedance spectra of hydrothermally, solid-state and sonochemically synthesized sample are shown in Figure 4.3.9 (a & b), (c & d) and (e & f) in presence of air and acetone, respectively, between 200°C to 350°C, temperature range. The phenomenon based on the effect of adsorption and desorption of the oxygen molecules with variation of operating temperature in presence of air and acetone can be explained from the interpretation of Nyquist plot. In this work, all the sensing measurements with variation of operating temperature in the region between 200°C to 350°C have been carried out and explained the mechanism for sensing properties. As we considered 260°C as the optimum operating temperature because the adsorption and desorption rate lead to the maximum state which exhibits the highest rate of sensitivity for the ZTO based sensor.

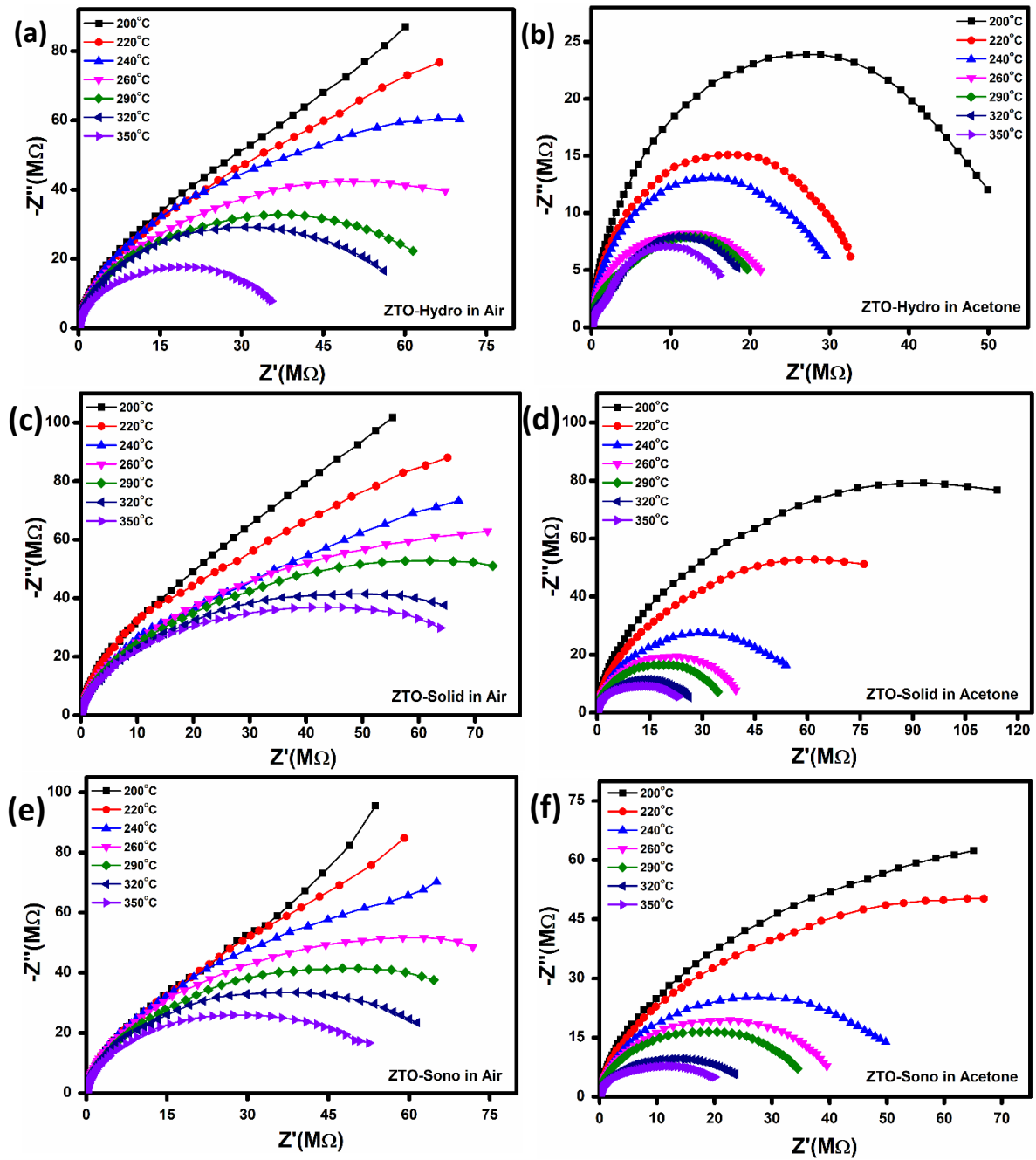


**Figure 4.3.9:** Nyquist diagram of (a) & (b) ZTO-Hydro (c) & (d) ZTO-Solid (e) & (f) ZTO-Sono in the presence of air and acetone.

Additionally, the impedance data was plotted against frequency at different temperature range as shown in Figure 4.3.10 (a, b, c) for ZTO-Hydro, ZTO-Solid and ZTO-Sono, respectively. From Figure 4.3.10 (a, b, c) it is clear that at lower frequency range the impedance curves showed dispersed nature at different temperature range as impedance value exhibited in decreasing nature with increasing temperature which is the main characteristics of



semiconductor. And at higher frequency region, the impedance plot anticipated into single line. The connection between resistance and temperature can be explained by Arrhenius equation (4.4) and can be explained by the impedance data. The activation energy calculated from the electrical parameter has been well plotted in Figure 4.3.10 (d, e, f) from the slope of  $\ln(R)$  vs  $1/KT$  graph with the value 0.214eV, 0.312eV and 0.385eV for ZTO-Hydro, ZTO-Solid and ZTO-Sono respectively. The lower activation energy value for ZTO-Hydro is the evidence that it needs lower energy for getting activated than ZTO-Solid and ZTO-Sono based sample.

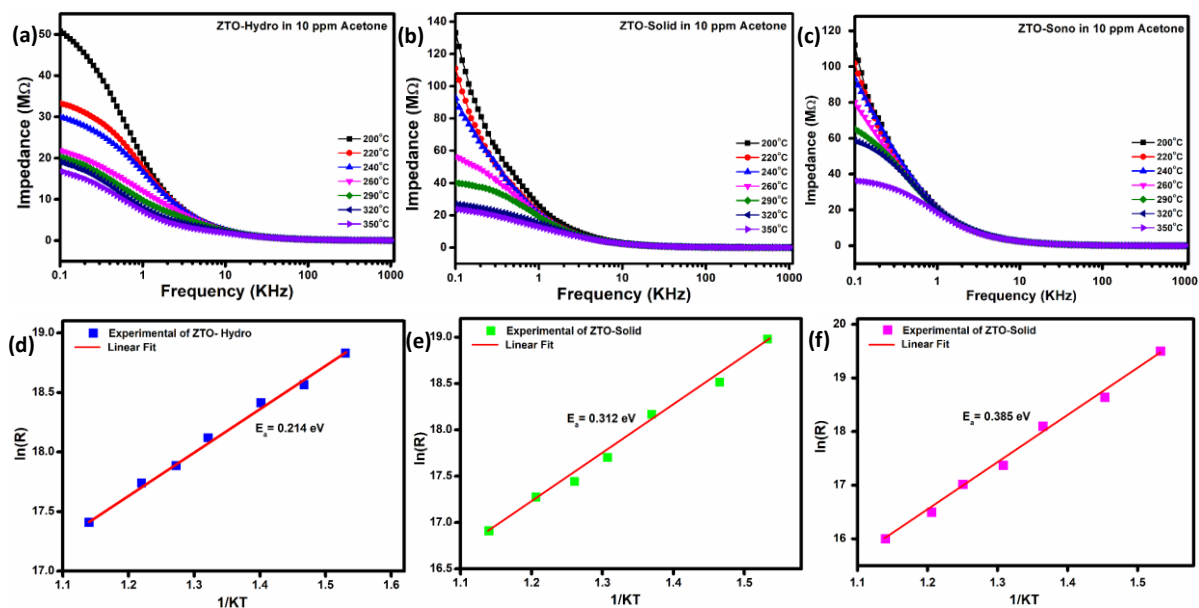


**Figure 4.3.10:** (a-c) Impedance variation with Frequency in presence of 10 ppm acetone and (d-f) Activation Energy calculation of ZTO-Hydro, ZTO-Solid and ZTO-Sono, respectively.

Further to understand the impact of AC parameters on the fabricated sensor, the Nyquist plot has been shown in Figure 4.3.11 (a, b, c) in presence of air and 10 ppm acetone for ZTO-Hydro, ZTO-Solid and ZTO-Sono, respectively. The measured impedance data has been fitted to a R-C parallel circuit by using Z view software (version 2.70), shown in Figure 4.3.11d which gives an idea about the effect of grain to control the adsorption mechanism.

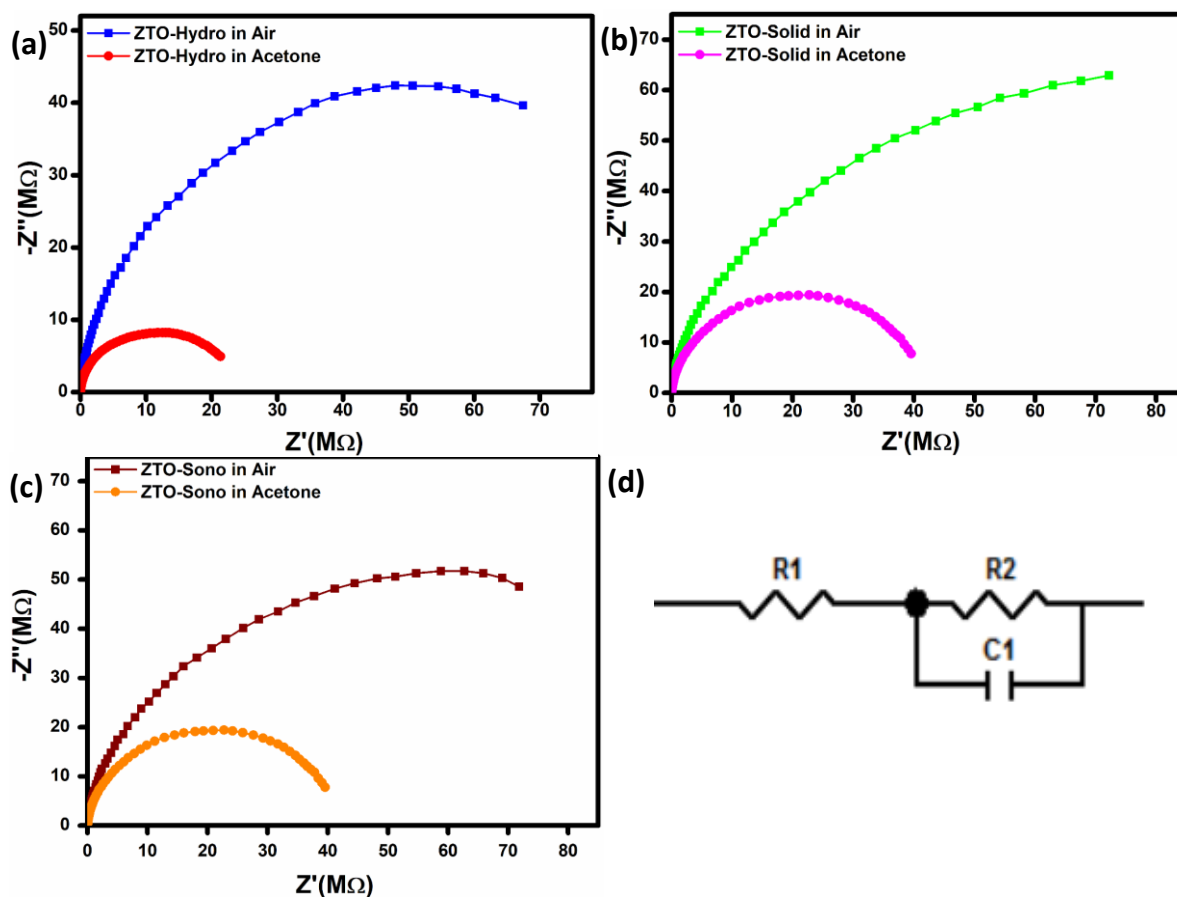


**Figure 4.3.11:** Nyquist diagram in presence of air and 10ppm acetone of (a) ZTO-Hydro (b) ZTO-Solid and (c) ZTO-Sono, respectively and (d) measured equivalent circuit diagram.

All the surface properties all synthesized samples and the sensing parameters obtained from the characterizations and the sensing measurements have been tabulated in Table 4.3.1 below for ZTO-Hydro, ZTO-Solid and ZTO-Sono, respectively.

**Table 4.3.1: Different surface and sensing properties of all ZTO synthesized based samples towards 10ppm acetone.**

Sensor Material	Particle Size (nm)	Surface Area (m <sup>2</sup> /g)	Binding Energy (eV)	Operating Temperature (°C)	Response/Recovery time (sec)	Sensitivity %
ZTO-Hydro	5	86.2	0.214	260	4/6	96
ZTO-Solid	50-100	16.9	0.312	260	7/18	85
ZTO-Sono	100-125	10.3	0.385	260	8/22	80

### 4.3.4. Conclusion

The exploration of different synthesis techniques to prepare different morphology of zinc stannate has taken special attention to develop the sensing properties. It is clear from our study that greater specific BET surface area led to improve different sensing performance as it gets larger area for adsorbing gas species. Actually, the gas sensing mechanism is completely based on the change of electrical conductivity of the semiconductor-based metal oxide at the exposure towards acetone on the surface. The resistance and conductivity are deeply depended upon the sensor materials' surface morphology and crystal structure. Here in our study the sensor material zinc stannate synthesized by hydrothermally synthesis process having good morphology with 50nm particle size is showing higher sensing response around 96% compared with other materials synthesized by solid-state and sonochemical synthesis process. The hydrothermally synthesized based sample has the ability of good selectivity nature as tested towards different target gases with same environmental condition with higher sensing stability and reproducibility which make this material very acceptable for further sensing application field.

### 4.4. References

1. Safi, R.; Shokrollahi, H. *Prog. Solid. State Ch.* **2012**, *40*, 6.
2. Lotey, G. S.; Verma, N. K.; *Mater. Sci. Semicond. Process* **2014**, *21*, 206.
3. Ruan, Q. J.; Zhang, W. D. *Mater. Lett.* **2008**, *62*, 4303.
4. Zenga, Y.; Zhanga, T.; Yuanb, M.; Kanga, M.; Lua, G.; Wanga, R.; Fana, H.; Hea, Y.; Yang, H. *Sens. Actuator B* **2009**, *143*, 93–98.
5. Tan, W.; Ruan, X.; Yu, Q.; Yu, Z.; Huang, X. *Sensors* **2015**, *15*, 352-364.
6. Liao, L.; Zheng, Z.; Yan, B.; Zhang, J. X.; Gong, H.; Li, J. C.; Liu, C.; Shen, Z. X.; Yu, T.; *J. Phys. Chem. C* **2008**, *112*, 10784-10788.
7. Chen, Z.; Cao, M.; Hu, C. *J. Phys. Chem. C* **2011**, *115*, 5522–5529.

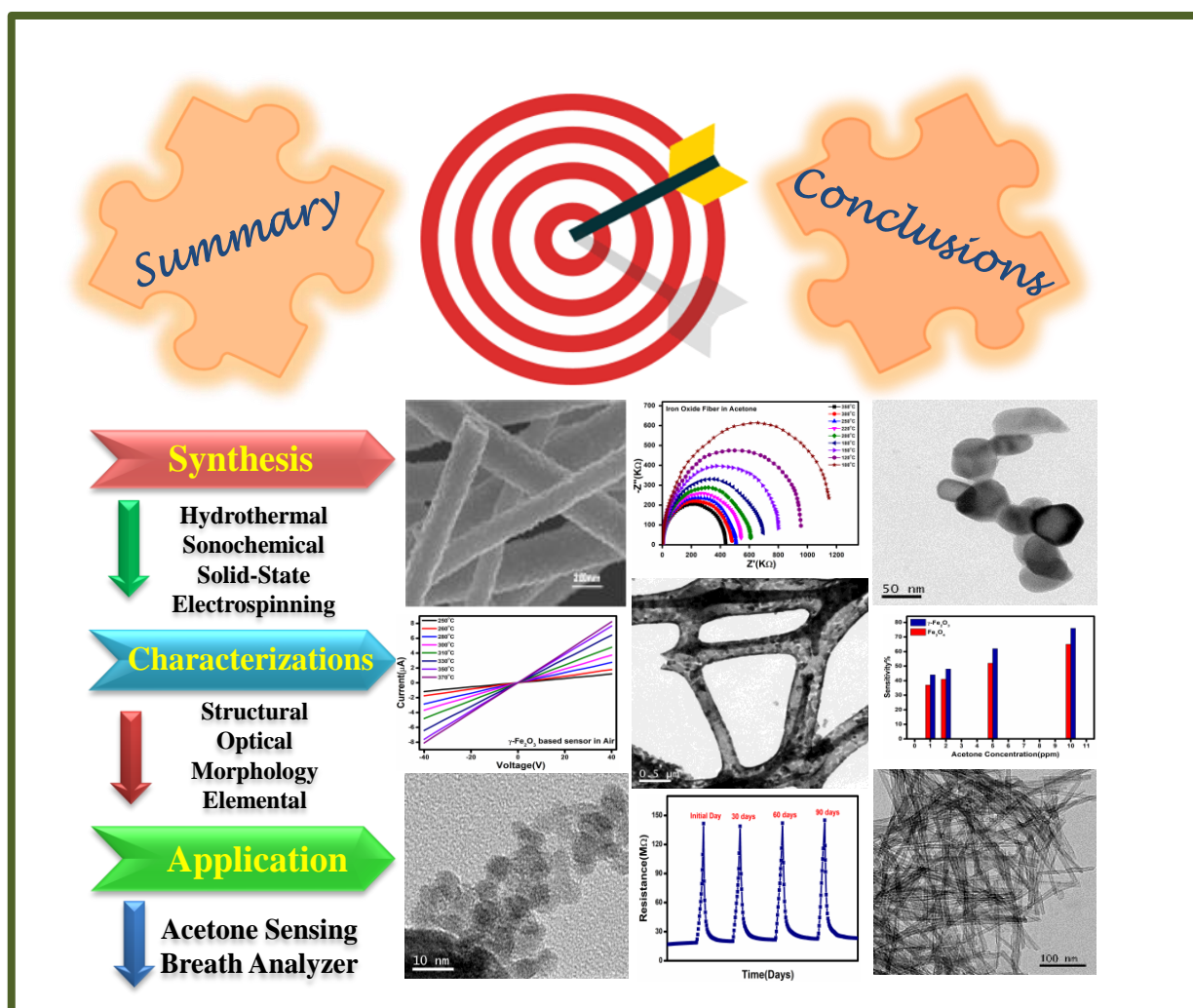
8. Park, H. J.; Kim, J.; Choi, N. J.; Song, H.; Lee, D. S. *ACS Appl. Mater. Interfaces* **2016**, *8*, 3233–3240
9. Chaudhuri, A.; Mandal, K.; Magn. J. *Magn. Mater.* **2014**, *353*, 57–64.
10. Hussain, T.; Siddiqi, S. A.; Atiq, S.; Awan, M. S. *Prog. Nat. Sci.: Mater. Int* **2013**, *23*, 487–492.
11. Ortiz-Quiñonez, J. L.; Díaz, D.; Zumeta-Dubé, I.; Arriola-Santamaría, H.; Betancourt, I.; Santiago-Jacinto, P.; Nava-Etzana, N. *Inorg. Chem.* **2013**, *52*, 10306.
12. Silva, J.; Reyes, A.; Esparza, H.; Camacho, H.; Fuentes, L. *Int. Ferroelec.* **2011**, *126*, 47.
13. Joshi, U. A.; Jang, J. S.; Borse, P. H.; Lee, J. S. *Appl. Phys. Lett.* **2008**, *92*, 242106.
14. Sun, B.; Wei, L.; Chen, H. L. P. *J. Mater. Chem. C* **2014**, *2*, 7547-7551.
15. Zhou, J. P.; Xiao, R. J.; Zhang, Y. X.; Shi, Z.; Zhu, G. Q. *J. Mater. Chem. C* **2015**, *3*, 6924-6931.
16. Waghmare, S. D.; Jadhav, V. V.; Gore, S. K.; Yoon, S. J.; Ambade, S. B.; Lokhande, B. J.; R. S. Mane, S. H. Han, *Mater. Res. Bull.* **2012**, *47*, 4169.
17. Poghosian, A. S.; Abovian, H. V.; Avakian, P. B.; Mkrtchian, V.; Haroutunian, M. *Sens. Actuators B* **1991**, *9*, 545.
18. Tong, T.; Chen, J.; Jin, D.; Cheng, J. *Mater. Lett.* **2017**, *197*, 160–162.
19. Dong, G.; Fan, H.; Tian, H.; Fang, J.; Li, Q. *RSC Adv.* **2015**, *5*, 29618.
20. Dziubaniuk, M.; Bujakiewicz-Korońska, R.; Suchanicz, J.; Wyrwa, J.; Rękas, M. *Sens. Actuator B* **2013**, *188*, 957–964.
21. Chakraborty, S.; Pal, M. *J. Alloys Compd.* **2019**, *787*, 1204-1211.
22. Mazumder, R.; Devi, P.S.; Bhattacharya, D.; Chowdhury, P.; Sen, A.; Raja, M. *Appl. Phys. Lett.* **2007**, *91*, 062510.
23. Nag, P.; Majumdar, S.; Bumajdad, A.; Devi, P. S. *RSC Adv.* **2014**, *4*, 18512.
24. Johnson, J. L.; Behnam, A.; An, Y.; Pearton, S. J.; Ural, A. *J. Appl. Phys.* **2011**, *109*, 124301

25. Dan, Y.; Lu, Y.; Kybert, N. J.; Luo, Z.; Johnson, A. T. C. *Nano Lett.* **2009**, *9*, 1472–5.
26. Hu, H.; Trejo, M.; Nicho, M. E.; Saaniger, J. M.; Garc'ia-Valenzuela, A. *Sens. Actuator B* **2002**, *82*, 14–23.
27. Banerjee, S.; Bumajdad, A.; Devi, P. S. *Nanotechnology* **2011**, *22*, 275506.
28. Labidi, A.; Jacolin, C.; Bendahan, M.; Abdelghani, A.; Guerin, J. *Sens. Actuator B* **2005**, *106*, 713-718.
29. Ling, Z.; Leach, C.; Freer, R. *Sens. Actuator B* **2002**, *87*, 215-221.
30. Aguir, K.; Labidi, A.; Mauriat, C. L. *IEEE Sensors* **2006**, 267-270.
31. Madou, J. M.; Morrison, S. R. *Academic Press* **1989**, Chapters 3 and 12.
32. Kadir, R. A.; Li, Z.; Sadek, A. Z.; Rani, R. A.; Zoolfakar, A. S.; Fxciold, M. R.; Ou, J. Z.; Chrimes, A. F.; Kalantar-zadeh, K. *J. Phys. Chem. C* **2014**, *118*, 3129–3139.
33. Chen, Y.; Qin, H.; Cao, Y.; Zhang, H.; Hu, J. *Sensors* **2018**, *18*, 3425.
34. Ruan Q. J.; Zhang, W. D. *Mater. Lett.* **2008**, *62*, 4303.
35. Park, H. J.; Kim, J.; Choi, N. J.; Song, H.; Lee, D. S. *ACS Appl. Mater. Interfaces* **2016**, *8*, 3233–3240
36. Poghossian, A. S.; Abovian, H. V.; Avakian, P. B.; Mkrtchian, V.; Haroutunian, M. *Sens. Actuators B* **1991**, *9*, 545.
37. Chen, Z.; Cao, M.; Hu, C. *J. Phys. Chem. C* **2011**, *115*, 5522–5529.
38. Chen, C.; Li, G.; Li, J.; Liu, Y. *Ceram. Int.* **2015**, *41*, 1857–1862.
39. Ma, G.; Zou, R.; Jiang, L.; Zhang, Z.; Xue, Y.; Yu, L.; Song, G.; Li, W.; Hu, J. *Cryst. Eng. Comm.* **2012**, *14*, 2172–2179.
40. Fu, G.; Chen, H.; Chen, Z. X.; Zhang, J. X.; Kohler, H. *Sens. Actuators B* **2002**, *81*, 308–312.
41. Yu, J. H.; Choi, G. M. *Sens. Actuators B* **2001**, *72*, 141-148.
42. Yamada, Y.; Seno, Y.; Masuoka, Y.; Yamashita, K. *Sens. Actuators B* **1998**, *49*, 248-252.

43. Tan, B.; Toman, E.; Li, Y. G.; Wu, Y. Y. *J. Am. Chem. Soc.* **2007**, *129*, 4162-4163.
44. Lana-Villarreal, T.; Boschloo, G.; Hegfeldt, A. *J. Phys. Chem. C* **2007**, *111*, 5549-5556.
45. Rong, A.; Gao, X. P.; Li, G. R.; Yan, T. Y.; Zhu, H. Y.; Qu, J. Q.; Song, D. Y. *J. Phys. Chem. B* **2006**, *110*, 14754-14760.
46. Lorotchenkov, G. *Sens. Actuators. B* **2005**, *107*, 209-232.
47. Liu, C. Y.; Chen, C. F.; Liu, J. P. *Electrochem. Solid State Lett.* **2009**, *156*, J16-J19.
48. Shon, J. K.; Kong, S. S.; Kim, Y. S.; Lee, J. H.; Park, W. K.; Par, S. C.; Kim, J. M. *Micropor. Mesopor. Mater.* **2009**, *120*, 441-446.
49. Waitz, T.; Wagne, T.; Sauerwald, T.; Kohl, C. D.; Tiemann, M. *Adv. Funct. Mater.* **2009**, *19*, 653-661.
50. Hoshikawa, T.; Ikebe, T.; Kikuchi, R.; Eguchi, K.; *Electrochim. Acta* **2006**, *51*, 5286-5294.
51. Vollmann, M.; Waser, R.; *J. Electroceram.* **1997**, *1*, 51.
52. Vollmann, M.; Hagenbeck, R.; Waser, R. *J. Am. Ceram. Soc.* **1997**, *80*, 2301.
53. Gupta, P.; Mahapatra, P. K.; Choudhary, R. N. P. *J. Alloys Compd.* **2021**, 863.
54. Kaur, A.; Singh, L.; Asokan, K. *Ceram. Int.* **2018**, *44*, 3751-3759.

# CHAPTER-V

## Summary and Conclusions



*A glance of previous chapters is reviewed in this chapter. All the studied materials and the synthesis techniques are mentioned properly. The salient features and major findings that arose from this thesis work with the key outcome of all the experiments have been highlighted. Significant characteristics of all the synthesized materials, perspective for applying the same in sensor fabrication and device development have been summarized in this chapter. Also, consequent future scopes and outlooks have been also anticipated at the end of this chapter.*

The development of chemiresistive metal oxide-based acetone sensors is the future of non-invasive point of care diagnosis. However, the use of metal oxides arises many challenges in chemiresistive sensing applications, the major ones are sensitivity, selectivity and stability. The improvement of such challenges will lead to better sensing materials and devices. Our group has been working in the area of metal oxide-based gas sensors for various applications. As a continuation of our previous work, current thesis work has been undertaken to extend our work towards developing materials and devices for non-invasive detection of volatile organic compounds for disease diagnosis. Thus, the major objective of this thesis work was to identify the existing challenges in developing better sensor materials and devices to enhance the chemiresistive behaviour of metal oxides for acetone detection. Therefore, in this thesis work, many n-type and p-type metal oxides have been synthesised with an intention to improve the sensing characteristics of metal oxides and compared the properties of the synthesized sensing materials with different operating conditions to detect acetone, the breath biomarker of diabetes.

In Chapter 1, a general introduction and literature review on sensors in general, the overview of the field of study and scope of the work has been described in detail. An overview of sensors in general and specifically acetone sensors based on semiconducting metal oxides and also emphasised on the brief history of semiconducting metal oxide-based gas sensor are also presented. The chapter also highlighted the principle and significant performance assessment of sensor mechanism. A detailed discussion on usefulness and justification of gas sensors, classification of gas sensors and different sensing technology has also been reported. On a different frontier, brief description of semiconducting nanomaterials, properties and effective use of semiconducting materials as gas sensors, different conventional semiconducting oxides with their crystal structure, band gap, applications etc. have been concisely presented in the subsequent sections. This chapter also gives special attention to the knowledge about gas



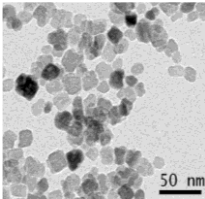
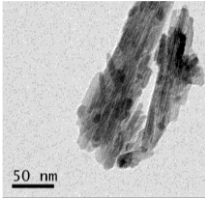
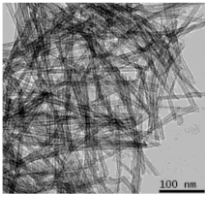
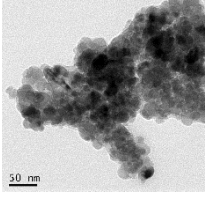
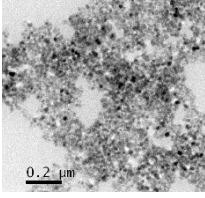
sensing mechanism of semiconducting metal oxides (SMO) based gas sensors and the physical and electrical properties related to surface modification and sensing mechanism and illuminated the kind of different metal oxides that can be considered for gas sensor applications, structural properties correlation and different published reports on metal oxide-based gas sensor. Motivation, scope and specific objectives of the present research work and finally the organization of the present thesis work has been presented at the end of the chapter.

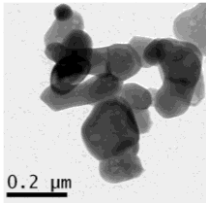
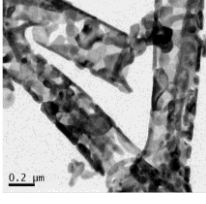
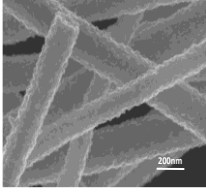
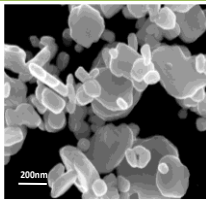
The major portion of Chapter 2 deals with synthesis, characterization techniques, sensor fabrication and various measurement technique. Details of different characterization techniques used in order to understand the structural, morphological, physicochemical, optical and electronic properties of the synthesized nanomaterials have been discussed methodically in this chapter. Different physico-chemical characterization techniques used for structural and chemical study of the synthesized materials like TGA, DTA-DSC, XPS, FTIR, Raman, UV-VIS Spectroscopy, PL Spectroscopy and different microstructural characterization like FESEM, TEM have been illuminated. Different powder characterization techniques like particle size distribution, zeta potential measurements, surface area and porosity measurement techniques like BET analysis with pore size, pore volume and pore distribution analysis using adsorption-desorption isotherm have also been discussed. In Chapter 2, the sensor fabrication details are also presented along with substrate preparation, coating, advantages and limitations of thick film coating technology etc.

In Chapter 3, binary metal oxide-based materials for acetone sensing applications have been presented. The entire results and discussion have been categorized under various sections. In this section three different binary metal oxides such as different phases of  $\text{TiO}_2$ , Iron Oxide and  $\text{WO}_3$  were selected for sensing application. After correlation of all the experimental results from the work output, it has been confirmed that the nature of synthesis process, phase purity and structural modification are quite decisive in monitoring the overall sensing performance of

binary metal oxide-based gas sensor. Major findings and acetone sensing performances derived from the binary metal oxides-based gas sensor are summarized in Table 5.1.

Table 5.1 Significant outcome of Chapter 3

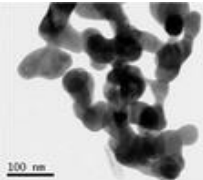
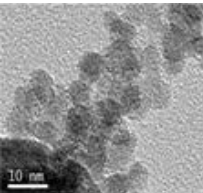
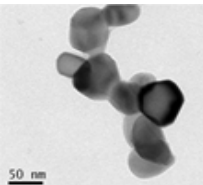
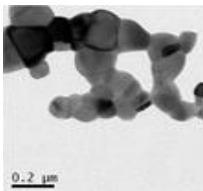
Material	Morphology	Highlights	OT (°C) & Response Recovery Time (sec)	Sensitivity % or Ratio at 10ppm Acetone
TiO <sub>2</sub>	Anatase		SA: 86.5m <sup>2</sup> /g Hydrothermally synthesized with particle size 21 nm	250 11/20 6.8
	Rutile		SA: 16.5 m <sup>2</sup> /g Elongated nanorods with a length of 300–350 nm and an average width of 15 nm	300 12/40 4.8
	Na <sub>0.23</sub> TiO <sub>2</sub> -TiO <sub>2</sub> Composite		SA: 90.03 m <sup>2</sup> /g average diameter of ≈10 nm and an aspect ratio of 25:1 showing p-type sensing nature	RT 10/7 7.1
Iron Oxide	γ-Fe <sub>2</sub> O <sub>3</sub> Nanoparticle		SA: 56 m <sup>2</sup> /g Particle size is around 15.82 nm	310 9/14 76%
	Fe <sub>3</sub> O <sub>4</sub> Nanoparticle		SA: 38 m <sup>2</sup> /g Particle size is 15.87 nm	310 10/40 65%

$\alpha$ -Fe <sub>2</sub> O <sub>3</sub> Nanoparticle		SA: 30.2 m <sup>2</sup> /g Particle size is around 95-100nm	300 18/50	62%
$\alpha$ -Fe <sub>2</sub> O <sub>3</sub> Fiber		SA: 86.2 m <sup>2</sup> /g Electrospun fiber with average 220-250 nm diameter	150 8/12	94.5%
Fiber		SA: 85.6 m <sup>2</sup> /g Electrospinning fiber with average 550 nm diameter along with exposed (002) facets	150 6/25	90%
WO <sub>3</sub> Particle		SA: 15.5 m <sup>2</sup> /g Hydrothermally synthesized and particle size is around 200 nm	200 8/35	84%

Among the investigated binary oxides,  $\alpha$ -Fe<sub>2</sub>O<sub>3</sub> fiber and WO<sub>3</sub> fiber exhibited one of the highest reported sensitivities towards 10ppm concentration of acetone there by highlighting the role of morphology in achieving high gas sensing property.

In Chapter 4, design and development of various multicomponent oxides and their performance towards acetone vapour sensing has been presented in detail. The overall significant findings and sensing performances are summarized in Table 5.2 considering their material aspects, calcination and operating temperature, concentration of acetone, response and recovery time, sensitivity performance.

Table 5.2 Significant outcome of Chapter 4

Material	Morphology	Highlights	OT (°C) & Response Recovery Time (sec)	Sensitivity% or Ratio at 10ppm Acetone
<b>BiFeO<sub>3</sub> Nanoparticle</b>		SA: 32.3 m <sup>2</sup> /g Synthesized by hydrazine assisted co-precipitation method with particle size 80-150 nm and established vacancy-induced p-type sensing properties	260 12/25	12.1
ZTO-Hydro		SA: 86.2 m <sup>2</sup> /g Hydrothermally synthesized nanoparticle with grain size 5 nm and showed ultrafast sensing response	260 4/6	96%
Zn <sub>2</sub> SnO <sub>4</sub> ZTO-Solid		SA: 16.9 m <sup>2</sup> /g Synthesized by solid-state process with particle size 50-100 nm	260 7/18	85%
ZTO-Sono		SA: 10.3 m <sup>2</sup> /g Sonochemically synthesized and the particle size is around 100-125nm	260 8/22	80%

**\*SA: Surface Area; OT: Operating Temperature; RT: Room Temperature.**

The sensing performances of multicomponent oxides have been investigated as presented in Table 5.2. BiFeO<sub>3</sub> nanoparticle-based sensor showed improved p-type sensing response with excellent sensing stability with better acetone sensitivity. The Zn<sub>2</sub>SnO<sub>4</sub> (ZTO) powder samples synthesized by three different synthesis processes showed more promising sensing response compared to other metal oxide-based sensor. Hydrothermally synthesized ZTO powder-based

sensor showed higher sensing response with lower base resistance and faster response and recovery time at comparatively lower operating temperature compared to other particles. The importance of phase modification, morphology, surface area, synthesis process followed by corresponding particle size, and different physico-chemical characterization have been found to be significant factors to achieve enhanced sensing response and sensing stability. A series of synthesis approaches, new morphology design, developing new phases, improvement in stability and sensing performance of the fabricated sensors have been processed throughout the thesis work.

In this thesis work, we have studied and compared five different major sensing materials having diverse crystallographic modifications and other physico-chemical properties exhibiting exceedingly high performance to detect acetone, the breath biomarker of diabetes. Among the studied materials, the nanostructured fiber shaped  $\text{Fe}_2\text{O}_3$ , and  $\text{WO}_3$  and particle shaped  $\text{Zn}_2\text{SnO}_4$  exhibited best response to acetone, with more than 90% efficiency and fast response at lower operating temperatures than commonly reported systems. Some of these systems could be projected as promising materials with great potential for fabricating hand-held devices for point of care detection of diabetes through breath analysis.

**SYMBOLS**

<b>Å</b>	<b>Angstrom</b>
<b>β</b>	<b>Selectivity Coefficient</b>
<b>ε<sub>0</sub></b>	<b>Permittivity of Free Space</b>
<b>ε<sub>r</sub></b>	<b>Relative Permittivity</b>
<b>°C</b>	<b>Degree Centigrade</b>
<b>d</b>	<b>Lattice Spacing</b>
<b>e-</b>	<b>Electron</b>
<b>σ</b>	<b>Conductivity</b>
<b>a.u.</b>	<b>Arbitrary Unit</b>
<b>E<sub>b</sub></b>	<b>Barrier Height</b>
<b>E<sub>g</sub></b>	<b>Band Gap Energy</b>
<b>eV</b>	<b>Electron Volt</b>
<b>Hz</b>	<b>Hertz</b>
<b>K</b>	<b>Kelvin</b>
<b>k<sub>B</sub></b>	<b>Boltzmann's Constant</b>
<b>KΩ</b>	<b>Kilo Ohm</b>
<b>λ</b>	<b>Wavelength of X-ray Radiation</b>
<b>M</b>	<b>Molar Concentration</b>
<b>MΩ</b>	<b>Mega Ohm</b>
<b>n<sub>d</sub></b>	<b>Carrier Concentration</b>
<b>S</b>	<b>Sensitivity</b>
<b>R<sub>a</sub></b>	<b>Resistance in Air</b>
<b>R<sub>g</sub></b>	<b>Resistance in Presence of Analyte Gas</b>
<b>S<sub>BET</sub></b>	<b>Surface Area</b>
<b>T</b>	<b>Temperature</b>
<b>T<sub>c</sub></b>	<b>Calcination Temperature</b>
<b>OT</b>	<b>Operating Temperature</b>
<b>T<sub>res</sub></b>	<b>Response Time</b>
<b>T<sub>rec</sub></b>	<b>Recovery Time</b>
<b>T<sub>s</sub></b>	<b>Thickness of the Space Charge Layer</b>
<b>Ω</b>	<b>Ohm</b>
<b>Θ</b>	<b>Diffraction Angle</b>

$\lambda$	Wavelength
$\nu$	Frequency
$V_o$	Oxygen Vacancy
I	Current
V	Voltage

**ABBREVIATIONS**

AC	Alternative Current
BE	Binding Energy
BET	Brunauer-Emmett-Teller
BJH	Barrett-Joyner-Halenda
BFO	BiFeO <sub>3</sub>
Conc.	Concentration
CR	Composite Rod
DC	Direct Current
DI	Deionized
DLS	Dynamic Light Scattering
DSC	Differential Scanning Calorimetry
DTA	Differential Thermal Analysis
FTIR	Fourier Transform Infrared
EDX	Energy Dispersive X-ray
FESEM	Field Emission Scanning Electron Microscopy
HRTEM	High Resolution Transmission Electron Microscopy
h	Hour
JCPDS	Joint Committee on Powder Diffraction Standards
LPG	Liquefied Petroleum Gas
Min	Minute
m <sup>2</sup>	Square Meter
mA	Milli Ampere
$\mu$ A	Micro Ampere
MEMS	Micro Electro Mechanical Systems
MOX	Metal Oxide

## *Symbols and Abbreviations*

---

<b>nm</b>	<b>Nanometer</b>
<b>PL</b>	<b>Photoluminescence Spectroscopy</b>
<b>ppm</b>	<b>Parts Per Million</b>
<b>PSD</b>	<b>Particle-Size Distribution</b>
<b>R&amp;D</b>	<b>Research and Development</b>
<b>R</b>	<b>Resistance</b>
<b>RT</b>	<b>Room Temperature</b>
<b>RH</b>	<b>Relative Humidity</b>
<b>rpm</b>	<b>Revolution Per Minute</b>
<b>S or sec</b>	<b>Second</b>
<b>SAED</b>	<b>Selected Area Electron Diffraction</b>
<b>SMO</b>	<b>Semiconducting Metal Oxide</b>
<b>SA</b>	<b>Surface Area</b>
<b>TTIP</b>	<b>Titanium Isopropoxide</b>
<b>TP</b>	<b>TiO<sub>2</sub> Particle</b>
<b>%T</b>	<b>Percentage Transmittance</b>
<b>TEM</b>	<b>Transmission Electron Microscopy</b>
<b>TGA</b>	<b>Thermogravimetric Analysis</b>
<b>UV-Vis</b>	<b>UV-Visible Spectroscopy</b>
<b>XPS</b>	<b>X-ray Photoelectron Spectroscopy</b>
<b>XRD</b>	<b>X-ray Diffraction</b>
<b>ZTO</b>	<b>Zn<sub>2</sub>SnO<sub>4</sub></b>
<b>1D</b>	<b>One Dimensional</b>
<b>3D</b>	<b>Three Dimensional</b>



**LIST OF PUBLICATIONS**

1. **Puja Ghosh**, Anurag Roy, Soumita Mukhopadhyay, Mousumi Narjinary, Senthilarasu Sundaram, Shrabanee Sen, and Parukuttyamma Sujatha Devi\*, A New Functional Composite for Photovoltaic and Sensor Applications, *Adv. Electron. Mater.* **2021**, 2000785. **(Impact Factor: 7.633)**
2. Anurag Roy, **Puja Ghosh**, Parukuttyamma Sujatha Devi, Senthilarasu Sundaram, Tapas K. Mallick. Efficient carbon counter electrodes for BaSnO<sub>3</sub>-based dye-sensitized solar cells, *Materials Today: Proceedings*. **(Impact Score: 1.46)**
3. **Puja Ghosh**, Manikandan M, Shrabanee Sen\*, and Parukuttyamma Sujatha Devi, Some Interesting insights into the Acetone Sensing Characteristics of Monoclinic WO<sub>3</sub>. **(Revision Submitted in Materials Advances, Manuscript ID is: MA-ART-06-2022-000651).**
4. **Puja Ghosh**, Anurag Roy, Mousumi Narjinary, Shrabanee Sen\* and Parukuttyamma Sujatha Devi\*, Oxygen Vacancy induced Acetone Sensing Behaviour of p-type BiFeO<sub>3</sub> Nanoparticles. (Submitted in Materials Letters)
5. **Puja Ghosh**, Partha Pratim Das, Shrabanee Sen\* and Parukuttyamma Sujatha Devi\*, Exceedingly high response towards Acetone by Zn<sub>2</sub>SnO<sub>4</sub> Nanoparticle. (Submitted in ACS Applied Electronic Materials)
6. **Puja Ghosh**, Susmita Kundu, Shrabanee Sen\* and Parukuttyamma Sujatha Devi\*, Acetone Sensing Properties of phase and morphology depended Iron oxide based Semiconducting Gas Sensor. (Manuscript under communication)
7. **Puja Ghosh**, Shrabanee Sen\* and Parukuttyamma Sujatha Devi\*, Interesting Sensing properties of  $\alpha$ -Fe<sub>2</sub>O<sub>3</sub>-PANI composite towards lower concentration acetone detection. (Manuscript under preparation)

**LIST OF PRESENTATION**

1. Poster presentation entitled as “Dual Applications of Hydrothermally Synthesized TiO<sub>2</sub> Nanorods” by **Puja Ghosh**, A. Roy, M. Narjinary and P. Sujatha Devi on National Symposium on New Trends of Research in Solid State Chemistry and Allied Arrears at Jammu University, Jammu organized by ISCAS Institute of Solid State and Materials Science, Jammu, 4-6 March, 2018. **(Best Poster Award)**
2. Poster presentation entitled as “Bi-functional Applications of Nano-Structural Zinc Stannate” by **Puja Ghosh**, A. Roy, M. Narjinary and P. Sujatha Devi in International Conference on Complex and Functional Materials (ICCFM-2018) held at Kolkata on December 13-16, 2018.
3. Poster presentation entitled as “Newer Applications of Multiferroic Bismuth Ferrite Clusters” by **Puja Ghosh**, A. Roy, M. Narjinary, S. Sen and P. Sujatha Devi in International Conference on Current Trends in Materials Science and Engineering (CTMSE 2019) organized by IEM, Kolkata and S. N. Bose National Centre for Basic Sciences, Kolkata held on 18<sup>th</sup>-20<sup>th</sup> July, 2019.
4. Poster presentation entitled as “Newer Applications of Anatase TiO<sub>2</sub>-Na<sub>0.23</sub>TiO<sub>2</sub> Composite Nanorods” by **Puja Ghosh**, A. Roy, M. Narjinary, S. Sen and P. Sujatha Devi on 3<sup>rd</sup> International Conference on Advanced Functional Materials ICAFM 2019, organized by CSIR-NIIST, ICS-Kerala Chapter and MRSI Thiruvananthapuram Chapter held at CSIR-NIIST, Thiruvananthapuram during 9-10 December 2019. **(Best Poster Award)**
5. Poster presentation entitled as “High Acetone Sensitivity and Selectivity Exhibited by Hydrothermally Synthesized WO<sub>3</sub> Nanoparticles” by **Puja Ghosh**, M. Narjinary, S. Sen and P. Sujatha Devi on 2<sup>nd</sup> Indian Materials Convclave and 31<sup>st</sup> AGM at Kolkata organized by Materials Research Society of India (MRSI), Kolkata Chapter during 11-14 Feb 2020 at CSIR-Central Glass & Ceramic Research Institute.
6. Poster presentation entitled as “Morphology depended acetone sensing behavior of Tungsten Oxides” by **Puja Ghosh**, M. Manikandan, S. Sen and P. Sujatha Devi on International Conference on Nanoscience and Nanotechnology (Virtual Conference) during 01-03 Feb 2021.
7. Poster presentation entitled as “Comparison Sensing Study of Antase Cube and Rutile Rod based Structure by **Puja Ghosh**, S. Sen and P. Sujatha Devi on International Symposium on Materials of the Millennium: Emerging Trends and Future Prospects (MMETFP-2021) on November 19-21, 2021.

**LIST OF COURSES, WORKSHOP AND SEMINARS ATTENDED**

1. National Workshop on Spectroscopic Techniques (WoST 2019) from 30<sup>th</sup> January to 1<sup>st</sup> February 2019 at Centre for Nanoscience and Nanotechnology, Sathyabama Institute of Science and Technology.
2. Workshop on Nanolithography and Nanofabrication (INDIA NANO 2019) at S N Bose National Centre for Basic Sciences on 9<sup>th</sup>-10<sup>th</sup> July 2019.
3. **“Young Scientists’ Colloquium 2017”** organised by: Materials Research Society of India (MRSI), Kolkata Chapter on Wednesday, October, 2017 at Indian Institute of Engineering Science and Technology, Shibpur, Howrah.
4. **CSIR Platinum Jubilee Celebration** at Indian Institute of Chemical Biology true campus, Kolkata on 16<sup>th</sup>-20<sup>th</sup> September, 2017.
5. MRSI-Young Scientist Colloquium-2018 organized by Material Research Society of India, Kolkata Chapter and Indian Association for the Cultivation of Sciences, Kolkata on 20.09.2018
6. Royal Society of Chemistry – Roadshow 2018 at Indian Association for the Cultivation of Sciences, Kolkata, 26<sup>th</sup> September, 2018.
7. One day theme meeting on PRECESSION ELECTRON DIFFRACTION - SOLUTION TO CRYSTAL STRUCTURE FROM NANOPARTICLES AND 3D TOMOGRAPHY organized by CGCRI – Kolkata on 19th February, 2019.
8. ‘Inside Raman India Seminar’ on 09.04.19 and 10.01.19 at CRNN, Kolkata in collaboration with Renishaw.
9. Seminar on “Safety during the use of Hazardous Chemicals” organized by CSIR-CGCRI & M/s Thermo Fisher Scientific India Pvt. Ltd. on 26<sup>th</sup> June, 2019.
10. Participating at India International Science Festival (IISF-2019) at Kolkata from 5<sup>th</sup> to 8<sup>th</sup> November 2019.
11. Participation in Online one week Faculty Development Programme on “Recent Advances in Science & Technology” from 21-27<sup>th</sup> May, 2020 organized by RPS Group of Institutions, Haryana.
12. Attending the webinar on the 'Steps Towards Life: Chemistry!' by Prof. Jean-Marie Lehn, organised by Department of Chemistry under the School of Basic & Applied Sciences, Adamas University dated 29<sup>th</sup> May, 2020.
13. Participation in the Webinar on “DEVELOPING CAREER ORIENTED SKILLS DURING PANDEMIC PERIOD” organized by the Department of APPLIED SCIENCE, RPSCET, MOHINDERGARH HARYANA, on 30<sup>th</sup> May, 2020.
14. Participation in the Webinar on “Importance of Soft Skills & Technology in Career Development” organized by Department of Applied Science (RPS Group of Institutions, Haryana) on 31<sup>st</sup> May, 2020.
15. Participating for “International online conference on Current Pandemic and Beyond: The Physicists Response”, organized by the Department of Physics, Manipal University Jaipur on 2<sup>nd</sup> June, 2020.

16. Attending the (online) Faculty Development Program on "Advanced Materials and Characterization" during 15<sup>th</sup> -19<sup>th</sup> June 2020 organized by the Department of Physics, School of Sciences, NIT Andhra Pradesh, Tadepalligudem, Andhra Pradesh.
17. Participating at the "International Virtual Conference on Advanced Nanomaterials Applications" (VCAN 2020) organized by the Centre for Nanotechnology Research (CNR), Vellore Institute of Technology, Vellore, Tamil Nadu - 632 014, India during 17<sup>th</sup> to 19<sup>th</sup> June, 2020.
18. Participating in National Level Webinar on "Our Cosmic Consciousness" held on 29<sup>th</sup> June, 2020 organized by department of Mathematics of Servite College of Arts and Science for Women, Tamilnadu, India.
19. Actively participated in the International Virtual Conference, AFM-2020, held on August 26-28, 2020, at Kalinga Institute of Industrial Technology (KIIT) Deemed to be University, Bhubaneswar, Odisha, India.
20. Participating in 'VIRTUAL INTERNATIONAL CONFERENCE ON MULTIFUNCTIONAL ADVANCED MATERIALS (VICMAM-2021)' organized by Department of Chemistry, JVM's Degree College in collaboration with Association of Chemistry Teachers (ACT) on 9th and 10th August, 2021.
21. Participating in IP Awareness/ Training Program under National Intellectual Property Awareness Mission on February 14, 2022.

### **AWARDS AND RECOGNITIONS**

- ✚ Vidyasagar Bhaban Scholarship in 2011.
- ✚ DST-INSPIRE Scholarship for five years.
- ✚ Madan Mohan Shee Memorial Medal for standing First in order of merit among the successful candidates in Physics of M.Sc. examination of year 2016 and was awarded the Gold Medal of the year at the 1<sup>st</sup> Convocation of the college held on 30<sup>th</sup> January 2019.
- ✚ Student Council Member of Science department in 2015-2016 at Midnapore College.
- ✚ Junior Research Fellowship awarded from INSPIRE program of Department of Science & Technology, Government of India (2017-2019)
- ✚ Senior Research Fellowship awarded from INSPIRE program of Department of Science & Technology, Government of India (2019-Onwards)
- ✚ Lifetime member of Electron Microscope Society of India (EMSI-LM1930)
- ✚ Lifetime member of Materials Research Society of India (LMB3375)
- ✚ Lifetime member of Indian Ceramic Society (EL-772).
  
- ✚ First best poster award entitled as "Dual Applications of Hydrothermally Synthesized TiO<sub>2</sub> Nanorods" by **Puja Ghosh**, A. Roy, M. Narjinary and P. Sujatha Devi on National Symposium on New Trends of Research in Solid State Chemistry and Allied Areas at Jammu University, Jammu organized by ISCAS Institute of Solid State and Materials Science, Jammu, 4-6 March, 2018.

- ✚ Best Poster Award entitled as “Newer Applications of Anatase  $\text{TiO}_2\text{-Na}_{0.23}\text{TiO}_2$  Composite Nanorods” by **Puja Ghosh**, A. Roy, M. Narjinary, S. Sen and P. Sujatha Devi on 3<sup>rd</sup> International Conference on Advanced Functional Materials ICAFM 2019, organized by CSIR-NIIST, ICS-Kerala Chapter and MRSI Thiruvananthapuram Chapter held at CSIR-NIIST, Thiruvananthapuram during 9-10 December 2019.
- ✚ Institute of Scholars selected my work for “**Young Achiever Award 2021**”.
- ✚ Institute of Scholars has recognized as Reviewer for the journal named International Journal of Basic and Applied Sciences.
- ✚ Institute of Scholars has recognized as Professional Member of Institute of Scholars (InSc) valid for lifetime.

*“Science never solves a problem  
without creating ten more”*

*-George Bernard Shaw*

# A New Functional Composite for Photovoltaic and Sensor Applications

Puja Ghosh, Anurag Roy, Soumita Mukhopadhyay, Mousumi Narjinary, Senthilarasu Sundaram, Shrabanee Sen, and Parukuttyamma Sujatha Devi\*

As a preliminary drive to eventually develop dye-sensitized solar cell (DSSC)-powered gas sensors, many oxide-based systems have been explored to fabricate sensors that can show response at room temperature for any analyte gas. As an outcome of recent work in this endeavor, a composite nanorod of anatase  $\text{TiO}_2$  with  $\text{Na}_{0.23}\text{TiO}_2$  is found to exhibit both photovoltaic performance and gas sensing at room temperature as demonstrated here. An interesting morphology change along with a phase change from nanoparticle to nanorod is observed during the hydrothermal synthesis of anatase  $\text{TiO}_2$  nanoparticles with sodium hydroxide under a highly basic condition. In order to understand the effect of the minor phase  $\text{Na}_{0.23}\text{TiO}_2$  on the inherent properties of anatase  $\text{TiO}_2$ , the application of nanorod composite in two unique potential application areas, DSSC and acetone sensings is investigated. The composite material exhibits an enhanced efficiency of 7.85% for a DSSC. Surprisingly, a resistive sensor fabricated with the synthesized composite material exhibits room temperature p-type sensing behavior toward different concentrations of acetone (10, 5, 3, 2, and 1 ppm) with high selectivity.

well-accepted electronic and optical properties.<sup>[1,2]</sup> For example, as a photocatalyst for environmental applications, anatase is more preferred than rutile due to its inherent optoelectronic properties.<sup>[3–5]</sup> There has been many efforts to improve the optoelectronic properties of titania and an effective way of further modifying the electronic properties of  $\text{TiO}_2$  is doping, though ion-implant, shape control, and surface modifications are also being explored to improve the properties of  $\text{TiO}_2$ . In dye-sensitized solar cells (DSSCs), the anatase phase is considered to be the best-suited material so far exhibiting higher photovoltaic performance than other polymorphs of  $\text{TiO}_2$ .<sup>[6–8]</sup> In order to enhance the performance and related efficiency of DSSC, significant efforts have been devoted in improving the host  $\text{TiO}_2$ , which acts as a framework for DSSCs. However, mixing different phases followed by a hetero-

## 1. Introduction

Titanium dioxide ( $\text{TiO}_2$ ) has been known to exist mainly in three primary crystallographic modifications such as anatase (tetragonal), rutile (tetragonal), and brookite (orthorhombic) forms at ambient conditions. During the past few decades, the above-mentioned  $\text{TiO}_2$  polymorphs have been widely investigated for diverse applications due to their

structure formation of  $\text{TiO}_2$  has been found to result in better power conversion efficiency (PCE) than the sole usage of pure anatase. The heterostructure and mixed-phase formation could directly affect the charge transfer process between the different phases, possibly by reducing the recombination of photogenerated electrons and enhancing the electron mobility. In many cases, the synergistic effects of the three factors, such as electron transfer efficiency, light scattering, and dye adsorption, together leading to higher current density ( $J_{SC}$ ) have been reported.<sup>[9,10]</sup> In order to improve the efficiency of  $\text{TiO}_2$ , 1D nanostructures of  $\text{TiO}_2$ , such as nanorods, nanotubes, and nanowires, have also been studied<sup>[11,12]</sup> that are expected to significantly improve the electron transport properties due to directionally smooth electron mobility and lower intercrystalline contacts.<sup>[13–16]</sup> As reported by others, sodium titanate ( $\text{Na}_{0.23}\text{TiO}_2$ ) with a monoclinic crystal structure is expected to form a p–n junction with  $\text{TiO}_2$  that allows faster electron–hole separation followed by mobility via synergistic effect.<sup>[17,18]</sup> Wang et al. reported  $\text{TiO}_2/\text{Na}_{0.23}\text{TiO}_2$  as a heterojunction photocatalyst helpful for the photogenerated electron–hole pairs separation, resulting in an enhanced photocatalysis.<sup>[19]</sup> The same group also reported an effective method to prove the surface plasmon property of a composite and highlighted the application of  $\text{Na}_{0.23}\text{TiO}_2$  in photocatalysis.<sup>[20]</sup> Recently, understanding the influence of

P. Ghosh, Dr. A. Roy, Dr. S. Mukhopadhyay, M. Narjinary, Dr. S. Sen, Dr. P. S. Devi

Functional Materials and Devices Division  
CSIR–Central Glass and Ceramic Research Institute  
Jadavpur, Kolkata, West Bengal 700032, India  
E-mail: psujathadevi@niist.res.in

Dr. A. Roy, Dr. S. Sundaram  
Environment and Sustainability Institute  
University of Exeter  
Penryn Campus, Cornwall TR10 9FE, UK

Dr. P. S. Devi  
Chemical Sciences and Technology Division  
CSIR–National Institute of Interdisciplinary Science and Technology  
Thiruvananthapuram, Kerala 695019, India

 The ORCID identification number(s) for the author(s) of this article can be found under <https://doi.org/10.1002/aelm.202000785>.

DOI: 10.1002/aelm.202000785

synthesis parameters on the structure, morphology, and properties of titanate nanorods derived by sodium hydroxide (NaOH) treatment of TiO<sub>2</sub> nanoparticles (TP) has been reported by Silva et al.<sup>[21]</sup> There are also reports confirming the lower photocatalytic activity of TiO<sub>2</sub>-coated soda–lime glass than that of the TiO<sub>2</sub>-coated quartz due to the diffusion of Sodium-ion (Na<sup>+</sup>) into the TiO<sub>2</sub> film from the soda–lime glass substrate.<sup>[22,23]</sup> However, there are only very few reports on the effect of Na<sup>+</sup> on the photovoltaic properties of TiO<sub>2</sub> materials in DSSCs. The photovoltaic properties of NaOH-washed anatase TiO<sub>2</sub> nanosheets with exposed {001} facets were also investigated for DSSC.<sup>[24]</sup> The effect of sodium doping in improving the performance of DSSC was reported by Shalini et al. They recorded a PCE of 6% for sodium-doped TiO<sub>2</sub>.<sup>[25]</sup> It is worth mentioning that only very few reports are available on Na<sub>0.23</sub>TiO<sub>2</sub>/TiO<sub>2</sub> nanorods for DSSC application.

Recently, we have reported the performance of Gold (Au)-decorated ZnO/TiO<sub>2</sub> as a stable photocatalyst and TiO<sub>2</sub>-polyaniline composite as a photoanode in DSSCs.<sup>[26,27]</sup> In addition, as a preliminary effort to eventually develop DSSC-powered gas sensor, we have been exploring many oxide-based systems to fabricate sensors that could exhibit response at room temperature for any analyte gas. As an outcome of our recent work in this endeavor, a composite nanorod (CR) of anatase TiO<sub>2</sub> with Na<sub>0.23</sub>TiO<sub>2</sub> has been found to exhibit both photovoltaic performance and gas sensing at room temperature as demonstrated in this work. Thus, in this article, we report the synthesis of TiO<sub>2</sub> anatase-Na<sub>0.23</sub>TiO<sub>2</sub> CR by a hydrothermal synthesis using NaOH and its dual functional application in DSSC and sensing. We investigated the formation of Na<sub>0.23</sub>TiO<sub>2</sub> nanorod and its influence and performance on TiO<sub>2</sub> anatase photoanode in DSSC. In addition, the synthesized CR has also been explored for gas-sensing applications. An enhanced p-type semiconducting sensing response was achieved for different concentrations of acetone (10, 5, 3, 2, and 1 ppm) along with strong selectivity and reproducibility towards acetone at room temperature.

## 2. Results and Discussion

### 2.1. Thermal Analysis

The thermal decomposition nature of the prepared sample at pH 12 is shown in Figure S1, Supporting Information, which exhibited an overall weight loss of ≈9% within the temperature range of room temperature to 550 °C. Initially, about 3% weight change was observed between 30 and 180 °C followed by a small weight change at 400 °C corresponding to the removal of water in the as-prepared powder sample. Finally, the weight loss became almost negligible above 400 °C. The corresponding differential thermal analysis (DTA) curve exhibited a broad exothermic change in the range of 150–400 °C, indicating crystallization of the as-prepared powder sample. Based on the information observed from the thermogravimetric analysis (TGA) and DTA, the as-prepared powder was calcined at 500 °C to form the phase pure final compound.

### 2.2. Effect of pH on Phase Change and Morphology

The effects of pH during the synthesis and its effect on the phase transformation were investigated through systematic analysis of the data collected from powder X-ray diffraction (XRD) and field emission scanning electron microscopy (FESEM) (Figures 1 and 2). In Figure 1, the XRD patterns of starting TiO<sub>2</sub> powder and as prepared powder at pH 8, 10, 12, and 14, using NaOH and calcined under identical conditions, are presented. The XRD pattern of the starting commercial TiO<sub>2</sub> powder confirmed it to be the anatase phase of TiO<sub>2</sub> only (JCPDS no. 21-1272). During the reaction, the same phase is retained up to pH 10. There is an indication of the formation of a second phase, Na<sub>0.23</sub>TiO<sub>2</sub>, at pH 12. The observed reflections of the new phase matched well with the monoclinic Na<sub>0.23</sub>TiO<sub>2</sub> phase (JCPDS no. 22-1404). Thus, the final resultant product obtained from the hydrothermal treatment of commercial TiO<sub>2</sub> anatase nanoparticle powder exhibits mainly anatase TiO<sub>2</sub> phase with a minor amount of Na<sub>0.23</sub>TiO<sub>2</sub> as a coexisted phase, thereby forming a composite powder. The growth of this phase continues at a higher pH of ≈14 also.

Therefore, pH 12 has been fixed as the optimum condition to form Na<sub>0.23</sub>TiO<sub>2</sub> phase along with the anatase phase. Systematic microstructural analysis was also performed to understand the effect of pH if any on the morphology of the starting material as shown in Figure 2. A change in the morphology of the starting material started to appear with change in pH, and a distinct change in morphology was observed at pH 12 and 14.

The topotactic transformation of particles and the formation of thin rod-shaped material are clearly evident in Figure 2. Further, at higher pH (≈14), the rods get fused as shown in Figure 2 (v) probably due to the extreme basic condition used. Below pH 12, the product remained as particles; at pH 12, they formed thin rods and above pH 12, the particles transformed to thick rods. Thus, it is evident from Figure 2 that the starting anatase particles have transformed to well-defined thin rods during the

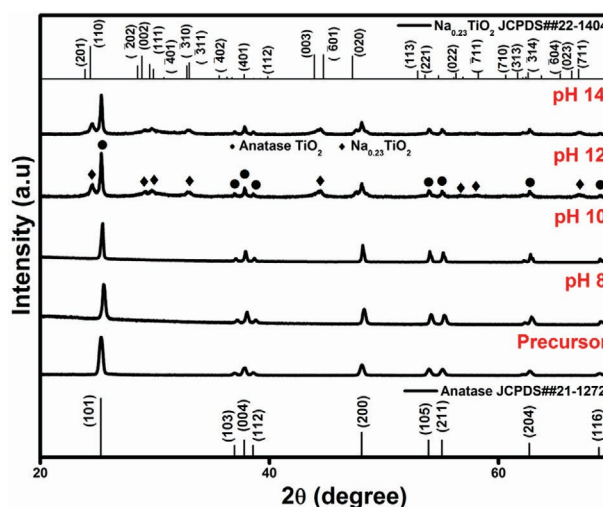


**Figure 1.** The XRD patterns of precursor powder and synthesized products obtained after hydrothermal treatment of anatase TP at 180 °C for different pH conditions followed by calcination at 500 °C.



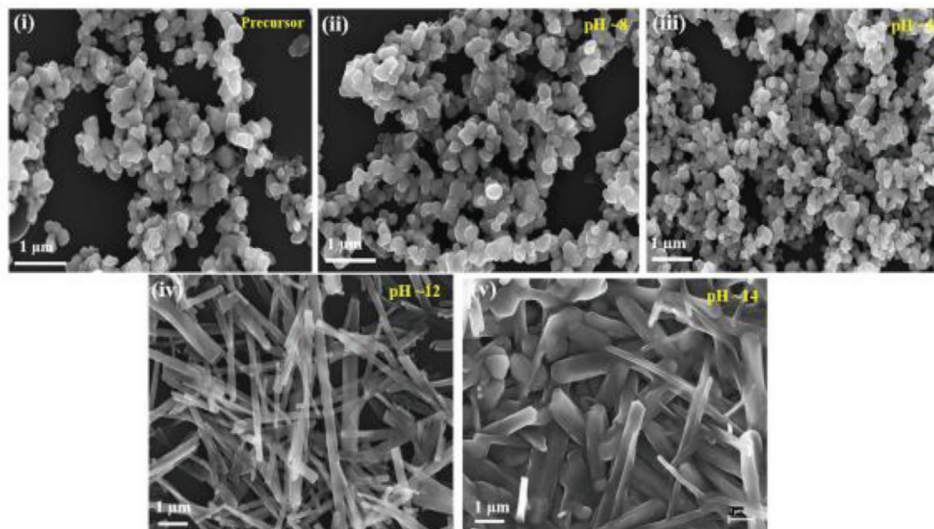


**Figure 2.** The FESEM microstructural images of precursor powder and hydrothermally synthesized samples at different solution pH conditions from 8 to 14.

hydrothermal reaction at 180 °C in the presence of NaOH at a pH of 12 and further annealing at 500 °C. Thus, based on the TGA–DTA and XRD results, the 500 °C calcined sample was selected for detailed characterization and further studies.

### 2.3. Optimization of Hydrothermal Conditions

In order to further evaluate the effect of duration of the hydrothermal reaction on the above-observed changes that led to the formation of anatase/ $\text{Na}_{0.23}\text{TiO}_2$  coexisted nanorods, the duration of the experimental conditions has been varied from 8 to 48 h. After optimizing the pH at 12, where a change in shape was noticed as shown in Figure 1, we varied the duration of the reaction at pH 12. The observed change in structure during this variation is shown in Figure 3 along with the corresponding X-ray data. Variation of hydrothermal reaction duration on the phase change formation and morphological changes from particles to rods is clearly evident in Figure 3. As observed from the XRD data, the anatase phase was retained up to 24 h of hydrothermal treatment, beyond which it transformed to a mixed phase of anatase and  $\text{Na}_{0.23}\text{TiO}_2$  by 36 h. Finally, the compound formed after 48 h of hydrothermal treatment at 180 °C temperature was a rod-shaped composite of anatase  $\text{TiO}_2$  with  $\text{Na}_{0.23}\text{TiO}_2$ . The increase of the hydrothermal reaction time from 36 to 48 h led to only a minor increase in surface area of the product along with complete crystallization of the titanate phase. In order to monitor the structural changes if any during the phase transformation, we have also taken successive FESEM images of the samples as shown in Figure 3. The precursor anatase  $\text{TiO}_2$  that was in the particle form successively transformed into nanorod on increasing the hydrothermal reaction duration from 12 to 48 h. This structural transformation could have happened by Ostwald ripening during which many small crystals slowly disappear, except for a few that grow larger at the expense of the small crystals, which act as fuel for the growth of bigger crystals.<sup>[28–30]</sup> Kolen'ko et al. reported the

synthesis of nanorods in one step by hydrothermal treatment in a NaOH solution followed by an acid treatment to produce sodium-free nanorods.<sup>[30]</sup> By following a similar type of acid-wash process, we also could generate  $\text{Na}^+$ -free samples. Acid treatment was found to be essential in removing excess sodium to obtain sodium-free nanorods. To confirm the absence of chloride ion in the sample after acid washing, a small amount of the filtrate was treated with silver nitrate ( $\text{AgNO}_3$ ) solution, where no white precipitate was formed, indicating the absence of chloride ion and sodium chloride ( $\text{NaCl}$ ) in the sample solution. Thus, successive acid washing and subsequent test with  $\text{AgNO}_3$  helped in getting sodium-ion-free composite rod sample.

In Figure S2, Supporting Information, XRD patterns confirming the effect of acid washing to remove the excess Na from the as-prepared sample followed by multiple washing with deionized water to form the targeted composite product have been presented. Initially, the as-collected powder sample appeared less crystalline (Figure S2a, Supporting Information). In order to remove the unreacted sodium ion from the precipitated sample, HCl washing was performed, which produced  $\text{NaCl}$  as a by-product as evident from Figure S2b, Supporting Information. At this stage, the solution pH also has been reduced to  $\approx 7$ . However, after thoroughly washing with deionized water, excess  $\text{NaCl}$  also gets completely dissolved, and the final product exhibited only a mixed-phase of  $\text{TiO}_2$ - $\text{Na}_{0.23}\text{TiO}_2$  with enhanced crystallinity (Figure S2c, Supporting Information). The corresponding energy-dispersive X-ray spectroscopy (EDX) analysis images of the as-prepared sample, HCl-washed sample, and deionized-water-washed sample are shown in Figure S3, Supporting Information. This further confirms the complete removal of unreacted  $\text{Na}^+$  ions and formation of composite powder in the final product.

Raman studies were also carried out to further understand the presence of both  $\text{TiO}_2$  anatase phase and  $\text{Na}_{0.23}\text{TiO}_2$  in the final product. Figure S4, Supporting Information, depicts the characteristic  $E_g$  band at 143.4 and 639  $\text{cm}^{-1}$ , the  $B_{1g}$  band at 397  $\text{cm}^{-1}$ , and the ( $A_{1g}+B_{1g}$ ) mode centred at 516  $\text{cm}^{-1}$  of anatase

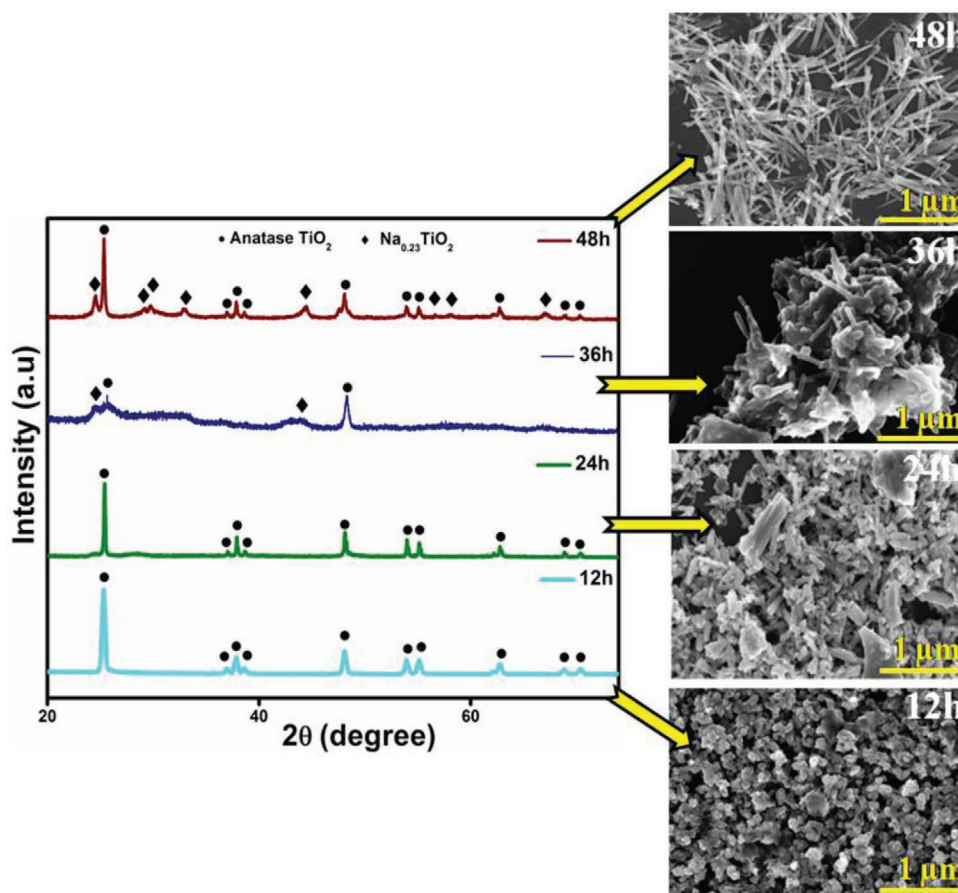


**Figure 3.** The XRD patterns along with the respective FESEM pictures of the hydrothermally prepared samples at pH 12 and at a temperature of 180 °C for different durations followed by calcination at 500 °C.

phase of  $\text{TiO}_2$ . After the hydrothermal treatment, the characteristic  $E_g$  mode becomes narrower and slightly blue-shifted from 143.4 to 148 cm. This may be due to the phonon-confinement-effect-developed strain owing to the change in size and shape of  $\text{TiO}_2$  during the hydrothermal synthesis process.<sup>[31]</sup> Also, the weaker Raman bands at 202.4, 285.3, and 449.6 cm confirm the presence of sodium titanate (NT) phase in the sample beside the anatase  $\text{TiO}_2$ .

#### 2.4. Microstructure Analysis by Transmission Electron Microscopic Study

More clear evidences for the formation of nanorod morphology can be found in **Figure 4a–i** from the detailed transmission electron microscopy (TEM) investigation of anatase/ $\text{Na}_{0.23}\text{TiO}_2$  coexisted composite in a single nanorod.

**Figure 4a,b** represents the TEM bright-field image of the precursor TP at different magnifications confirming an average particle size of 30 nm. The high-resolution TEM (HRTEM) image (**Figure 4c**) clearly shows an interlayer spacing value of 0.351 nm corresponding to (101) crystal plane of anatase  $\text{TiO}_2$  phase. On the other hand, TEM bright-field images of the prepared anatase/ $\text{Na}_{0.23}\text{TiO}_2$  coexisted sample exhibited a rod-like

structure having an average diameter of 22 nm, as shown in **Figure 4d,e** at different magnifications. The corresponding HRTEM image shown in **Figure 4f** indicates the coexistence of (001) plane of  $\text{Na}_{0.23}\text{TiO}_2$  and (101) plane of anatase  $\text{TiO}_2$ .

Further, the TEM bright-field images of calcined sample exhibit randomly distributed fine thinner rod-like structure having an average diameter of  $\approx 10$  nm and an aspect ratio of 25:1. The excellent crystallinity of the synthesized nanorods is clear from the HRTEM image, as shown in **Figure 4i**. Further, the interlayer spacing of the most intense (101) peak is found at 0.351 nm along with (004) plane (0.237 nm) corresponding to anatase  $\text{TiO}_2$  phase, which corroborates with the XRD and Raman studies. The color elemental mapping of the same sample was carried out as shown in **Figure S5a**, Supporting Information, EDX analysis. The extensive area mapping ensures homogeneous distribution of Ti and O, and successful incorporation of sodium, as the only other element in the CRs. Besides, the quantitative EDX analysis stipulates an insufficient amount of O in CRs, as shown in **Figure S5b**, Supporting Information. The atomic percentage of elemental composition indicates  $\approx 5.6\%$  of Na availability in the CR (inset of **Figure S5b**, Supporting Information). Based on the available evidences, it is very difficult to predict the exact reason for the conversion of particles to rod during hydrothermal reaction. As described in other reports,

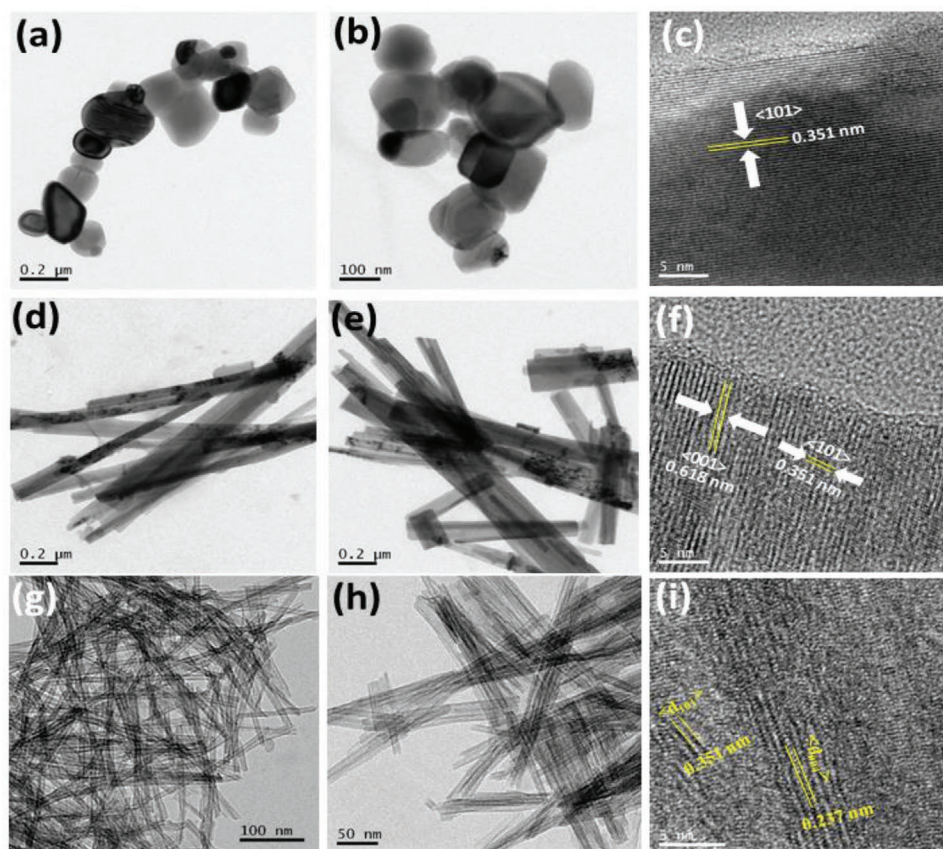


**Figure 4.** a,b) TEM bright-field images of starting anatase  $\text{TiO}_2$  powder at different magnifications. c) Corresponding HRTEM image. d,e) TEM bright-field images at different magnifications. f) Corresponding HRTEM image of the as-prepared nanorod. g,h) TEM bright-field images at different magnifications. i) Corresponding HRTEM image of CR calcined at  $500^\circ\text{C}$ .

formation of layered nanosheets might be the initial step for the formation of rods that then become seeds for an oriented crystal growth process leading to thinner titanate nanorods.<sup>[32,33]</sup>

According to many reports, the phase and morphology transformation during hydrothermal synthesis strongly depends on the NaOH content in the reaction mixture.<sup>[22,32]</sup> The TP in the highly basic medium of NaOH could lead to the formation of lamellar sheets due to the breakage of Ti–O–Ti bonds and formation of O–Ti and Ti–OH bonding and the loose O–Ti could bind to  $\text{Na}^+$  forming Ti–O–Na. The ion exchange of  $\text{Na}^+$  by  $\text{H}^+$  is a well-known mechanism reported in the literature.<sup>[35,36]</sup> The intermediates such as Ti–OH could rearrange to form sheets of edge-sharing  $\text{TiO}_6$  octahedra with  $\text{Na}^+$  and  $\text{OH}^-$  intercalated between the sheets leading to the gradual formation of layered titanate.<sup>[34]</sup> Thus, the hydrothermal reaction of TP in high-pH condition with NaOH might have helped in the formation of sodium titanate particles with a rod-like morphology.<sup>[37]</sup>

For instance, for protonated  $\text{TiO}_2$  nanorods, pure anatase phase is usually formed, whereas for  $\text{Na}^+$  rich nanorods, post-annealing leads to the mixed phase. The measured zeta potential of the precursor anatase nanoparticle was  $-49.2$  mV, indicating a highly water-soluble colloidal solution, whereas in case of the synthesized nanorod, the zeta potential value gets reduced to  $-12.6$  mV.

## 2.5. X-Ray Photoelectron Spectroscopic Analysis

To understand the chemical and binding states of the elements present in TP and CR, X-ray photoelectron spectroscopy (XPS) studies were carried out as shown in Figure 5a–e. It is evident that both samples contain Ti and O, as shown in the XPS survey spectra in Figure 5a. The appearance of metallic Na specifies the existence of Na in CR sample. The core level binding energy peaks at 493.2 and 1070.1 eV indicate Na KLL and Na 1s states, respectively (Figure 5b). The XPS peaks at 464.42 and 458.62 eV correspond to binding energies of the Ti  $2p_{3/2}$  and  $2p_{1/2}$  states, respectively, of TP sample. The binding energy of CR exhibited a significant Stokes shift, i.e., 463.75 and 457.95 eV of the Ti  $2p_{3/2}$  and  $2p_{1/2}$  states, respectively, as shown in Figure 5c. This may be due to the coexistence of tetragonal-monoclinic phase.<sup>[15,38]</sup> Besides, the peak shifting sometimes may be attributed to the lower electronegativity of Na (0.93) than that of Ti (1.52), which confirms the substitutional incorporation of  $\text{Na}^+$  at  $\text{Ti}^{4+}$  site.<sup>[39]</sup> For both the samples, the spin–orbit splitting energy of 5.8 eV is characteristic of  $\text{Ti}^{4+}$  in the  $\text{TiO}_2$  form. At the same time, the O1s binding energy gets decreased for CR than TP. By deconvolution, the observed three peaks of O1s shown in Figure 5d,e represent the high-resolution O1s spectrum of TP and CR samples, respectively. The observed two different binding energies are attributed

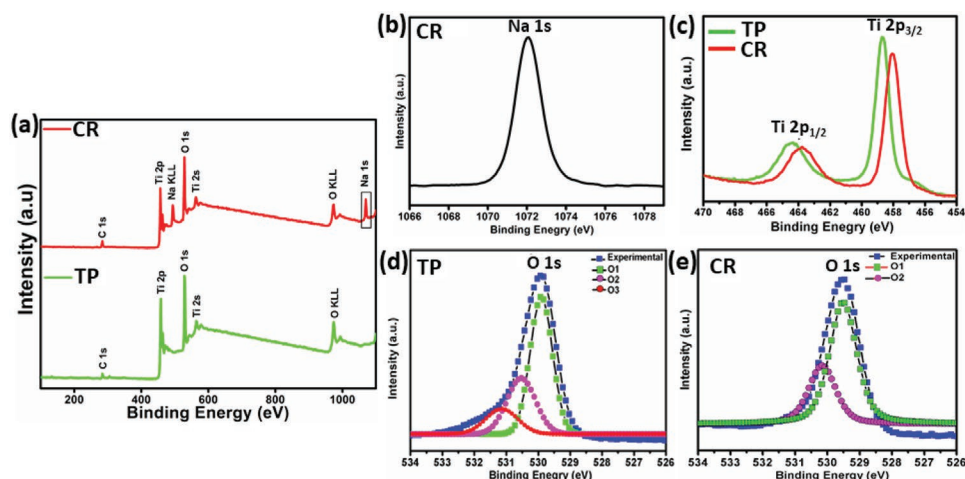


**Figure 5.** a) XPS survey. Core level spectra of b) Na spectrum of CR sample, c) Ti spectrum of TP and CR samples, respectively. Corresponding deconvoluted O 1s spectrum of d) TP and e) CR samples.

to Ti–O–Ti for both the samples as O1 component and Ti–O–H as O2 component for both the samples (Figure 5d,e). The oxygen deficiency of CR sample as observed from XPS analysis for O1s spectrum further corroborates the quantitative EDX data (Figure S5b, Supporting Information). Table S1, Supporting Information, indicates the individual core level binding energies and their difference for both the samples. Interestingly, TP exhibiting an additional component of O3 at 531.16 eV is associated with the  $O^{2-}$  ions in oxygen-deficient regions within the  $TiO_2$  matrix.<sup>[40]</sup> Moreover, the absence of any signal of Cl as an element or relative derivatives in the survey spectrum (Figure 5a) indicates the nanorods are free of NaCl and its derivatives.

## 2.6. Structural and Optical Studies of the Composite

UV–vis absorption spectra of TP sample exhibit a broad absorption  $\approx 348$  nm, whereas a bathochromic shift (362 nm) was observed in the absorption of CR sample shown in Figure 6a. The corresponding band gap was calculated using Taucs' equation, and it was found to be  $\approx 3.21$  and 3.01 eV for TP and CR (shown in Figure S6, Supporting Information), respectively. The indirect band gap value of CR (3.01 eV) falls between the reported band gap values of  $Na_{0.23}TiO_2$  phase, which could be suitable as a photoanode material candidate in DSSCs. The relatively higher reflectance spectrum of the CR shown in Figure 6b is attributed mainly to the random orientation of rod structures. The average thickness of the CR-based photoanode film was around 9.42  $\mu m$  as evident from the FESEM microstructural image, as shown in the inset of Figure 6b.

In order to unravel the effect of change in morphology and the photovoltaic performance, the Brunauer–Emmett–Teller (BET) surface area of TP and CR samples was measured by nitrogen isothermal adsorption process (Figure 6c). The corresponding pore size was calculated by the Barrett–Joyner–Halenda (BJH) method, as shown in the inset of Figure 6c. As evident from Figure 6c, the type IV isotherm

was observed for both the morphologies. The CR exhibited an enhanced BET specific surface area of 90.03  $m^2 g^{-1}$  than the TP (56.65  $m^2 g^{-1}$ ), mainly attributed to the thinner rod-based structure. Also, in case of TP sample, a well-defined hysteresis loop indicates the well-developed mesoporous characteristics with an average pore size of  $\approx 6$  nm. Whereas, the pore size for nanorods was  $>50$  nm mainly originated from the interlayer space of nanorods, as shown in the inset of Figure 6c. The UV–vis absorption spectra of the residual dye solution collected after 24 h adsorption on the different morphology of  $TiO_2$  surface were measured by the dye desorption method as shown in Figure 6d. The reduction in the characteristic intensity of the residual N719 dye solution at  $\approx 384$  and 525 nm was more for CR than TP sample, which is an indirect evidence for a higher amount of dye adsorbed by the CR sample. The higher interlayer space and surface area of the CR sample could have favored a higher dye loading for the CR sample.

## 2.7. Application of $TiO_2$ - $Na_{0.23}TiO_2$ Composite in DSSC: DSSC Performance and Electrochemical Impedance Spectroscopy Analysis

In order to evaluate the photovoltaic performance of the synthesized composite rods with the starting precursor  $TiO_2$  and also a standard P25  $TiO_2$  sample, DSSC devices have been fabricated as per our previous methods.<sup>[11,27]</sup> The measured performance of the fabricated DSSC device is shown in Figure 7. The  $J$ - $V$  characteristics of the DSSCs fabricated with synthesized CR, TP, and P25 are presented in Figure 7a. The fabricated DSSC with CR exhibited a PCE of 7.85% with a short circuit current ( $J_{SC}$ ) of 16.82  $mA cm^{-2}$ , open-circuit voltage ( $V_{OC}$ ) of 0.75 V, and a fill factor (FF) of 0.66. On the contrary, TP exhibited a PCE of 3.25% with a  $J_{SC}$  of 8.77  $mA cm^{-2}$ ,  $V_{OC}$  of 0.71 V, and FF of 0.53. The details of the device testing parameters for individual tested cells are presented in Table S2, Supporting Information.

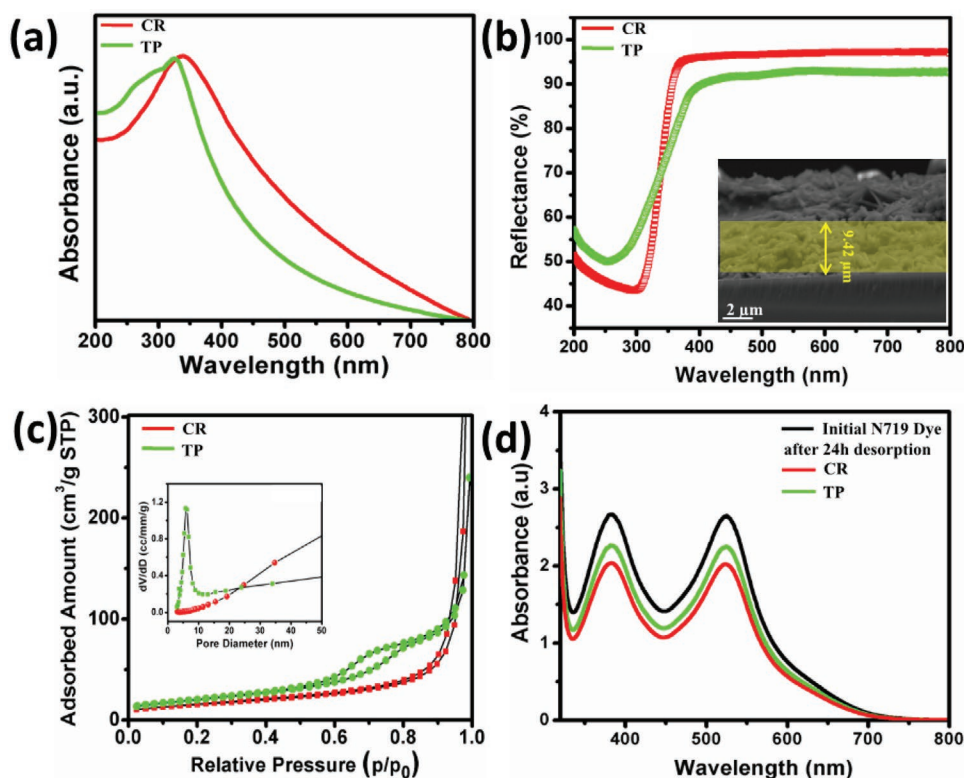


**Figure 6.** a) UV-vis absorption spectra. b) Diffuse reflection spectra of TP- and CR-based films (at inset: cross-sectional FESEM image of the CR-based film). c) Nitrogen adsorption-desorption isotherm of TP and CR samples; corresponding BJH pore size distribution curves are shown in the inset, respectively. d) UV-vis absorption spectra of initial N719 dye and remaining N719 dye after adsorption on TP- and CR-based photoanode films, respectively.

We have also compared the photovoltaic performance of P25 nanoparticles that exhibited an efficiency of 3.95% only with an enhanced  $V_{OC}$  (0.77 V) and FF (0.56) than the starting  $TiO_2$  samples under identical conditions. The higher efficiency of CR without any surface modification such as applying a scattering layer, or  $TiCl_4$  treatment reflects the influence of the unique rod-structured morphology of CR compared to the particle morphology of TP and P25 samples.

The electrochemical impedance spectroscopy (EIS) measurements were carried out to understand the transport properties

at different interfaces in the DSSC assembly, as shown in Figure 7b. On illumination under 1 sun, the CR-based device exhibited a series resistance ( $R_s$ ) of  $37.92 \Omega \text{ cm}^{-2}$  and an electrochemical charge transfer resistance ( $R_{CT}$ ) of  $68.02 \Omega \text{ cm}^{-2}$ , whereas the TP-based device exhibited an  $R_s$  of  $37.96 \Omega \text{ cm}^{-2}$  and  $R_{CT}$   $78.96 \Omega \text{ cm}^{-2}$ , respectively. Interestingly, the  $R_s$  value found almost the same for both the devices. However, the  $TiO_2/Na_{0.23}TiO_2$  coexisted phase showed a smaller  $R_{CT}$  value, which in turn promotes the transfer of more electrons from the external circuit as evident from the incident photon-to-current

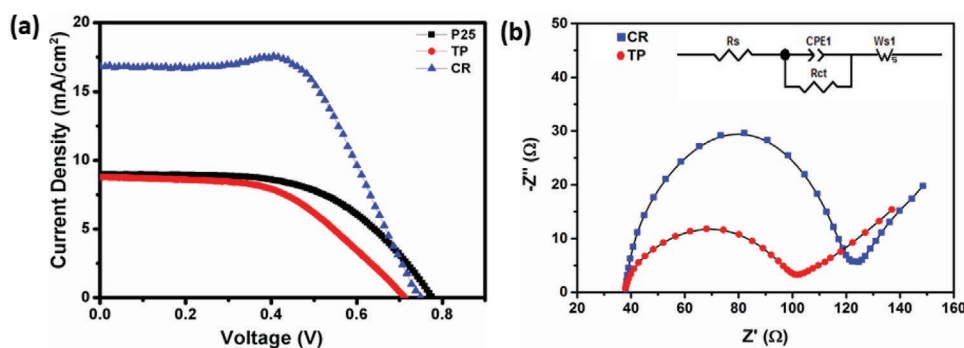


**Figure 7.** a) Current density ( $J$ )–voltage ( $V$ ) curve of DSSCs fabricated with P25, TP, and CR samples, respectively. b) Nyquist plots of TP- and CR-based DSSC devices (inset: corresponding equivalent circuit diagram).

efficiency (IPCE) measurements. The measured parameters are summarized in Table S2, Supporting Information.

## 2.8. IPCE and Cyclic Voltammetry Analysis

The IPCE curve for the N719 dye-sensitized devices exhibited a broad peak over the range of 300–700 nm with a maximum value of  $\approx 62\%$  at 540 nm for the CR-based device and  $\approx 46\%$  for TP-based device, as shown in Figure 8a. In order to check the cycling ability of the composite photoanode, the cyclic voltammetric (CV) curves were recorded for the champion CR cell, with different numbers of CV cycles, in the voltage window of  $-1.0$  to  $+1.0$  V with a scan rate of  $0.05 \text{ mV s}^{-1}$ . A typical voltammogram of different cycles executed for a CR film is presented in Figure 8b. Both the anodic and cathodic currents simultaneously vary as the number of cycles from 5 to 25. With increasing the testing cycle, current responses are increased and reach a maximum with 20 cycles. The peak currents are dropped with 25 cycles. Moreover, all the cycles trending the voltammogram with similar pattern and narrower peak-to-peak separation, indicating higher electron transfer kinetics, which would enhance the performance of the cell. These results adequately agree with the  $J$ - $V$  result.

In comparison to the reported results on the performance of  $\text{TiO}_2$  nanorod-based photoanodes in DSSCs, the performance of CR is quite competitive and promising, as shown in Table S3, Supporting Information.<sup>[34,41–47]</sup> The device performance has been repeatedly checked for a week. The high  $V_{\text{OC}}$  of  $>0.7$  V facilitates  $\text{TiO}_2/\text{Na}_{0.23}\text{TiO}_2$  nanorods to establish as a potential and new form of a composite photoanode candidate for DSSCs. Interestingly, in this study, the nanorods are formed as the coexisted phase of anatase  $\text{TiO}_2/\text{Na}_{0.23}\text{TiO}_2$  in a single morphology, thereby exhibiting a higher efficiency compared to TPs and P25 nanoparticles.

We propose that the mixed-phase formation could facilitate faster electron mobilization probably due to the p–n junction formed at the interface, resulting in better photovoltaic performance, as shown in Figure 9. We believe that the electrons generated in dye-sensitized nanorods migrate first to the anatase phase (n-type) followed by the titanate phase (p-type) in the composite and finally to the external on fluorine-doped tin oxide (FTO). Due to the very close band gap of  $\approx 3.21$  eV for TP and

3.01 eV for CR, the excited electrons generated in the anatase  $\text{TiO}_2$  phase may swiftly migrate towards the CB of the titanate phase in the composite on illumination. Both transferred electrons from anatase  $\text{TiO}_2$  and electrons directly excited to the CB of the titanate phase can supply more free electrons to FTO resulting in a better performance.<sup>[48–50]</sup>

Furthermore, the rods are expected to facilitate direct conduction pathway with lesser grain boundaries for rapid electron transport than other morphologies as observed in our earlier publications.<sup>[51,52]</sup> As evident from the microstructure analysis and the diffuse reflection spectra in Figure 6b, the slanting rods in the current case could favor adequate light scattering property and rapid electron transfer both could be responsible for the enhanced light harvesting to enhance the cell efficiency.<sup>[27,53,54]</sup> The particles, on the other hand, suffer from trapping/detrapping phenomenon in the conduction pathway between the grain boundaries, and therefore result in lesser efficiency than a rod. The enhanced photovoltaic performance of the composite may also arise from the band gap position of the mixture of phases. Therefore, the observed preliminary result of the device performances based on the synthesized anatase/ $\text{Na}_{0.23}\text{TiO}_2$  coexisted nanorods indicates the advantage of the existence of  $\text{Na}_{0.23}\text{TiO}_2$  phase along with  $\text{TiO}_2$  in enhancing its performance in DSSC.

## 2.9. Application of $\text{TiO}_2$ - $\text{Na}_{0.23}\text{TiO}_2$ Composite in Acetone Sensing

As an initiative to eventually develop DSSC-powered gas sensor, we have also explored application of the synthesized powder in gas sensor fabrication. The resistive sensor fabricated using the synthesized CR powder has been tested for the detection of acetone that has been considered as a biomarker to detect blood glucose level from breath noninvasively. The acetone concentration for diabetic patients in breath lies in the range from 1.7 to 3.7 ppm, whereas for a healthy person, the concentration range will be below 1 ppm.<sup>[55,56]</sup> After fabrication of the sensor with CR, the change of resistance was monitored at different acetone concentrations. The sensor was exposed to 10, 5, 3, 2, and 1 ppm acetone at room temperature. The CR-based sensor exhibited response ( $R_g/R_a$ ) signal as 7.1, 4.7, 4.1, 3.8, and 3.6 for 10, 5, 3, 2, and 1 ppm acetone, respectively, at room temperature with

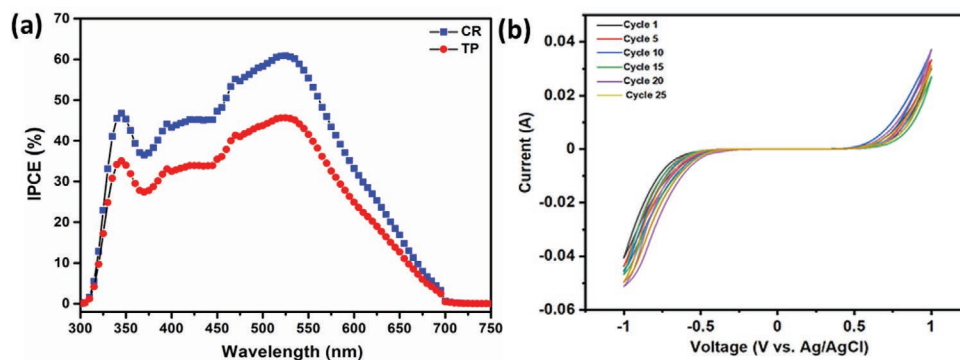
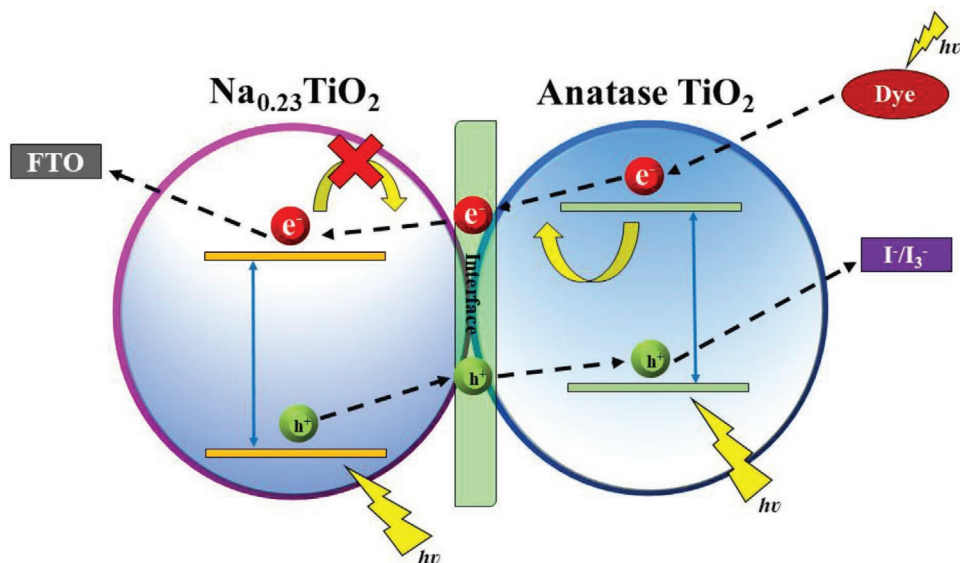


Figure 8. a) IPCE measurements of TP- and CR-based DSSC devices. b) Cyclic voltammogram of CR for different numbers of CV cycles.



**Figure 9.** Schematic description of the proposed electron transfer processes and energy band structures of the composite phase and anatase.

15 s of exposure time, as shown in **Figure 10a**. The dynamic response curve of the sensor towards 10, 3, and 1 ppm acetone is presented in **Figure 10b–d**. The single cycle of the dynamic response curve of the CR-based sensor for 3 ppm of acetone showing the response and recovery time as 12 and 20 s, respectively, is shown in **Figure 10c**. Besides, the CR-based gas sensor exhibits enhanced acetone response compared to carbon monoxide (CO), ethanol, and nitrogen gases, which are considered as the interfering gases, as shown in **Figure 10e**.

Along with the direct current (DC) measurements, we have also used the alternating current (AC) method by using a precision impedance analyzer in the 100 Hz to 1 MHz frequency range to understand the conduction process and the sensing mechanism where  $Z'$  indicates the real part and  $Z''$  represents the imaginary part of the complex impedance data. The variation of Nyquist diagram of CR-based sensor is presented in **Figure 10f** in the presence of air and acetone at room temperature. An attempt to record the response of a sensors made

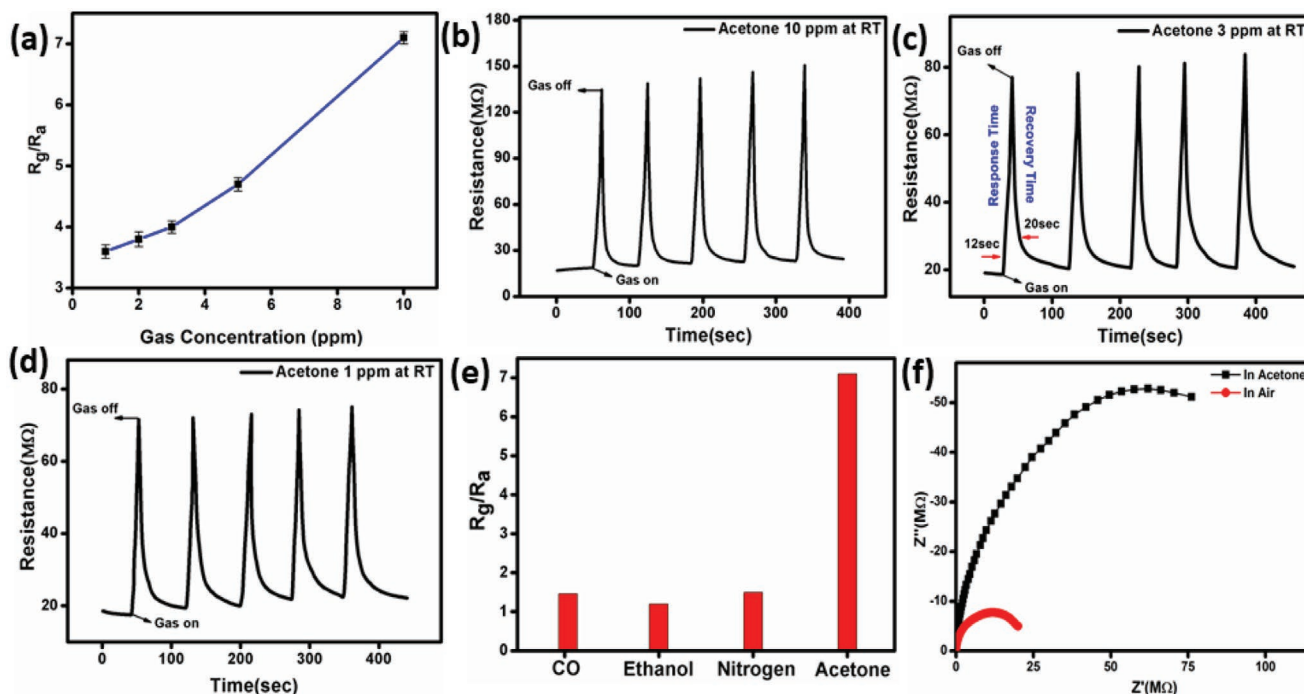


**Figure 10.** a) The response of the sensor towards different concentrations of acetone at room temperature. Dynamic response curve towards b) 10 ppm, c) 3 ppm, and d) 1 ppm acetone, respectively. e) Selectivity of CR-based sensor towards different gases. f) Nyquist plot of CR-based sensor in air and in the presence of acetone.

with the precursor powder TP was not successful. The TP-based sensor showed an exceptionally low sensing response ( $R_g/R_a$ ) of only 1.2 towards 10 ppm acetone at 350 °C operating temperature.

Interestingly the composite exhibited a p-type sensing behavior compared to TiO<sub>2</sub>, which is an n-type semiconducting material. However, further studies are in progress to understand the acetone-sensing behavior of the composite powder.

As demonstrated through various experimental evidences, the composite rods of TiO<sub>2</sub>-Na<sub>0.23</sub>TiO<sub>2</sub> formed during the hydrothermal synthesis at 180 °C and pH 12 for 48 h and further calcination at 500 °C exhibited room temperature acetone-sensing behavior in addition to its enhanced performance as a photoanode for DSSC probably due to the closely related p-n junction formed between the two phases.

### 3. Conclusions

Anatase TiO<sub>2</sub> with Na<sub>0.23</sub>TiO<sub>2</sub> nanorod was synthesized by hydrothermal treatment of the commercially available anatase TP with NaOH solution at 180 °C and pH 12. It was possible to establish the crucial role of NaOH to obtain the composite phase with interesting nanorod morphology. The TEM study reveals an average diameter of the synthesized nanorod as ≈10 nm with an aspect ratio of 25:1 having a BET specific surface area of ≈90 m<sup>2</sup> g<sup>-1</sup>. The mixed-phase sample exhibited higher dye loading capacity than the pure anatase sample for DSSC application. Further, the composite phase sample exhibited an enhanced photon-to-current conversion efficiency of 785% as compared to the precursor anatase sample (3.25%) and the standard commercially available P25 sample (3.95%). The increased performance of CR-based DSSCs was attributed to the high activity and surface area for increased dye adsorption along with the aligned rod shape for faster electron mobility and light scattering property. Besides, our studies could pave a way to future advancements in the area of DSSCs using TiO<sub>2</sub>-based composite materials as photoanode. An enhanced p-type semiconducting sensing response was achieved for different concentrations of acetone (10, 5, 2, 3, and 1 ppm) followed by strong selectivity and reproducibility towards acetone at room temperature. Thus, the synthesized composite could be projected as a material with renewed dual applications in the field of DSSC and gas sensor. The experimental results, thus, indicate that this simple and cost-effective synthesis process and the materials produced thereby can be used as a promising candidate for integrated DSSC-powered sensor developments for futuristic application.

### 4. Experimental Section

**Synthesis of CRs:** The composite powder was synthesized from standard anatase TiO<sub>2</sub> powder by hydrothermal reaction under extreme basic condition using NaOH. In the initial stage, 2 g of commercial anatase TiO<sub>2</sub> powder (Baker ANALYZED reagent 1-4162, J. T. Baker Chemical Company, USA) was mixed with 10 g of NaOH (Merck, Germany) and 25 mL of deionized water. The mixture was stirred continuously for 2 h to get a pH of 12 for the reaction mixture. The reaction mixture was transferred into a 50 mL Teflon-lined autoclave that was kept in a furnace maintained at 180 °C for 48 h. The reaction pH

was varied to 8, 10, 12, and 14 by changing the amount of NaOH added to the reaction mixture. Under each step, pH was measured and fixed by varying the amount of NaOH used prior to transferring the reaction mixture to the autoclave. The product formed was characterized to ascertain the nature of the product formed under each pH condition. The as-prepared white product was centrifuged at 10000 rpm and washed with deionized water. However, it was difficult to remove the excess sodium by water washing. Therefore, the precipitate was washed with 0.1 M HCl (Merck, Germany) prior to washing with deionized water. The filtrate was treated with AgNO<sub>3</sub> solution to test for the presence of chloride ions. The washing was continued till no white precipitate was formed with silver nitrate, indicating the absence of chloride ion as NaCl form in the sample solution. The synthesis process was repeated under different pH conditions (8, 10, and 14) by varying the amount of NaOH used. To further perceive the effect of the hydrothermal reaction duration, the reaction time was also varied from 24 to 48 h under pH 12. Finally, NaCl-free product was dried under the IR lamp (considered as-prepared sample) and then annealed at 500 °C in air for 2 h to convert into the final product (CR sample). Two grams of commercial anatase TP was converted into 1.87 g of a mixed phase of anatase TiO<sub>2</sub> and Na<sub>0.23</sub>TiO<sub>2</sub> CR. Around 90% and above yield was obtained in all the cases.

**Material Characterization:** TGA and DTA of the as-synthesized sample were carried out from room temperature to 550 °C with a heating rate of 10 °C min<sup>-1</sup> on a NETZSCH 449C simultaneous thermal analyzer to understand the thermal decomposition nature. Structural properties of the as-prepared and calcined powders were characterized by XRD method on an X'Pert Pro MPD XRD of PANanalytical system with CuK $\alpha$  radiation ( $\lambda = 1.5406 \text{ \AA}$ ). The optical property of the composite sample and its dye (N719) loading capability was measured by a UV-vis-NIR spectrophotometer (Shimadzu, UV-3600). The morphology of the precursor, as-prepared and calcined samples, was monitored through FESEM (LEO 430i, Carl Zeiss) and a high-resolution transmission electron microscope operating at 300 kV (Tecnai G2 30ST, FEI). The surface charge analysis (zeta potential) of the sample was measured using a Horiba nanoparticle analyzer SZ100. Besides, the XPS measurements were carried out by a PHI 5000 VersaProbe II scanning XPS microprobe (ULVAC-PHI, USA). BET specific surface area of a sample was measured using a Quantachrome (iQ3) instrument after evacuation at 150 °C for 4 h including the BJH pore size distribution. Thickness measurement and EDX of fabricated nanorod film was performed in the same instrument used for FESEM. The diffuse reflectance spectrum of the films was measured using UV-vis-NIR spectrophotometer (Shimadzu, UV-3600).<sup>[11,45]</sup>

**Fabrication of DSSC:** The photoanode films having an area of 0.2826 cm<sup>2</sup> were fabricated by a screen printing method (120T mesh in<sup>-1</sup>, Mascoprint, UK) on FTO (7  $\Omega$  cm<sup>-2</sup>) glass substrate using a homemade paste made with ethyl cellulose and  $\alpha$ -terpinol (Sigma-Aldrich). The coated films were annealed in an oven at 450 °C for 30 min. The prepared photoanode films were soaked in the Di-tetrabutylammonium cis-bis(isothiocyanato)bis(2,2'-bipyridyl)-4,4'-dicarboxylato)ruthenium (II), N719 dye (0.5  $\times 10^{-3}$  M, Solaronix) with absolute ethanol (Merck, Germany) at room temperatures for 24 h for the dye adsorption on the film. After dye adsorption, the prepared films were thoroughly washed with absolute ethanol for removing the excess dye molecules present at the surface of the film. Platinum (Pt) solution (Platisol T, BN 40/170311FM, Solaronix, Switzerland) having Pt particles in size range of 10–20 nm was drop cast on a cleaned FTO glass. The deposited layer was gradually dried in air and then heated at 450 °C for 15 min to activate the platinum layer for working. Finally, the prepared I<sub>3</sub><sup>-</sup>/I<sup>-</sup> liquid electrolyte was infiltrated into the photoanode cell, and a sandwiched DSSC device with the Pt counter electrode was fabricated. The dye adsorbed TiO<sub>2</sub>, and Pt-FTO glass was merged like sandwich-type with a hot-melt film (≈25  $\mu$ m, Surlyn, Dyesol) between them. The photovoltaic performance of the prepared sandwich-type devices was measured under 1000 W m<sup>-2</sup> light from a Wacom AAA continuous solar simulator (model: WXS-210S-20, AM1.5G). The I–V characteristic study was carried by using an EKO MP-160i I–V Tracer.<sup>[11,27]</sup> All the data represented are



an average of measurements taken on five different devices for all the samples. EIS measurements were performed with an Autolab frequency analyzer setup equipped with an Autolab PGSTAT 10 and a frequency response analyzer module under solar simulator condition with the frequency range from 0.1 Hz to 100 kHz and at the 0.70 V open-circuit voltage of the devices. The cyclic voltammetry analysis was carried out in a three-electrode assembly cell comprising the composite film as the working electrode, Ag/AgCl as reference electrode, and platinum as the counter electrode in the presence of  $I^-/I_3^-$  electrolyte using the NOVA software equipped with the Autolab potentiostat/galvanostat instrument. Besides, the IPCE was measured on a Bentham PVE300 photovoltaic EQE (IPCE) under 300–800 nm wavelength range.

**Fabrication of Gas Sensor and Measurements:** The optimized powder samples were used for preparing the paste for sensor fabrication. Sensor fabrication and details are reported elsewhere.<sup>[57,58]</sup> After making a coating of the paste on the alumina substrate, it was dried at 80 °C. When the fabricated sensor element was exposed to acetone, the resistance of the sample changed, and the response was calculated from the change in resistance at room temperature. The response level was measured towards various concentration levels of acetone, and sensitivity percentage (*S*) was calculated as the ratio of  $R_g/R_a$  where the electrical resistances are denoted as  $R_g$  and  $R_a$  in the presence of acetone and air, respectively. The electrical measurements were performed by using an Agilent multimeter (model no. U1253A). The AC measurements were carried out on a precision impedance analyzer (6500B, Wayne Kerr) within a wide range of frequency from 100 Hz to 1 MHz.

## Supporting Information

Supporting Information is available from the Wiley Online Library or from the author.

## Acknowledgements

PSD acknowledges the financial support from CSIR through the Nano-Bio Mission (HCP12) program. P.G. gratefully acknowledges INSPIRE program of the Department of Science and Technology (DST), Government of India, for the Ph.D. fellowships. A.R. acknowledges Newton-Bhabha Fellowship Program 2016–2017 funded by DST, Government of India and the British Council. The authors acknowledge the help rendered by Dr. Jiten Ghosh, Principal Scientist, Advanced Mechanical and Material Characterization Division, CSIR-Central Glass and Ceramic Research Institute, Jadavpur, Kolkata, for the XRD analysis.

## Conflict of Interest

The authors declare no conflict of interest.

## Keywords

acetone sensors, anatase, hydrothermal synthesis, nanorods, photovoltaics, sodium titanate

Received: July 31, 2020

Revised: November 3, 2020

Published online:

[1] H. Zhang, J. F. Banfield, *Chem. Rev.* **2014**, *114*, 9613.

[2] R. Verma, J. Gangwar, A. K. Srivastava, *RSC Adv.* **2017**, *7*, 44199.

- [3] F. D. Angelis, C. D. Valentin, S. Fantacci, A. Vittadini, A. Selloni, *Chem. Rev.* **2014**, *114*, 9708.
- [4] S. D. Mo, W. Y. Ching, *Phys. Rev. B* **1995**, *51*, 13023.
- [5] D. A. H. Hanaor, C. C. Sorrell, *J. Mater. Sci.* **2011**, *46*, 855.
- [6] P. Selvaraj, A. Roy, H. Ullah, P. S. Devi, A. A. Tahir, T. K. Mallick, S. Sundaram, *Int. J. Energy Res.* **2019**, *43*, 523.
- [7] B. Liu, E. S. Aydil, *J. Am. Chem. Soc.* **2009**, *131*, 3985.
- [8] N.-G. Park, J. van de Lagemaat, A. J. Frank, *J. Phys. Chem. B* **2000**, *104*, 8989.
- [9] G. Li, C. P. Richter, R. L. Milot, L. Cai, C. A. Schmuttenmaer, R. H. Crabtree, G. W. Brudvig, V. S. Batista, *Dalton Trans.* **2009**, <https://doi.org/10.1039/B908686B>.
- [10] J. Tian, Z. Zhao, A. Kumar, R. I. Boughton, H. Liu, *Chem. Soc. Rev.* **2014**, *43*, 6920.
- [11] A. Roy, P. P. Das, P. Selvaraj, S. Sundaram, P. S. Devi, *ACS Sustainable Chem. Eng.* **2018**, *6*, 3299.
- [12] K. Lee, A. Mazare, P. Schmuki, *Chem. Rev.* **2014**, *114*, 9385.
- [13] Y. Bai, I. Mora-Sero, F. D. Angelis, J. Bisquert, P. Wang, *Chem. Rev.* **2014**, *114*, 10095.
- [14] T. Sagawa, S. Yoshikawa, H. Imahori, *J. Phys. Chem. Lett.* **2010**, *1*, 1020.
- [15] S. Mukhopadhyay, D. Maiti, A. Saha, P. S. Devi, *Cryst. Growth Des.* **2016**, *16*, 6922.
- [16] P. I. Gouma, M. J. Mills, *J. Am. Ceram. Soc.* **2001**, *84*, 619.
- [17] M. Evain, M. H. Whangbo, L. Brohan, R. Marchand, *Inorg. Chem.* **1990**, *29*, 1413.
- [18] Z. Q. Guo, J. P. Zhou, L. L. An, J. X. Jiang, G. Q. Zhu, C. Y. Deng, *J. Mater. Chem. A* **2014**, *2*, 20358.
- [19] J. Z. Wang, J. P. Zhou, Z. Q. Guo, Y. X. Lei, Q. U. Hassan, *Cryst. Res. Technol.* **2018**, *53*, 1700153.
- [20] J. Huang, R. Meng, L. Zua, Z. Wang, N. Feng, Z. Yang, Y. Yu, J. Yang, *Nano Energy* **2018**, *46*, 20.
- [21] D. Morais da Silva, B. S. Canuto de Menezes, V. D. N. Bezzon, T. L. A. Montanheiro, E. F. Macedo, D. B. Tada, G. Petracconi, G. P. Thim, *SN Appl. Sci.* **2019**, *1*, 945.
- [22] A. Fujishima, T. N. Rao, *J. Chem. Sci.* **1997**, *109*, 471.
- [23] Y. Paz, A. Heller, *J. Mater. Res.* **1997**, *12*, 2759.
- [24] X. Wu, G. M. Lu, L. Wang, *J. Colloid Interface Sci.* **2013**, *391*, 70.
- [25] S. Shalini, R. Balasundaraprabhu, T. S. Kumar, N. Muthukumarasamy, S. Prasanna, K. Sivakumaran, M. D. Kannan, *Mater. Lett.* **2018**, *221*, 192.
- [26] S. Mukhopadhyay, D. Maiti, S. Chatterjee, P. Sujatha Devi, G. S. Kumar, *Phys. Chem. Chem. Phys.* **2016**, *18*, 31622.
- [27] A. Roy, S. Mukhopadhyay, P. Sujatha Devi, S. Sundaram, *ACS Omega* **2019**, *4*, 1130.
- [28] B. Fan, Y. Zhang, R. Yan, J. Fan, *CrystEngComm* **2016**, *18*, 6492.
- [29] M. Lin, Z. Y. Fu, H. R. Tan, J. P. Y. Tan, S. C. Ng, E. Teo, *Cryst. Growth Des.* **2012**, *12*, 3296.
- [30] Y. V. Kolen'ko, K. A. Kovnir, A. I. Gavrilo, A. V. Garshev, J. Frantti, O. I. Lebedev, B. R. Churagulov, G. Van Tendeloo, M. Yoshimura, *J. Phys. Chem. B* **2006**, *110*, 4030.
- [31] J. NoéDíaz de León, J. R. Rodríguez, J. Rojas, Y. E. Barrón, L. Cardenas, C. R. Kumar, G. A. Nuñez, S. F. Moyado, *Front. Chem.* **2019**, *7*, 750.
- [32] C. C. Tsai, H. Teng, *Chem. Mater.* **2006**, *18*, 367.
- [33] S. Shalini, N. Prabavathy, R. Balasundaraprabhu, T. S. Kumar, P. Walke, S. Prasanna, D. Velayuthapillai, *J. Mater. Sci.: Mater. Electron.* **2017**, *28*, 3500.
- [34] V. M. Ramakrishnan, N. Muthukumarasamy, P. Balraju, S. Pitchaiya, D. Velauthapillai, A. Pugazhendhi, *Int. J. Hydrogen Energy* **2020**, *45*, 15441.
- [35] J. Y. Eom, S. J. Lim, S. M. Lee, W. H. Ryu, H. S. Kwon, *J. Mater. Chem. A* **2015**, *3*, 11183.
- [36] M.-N. Li, Z.-Y. Chi, Y.-C. Yu, *J. Am. Ceram. Soc.* **2012**, *95*, 3297.
- [37] L. Lan, Z. Yichao, L. Yanzhong, Z. Kaiqiang, H. Jinxian, H. Zhigao, M. Sanjay, H. Zhensheng, *Nanoscale* **2020**, *12*, 230.

- [38] D. Nassoko, Y. F. Li, J. L. Li, X. Li, Y. Yu, *Int. J. Photoenergy* **2012**, 2012, 716087.
- [39] I. Singh, B. Birajdar, *RSC Adv.* **2017**, 7, 54053.
- [40] A. Sinhamahapatra, J.-P. Jeon, J.-S. Yu, *Energy Environ. Sci.* **2015**, 8, 3539.
- [41] Y. Dong, K. Pan, G. Tian, W. Zhou, Q. Pan, T. Xie, D. Wang, H. Fu, *Dalton Trans.* **2011**, 40, 3808.
- [42] L. Qi, C. Li, Y. Chen, *Chem. Phys. Lett.* **2012**, 539, 128.
- [43] J.-Y. Liao, J.-W. He, H. Xu, D.-B. Kuang, C.-Y. Su, *J. Mater. Chem.* **2012**, 22, 7910.
- [44] T. Peng, J. Xu, R. Chen, *Chem. Phys. Lett.* **2020**, 738, 136902.
- [45] P. P. Das, A. Roy, S. Das, P. S. Devi, *Phys. Chem. Chem. Phys.* **2016**, 18, 1429.
- [46] L. Wei, P. Wang, Y. Yang, R. Fan, Y. Yang, Y. Qiu, *Sustainable Energy Fuels* **2017**, 1, 1112.
- [47] A. Latin, C. Cavallo, F. K. Aldibaja, D. Gozzi, *J. Phys. Chem. C* **2013**, 117, 25276.
- [48] G. Yang, H. Ding, J. Feng, Q. Hao, S. Sun, W. Ao, D. Chen, *Sci. Rep.* **2017**, 7, 14594.
- [49] D. Yang, H. Liu, Z. Zheng, Y. Yuan, J. Zhao, E. R. Waclawik, X. Ke, H. Zhu, *J. Am. Chem. Soc.* **2009**, 131, 17885.
- [50] Y. Chimupala, P. Junploy, T. Hardcastle, A. Westwood, A. Scott, B. Johnson, R. Brydson, *J. Mater. Chem. A* **2016**, 4, 5685.
- [51] P. P. Das, S. A. Agarkar, S. Mukhopadhyay, U. Manju, S. B. Ogale, P. S. Devi, *Inorg. Chem.* **2014**, 53, 3961.
- [52] A. Roy, P. P. Das, M. Tathavadekar, S. Das, P. S. Devi, *Beilstein J. Nanotechnol.* **2017**, 8, 210.
- [53] M. Ge, C. Cao, J. Huang, S. Li, Z. Chen, K. Q. Zhang, S. S. Al-Deyab, Y. Lai, *J. Mater. Chem. A* **2016**, 4, 6772.
- [54] P. Mazzolini, T. Acartürk, D. Chrastina, U. Starke, C. S. Casari, G. Gregori, A. L. Bassi, *Adv. Electron. Mater.* **2016**, 2, 1500316.
- [55] A. Staerz, U. Weimar, N. Barsan, *Sensor* **2016**, 16, 1815.
- [56] N. Zhang, S. Ruan, Y. Yin, S. Wen, Y. Chen, *ACS Appl. Nano Mater.* **2018**, 1, 4671.
- [57] P. Nag, S. Banerjee, Y. Lee, A. Bumajdad, Y. Lee, P. S. Devi, *Inorg. Chem.* **2012**, 51, 844.
- [58] P. Nag, S. Majumdar, A. Bumajdad, P. S. Devi, *RSC Adv.* **2014**, 4, 18512.



## Efficient carbon counter electrodes for BaSnO<sub>3</sub>-based dye-sensitized solar cells

Anurag Roy <sup>a,b,\*</sup>, Puja Ghosh <sup>a</sup>, Parukuttyamma Sujatha Devi <sup>a,c</sup>, Senthilarasu Sundaram <sup>b</sup>, Tapas K. Mallick <sup>b</sup>

<sup>a</sup> Functional Materials and Devices Division, CSIR-Central Glass and Ceramic Research Institute, 196 Raja S.C. Mullick Road, Jadavpur, Kolkata 700032, India

<sup>b</sup> Environment and Sustainability Institute, University of Exeter, Penryn Campus, Cornwall TR10 9FE, UK

<sup>c</sup> Chemical Science and Technology Division, CSIR-National Institute for Interdisciplinary Science and Technology, Thiruvananthapuram, Kerala 695019, India

### ARTICLE INFO

#### Article history:

Received 27 August 2020

Accepted 11 November 2020

Available online 4 January 2021

#### Keywords:

DSSC

BaSnO<sub>3</sub>

Carbon

Counter Electrode

Photovoltaic

### ABSTRACT

Natural source derived carbon materials make them ideally suited alternative to costly Pt counter electrode for their good catalytic activity, resistance to iodine corrosion, and high stability of the device. Apart from the extensively acclaimed photoanode TiO<sub>2</sub>, BaSnO<sub>3</sub> (BSO) has been projected as an efficient alternative to it. In this study, remarkable efforts have been endeavoured to establish BSO-carbon-based dye-sensitized solar cell (DSSC) device. Investigation on the adequate performance of natural source derived carbon-based counter electrodes for BSO-based DSSCs, explored as a significant alternative to costly Pt and TiO<sub>2</sub>, respectively, which could elucidate better photo-stability and more extended device performance compared to TiO<sub>2</sub>-Pt-based DSSCs.

© 2020 Elsevier Ltd. All rights reserved.

Selection and peer-review under responsibility of the scientific committee of the Second International Symposium “Functional Nanomaterials in Industrial Applications: Academy – Industry Meet”.

### 1. Introduction

The trilemma of cost of energy, the security of supply, and human-made climate change are driving the move to the development and use of sustainable non-polluting energy sources that can also achieve low cost. While researching new ways to increase the efficiency of utilizing solar energy, technology is continuously being developed into new and better-advanced result. The discovery of dye-sensitized solar cells (DSSCs) in 1991 by Grätzel and co-workers stands out as one of the front-runners given the fundamental novelty of the concept derived from nature's principles [1]. The chemical way of assembling the cell architecture, which allows easy and cost-effective processing alternatives [2]. The current efficiency of DSSC reaches 14.2% [3]. The primary advantage of DSSCs lies on higher solar to electricity conversion efficiencies with lower production costs, flexibility and eco-friendliness. The efficiency can be enhanced in many ways such as light scattering effect of the photoanode materials, stability of the dye, using electron-transporting layer, enhancement of open-circuit voltage

and fill factor and modification of DSSC device fabrication process [4]. In addition, the development of Pt-free counter electrode (CE) material can make DSSCs more competitive among various photovoltaic devices. An excellent CE material should possess (a) high stability and (b) high catalytic activity and Pt holds two properties; that is the reason for using it as the best CE material [5]. However, Pt is costly and resulting in iodine corrosion. In this regard, attempts have been in progress to replace the costly Pt electrode with other cost-effective materials. Different nanostructured materials, including metal oxides, oxide perovskites and carbon-based composites, have been studied for photoanodes, and counter electrodes, which are crucial to achieving DSSC devices with higher efficiency and better stability. Many studies have been carried out to reduce the amount of Pt used in DSSCs and/or to explore alternatives to Pt, but mostly they deal with the TiO<sub>2</sub> based photoanode, which becomes stagnant and attained a limited area of research [6–8].

Carbon, which is one of the most abundant material in the earth's crust, is the best material to replace Pt. Mainly due to its core features like cost-effectiveness, environmental friendliness, availability, corrosion resistance and excellent catalytic activity towards the redox species. At the same time, the development of

\* Corresponding author.

E-mail address: [A.Roy30@exeter.ac.uk](mailto:A.Roy30@exeter.ac.uk) (A. Roy).

new materials as such carbon using cost-effective and abundant elements such as carbon for fabricating novel electrodes have also become technologically desirable [9–12]. Introduction of different carbon materials and device developments can significantly increase the regular performance of the conventional DSSC device. The different combinations in which carbon atoms can be arranged to produce a wide variety of compounds that have unique and exciting physical, chemical, and electronic properties. Thus, carbon-based devices offer several attractive features for use in next-generation electronics. Ramuz et al. (2012) reported their efforts into the fabrication of the first reported all-carbon solar cell in which all components were carbon-based [13]. Similarly, Lee et. Al. (2012) described all-carbon counter electrodes for DSSCs. An efficient way to developed fibre-shaped DSSC based on an all-carbon electrode was also reported by Cai et. Al. (2012) [14]. However, the stability of these cells is yet to be studied for practical implementation.

Lesser electron mobility, higher dye absorption time, metal ion dye complex formation, interfacial charge recombination between a metal oxide, electrolyte and overall limited synthesis strategies are issued that restrict the scope of binary oxides in DSSCs [2]. In the search for alternative oxide to  $\text{TiO}_2$ ,  $\text{BaSnO}_3$  (BSO) exhibits different morphology, and interesting physicochemical properties, which can be established as a suitable alternative photoanode candidate for DSSCs [15,16]. In this report, a systematic evaluation of the DSSCs performances of the cells fabricated with the facile, cheaper and more stable BSO-based photoanode with a carbon-based CE, the synthesized materials as an alternative to costly  $\text{TiO}_2$  and Pt has been evaluated. At the same time, the performance of  $\text{TiO}_2$  based photoanode with carbon counter electrodes are also taken into account and compared with the BSO-carbon system in DSSCs. To best of our knowledge, this may be the first time we report here the BSO-Carbon photoanode-CE combination as an alternative materials based system for DSSC application.

## 2. Materials and methods

### 2.1. Development of carbon CEs for DSSC

To fabricate carbon-based CE, we have taken two different types of carbon; namely, glucose derived graphitic carbon sheet (GCS), and sesame oil derived graphitic carbon nanoparticles (GCP), the synthesis and various physicochemical characterizations of the

synthesized carbon have been already reported in our previous publication [17,18]. The synthesized powders have been now introduced to prepare CEs for DSSCs. Individually, 5.1 mg of synthesized carbon powder was added to 5 mg of Triton X-100 (Sigma Aldrich) in 3 mL of ethanol and stirred for 30 min, followed by ultrasonication for 1 h. Finally, the supernatant was carefully decanted and the rest of the part used for further process. The conductive side of a dried FTO was placed on the holder of a spin coater unit (Midas Spin-3000A, Korea) and the solution was spin-coated at 5500 rpm for 90 sec. We have repeated three cycles for the same and after that carefully washed with distilled water and baked for 30 min, at 120 °C. The film was further dipped in 60%  $\text{HNO}_3$  (Merck, India) for 1 h to enhance the electrical conductivity of the synthesized carbon powder and removal of Triton X-100. Finally, the spin-coated film was dried entirely under an infrared (IR) lamp and used as a CE in a DSSC device. The overall scheme of this study has been described in Fig. 1.

### 2.2. Synthesis of $\text{BaSnO}_3$ nanoparticle

$\text{BaSnO}_3$  (BSO) nanoparticles were prepared as reported in the literature [15]. In short, 10 mM each of  $\text{BaCl}_2 \cdot 2\text{H}_2\text{O}$  (Emsure, Merck, India) and  $\text{SnCl}_4 \cdot 5\text{H}_2\text{O}$  (98% pure, Loba Chemicals, India) were thoroughly stirred under 30%  $\text{H}_2\text{O}_2$  (Emparta, Merck, India) medium for 30 min to form a homogeneous solution. A 25%  $\text{NH}_4\text{OH}$  (Merck, India) solution was added dropwise to the mixed solution until the pH of the resultant solution reached 10. The solution was centrifuged at 10,000 rpm, and a white product was collected. The product was entirely dried under an IR lamp, and further calcined at 1000 °C for 8 h to produce the  $\text{BaSnO}_3$  phase. The obtained powder was allowed to make a paste using ethyl cellulose and terpinol (Sigma Aldrich). Finally, the paste was used to prepare the photoanode using the screen printing method.

### 2.3. Material characterizations

The Raman spectra have been performed on a STR500 (Cornes Technologies system by using 514.5 nm  $\text{Ar}^+$  green laser with 50 mW power). The room temperature photoluminescence (PL) spectra with a steady-state spectrofluorometer (QM-40, Photon Technology International, PTI) using a 150 W xenon lamp as an excitation source, using 5 nm band-pass. Nitrogen physisorption measurements of all the samples were carried out by using a

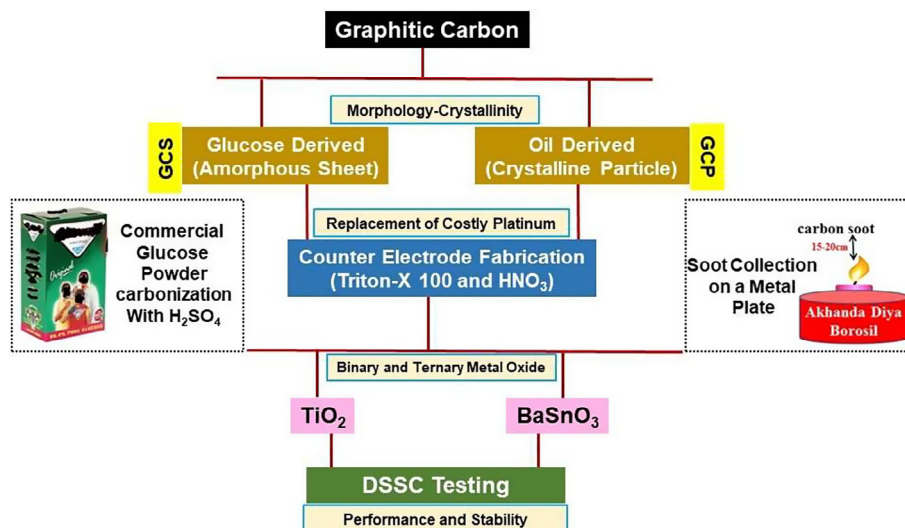


Fig. 1. Schematic illustration of the overall approach of this study.

Quantachrome (iQ3) instrument after evacuation at 80 °C for 2 h. The specific surface area was calculated by the Brunauer-Emmett-Teller (BET) method, whereas desorption cumulative pore volume and pore size distribution were calculated by the Barrett-Joyner-Halenda (BJH) method. The morphology of the synthesized powder has been monitored on a Tecnai G2 30ST (FEI) high-resolution transmission electron microscope (TEM) operating at 300 kV. The transmittance spectra of the fabricated carbon films were measured on a UV-vis-NIR spectrophotometer (Shimadzu UV-3600). The surface microstructure of the fabricated carbon films was checked on a field emission scanning electron microscope (FESEM) (Supra 35VP, Carl Zeiss).

#### 2.4. DSSC device assembly and testing

The TiO<sub>2</sub> paste (18 NR-T and 18 NR-O) was obtained from Dyesol(R), now known as Greatcell Solar. Ruthenium 535 bis-TBA (N719) dye, Pt electrode, and plastic spacer (Meltonix) were obtained from Solaronix, SA in this work.

The prepared I<sup>-</sup>/I<sub>3</sub> electrolyte has been used for the device testing. The complete assembling and final device fabrication protocol of the DSSC testing have been described in our previous report [15,16]. The active area of the dye-coated BSO and TiO<sub>2</sub> film was 0.2826 cm<sup>2</sup>. The only difference is instead of Pt electrode, we have used the fabricated carbon CEs in this study. Further, the photovoltaic testing of the fabricated DSSCs was executed under 1000 W.m<sup>-2</sup> of light from a Wacom AAA continuous solar simulator (model: WXS-210S-20, AM1.5G). The I-V characteristic of the devices was recorded using an EKO MP-160i I-V Tracer.

### 3. Results and discussions

#### 3.1. TEM analysis

The transmission electron microscopic (TEM) images obtained from the as-prepared GCS sample are shown in Fig. 2a-c. The sample exhibited a layered elliptical sheet-like structure, with visible

porosity as evident in the bright field images, as shown in Fig. 2a and b. The selected area electron diffraction (SAED) pattern of the as-prepared sheet appears amorphous, as shown in Fig. 2c. Similarly, the TEM images obtained from GCP sample has been shown in Fig. 2d-f. The particles exhibited chain-like structures as evident from Fig. 2d and e. The size of the individual carbon nanoparticles varied in the range of 20–45 nm and the average particle size varied as 30.5 ± 2 nm. The corresponding SAED pattern suggests the absence of distinguishable lattice structures for carbon nanoparticle indicating a partially crystalline nature of individual carbon nanoparticles indicating (002) and (101) planes of graphitic carbon, respectively.

#### 3.2. Optical and surface area analysis

To further evaluate the optical properties of the two different carbon material, the Raman and photoluminescence characteristics were studied. The Raman spectra of the synthesized carbons are presented in Fig. 3a. Raman spectrum of the GCS sample exhibits the characteristics graphite band (G) appearing at 1540 cm<sup>-1</sup>, defect (D) for disorder band (sp<sup>3</sup>) appearing at 1358 cm<sup>-1</sup> and G', or 2D band at 2896 cm<sup>-1</sup> dominate in the Raman spectrum of graphitic carbon nanoparticles. The G band corresponds to the high-frequency Raman active E<sub>2g</sub> mode (sp<sup>2</sup> carbon) of single-crystal graphite, and the broad D band corresponds to A<sub>1g</sub> mode arising out of disordered graphite and indicates the presence of nanocrystalline graphitic nanoparticles [17,18]. The I<sub>D</sub>/I<sub>G</sub> ratio of around 0.883 confirms the graphitic nature of the synthesized carbon along with a broad 2D band, as shown in Fig. 3a. The existence of a broad 2D band could be a clear indication of the formation of disordered graphitic carbon with more graphene layers. In case of GCP sample, we have observed the G band around ~1586 cm<sup>-1</sup> and D band around ~1349 cm<sup>-1</sup> as appeared due to the presence of sp<sup>2</sup> and sp<sup>3</sup> kind of carbon with I<sub>D</sub>/I<sub>G</sub> ratio of 0.9293, indicating a high degree of graphitization (Fig. 3a). This ratio is also a measure of the extent of the disorder and sp<sup>3</sup>/sp<sup>2</sup> carbon atoms. There is also a starking difference in the full width at half maxima (FWHM) of

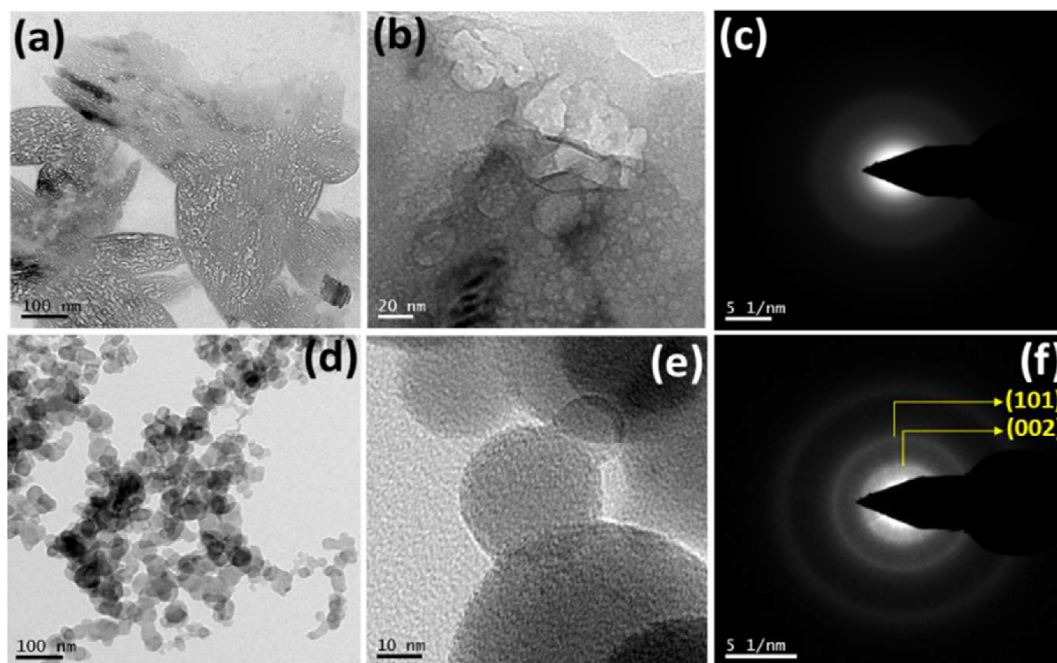


**Fig. 2.** TEM bright-field images of glucose-derived porous carbon sheet (a)-(b) at different magnification, (c) corresponding SAED pattern, (d)-(e) TEM bright-field images of sesame oil-derived carbon nanoparticles at different magnifications and (f) corresponding SAED pattern.

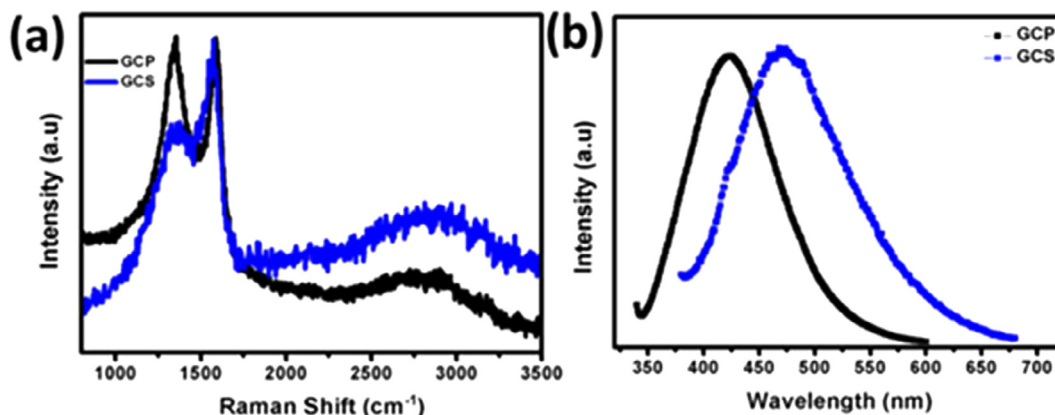


Fig. 3. (a) Raman and (b) photoluminescence spectra of GCP and GCS samples.

both G and D bands of the synthesized carbon sample compared to that of the standard graphite powder. This broadening represents a direct indication of an increased level of disorder due to the presence of  $sp^3$ -G and a decrease in the graphitic domain size. The broadening of the D band also implies an increased level of disorder and a decrease in the graphitic domain size. The recombination of carbon bonds during carbon nanoparticle formation introduces smaller graphitic domains with a different bond. This could again be a clear indication of the formation of disordered graphitic carbon with more graphene layers. To gain insight into the optical properties of the prepared synthesized carbon samples, we carried out the fluorescence studies on the water dispersions of the particles at a pH of  $\sim 6.8$ . As evident from Fig. 3b, the most substantial emission maximum appeared at 458 nm upon 360 nm excitation exhibited excellent blue emission without any surface functionalization or surface treatment for glucose-derived carbon sheet. Whereas, the sesame oil-derived carbon nanoparticles exhibited excellent blue emission at a lower wavelength than the other one. The maximum UV emission occurred on 280 nm excitation, and the maximum visible emission occurred on 350 nm excitation. The most exciting feature of the PL of these samples is the explicit dependence of the excitation wavelength on both emission wavelength and intensity [18]. The distinct PL characteristics entirely generated due to the presence of defect mediated states (D and 2D band) and their different distribution in the synthesized carbon sample as observed from Fig. 3b. The zeta potential measurement result further indicates carbon sheets containing more surface-functionalized group form stable aqueous dispersion, whereas the nanoparticles are comparably weaker to form an aqueous dispersion. Though, in case of electrophoretic mobility analysis, the later one shows higher value than the previous one may be due to discrete particle formation compared to the stacked sheet-like assembling. The comparative data has been tabulated in Table 1. Surface area analysis also plays a pivotal role in the catalytic activity of carbon. There is a significant difference in the BET surface area measurement. Due to multi-oriented distribution of the sheet-like structure and visible porosity appearance, the glucose derived carbon possess higher BET surface area and pore size of  $140 \text{ m}^2 \cdot \text{g}^{-1}$  and 5–8 nm, respectively than sesame oil derived particle carbons where the later having the value of BET surface area

and pore size distribution was  $55 \text{ m}^2 \cdot \text{g}^{-1}$ , and 10–20 nm, respectively (Table 1).

### 3.3. Characterization of the carbon films

FESEM microstructural analyses of the carbon films are shown in Fig. 4a and b. In the case of graphitic carbon series, the GCP film exhibits the porous exfoliated structure of the film surface as obtained from the FESEM analysis as shown in Fig. 4a. Agglomeration of particles may have resulted in the formation of a sheet-like continuous layer of carbon materials. Whereas, the GCS film exhibited a sheet like the one structure spread over the FTO surface and attained a high degree of porosity and surface area, as shown in Fig. 4b. It is also interesting to notice the transmittance spectra of the fabricated films (Fig. 4c). The effective performance can satisfy the compromise between efficiency and transparency of the cell. As per Fig. 4c, GCP films show higher order of transparency,  $\sim 60\%$  in the visible region (200–800 nm) than the GCS film where the transmittance of the film was observed  $\sim 50\%$  at the same wavelength region. The digital images of respective carbon films along with the bare FTO glass, as shown in Fig. 4d indicates the relative transparency of the sample. Finally, the carbon electrodes were explored in DSSCs with BSO, and the result has been compared with the commercial  $\text{TiO}_2$ .

### 3.4. Photovoltaic performance of the carbon CEs

The comparative photovoltaic performance as  $J$ - $V$  characteristics plot is shown in Fig. 5a and corresponding parameters for each of them have been further illustrated in Table 2. The fabricated GCP CE exhibited a maximum conversion efficiency ( $\eta$ ) of 3.81% with a short circuit current ( $J_{sc}$ )  $9.60 \text{ mA} \cdot \text{cm}^{-2}$ , open-circuit voltage ( $V_{oc}$ ) 0.74 V and a fill factor (FF) of 0.54 for BSO based photoanode. On the contrary, with the same photoanode, the GCS counter electrode exhibited a  $\eta$  of 2.24% with a  $J_{sc}$   $9.05 \text{ mA} \cdot \text{cm}^{-2}$ ,  $V_{oc}$  0.84 V and FF of 0.64. At the same time, the GCP and GCS CEs were further tested with  $\text{TiO}_2$ -based devices, and maximum efficiency of 4.61 and 3.27% were achieved, respectively. It has been observed that crystallinity does not make any significant effect on CE performance as seen from the performance of GCS and GCP based films. Instead,

Table 1

Comparative physicochemical characteristics of synthesized carbon samples.

Sample	Morphology	Zeta Potential (mV)	Electrophoretic Mobility at $300 \text{ K} \times 10^{-3} (\text{cm}^2 \cdot \text{V}^{-1} \cdot \text{s}^{-1})$	BET Surface Area ( $\text{m}^2 \cdot \text{g}^{-1}$ )	BJH Pore Size (nm)
GCS	Sheet	-31.1	0.067	140	5–8
GCP	Particle	-12.5	0.175	55	10–20

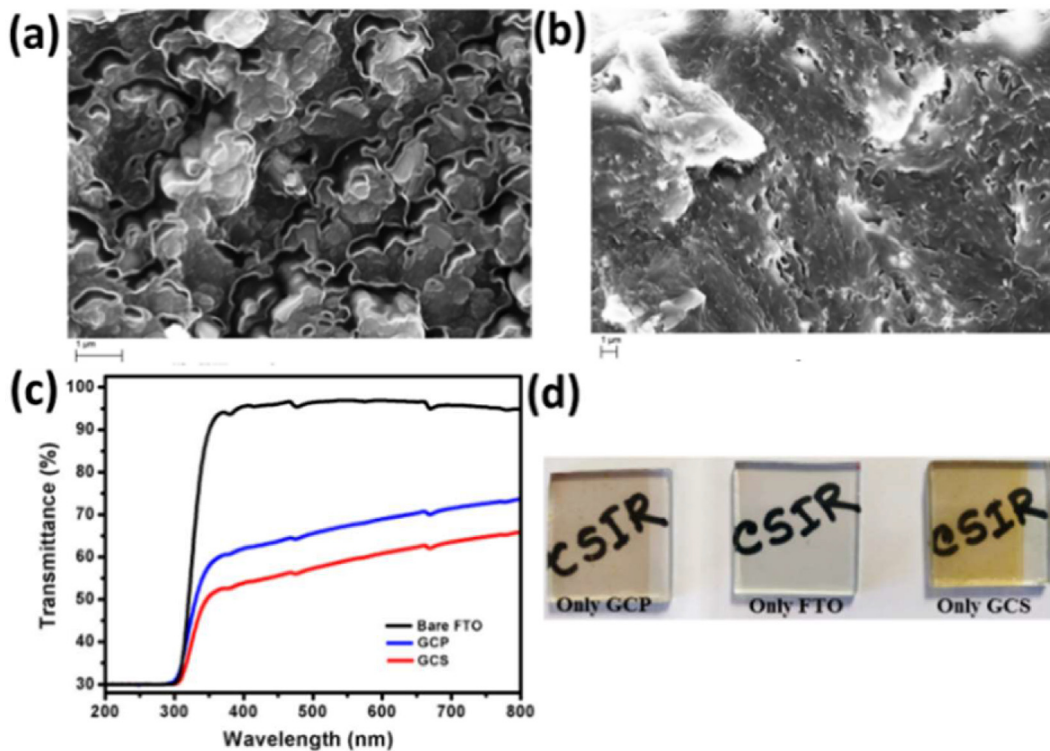


Fig. 4. FESEM images of (a) GCP, (b) GCS films, respectively, (c) Transmittance spectra of the GCP and GCS film compared with bare FTO glass and (d) photograph of fabricated films compared with bare FTO glass.

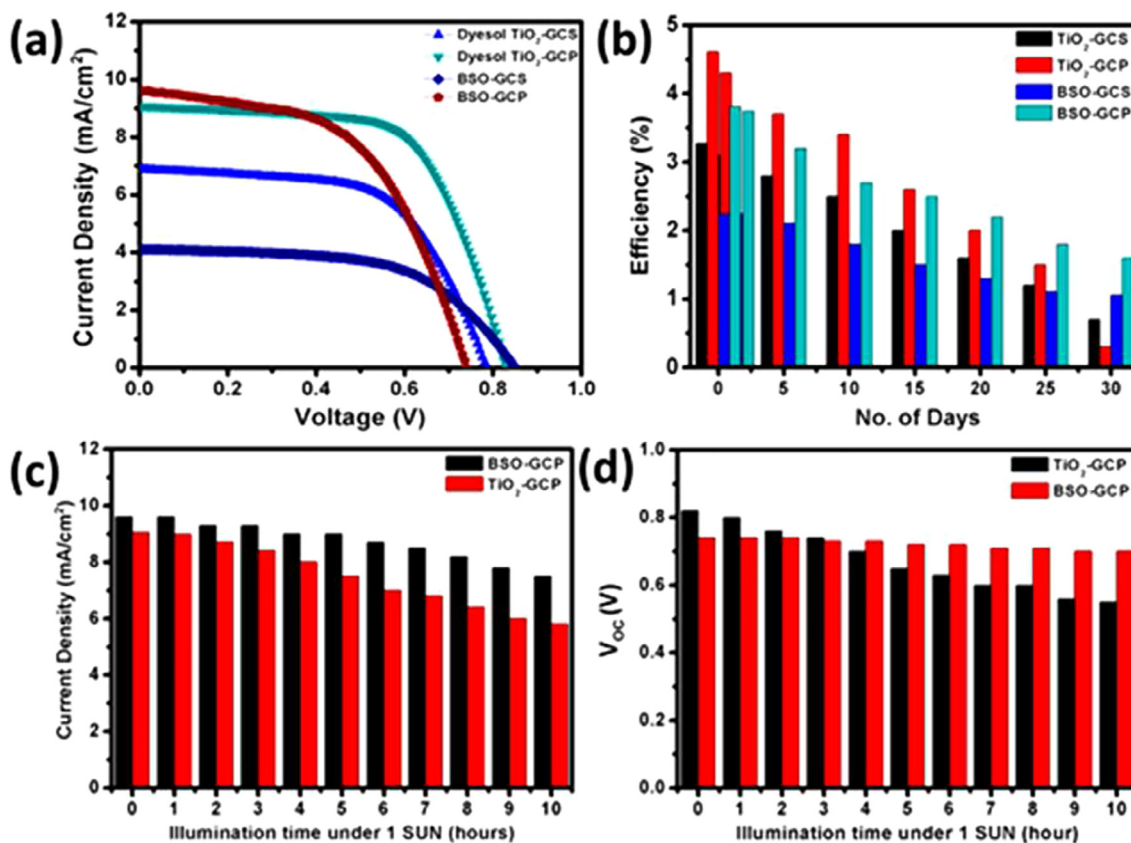


Fig. 5. (a) Current density–voltage characteristics plot, (b) efficiency stability plot of GCP and GCS counter electrodes for TiO<sub>2</sub> and BSO-based DSSC devices, respectively, (c) and (d) comparative plot of current density (J<sub>sc</sub>) and open-circuit voltage (V<sub>oc</sub>) of the BSO-GCP and TiO<sub>2</sub>-GCP cells under constant 1 SUN 1.5 AM illumination for 10 h.

**Table 2**  
Photovoltaic performance of carbon CEs for TiO<sub>2</sub> and BSO-based DSSCs.

Device (Photoanode-CE)	J <sub>SC</sub> ± 0.2 (mA/cm <sup>2</sup> )	V <sub>OC</sub> (V)	FF	PCE (%) ± 0.2
TiO <sub>2</sub> -GCS	6.88	0.78	0.61	3.27
TiO <sub>2</sub> -GCP	9.05	0.82	0.64	4.61
BSO-GCS	4.11	0.84	0.64	2.24
BSO-GCP	9.60	0.74	0.54	3.81

the performance more depends on the morphology and physico-chemical properties. The *J-V* characteristics evaluate the TiO<sub>2</sub> based devices exhibit higher efficiency than the BSO based devices for both types of carbon CE. Among the two different carbon CEs, GCP films show enhanced performance for both the photoanodes than GCS film. The exciting fact is here to be noted that both the carbon-based devices exhibit a V<sub>OC</sub> of >0.7 V for BSO-based photoanode, which is almost identical with the TiO<sub>2</sub>-based photoanode. The results interpret that carbon-based CE performs superior for BSO compared to TiO<sub>2</sub> based photoanodes. In order to further understand the sufficient stability of the BSO-carbon based devices, we have further investigated the performance stability of the BSO-carbon device and compared with TiO<sub>2</sub>-carbon device over 30 days, as shown in Fig. 5b. The efficiency of the TiO<sub>2</sub> based devices was drastically depleted for both the GCP and GCS films. Whereas, there is a steady reduction in efficiency was observed in the case of BSO-based devices for carbon films. Besides, the photovoltaic performance of GCP CEs finds better compared to GCS CE and therefore, has been selected for the photo-stability study.

We recorded the device performance as a function of illumination time under constant light power, as illustrated in Fig. 5c and d. We are interested in looking at the J<sub>SC</sub> and V<sub>OC</sub> and observed that BSO-GCP devices do not degrade over time with light soaking. Whereas, TiO<sub>2</sub>-GCP devices show comparatively faster degradation in J<sub>SC</sub>. (Fig. 5c). We recall that the photo-degradation in the J<sub>SC</sub> was attributed to the formation of light-activated metastable trap

states and their accumulation in the dye layers over a long duration, resulting in a slight decrease of photocurrent overtime under 1 SUN illumination condition [19]. The V<sub>OC</sub> measurements exhibit excellent stability of BSO-GCP devices compared to TiO<sub>2</sub>-GCP devices as observed up to 10 h constant 1 SUN illumination without additional UV filters, as shown in Fig. 5d. The overall degradation may cause due to an increase in temperature of the solar cell on constant illumination of 1 SUN [20]. Therefore, as per the overall observation from Fig. 5, as an alternative new material, the BSO-GCP device pair could be a promising competitor to TiO<sub>2</sub>-Pt in terms of photo-stable and cheaper material for DSSCs.

Fig. 6a illustrates the electronic bandgap (E<sub>g</sub>) alignment diagram of BSO and TiO<sub>2</sub>, along with the N719 dye. In term of the E<sub>g</sub> alignment, the conduction band (CB) of BSO places in a higher position compared to the CB of TiO<sub>2</sub> and bring closure to the HOMO (highest energy occupied molecular orbital) of the N719 dye molecule [21]. Actually, for BSO, the CB reveals a highly dispersed band structure leading to a small effective mass and high mobility of electrons [22]. This implies that the electrons in the conduction band of BSO can diffuse rapidly, which is also consistent with the above results. The rapid electron capture of the BSO photoanode is beneficial for efficient DSSC development.

In addition, it is anticipated that due to the higher the cathodic peak current density, carbon shows better the catalytic activity as a CE compared to Pt [23]. Besides, acidic dye aggregations turned out as a significant factor, which might be hindered the smooth diffusion of the electrons and restrict interpenetration of electrolyte through making blockage into the pores as well as the surface of the TiO<sub>2</sub> affecting the electron transportation process of the device severely as shown in Fig. 6b. The formation of the inhomogeneous metal-dye complex on the surface changes the surface properties from comparatively hydrophobic to hydrophilic nature and thus degrade the performance [24,25]. BSO-based photoanode is relatively stable to this type of acidic dyes and does not allow any dye blockage, leading to provide stability to the device.

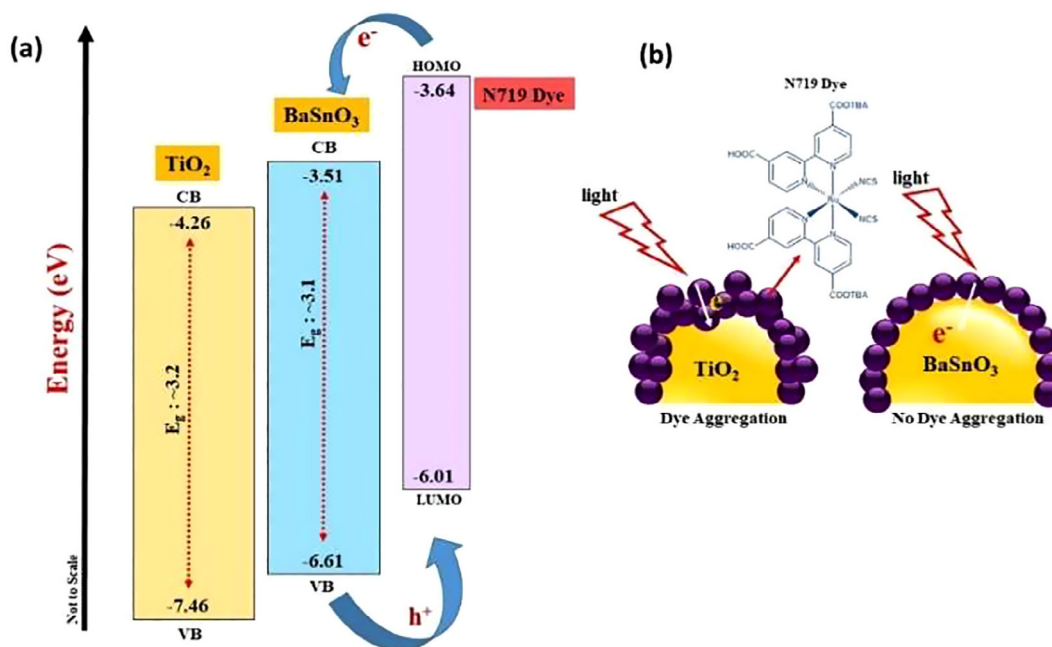


**Fig. 6.** Schematic diagram of (a) energy band alignment to TiO<sub>2</sub>, BaSnO<sub>3</sub> with the N719 dye (where HOMO: Highest energy occupied molecular orbital; LUMO: Highest energy occupied molecular orbital; VB: Valence band; CB: Conduction band; E<sub>g</sub>: Bandgap) and (b) N719 dye interaction occurs at the surface of TiO<sub>2</sub> and BaSnO<sub>3</sub> photoanodes.



#### 4. Conclusion

In conclusion, the development of carbon-based material develops an efficient replacement of the Pt-free counter electrode material, which can make DSSCs more competitive among various photovoltaic devices. Significant results of various carbon counter electrodes were further extracted with one of the major leading alternative photoanodes such as BaSnO<sub>3</sub> (BSO). Natural source derived carbon material series, 3.81% (GCP) and 2.24% (GCS) efficiencies were observed for BSO-based DSSCs. Besides, we have compared our results with the TiO<sub>2</sub> based photoanode systems. We found that BSO-GCP devices exhibit better stability than TiO<sub>2</sub>-GCP devices. The later relatively undergoes faster photodegradation in photocurrent and open-circuit voltage and therefore efficiency. Through this work, we show that improving the crystalline quality of the physicochemical characteristics and synthesis of carbon material leads to create a more reliable interface of charge carrier transport with BSO rather TiO<sub>2</sub> for DSSCs. Altogether, this constitutes an important step toward achieving photo-stable alternative material based DSSC devices for futuristic conceivable optoelectronic applications. The performance of various non-Pt based counter electrode materials can exhibit a significant performance and more efficiency on proper modification and optimization of the fabrication process. Thus, the development and evaluation of new organic and inorganic compounds as an alternative material to Pt in DSSCs is a promising research area, which is essential to reduce the cost of the devices for commercialization.

#### CRedit authorship contribution statement

**Anurag Roy:** Conceptualization, Methodology, Writing - original draft. **Puja Ghosh:** Data curation, Visualization, Resources. **Parukuttyamma Sujatha Devi:** Supervision, Investigation. **Senthilarasu Sundaram:** Supervision, Validation. **Tapas K. Mallick:** Project administration.

#### Declaration of Competing Interest

The authors declare that they have no known competing financial interests or personal relationships that could have appeared to influence the work reported in this paper.

#### Acknowledgements

A.R. gratefully acknowledges the INSPIRE program of Department of Science and Technology (DST), Govt. of India, for the PhD fellowship and Newton-Bhabha Fellowship Program 2016–2017 funded by DST, Govt. of India, and British Council. This work is partly funded by the EPSRC funded JUICE project (EP/P003605/1).

#### References

- [1] B. O'Regan, M.A. Grätzel, *Nature* 353 (1991) 737–740.
- [2] J. Gong, K. Sumathy, Q. Qiao, Z. Zhou, *Renew. Sust. Energ. Rev.* 68 (2017) 234–246.
- [3] J.-M. Ji, H. Zhou, Y.K. Eom, C.H. Kim, H.K. Kim, *Adv. Energy Mater.* 10 (2020) 2000124.
- [4] K. Sharma, V. Sharma, S.S. Sharma, *Nanoscale Res. Lett.* 13 (2018) 381.
- [5] S. Thomas, T.G. Deepak, G.S. Anjusree, T.A. Arun, S.V. Naira, A.S. Nair, *J. Mater. Chem. A* 2 (2014) 4474–4490.
- [6] S. Yun, P.D. Lund, A. Hinsch, *Energy Environ. Sci.* 8 (2015) 3495–3514.
- [7] A. Roy, P.S. Devi, S. Karazhanov, D. Mamedov, T.K. Mallick, S. Sundaram, *ALP Adv.* 8 (2018) 070701.
- [8] B. Lee, D. Buchholz, R. Chang, *Energy Environ. Sci.* 5 (2012) 6941–6952.
- [9] E. Meyer, R. Taziwa, D. Mutukwa, N. Zingwe, *Metals* 8 (12) (2018) 1080.
- [10] S. Yun, A. Hagfeldt, T. Ma, *Adv. Mater.* 26 (2014) 6210–6237.
- [11] J.D. Roy-Mayhew, I.A. Aksay, *Chem. Rev.* 114 (12) (2014) 6323–6348.
- [12] A. Roy, A. Ghosh, S. Bhandari, S. Sundaram, T.K. Mallick, *Ind. Eng. Chem. Res.* 59 (2020) 11063–11071.
- [13] M.P. Ramuz, M. Vosgueritchian, P. Wei, C. Wang, Y. Gao, Y. Wu, Y. Chen, Z. Bao, *ACS Nano* 6 (2012) 10384–10395.
- [14] X. Cai, S. Hou, H. Wu, Z. Lv, Y. Fu, D. Wang, C. Zhang, H. Kafafy, Z. Chu, D. Zou, *Phys. Chem. Chem. Phys.* 14 (2012) 125–130.
- [15] A. Roy, P.P. Das, P. Selvaraj, S. Sundaram, P.S. Devi, *ACS Sustainable Chem. Eng.* 6 (2018) 3299–3310.
- [16] A. Roy, P. Selvaraj, P.S. Devi, S. Sundaram, *Mater. Lett.* 219 (2018) 166–169.
- [17] A. Roy, S. Chatterjee, S. Pramanik, P.S. Devi, G.S. Kumar, *Phys. Chem. Chem. Phys.* 18 (2016) 12270–12277.
- [18] P.P. Das, S. Pramanik, S. Chatterjee, A. Roy, A. Saha, P.S. Devi, G.S. Kumar, *ACS Sustainable Chem. Eng.* 6 (2018) 10127–10139.
- [19] P. Salvador, M.G. Hidalgo, A. Zaban, J. Bisquert, *Phys. Chem. B* 109 (2005) 15915–15926.
- [20] I.J. Junger, D. Werner, E. Schwenzfeier-Hellkamp, A. Ehrmann, *Optik* 177 (2019) 8–12.
- [21] D.W. Kim, S.S. Shin, S. Lee, I.N. Cho, et al., *Chem. Sus. Chem.* 6 (2013) 449–454.
- [22] N. Rajamanickama, P. Soundarajan, K. Jayakumara, K. Ramachandran, *Sol. Energy Mater. Sol. Cells* 166 (2017) 69–77.
- [23] S. Gnanasekar, P. Kollu, S.K. Jeong, et al., *Sci. Rep.* 9 (2019) 5177.
- [24] J.S. Shaikh, N.S. Shaikh, S.S. Mali, J.V. Patil, et al., *Nanoscale* 10 (2018) 4987–5034.
- [25] K. Fan, J. Yu, W. Ho, *Mater. Horiz.* 4 (2017) 319–344.